

A SEARCH FOR B-L R-PARITY-VIOLATING SCALAR TOP
DECAYS IN $\sqrt{s} = 8$ TeV pp COLLISIONS WITH THE ATLAS
EXPERIMENT

Brett Jackson

A DISSERTATION

in

Physics and Astronomy

Presented to the Faculties of The University of Pennsylvania
in Partial Fulfillment of the Requirements for the Degree of Doctor of Philosophy
2015

Evelyn Thomson, Associate Professor, Physics
Supervisor of Dissertation

Marija Drndic, Professor, Physics
Graduate Group Chairperson

Dissertation Committee

I. Joseph Kroll, Professor, Physics

Burt Ovrut, Professor, Physics

Ravi Sheth, Professor, Physics

Hugh Williams, Professor, Physics

Evelyn Thomson, Associate Professor, Physics

A SEARCH FOR B-L R-PARITY-VIOLATING SCALAR TOP DECAYS IN $\sqrt{s} = 8$ TeV pp
COLLISIONS WITH THE ATLAS EXPERIMENT

COPYRIGHT
2015
Brett Jackson

All rights reserved.

Acknowledgements

I would like take a moment to thank many people who provided support throughout my graduate studies. Without their support, this thesis certainly would not have been possible. Working on ATLAS has taught me that Physics truly is a team sport. Unfortunately, I will, no doubt, miss people who helped me throughout my years as a graduate student, otherwise, this acknowledgements section would be longer than the rest of the thesis. Even if your name is not mentioned specifically, I still appreciate your help and support over the years, and I could not have done it without you.

First and foremost, I would like to thank my parents, David and Brenda Jackson, and my brother, Eric Jackson. They have been by my side through this whole journey, providing support and encouragement at every step along the way. They have pushed me to excel in my education, and to keep reaching higher, and I try to make them proud with everything I do

I must give special thanks to Evelyn Thomson and the rest of the HEP faculty at Penn, Brig Williams, Elliot Lipeles, and Joe Kroll. They offered me an opportunity to work on the ATLAS experiment, and pushed me to take on challenging projects. I have learned an incredible amount from them during my time at Penn.

In particular, this thesis would not have been possible without my advisor and mentor Evelyn, who provided guidance through my time as a graduate student. She also supported and even encouraged my idea to find analysis that I could take ownership of.

There are several other people at Penn who deserve acknowledgements. Jean O'Boyle managed to stay on top of things, even while I was disorganized with my paperwork or requesting a hotel with short notice. She certainly helped to make things run smoothly. Millicent Minnick also helps to keep the whole department running smoothly. They deserve more thanks than I can fit here.

I would like to thank the theorist at Penn, Burt Ovrut, Sogee Spinner, and Austin Purves. Not only did their work motivate the search described in this thesis, but we have spent many hours

discussing the details of the model, and how best to search for it in ATLAS. Their knowledge and patience was crucial to me completing my analysis.

I would also like to thank my professors and teachers that inspired me to study Physics and pursue graduate school. Matthew Mitchell introduced me to Physics while I was in high school, setting me on this journey. At the University of Florida, Darin Acosta took me on as an undergraduate research assistant, working on the CMS endcap trigger system, long before I knew anything about High Energy Physics. Working in Darin's lab introduced me to research, and convinced me to go to graduate school.

The graduate students and post docs of the Penn army have been an amazing group. I want to thank Alex Tuna, Chris Lester, Dominick Olivito, Doug Schaefer, Jamie Saxon, Jim Degenhardt, John Alison, Jon Stahlman, Josh Kunkle, Kurt Brendlinger, Rami Vanguri, Ryan Reece, Sarah Heim, and Tae Min Hong. They are all incredibly smart and fun, and I can't imagine a better group to be part of. I have learned so much working with this group, and had a lot of fun in the process.

I want to give special thanks to Saša Fratina, Leigh Schaefer, and Liz Hines. During my first three years at Penn, Saša taught me all about the TRT software, and worked with me through all my performance work. Then, when it was time to transition to a Physics analysis, Saša helped Liz and me enter the SUSY group. Leigh joined this stop analysis as a young graduate student, and teaching her has been one of the most rewarding things I have done as a graduate student. With her taking over for Run II, I know I'm leaving this analysis in good hands! Finally, Liz and I worked closely together for several years, and survived some tough times breaking into the SUSY electroweak analysis, but we made it through!

There are many people I have worked with at ATLAS who deserve recognition. I can't list all of them, but I would like to thank my friends out at CERN, including Brokk Toggerson, Dan Guest, Emily Thompson, Mia Liu, Nicky Santoyo, Sarah Williams, and Zach Marshall. They have made my experience, working in the ATLAS experiment and living in Geneva, an enjoyable one.

I would also like to thank the many other people I worked with in the SUSY group including David Miller, Estel Perez Codina, Lea Gauthier, Jamie Boyd, Jean-Francois Arguin, Mike Flowerdew, Monica D'Onofrio, Serhan Mete, Takashi Yamanaka, and Tommaso Lari. In particular, I want to thank Jamie Boyd, Tommaso Lari, Takashi Yamanaka, and Mike Flowerdew for all their help in the final push of the analysis, leading up to the Moriond conference. Their help made it finish the note and quickly get ATLAS approval in time for the conference.

I have to thank my friends in Philadelphia, Austin Joyce, Cristi Resczenski, Elio Angilè, Kim Venta, Matthew Gratale, and Mitch Lerner. We spent many hours, and late nights, working through homework problems in the Zoo, but also had a lot of fun together. They made my time in Philadelphia

a wonderful experience.

Finally, I would like to thank Nadja Strobbe. Getting to know each other over the last several years has been amazing. We have been by each others side, even through some crazy times; whether rushing to meet a tough deadline, or moving across the Atlantic Ocean to Chicago. Living in separate countries was tough, but we got through it. I look forward to our new life together in Chicago, and whatever the future holds for us. I know that we can handle it together. I love you!

ABSTRACT

A SEARCH FOR B-L R-PARITY-VIOLATING SCALAR TOP DECAYS IN $\sqrt{s} = 8$ TeV pp
COLLISIONS WITH THE ATLAS EXPERIMENT

Brett Jackson

Evelyn Thomson

This thesis presents a search for direct scalar top pair production where the scalar tops decay via an R -parity-violating coupling to a final state with two leptons and two identified b -jets. The analysis uses 20.3 fb^{-1} of $\sqrt{s} = 8$ TeV proton-proton collision data collected with the ATLAS detector at the LHC. No significant excess is observed over the Standard Model background. Assuming a supersymmetric minimal $B - L$ extension to the Standard Model, limits on the scalar top mass are placed between 500 GeV and 1 TeV with a branching fraction above 20% for the scalar top to decay to an electron or a muon and a b -quark.

Contents

Acknowledgements	iii
Abstract	vi
Contents	vii
List of Tables	xi
List of Figures	xii
Preface	xvii
1 General introduction	1
2 Theoretical overview	3
2.1 Standard Model	3
2.1.1 Matter	5
2.1.2 Electroweak Theory	5
2.1.3 Quantum chromodynamics	6
2.1.4 Brout-Englert-Higgs mechanism	7
2.2 Shortcomings	12
2.2.1 Gravity	12
2.2.2 Dark matter and dark energy	13
2.2.3 Neutrino masses	13
2.2.4 Hierarchy problem	13
2.3 Supersymmetry	14

2.3.1	Motivation	15
2.3.2	Formalism	16
2.3.3	Minimal supersymmetric Standard Model	17
2.3.4	Supersymmetric Lagrangian	19
2.3.5	R-Parity	19
2.4	B-L extension	20
2.4.1	Phenomenology	20
2.4.2	Previous results	24
3	The LHC and the ATLAS experiment	27
3.1	The LHC machine	27
3.1.1	CERN accelerator complex	28
3.1.2	LHC beam conditions	29
3.2	The ATLAS experiment	30
3.2.1	Coordinate system	31
3.2.2	Inner detector	32
3.2.2.1	Pixel detector	32
3.2.2.2	Silicon semiconductor tracker	34
3.2.2.3	Transition radiation tracker	34
3.2.2.4	Tracking	36
3.2.3	Calorimetry	37
3.2.3.1	Electromagnetic calorimeter	38
3.2.3.2	Hadronic calorimeter	39
3.2.3.3	Forward calorimeter	39
3.2.4	Muon spectrometer	39
3.3	Trigger system	41
3.4	Event reconstruction and object identification	41
3.4.1	Electrons	42
3.4.2	Muons	43
3.4.3	Jets	43
3.4.3.1	Flavor tagging	43
3.4.4	Missing energy	44
4	Monte Carlo simulation	45

4.1	Event Generation	45
4.1.1	Parton distribution function	47
4.1.2	Hard interaction	48
4.1.3	Parton shower	49
4.1.4	Jet matching	49
4.2	Detector simulation	51
5	B-L stop search	53
5.1	Signal model simulation	54
5.2	Object selection	55
5.3	Event cleaning	59
5.4	Trigger selection	60
5.5	Signal regions	64
5.6	Background estimate	68
5.6.1	Monte Carlo simulation samples	70
5.6.2	Control regions	74
5.6.3	Validation regions	76
5.6.4	Background fit	80
5.7	Systematic uncertainties	85
6	Results	89
6.1	Event yields	89
6.2	Model dependent limits	90
6.2.1	Single mass limit	90
6.2.2	Branching fraction scan	91
7	Conclusion	105
A	Statistical interpretation technique	107
A.1	Likelihood function	107
A.2	The CL_s method	108
B	Signal model interpretation	113
B.1	400 GeV stop mass	114
B.2	500 GeV stop mass	117

B.3	600 GeV stop mass	120
B.4	700 GeV stop mass	123
B.5	800 GeV stop mass	126
B.6	900 GeV stop mass	129
B.7	1000 GeV stop mass	132
B.8	1100 GeV stop mass	135
	Bibliography	139

List of Tables

2.1	Summary of the matter particles described by the SM, along with the associated quantum numbers.	5
2.2	Summary of the chiral supermultiplet fields in the MSSM [1].	18
2.3	Summary of the gauge supermultiplet fields in the MSSM [1].	19
2.4	Ranges for the parameter scan used to generate the simulated models shown in Figures 2.5 and 2.6 [2].	22
3.1	Specifications of the three levels of the ATLAS trigger system.	41
5.1	Stop cross sections and their associated uncertainties [3, 4, 5].	54
5.2	Baseline electron requirements.	55
5.3	Baseline muon requirements.	56
5.4	Baseline jet requirements.	56
5.5	Trigger selection for each final state.	61
5.6	Requirements for the triggers used in this analysis.	61
5.7	The number of expected signal events passing each of the signal for stop masses of 500 GeV, 800 GeV, and 1000 GeV.	68
5.8	Summary of signal, control, and validation regions used for this analysis.	70
5.9	Partial summary of background samples and their cross sections used in this analysis.	72
5.10	Summary of other background samples and their cross sections used in this analysis.	73
5.11	The observed and expected event yields in the CRs and VRs. The expected event yields are shown before and after a fit to the data in the CRs.	80
5.12	Summary of the effect of each considered sources of systematic uncertainty on the total background estimate in SR 400 and SR 600.	86
6.1	The expected and observed event yields in SR 400. The expected event yields. The last three rows show the model-independent 95% CL on the visible cross section and the upper limit on the number of events.	93
6.2	The expected and observed event yields in SR 600. The expected event yields. The last three rows show the model-independent 95% CL on the visible cross section and the upper limit on the number of events.	94
6.3	The event and object kinematics for the two events passing the signal region selection.	95

List of Figures

1.1	Simplified model of pair production of scalar top quarks, with decay to a charged lepton and b -quark.	1
2.1	Fundamental particles described by the Standard Model. The mass of each particles are given in parentheses.	4
2.2	The scalar potential under two configurations: $\mu^2 > 0$ and $\mu^2 < 0$ [6].	10
2.3	The Higgs boson corresponds to an excitation in the radial direction of the scalar potential [6].	11
2.4	One-loop quantum corrections to the Higgs boson mass.	14
2.5	The allowed branching ratios for the stop LSP for various choices of the neutrino mass hierarchy and $\sin^2 \theta_{23}$, obtained by varying various model parameters within a range of natural values shown in Table 2.4 [2].	21
2.6	The stop decay branching ratio (a) and stop decay length (b) versus the stop mixing angle, assuming the stop is the LSP. Each point represents a simulation with a particular choice of model parameters, which are sampled from a range of natural values [2].	23
2.7	Stop cross sections and their associated uncertainties [3, 4, 5].	24
2.8	Limits on the stop mass obtained by reinterpreting leptoquark searches performed at ATLAS [2].	26
3.1	Areal view of the Geneva area with an overlaid drawing of the LHC and experiments [7].	28
3.2	Schematic view of the CERN accelerator complex [8].	29
3.3	Instantaneous luminosity collected by the ATLAS detector throughout Run 1 [9]. . . .	30
3.4	(Left) Integrated luminosity of proton-proton collision data collected by ATLAS during the three years of Run 1. The rate of data collection was increased in part by increasing the number of interactions per crossing (right).	31
3.5	The ATLAS experiment [10].	32
3.6	Schematic of the inner detector of the ATLAS experiment [11].	33
3.7	The Silicon pixel tracker of the ATLAS experiment [12].	34
3.8	Photograph of the silicon semiconductor tracker of the ATLAS experiment [13]. . . .	35
3.9	Photograph of the transition radiation tracker of the ATLAS experiment during its commissioning [14].	36
3.10	Schematic of the calorimeter system of the ATLAS experiment [15].	38
3.11	Schematic of the muon systems of the ATLAS experiment [16].	40

3.12 Schematic view of the signatures left in the various sub-detectors of ATLAS in response to the primary particles which pass through it [17].	42
4.1 Pictorial representation of a $t\bar{t}H$ event as produced by an event generator [18].	46
4.2 Parton distribution function (PDF) distributions for different parton species within the proton as obtained by the NNPDF collaboration. The two PDF distributions are obtained for different energy scales (μ^2) [19].	48
4.3 Illustration of the double counting issue that arises when combining the matrix element and parton shower event generation techniques [20].	50
4.4 Illustration of the jet matching technique used to eliminate the double counting issue shown in Figure 4.3 [20].	51
4.5 Candidate $t\bar{t}H$ event, observed in the ATLAS detector [21].	52
5.1 The relative abundance of events where two, one, and zero pairs are grouped correctly.	58
5.2 Integrated luminosity of proton-proton collision data delivered by the LHC (green) and recorded by the ATLAS experiment (yellow) throughout 2012. The blue area shows the integrated luminosity that passes data quality requirements, and is declared good for Physics [9].	59
5.3 Efficiency of simulated stop events passing each single lepton trigger broken down by flavor channel.	62
5.4 Efficiency of simulated stop events passing each of the single electron triggers for several ranges of electron E_T	63
5.5 Efficiency of simulated stop events passing the full trigger selection broken down by flavor channel.	63
5.6 Expected $m_{\ell\ell}$, H_T , $m_{b\ell}$ asymmetry, and $m_{b\ell}^0$ distributions for SM background processes and three simulated stop samples with different masses.	66
5.7 Distributions of the variables which are used to define the SRs. These plots show the MC simulated background samples and three signal models, and are made after applying all the SR selection criteria except for that on the variable shown.	67
5.8 Position of the control, validation, and signal regions in the E_T^{miss} significance versus H_T plane.	69
5.9 Expected and observed $m_{b\ell}^0$ distribution in the Top CR and Z CR when all flavor channels are combined.	75
5.10 Expected and observed $m_{b\ell}^0$ distribution in the Top CR and Z CR after applying the k_Z normalization factor derived in the Z CR when all flavor channels are combined.	76
5.11 Expected and observed p_T distribution for the leading lepton in the Top CR and Z CR after applying the k_Z normalization factor derived in the Z CR when all flavor channels are combined.	77
5.12 Expected and observed p_T distribution for the sub-leading lepton in the Top CR and Z CR after applying the k_Z normalization factor derived in the Z CR when all flavor channels are combined.	77
5.13 Expected and observed p_T distribution for the leading b -jet in the Top CR and Z CR after applying the k_Z normalization factor derived in the Z CR when all flavor channels are combined.	78
5.14 Expected and observed p_T distribution for the sub-leading b -jet in the Top CR and Z CR after applying the k_Z normalization factor derived in the Z CR when all flavor channels are combined.	78
5.15 Expected and observed $m_{b\ell}$ and H_T distributions in the VRs.	79

5.16	The number of observed and expected events in the CRs, broken down by flavor channel. The deviation of that channel's prediction from the observed number of events divided by the uncertainty in the prediction is also shown.	82
5.17	The number of observed and expected events in the VRs, broken down by flavor channel. The deviation of that channel's prediction from the observed number of events divided by the uncertainty in the prediction is also shown.	83
5.18	The $m_{b\ell}^0$ distribution in Top VR 3 (left) and Z VR (right).	84
5.19	The H_T distribution in Top VR 3 (left) and Z VR (right).	84
6.1	The $m_{b\ell}^0$ (top) and H_T (bottom) distributions in SR 400.	96
6.2	Event displays for the two observed events passing the signal region criteria.	97
6.3	Expected and observed CL_S value as a function of stop mass for the scenario with $Br(\tilde{t} \rightarrow eb) = Br(\tilde{t} \rightarrow \mu b) = 0.5$.	98
6.4	Stop pair branching fraction and corresponding scale factor to each di-lepton flavor channel depending on the branching fractions of a single stop.	99
6.5	The expected and observed CL_S values in SR 400 for a stop mass of 500 GeV, shown across the plane of physical stop branching fractions.	100
6.6	The expected and observed CL_S values in SR 600 for a stop mass of 900 GeV, shown across the plane of physical stop branching fractions.	100
6.7	The selected SR for several stop branching fractions for a stop mass of 500 GeV(left) and 900 GeV(right). The SR is selected by choosing the SR with the smallest expected CL_S value for a given branching fraction.	101
6.8	The expected mass limit on the stop at 95% CL.	102
6.9	Expected and observed limit on the branching fractions for the stop decaying to different lepton flavors shown for different stop mass hypotheses between 400 GeV and 1.1 TeV.	103
6.10	The observed mass limit on the stop at 95% CL.	104
A.1	Examples probability distribution functions for signal+background and background-only hypotheses.	109
A.2	Examples probability distribution functions used to calculate the CL_S quantity.	110
B.1	Expected CL_S values for SR 400 (top) and SR 600 (bottom) for a stop mass of 400 GeV, shown across the plane of physical stop branching ratios.	114
B.2	Observed CL_S values for SR 400 (top) and SR 600 (bottom) for a stop mass of 400 GeV, shown across the plane of physical stop branching ratios.	115
B.3	SR selection for a stop mass of 400 GeV.	116
B.4	Expected CL_S values for SR 400 (top) and SR 600 (bottom) for a stop mass of 500 GeV, shown across the plane of physical stop branching ratios.	117
B.5	Observed CL_S values for SR 400 (top) and SR 600 (bottom) for a stop mass of 500 GeV, shown across the plane of physical stop branching ratios.	118
B.6	SR selection for a stop mass of 500 GeV.	119
B.7	Expected CL_S values for SR 400 (top) and SR 600 (bottom) for a stop mass of 600 GeV, shown across the plane of physical stop branching ratios.	120
B.8	Observed CL_S values for SR 400 (top) and SR 600 (bottom) for a stop mass of 600 GeV, shown across the plane of physical stop branching ratios.	121
B.9	SR selection for a stop mass of 600 GeV.	122
B.10	Expected CL_S values for SR 400 (top) and SR 600 (bottom) for a stop mass of 700 GeV, shown across the plane of physical stop branching ratios.	123
B.11	Observed CL_S values for SR 400 (top) and SR 600 (bottom) for a stop mass of 700 GeV, shown across the plane of physical stop branching ratios.	124

B.12 SR selection for a stop mass of 700 GeV.	125
B.13 Expected CL_S values for SR 400 (top) and SR 600 (bottom) for a stop mass of 800 GeV, shown across the plane of physical stop branching ratios.	126
B.14 Observed CL_S values for SR 400 (top) and SR 600 (bottom) for a stop mass of 800 GeV, shown across the plane of physical stop branching ratios.	127
B.15 SR selection for a stop mass of 800 GeV.	128
B.16 Expected CL_S values for SR 400 (top) and SR 600 (bottom) for a stop mass of 900 GeV, shown across the plane of physical stop branching ratios.	129
B.17 Observed CL_S values for SR 400 (top) and SR 600 (bottom) for a stop mass of 900 GeV, shown across the plane of physical stop branching ratios.	130
B.18 SR selection for a stop mass of 900 GeV.	131
B.19 Expected CL_S values for SR 400 (top) and SR 600 (bottom) for a stop mass of 1 TeV, shown across the plane of physical stop branching ratios.	132
B.20 Observed CL_S values for SR 400 (top) and SR 600 (bottom) for a stop mass of 1 TeV, shown across the plane of physical stop branching ratios.	133
B.21 SR selection for a stop mass of 1 TeV.	134
B.22 Expected CL_S values for SR 400 (top) and SR 600 (bottom) for a stop mass of 1.1 TeV, shown across the plane of physical stop branching ratios.	135
B.23 Observed CL_S values for SR 400 (top) and SR 600 (bottom) for a stop mass of 1.1 TeV, shown across the plane of physical stop branching ratios.	136
B.24 SR selection for a stop mass of 1.1 TeV.	137

Preface

My time as a graduate student at the University of Pennsylvania has been an amazing experience, where I learned an incredible amount, and met many amazing people. I was around for the startup of the Large Hadron Collider (LHC) and the ATLAS experiment, and was able to take part in the first LHC run. I am very fortunate to have had the opportunity to work on the LHC during this exciting time. In particular, being part of the ATLAS group at the University of Pennsylvania has been a wonderful experience, offering me the opportunity to take on many responsibilities and grow as a physicist.

I began my graduate student career in 2008, when I spent my first summer at CERN learning about ATLAS, the TRT, and the software tools that make everything work together. I even had the opportunity to get my hands dirty, repairing TRT patch panels, and climbing through the ATLAS detector to reinstall them. This was immediately followed by me moving to Philadelphia to take classes. I still found time to continue my work on TRT detector performance, including several studies of the TRT timing resolution, documented in ATL-COM-INDET-2010-045 and ATL-COM-INDET-2011-007 [22, 23].

Once my classes were complete in 2010, I moved to CERN in order to immerse myself in research. I continued my work on the TRT, and began studying muon isolation in the muon combined performance group. I also joined the search for a massive Z' boson, where I performed several small studies. The Z' search was my first introduction to the world of physics analysis.

In 2012, I switched from exotics to the Supersymmetry group to continue my research. During 2012 and 2013, I worked on a team, searching for SUSY signatures, produced through electroweak interactions. These include direct production of electroweak gauginos and sleptons. I performed many cross check studies, worked on signal region optimization, and wrote and maintained tools to provide a “fake lepton” background estimate for the rest of the analysis group. Additionally, I wrote an analysis framework used by several colleagues at Penn and Harvard to analyze the large ATLAS datasets and

Monte Carlo simulation samples. These two years taught me a lot about software development, analysis techniques, and working on a large team toward a common goal.

Finally, toward the end of 2013, I was ready to take on my own analysis, which became the topic of this thesis. Through conversations with Burt Ovrut, Sogee Spinner, and Austin Purves, I became interested in SUSY models which allow for *R*-Parity violation. These models provide a large range of experimental signatures, not covered by other searches at ATLAS. I chose to pursue a completely new search, looking for a stop LSP, which decayed as a leptoquark. While there are many leptoquark searches, a direct search for this model provides additional sensitivity compared to reinterpretations of other searches. Ultimately, we extended the limits on the allowable stop masses, as described in this thesis and in the conference note ATLAS-CONF-2015-015 [24].

In addition to myself, the analysis team consisted Leigh Schaefer, Evelyn Thomson, and Joseph Kroll and Zachary Marshall who acted as additional advisers. Being the primary analyzer on such a small team gave me the opportunity to take part in every piece of the analysis, from the Monte Carlo simulation of our simulated signal samples to the selection optimization, and finally the background estimates and limit setting. This gave me a strong feeling of ownership of the work. Additionally, working with Leigh allowed me to experience what it's like to train a junior graduate student, which was one of the most enjoyable things I did during my time as a graduate student. All this work culminated in a conference note that was presented at the Moriond 2015 conference.

The LHC and the ATLAS experiment are extremely complex machines, so I reference other documents heavily while describing them in this thesis. Additionally, I took much of the text from the conference note ATLAS-CONF-2015-015, and the corresponding internal support note ATL-COM-PHYS-2015-168 verbatim, as I was the primary author. When sourcing material, for which I am not the primary author, I attempted to rewrite the text in my own words.

I would like to wish the ATLAS experiment and the Penn army good luck in Run II! It will surely be an exciting time.

Brett Jackson

Philadelphia, July 2015

CHAPTER 1

General introduction

This thesis describes the search for direct scalar top pair production, with the decay of each stop via an R -parity-violating (RPV) interaction to a charged lepton (electron or muon) and a b -quark, as shown in Figure 1.1. The analysis uses 20.3 fb^{-1} of $\sqrt{s} = 8 \text{ TeV}$ proton-proton collision data collected with the ATLAS detector at the Large Hadron Collider (LHC).

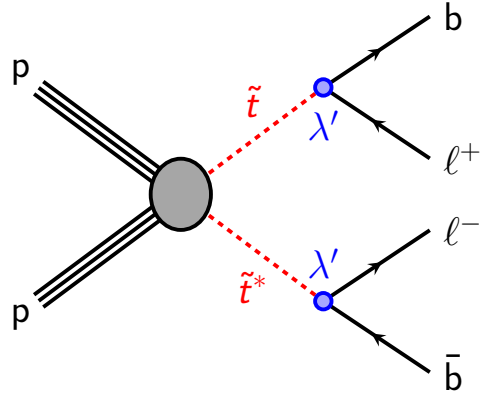


Figure 1.1: Simplified model of pair production of scalar top quarks, with decay to a charged lepton and b -quark.

The experimental signature is two oppositely charged leptons and two identified b -jets. The analysis considers $eebb$, $e\mu bb$, and $\mu\mu bb$ final states. Final states with τ leptons are not considered for this search. The distinguishing features are two pairs, each of a lepton and a b -jet, with a resonance in the invariant mass distribution of each pair. In contrast to R -parity conserving searches, there is no

significant missing transverse momentum.

Previous searches for lepto-quarks at ATLAS [25, 26, 27, 28] and CMS [29, 30, 31, 32] have considered pair production of first, second, and third generation lepto-quarks, but have not examined the signature of a resonance in the invariant mass of an electron and a b -jet or a muon and a b -jet. The results of these searches have already been interpreted to set limits on the stop mass and its decay branching fractions in the $B - L$ model [2, 33].

Chapter 2 describes the Standard Model (SM) of particle physics and Supersymmetry, a popular extension to the SM. The concept of R -parity, and the $B - L$ extension to the SM is also discussed in this chapter. Emphasis is placed on the phenomenology of this model.

Chapter 3 introduces the LHC and ATLAS, along with the triggering system and event reconstruction. Chapter 4 reviews the Monte Carlo event generator tools used to estimate the detector response and efficiency to reconstruct the signal process, and to predict the backgrounds from SM processes.

Chapters 5 and 6 describe the stop search. Chapter 5 reviews the search strategy and event selection. Chapter 6 presents the results and interpretation.

CHAPTER 2

Theoretical overview

The universe, as we know it, comprises fundamental matter particles, and four fundamental forces. These forces include gravity, electromagnetism, and the strong and weak nuclear forces. Despite being the weakest of the four forces, gravity is certainly the most familiar to everyday life, as it assures objects fall to the ground. The Gravitational force is described by the general theory of relativity, but a successful quantum theory of gravity has yet to be developed. Since gravity is so weak, it does not significantly affect the physics at the LHC energy scale, and can safely be ignored for the purpose of this thesis. Of the remaining three forces, electromagnetism and the weak force have been shown to come from the same underlying interactions, called the electroweak force. The electroweak and strong forces are described by the Standard Model of Particle Physics.

In this chapter, a brief overview of the theoretical background for this thesis is presented. The Standard Model and its shortcomings are discussed in Sections 2.1 and 2.2. Supersymmetry, a popular extension to the Standard Model, is introduced in Section 2.3. The chapter concludes with a presentation of the particular $B - L$ extension to the SM, which is the focus of the search presented in this dissertation. Section 2.4 presents a brief description of the underlying theory, as well as some of the interesting phenomenology expected in the scenario where the scalar top is the LSP.

2.1 Standard Model

In this section, the Standard Model (SM) of particle physics is described in brief. The SM is a very rich subject, and a more complete description can be found in References [34, 35, 36]. The SM is a quantum field theory which encapsulates the current understanding of the elementary particles, and

their interactions, and has been developed, and rigorously tested by experiments over the last fifty years. In 2012, the final particle predicted by the SM, the “Higgs boson” was discovered at CERN by the ATLAS and CMS collaborations, marking a great achievement for both the experimental collaborations and the theorists who predicted the particle’s existence. The SM Lagrangian is a non-Abelian gauge theory with symmetry group $SU(3)_C \times SU(2)_L \times U(1)_Y$, which describes the matter content of the universe, as well as the interactions of the strong and electroweak forces. The matter content in the SM is made up of fermions (spin $1/2$), called quarks and leptons. Massless gauge bosons (spin 1) mediate the interactions of the electroweak and strong forces.

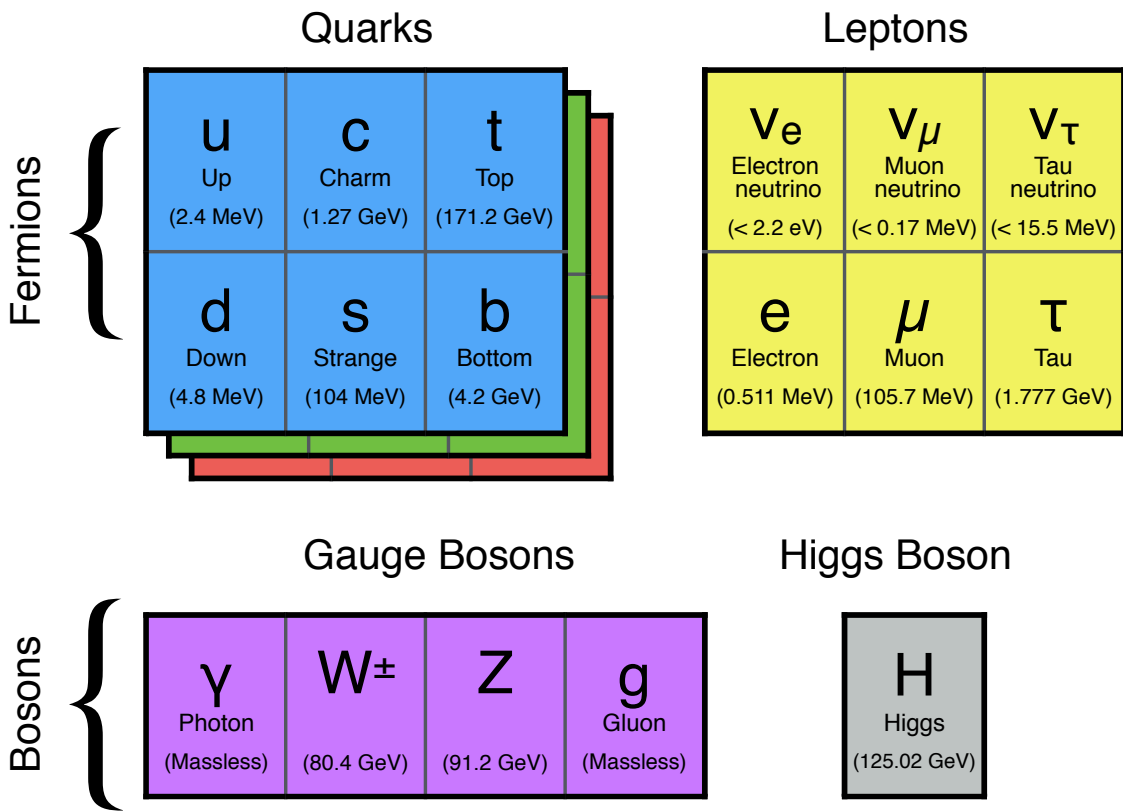


Figure 2.1: Fundamental particles described by the Standard Model. The mass of each particles are given in parentheses.

Table 2.1: Summary of the matter particles described by the SM, along with the associated quantum numbers. The quantum numbers include the spin, electric charge Q , the third component of weak isospin T_3 , hypercharge $Y = 2(Q - T_3)$, and the allowable color charges.

Fermions	Generation			Spin	Q	T_3	Y	Color
	1	2	3					
Quarks	$\begin{pmatrix} u \\ d \end{pmatrix}_L$	$\begin{pmatrix} c \\ s \end{pmatrix}_L$	$\begin{pmatrix} t \\ b \end{pmatrix}_L$	$\frac{1}{2}$	$+\frac{2}{3}$ $-\frac{1}{3}$	$+\frac{1}{2}$ $-\frac{1}{2}$	$\frac{1}{3}$	r, g, b
	u_R	c_R	t_R	$\frac{1}{2}$	$+\frac{2}{3}$	0	$+\frac{4}{3}$	r, g, b
	d_R	s_R	b_R	$\frac{1}{2}$	$-\frac{1}{3}$	0	$-\frac{2}{3}$	r, g, b
	$\begin{pmatrix} \nu_e \\ e \end{pmatrix}_L$	$\begin{pmatrix} \nu_\mu \\ \mu \end{pmatrix}_L$	$\begin{pmatrix} \nu_\tau \\ \tau \end{pmatrix}_L$	$\frac{1}{2}$	0 -1	$+\frac{1}{2}$ $-\frac{1}{2}$	-1	-
	e_R	μ_R	τ_R	$\frac{1}{2}$	-1	0	-2	-

2.1.1 Matter

The fermionic matter is arranged into three families, or generations, each containing quarks and leptons. These particles can be charged under each part of the SM symmetry group, where the particle's charge determines how it interacts with each of the forces. Each generation contains two chiral left-handed quarks, arranged in a isospin doublet, consisting of an up-type and a down-type quark. There are also two chiral left-handed leptons, one with electric charge, and a neutrino, which is electrically neutral. As with the quarks, the two left-handed leptons are arranged into an isospin doublet. Finally, each fermionic family contains chiral right-handed counterparts to the two quarks, and the charged lepton. No right-handed neutrinos are included in the SM, as they would not react with any known forces, as will be explained shortly. The right-handed fermions are isospin singlets. The three generations are essentially copies of one another, differing only in the mass of the constituent particles, and the familiar world is made up entirely of particles from the first generation. The reason for exactly three generations, not more or less, remains a mystery. A summary of the SM matter content, with the charges under the various parts of the SM symmetry group is shown in Table 2.1.

2.1.2 Electroweak Theory

Each piece of the SM symmetry group is associated with a massless gauge boson, which mediates the interactions between particles. The electroweak sector has the symmetry group $SU(2)_L \times U(1)_Y$, and describes the interactions with fields with isospin or hypercharge (Y). The electroweak sector is a

chiral theory, meaning right- and left-handed particles transform differently under the gauge group. Left-handed fermions have a value of the third component of isospin equal to $\pm 1/2$, while right-handed particles have no isospin, and do not interact with the weak force. The gauge bosons associated with the electroweak sector are three W^i bosons, arranged in a weak isospin triplet, and a B^0 boson, which is a weak isospin singlet.

Since chiral fields translate differently, depending on their chiral handedness, there can be no mixing between the right- and left-handed states, as this would break gauge invariance. Unfortunately, a mass term allows for exactly this mixing, implying the fermions must be massless. On the other hand, the weak force is observed to be short ranged, implying massive gauge bosons, and fermions do indeed have measurable masses. Adding masses to a chiral quantum field theory is a difficult endeavor, and is achieved through a process called “spontaneous symmetry breaking,” which is explained in Section 2.1.4. The broken symmetry leads to a mixing of the electrically neutral W^3 and B^0 gauge bosons into a massless photon, and the massive Z boson. The W^1 and W^2 mix to form the massive W^+ and W^- . The W^\pm and Z bosons both have mass, and act as the propagator of the weak force, while the massless photon mediates the electromagnetic force. The first quantum field theory, developed earlier than the electroweak theory, describes the interaction of the massless photon with electrically charged particles and is known as quantum electrodynamics (QED).

Since right-handed neutrinos have no charge under any part of the SM symmetry group, they are not expected to interact with the known components of the SM, and are therefore not included as part of the theory. There are extensions to the SM, however, which do include right-handed neutrinos, including the one described in Section 2.4.

2.1.3 Quantum chromodynamics

The $SU(3)_C$ part of the SM Lagrangian corresponds to the strong force, with a corresponding “color” charge, and is described by the theory of quantum chromodynamics (QCD). Quarks are colored objects, having red, green, or blue charge, while leptons have no color charge, and thus do not interact directly with the strong force. The eight massless gauge bosons associated with the $SU(3)_C$ symmetry group are called gluons, and are themselves colored objects. This leads to self interaction, and some interesting phenomenology!

The gluons of QCD are allowed to interact with each other, while the photon of QED is not self-interacting. This leads to some important differences between the strong force and the electromagnetic force. Perhaps, the most interesting, is related to the concept of “screening”. In QED, as one moves further from a charged particle, the charge tends to look smaller as a result of the polarization of the

vacuum around the charge, where electron-positron pairs pop out of the vacuum. The further from the particle one is, the more electron-positron pairs are visible, obscuring the initial charge more. In QCD, this same screening effect occurs, with quark anti-quark pairs being pair-produced from the vacuum, however gluon pairs may also be produced out of the vacuum. These gluon pairs produce the opposite screening effect, known as “anti-screening,” increasing the effective charge observed. Rather than charges being screened, as in QED, there is a net anti-screening effect for objects with color charge.

As two colored particles get very close together, the anti-screening is very small, and they can be treated as free particles, in an effect known as “asymptotic freedom.” Alternatively, as two charged particles move apart, the polarization of the vacuum between them results in an increasing energy buildup, until it is energetically favorable to pair produce a quark anti-quark pair from the vacuum. For this reason, no free quarks or gluons have been observed, rather any objects with color charge will tend to form bound states called “hadrons,” which has no net color charge. Hadrons can either be a bound state of a quark anti-quark pair, called mesons, or three-quark bound states, called baryons. Additionally, five-quark bound states have recently been found by the LHCb experiment [37]. The anti-quark contained in a meson must have the corresponding anti-color of the constituent quark. Similarly, the three quarks, which make up a baryon, must have colors that add to “white,” meaning one red, one green, and one blue quark.

In particle collisions, this effect also leads to the phenomenon of “jets,” where a spray of hadrons is projected at the particle detector, resulting from multiple colored objects flying apart after the collision.

2.1.4 Brout-Englert-Higgs mechanism

As mentioned in Section 2.1.2, the fermions and gauge bosons described in the SM Lagrangian are massless, however, many of those observed in nature do, in fact, have a non-zero mass. This would seem to allow for the mixing of chiral left-handed and singlet right-handed fields, which would in turn break gauge invariance. A method to add mass terms to the SM Lagrangian without breaking the necessary gauge invariance was developed during the 1960’s by several groups of theorists, including Robert Brout and Francois Englert [38], Peter Higgs [39, 40], and Gerald Guralnik, Carl R. Hagen, and Tom Kibble [41] working in parallel, and is commonly called the Brout-Englert-Higgs (BEH) mechanism. The BEH mechanism adds an additional complex scalar field to the Lagrangian, which acquires a vacuum expectation value (vev), which “spontaneously” breaks the symmetry of the SM Lagrangian.

Each spontaneously broken symmetry leads to a new massive scalar particle, known as a “Goldstone boson.” The gauge bosons can then absorb these Goldstone bosons in a process where they acquire a mass. Recall, before symmetry breaking, the electroweak sector has four massless gauge bosons, the W^1 , W^2 , W^3 , and the B^0 , however experiments observe massive W^\pm , and the Z bosons, associated with the weak force, and a massless photon to mediate the electromagnetic force. An electric charge Q is also conserved. This implies that the $SU(2)_L \times U(1)_Y$ of electroweak theory is broken in a way that gives a different $U(1)$ symmetry group corresponding to electromagnetism. This symmetry breaking requires at least three Goldstone bosons to be absorbed, and give masses to the gauge bosons. The simplest method to accomplish this is to add a complex scalar field

$$\Phi = \begin{pmatrix} \phi^+ \\ \phi^0 \end{pmatrix}, \quad (2.1)$$

which is a doublet with positive hypercharge ($Y = 1$).

To show this, it is useful to consider the SM Lagrangian, ignoring the QCD part,

$$\mathcal{L} = -\frac{1}{4}W_{\mu\nu}^a W_a^{\mu\nu} - \frac{1}{4}B_{\mu\nu}B^{\mu\nu} + \bar{L}_i(iD_\mu\gamma^\mu)L_i + \bar{e}_{R,i}(iD_\mu\gamma^\mu)e_{R,i}, \quad (2.2)$$

where the i index runs over the three generations, the μ and ν are Lorentz indices, and a runs over the generators in the gauge group. The field strengths are given by

$$W_{\mu\nu}^a = \partial_\mu W_\nu^a - \partial_\nu W_\mu^a + g_2\epsilon^{abc}W_\mu^b W_\nu^c \quad (2.3)$$

$$B_{\mu\nu} = \partial_\mu B_\nu - \partial_\nu B_\mu, \quad (2.4)$$

and the covariant derivatives for the left- and right-handed lepton fields are

$$D_\mu L_L = (\partial_\mu - ig_2 T_a W_\mu^a - ig_1 Y B_\mu) L_L \quad (2.5)$$

$$D_\mu e_R = (\partial_\mu - ig_1 Y B_\mu) e_R. \quad (2.6)$$

Where T_a are the generators of the gauge group, and g_1 and g_2 are the coupling constants for electroweak interactions.

Adding the complex scalar field from Equation 2.1 adds an additional scalar part to the Lagrangian,

$$\mathcal{L} = (D^\mu\Phi)^\dagger(D_\mu\Phi) - V(\Phi), \quad (2.7)$$

where the first term is the kinetic term, and $V(\Phi)$ is the scalar potential. The exact form of the scalar potential is not known, however, the simplest possible form that has the desired properties can be used

$$V(\Phi) = \mu^2\Phi^\dagger\Phi + \lambda(\Phi^\dagger\Phi)^2. \quad (2.8)$$

This form is an assumption that provides the required spontaneous symmetry breaking, while remaining renormalizable. In order for the vacuum to be stable, λ must be positive. The choice of the μ^2 parameter affects the shape of the scalar potential, as shown in Figure 2.2. In the configuration with $\mu^2 > 0$, the scalar potential is always positive, and the minimum occurs at

$$\langle 0 | \Phi | 0 \rangle = \begin{pmatrix} 0 \\ 0 \end{pmatrix}. \quad (2.9)$$

There is no spontaneous symmetry breaking in this scenario. On the other hand, if $\mu^2 < 0$, the scalar potential takes on the famous ‘‘Mexican hat’’ shape, and the minimum of the potential is no longer located at the origin. With the minimum of the scalar potential located away from the origin, the neutral part of the scalar field acquires a vacuum expectation value (vev) v ,

$$\langle 0 | \Phi | 0 \rangle = \Phi_0 = \frac{1}{\sqrt{2}} \begin{pmatrix} 0 \\ v \end{pmatrix}, v = \sqrt{\frac{-\mu^2}{\lambda}}. \quad (2.10)$$

By acquiring a vev, electroweak symmetry is spontaneously broken. The green line in Figure 2.2, corresponds to the circle of minimum potential, represents the massless Goldstone mode.

Since the charged part of the scalar field does not acquire a vev, electromagnetism is not broken, leaving a remaining $U(1)_{\text{EM}}$ symmetry with a conserved charge of

$$Q = T_3 + \frac{Y}{2}, \quad (2.11)$$

corresponding to the electric charge.

Expanding the scalar field Φ around its minimum Φ_0 , one gets

$$\Phi(x) = \frac{1}{\sqrt{2}} \begin{pmatrix} 0 \\ v + h(x) \end{pmatrix}, \quad (2.12)$$

with $h(x)$ being a new scalar field. Inserting this into the kinetic term of Equation 2.7, and redefining the gauge fields as

$$W_\mu^\pm = \frac{1}{\sqrt{2}} (W_\mu^1 \mp W_\mu^2), \quad (2.13)$$

$$Z_\mu = \frac{1}{\sqrt{g_1^2 + g_2^2}} (g_2 W_\mu^3 - g_1 B_\mu), \quad (2.14)$$

$$A_\mu = \frac{1}{\sqrt{g_1^2 + g_2^2}} (g_2 W_\mu^3 + g_1 B_\mu), \quad (2.15)$$

where the redefined gauge fields correspond to the physical gauge bosons of electroweak theory, the W^\pm , Z , and the photon. The covariant derivative becomes

$$|D_\mu \Phi|^2 = \frac{1}{2} (\partial_\mu H)^2 + \frac{1}{2} g_2^2 (v + H)^2 W_\mu^+ W^{\mu-} + \frac{1}{8} (v + H)^2 (g_1^2 + g_2^2) Z_\mu Z^\mu. \quad (2.16)$$

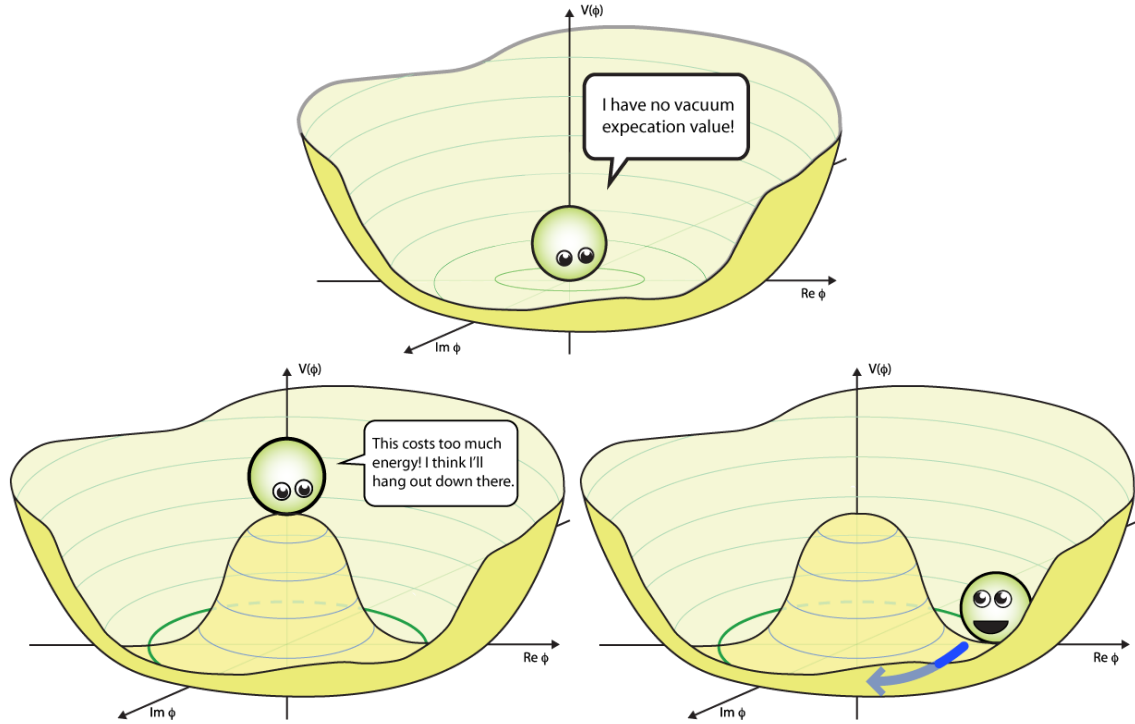


Figure 2.2: The scalar potential under two configurations. The configuration on the top shows the case where $\mu^2 > 0$, where the scalar potential is always positive. In this configuration, the scalar potential has a minimum at the origin. The configuration with $\mu^2 < 0$ is shown on the bottom. In this case, the minimum of the scalar potential occurs away from the origin [6].

It can be seen that the gauge bosons take on the following masses through their interactions with the scalar field

$$M_W = \frac{1}{2} v g_2 \quad (2.17)$$

$$M_Z = \frac{1}{2} v \sqrt{g_1^2 + g_2^2} \quad (2.18)$$

$$M_A = 0 \quad (2.19)$$

It is important to note that there is no term for the photon, implying it does not interact with the scalar field, and therefore, does not pick up a mass term. Three of the degrees of freedom from the scalar field that would be Goldstone bosons have been absorbed by the gauge bosons, giving them mass. There is one remaining degree of freedom, which becomes the Higgs boson. The Higgs boson

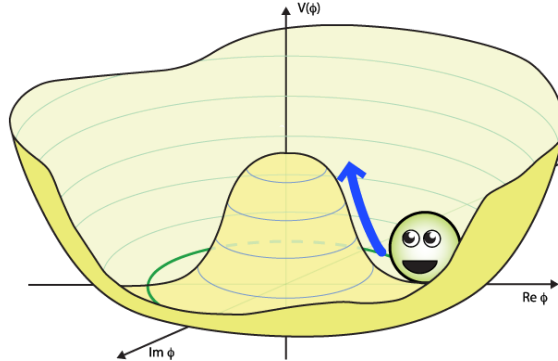


Figure 2.3: The Higgs boson corresponds to an excitation in the radial direction of the scalar potential [6].

itself has mass, equal to

$$m_H = 2\lambda v^2 \quad (2.20)$$

$$= 2\mu^2. \quad (2.21)$$

This mass corresponds to the remaining degree of freedom in the scalar potential, where the field can oscillate in the radial direction, as shown in Figure 2.3. The Higgs mass has no other handles in the SM, and must be determined experimentally. It was found to be equal to $125.09 \pm 0.21(\text{stat}) \pm 0.11(\text{syst})$ GeV by the ATLAS and CMS experiments [42].

The final piece to add to the SM are masses for the fermions, which are introduced through Yukawa couplings between the fermion fields and the scalar field. An additional set of terms are added to the Lagrangian for the interactions between the scalar field and the fermion sector. The portion that represents the first generation of fermions is

$$\mathcal{L}_F = -G_e \bar{L} \Phi e_R - G_d \bar{Q} \Phi d_R - G_u \bar{Q} \tilde{\Phi} u_R + \text{h.c..} \quad (2.22)$$

There are copies of these terms for the second and third generations of fermions. A new term, $\tilde{\Phi}$ was introduced, which is the conjugate of Φ with negative hypercharge ($Y = 1$), and is equal to

$$\tilde{\Phi} = i\tau_2 \Phi^* \quad (2.23)$$

$$= \frac{1}{\sqrt{2}} \begin{pmatrix} v + h \\ 0 \end{pmatrix}. \quad (2.24)$$

Substituting terms into Equation 2.22 gives

$$\begin{aligned}\mathcal{L}_F = & -\frac{1}{\sqrt{2}} \left[G_e \begin{pmatrix} \bar{\nu} & \bar{e} \end{pmatrix}_L \begin{pmatrix} 0 \\ v+h \end{pmatrix} e_R + G_d \begin{pmatrix} \bar{u} & \bar{d} \end{pmatrix}_L \begin{pmatrix} 0 \\ v+h \end{pmatrix} d_R \right. \\ & \left. + G_u \begin{pmatrix} \bar{u} & \bar{d} \end{pmatrix}_L \begin{pmatrix} v+h \\ 0 \end{pmatrix} u_R \right] + \text{h.c.}\end{aligned}\quad (2.25)$$

$$\mathcal{L}_F = -\frac{1}{\sqrt{2}}(v+h) (G_e \bar{e}_L e_R + G_d \bar{d}_L d_R + G_u \bar{u}_L u_R) + \text{h.c.} \quad (2.26)$$

Generic fermion mass terms are of the form $m \bar{f}_L f_R + \text{h.c.}$, so reading Equation 2.26, one can see the fermion masses are

$$m_e = \frac{G_e v}{\sqrt{2}}, \quad m_u = \frac{G_u v}{\sqrt{2}}, \quad m_d = \frac{G_d v}{\sqrt{2}}. \quad (2.27)$$

The h is dropped because it is the remnant of the Higgs doublet, and expected to be negligible. There are of course similar mass terms for the second and third generation fermions. Since the neutrinos have no isospin, they do not interact with the scalar potential, and therefore, do not pick up a mass. It should also be noted that the G 's, thus the fermion masses, are not predicted by the SM, and the fermion masses must be measured, and put into the theory.

2.2 Shortcomings

While the SM has been a very successful theory in describing particles and their interactions across many orders of magnitude, it does have some shortcomings. Some of these shortcomings, such as the existence of dark matter, arise from experimental observations, which point toward potential problems with the SM. Others, such as the Hierarchy problem, arise from parts of the SM that require unnatural, amounts of “fine tuning” of the parameters of the theory.

2.2.1 Gravity

One (seemingly obvious) feature, missing from the SM is the gravitational force. This seems counter-intuitive because this is the force people are most familiar with, in their daily lives. However, gravity remains a very weak force, compared to the electroweak force, and no successful quantum theory of gravity has been created. A spin 2 graviton particle has been proposed, which seems as if it can be added to the SM, but experiments have yet to observe such a particle.

2.2.2 Dark matter and dark energy

Cosmological experiments over the past several decades[43, 44] have shown that observable matter only makes up 5% of the observable universe. It is still unknown what makes up the remaining 95%! The unknown component is generally broken up into two categories, based on their expected properties. Dark matter is localized, and tends to be found in clumps, while dark energy permeates all of space.

From the perspective of gravity, dark matter is expected to behave similar to normal matter in that gravity exerts an attractive force on the dark matter. Dark matter differs in that it does not interact via the electromagnetic force, which is why it is called “dark.” The other properties of dark matter are unknown. It is possible that it interacts with the strong or weak forces, however, this is by no means guaranteed.

Dark energy, on the other hand, opposes the force of gravity and appears to be responsible for the acceleration of the expansion of the universe. The nature of dark energy is unknown.

2.2.3 Neutrino masses

As shown in Section 2.1.4, the BEH mechanism leaves the neutrinos massless in the SM because they have no chiral right-handed counterpart, and don’t have the Yukawa coupling with the scalar field. Neutrino experiments have observed neutrino flavor oscillation [45]. For these oscillations to occur, the physical neutrino eigenstates must be a mixture of the flavor eigenstates and have distinct masses. This provides evidence that there is a non-zero mass for at least two of the three neutrino. Some of the proposed mechanisms to generate massive neutrino masses with the SM are the addition of “sterile” right-handed neutrinos, or the possibility that neutrinos are Majorana particles, and they are their own anti-particle.

2.2.4 Hierarchy problem

Several potential problems arise from the large differences in energy scale between the electroweak scale ($\mathcal{O}(100)$ GeV), where experiments are able to effectively probe, and the Planck scale ($\mathcal{O}(10^{18})$ GeV), where the effects of gravity can no longer be ignored, and the theory is no longer valid as it stands. Because the scales are so different, the bare parameters of the theory can differ from their renormalized values, or other values in the theory, by several orders of magnitude. These problems are classified as “hierarchy problems,” and do not immediately lead to contradictions, as the theory can remain



Figure 2.4: One-loop quantum corrections to the Higgs boson mass. From left to right: contribution from the Yukawa interaction; two contributions from the gauge interaction; contribution from the Higgs self-interaction.

consistent with these large differences. However, in order to construct a consistent theory, one is required to accept a certain amount of “fine tuning,” that many find unsatisfying.

A particularly famous hierarchy problem is associated with the mass of the Higgs boson. Observed particles masses are a combination of the “bare” mass (tree level) and radiative corrections from additional loop diagrams. The one-loop corrections to the Higgs mass are shown in Figure 2.4. These loop momenta are cut off at the Planck scale, which leaves a lot of room for these radiative corrections to increase. Fermion and gauge boson masses are protected from this high cutoff scale. Fermions are protected through chiral symmetry, and are only logarithmically dependent on the cutoff scale. Gauge bosons are similarly protected through the local gauge symmetry. The Higgs boson is a scalar, and has a quadratic dependence on the cutoff scale.

The Higgs mass is observed to be at 125 GeV, so if the bare mass and the radiative correction terms are truly at such a high scale, it would be a large coincidence if they simply happen to cancel so precisely. While it is not impossible, it is extremely unlikely this would happen. This is the essence of the fine tuning problem.

A way to remove the quadratic dependence on the Planck scale is to introduce new particles, which have the opposite loop behavior to their SM counterparts. This is the basic idea of supersymmetry, which is discussed in Section 2.3.

2.3 Supersymmetry

Supersymmetry (SUSY) is a popular extension to the SM that describes the interactions between the fermions and bosons with a quantum field theory [46, 47, 48, 49, 50, 51, 52, 53, 54, 55, 56, 57]. The idea behind SUSY was first proposed by Miyazawa, in 1966, to relate mesons and baryons in the context of hadronic physics. During the early 1970s, it was independently rediscovered in the context of quantum field theory by several research groups. In this case, SUSY acts as a new spacetime symmetry relating the fermions and the bosons within the theory. SUSY is also needed for grand unified theories and string theories, where it is necessary to have a link between particles of different

spin.

2.3.1 Motivation

A new operator Q is defined to generate the transformations of fermions into bosons and conversely bosons into fermions.

$$\begin{aligned} Q |\text{fermion}\rangle &= |\text{boson}\rangle \\ Q |\text{boson}\rangle &= |\text{fermion}\rangle \end{aligned} \tag{2.28}$$

Since Q transforms a field between fermionic and bosonic states, it must have spin $1/2$. The operator also has the following commutation and anti-commutation relationships

$$\begin{aligned} \{Q, Q^\dagger\} &= P^\mu \\ \{Q, Q\} = \{Q^\dagger, Q^\dagger\} &= 0 \\ [Q, P^\mu] = [Q^\dagger, P^\mu] &= 0, \end{aligned} \tag{2.29}$$

where P^μ is the generator of spacetime transformations.

The particles are now arranged in “supermultiplets,” each containing a fermion and a boson. Another effect of adding the Q generator is that new particles are added. Each supermultiplet contains one SM particle and one new field, and Q translates between the two fields within a particular multiplet. Q and Q^\dagger commute with generators of the gauge transformations, so the particles within a supermultiplet have the same gauge transformations. This implies that the supersymmetric partners undergo the same interactions as their SM counterparts, with the same coupling strengths. Q and Q^\dagger also commute with P^μ , which implies the supersymmetric partners have the same mass as the SM particles. This is clearly not the case, as SUSY has not yet been observed at these low mass scales; thus, if supersymmetry is a real symmetry of nature, it must be a broken symmetry.

Despite being a broken symmetry, SUSY has some nice features, providing potential solutions to some of the shortcomings of the SM listed in Section 2.2.

Hierarchy problem

The hierarchy problem may be addressed by supersymmetry through the addition of new, massive particles which enter loop diagrams of the Higgs boson. These new particles provide radiative corrections to the Higgs mass which have opposite sign compared to the corrections from their SM counterparts. These radiative corrections can remove the quadratic dependence on the Planck scale, preventing the Higgs mass from becoming too large.

Dark matter

The SM does not include any particles with the properties necessary to describe the dark matter content of the universe. By adding new, massive particles, SUSY can offer a dark matter candidate. In many SUSY models, the lightest supersymmetric particle (LSP) is massive, stable, and has no electric charge. These are exactly the properties needed by a dark matter candidate! Even in models where the LSP is unstable, its lifetime may be long enough to be consistent with a dark matter particle.

2.3.2 Formalism

In this section, the formalism of SUSY is briefly introduced. A more complete discussion of the formalism is provided in References [1, 58, 59].

Within the supersymmetry framework, the fields representing the matter particles and force propagators of the SM are placed into supermultiplets, along with their supersymmetric counterparts, which have a spin differing by $1/2$, but otherwise the same quantum numbers. These supermultiplets, therefore, have one fermion and one boson each. Rather than formulating interactions between the fields directly, the supersymmetric Lagrangian formulates interactions between superfields, resulting in several new terms.

The supermultiplets take on two forms. The simplest form including a two-component Weyl fermion and a complex scalar field, and is called a “chiral” or “matter” superfield. This class of supermultiplets describes the SM fermions, along with their supersymmetric partner, the scalar fermion (sfermion). The scalar Higgs fields also form these types of supermultiplets. Unlike the case of fermions, however, the Higgs fields have spin-0, and their partners, the Higgsino, are fermions, with spin- $1/2$. The left- and right-handed fermions reside in different multiplets. For this reason, the sfermions are assigned a “handedness” even though the concept of handedness is somewhat ambiguous for a scalar particle. In this case, it simply refers to the handedness of the fermionic partner.

The second class of supermultiplets, called a “gauge” or “vector” multiplet, and includes a spin-1 gauge boson, and a massless spin- $1/2$ Weyl fermion. The supersymmetric partners of the gauge bosons are fermions called gauginos, and transform the same as their boson counterparts under gauge transformations. Therefore, the left- and right-handed gauginos are in the same supermultiplet.

As mentioned in Section 2.3.1, no supersymmetric particles have been observed with the same mass as their SM counterparts; for this reason, if SUSY is a true symmetry of nature, it must be broken. In order to solve the hierarchy problem, only soft SUSY breaking is allowed, otherwise, quadratic divergences reappear. This means that the relation between dimensionless coupling constants must

still hold. This leaves only logarithmically diverging terms of the form

$$\Delta m_H^2 = m_{\text{soft}}^2 \left(\frac{\lambda}{16\pi^2} \ln \frac{\Lambda}{m_{\text{soft}}} + \dots \right), \quad (2.30)$$

m_{soft} is related to the masses of the supersymmetric partners, so if the masses of the supersymmetric partners become too large, the corrections to the Higgs mass become large again, reintroducing the hierarchy problem. This suggests at least some of the new particles must be light to avoid the fine-tuning of the hierarchy problem.

2.3.3 Minimal supersymmetric Standard Model

In order to construct a minimal supersymmetric Standard Model (MSSM), the SM particles must be placed into the context of supersymmetric multiplets. As discussed in Section 2.3.2, there are two types of supermultiplets which can be used to construct the model, chiral superfields, and gauge superfields. The SM fermions transform differently under the gauge transformations depending on the chirality (left- or right-handedness); for this reason, the SM fermions must be placed into chiral supermultiplets, where the left- and right-handed particles are treated separately. The supersymmetric partners of the fermions have spin-0, and are called scalar fermions, or sfermions. As with the SM fermions, the sfermions are made up of the partners come in two types, called scalar quarks (squarks), which have color charge, and scalar leptons (sleptons), which do not interact with the strong force. As the names suggest, the squarks and sleptons are the supersymmetric counterparts of the SM quarks and leptons. Despite the fact that these sfermions are scalar particles, they are assigned a handedness, corresponding to the handedness of the SM counterpart. This should not be confused with the particles being truly left- or right-handed chiral fields.

The gauge bosons have spin-1, and are placed in gauge supermultiplets with their supersymmetric partners, the gauginos. The gauginos have spin-1/2, and are fermions. Unlike the SM fermions however, the gauginos transform the same as the gauge bosons under gauge transformations in a way that does not depend on the handedness of the particle.

The Higgs boson is the final particle to include in this MSSM. Since the Higgs boson is a scalar, it must be placed into a chiral supermultiplet, with a fermion Higgsino. It should be noted that in the supersymmetric model, a single Higgs boson is not sufficient, and a second chiral Higgs supermultiplet is added. A second supermultiplet is necessary due to the basic structure of supersymmetric models and to cancel anomalies that arise due to the additional symmetry breaking.

Structure

In the SM, the scalar field gives mass to the up-type quarks and the conjugate field gives mass

to the down-type quarks and charged leptons. In supersymmetric models, the Higgs field has hypercharge $Y = +1/2$, and gives mass to the up-type quarks, however the conjugate of the Higgs field no longer gives mass to the particles with negative hypercharge. A second scalar field with hypercharge $Y = -1/2$ is added to give masses to the down-type quarks and the charged leptons

Anomaly cancellation

In general, breaking a gauge symmetry of the Lagrangian can introduce anomalies and cause the theory to be inconsistent. While the SM has several broken symmetries, it remains a consistent theory because it satisfies the condition $\text{Tr} [T_3^2 Y] = \text{Tr} [Y^3] = 0$, where the trace is run over the left-handed Weyl fermionic degrees of freedom. If a single Higgsino field, with either $Y = +1/2$ or $Y = -1/2$ is added to the theory, the cancellation is broken, and the theory becomes inconsistent. Adding a second Higgsino field with the opposite hypercharge restores the cancellation.

The two Higgs superfields in the MSSM are named H_u and H_d , and have $Y = +1/2$ and $Y = -1/2$ respectively. The subscript represents the types of quark which interact with the Higgsino field. The additional Higgs fields adds four more degrees of freedom to the MSSM, which adds four additional Higgs bosons (five in total).

The full list of chiral and gauge supermultiplets contained in the MSSM are shown in Tables 2.2 and 2.3. It should also be noted that, just as the W^3 and B fields of the SM mix to form the photon and the Z boson, the neutral (charged) gauginos and Higgsinos mix to form the neutralinos (charginos).

Table 2.2: Summary of the chiral supermultiplet fields in the MSSM [1].

Names		Spin 0	Spin 1/2	SU(3) _C , SU(2) _L , U(1) _Y
Squarks, quarks (3 families)	Q	$(\tilde{u}_L, \tilde{d}_L)$	(u_L, d_L)	3, 2, 1/3
	\bar{u}	$\tilde{\bar{u}}_L = \tilde{u}_R^\dagger$	$\bar{u}_L = (u_R)^c$	3, 1, -4/3
	\bar{d}	$\tilde{\bar{d}}_L = \tilde{d}_R^\dagger$	$\bar{d}_L = (d_R)^c$	3, 1, 2/3
Sleptons, leptons (3 families)	L	$(\tilde{\nu}_{e,L}, \tilde{e}_L)$	$(n\nu_{e,L}, e_L)$	1, 2, -1
	\bar{e}	$\tilde{\bar{e}}_L = \tilde{e}_R^\dagger$	$\bar{e}_L = (e_R)^c$	1, 1, 2
Higgs, Higgsinos	H_u	(H_u^+, H_u^0)	$(\tilde{H}_u^+, \tilde{H}_u^0)$	1, 2, 1
	H_d	(H_d^0, H_d^-)	$(\tilde{H}_d^0, \tilde{H}_d^-)$	1, 2, -1

Table 2.3: Summary of the gauge supermultiplet fields in the MSSM [1].

Names	Spin 1/2	Spin 1	SU(3) _C , SU(2) _L , U(1) _Y
Gluinos, gluons	\tilde{g}	g	8, 1, 0
Wino, W boson	$\tilde{W}^\pm, \tilde{W}^0$	W^\pm, W^0	1, 3, 0
Bino, B boson	\tilde{B}	B	1, 1, 0

2.3.4 Supersymmetric Lagrangian

In constructing a supersymmetric model, a new Lagrangian is constructed, with kinetic and interaction terms. The kinetic terms of a supersymmetric Lagrangian are of the form

$$\mathcal{L}_{\text{kinetic}} = -\frac{1}{4}G_{\mu\nu}^a G_a^{\mu\nu} + \tilde{G}^{\dagger a} i\bar{\sigma}^\mu D_\mu \tilde{G}_a + f^{\dagger i} i\bar{\sigma}^\mu D_\mu f_i - (D_\mu \phi_i)^\dagger D^\mu \phi^i, \quad (2.31)$$

where G and \tilde{G} represent any gauge boson and gaugino in the theory respectively, f is any fermion, and ϕ is any scalar field.

The interaction terms are written in terms of a superpotential \mathcal{W} , and take the form.

$$\mathcal{L}_{\text{int}} = -\sum_i \left| \frac{\partial \mathcal{W}}{\partial z_i} \right|^2 - \frac{1}{2} \sum_{ij} \left(\bar{f}_i \frac{\partial^2 \mathcal{W}}{\partial z_i \partial z_j} f_j + \text{h.c.} \right). \quad (2.32)$$

z_i are the superfields of theory, and the theory is specified by \mathcal{W} . The particular form of \mathcal{W} that leads to the MSSM is

$$\mathcal{W} = \sum_{ij} \left(-Y_{ij}^u \bar{u}_i H_u \cdot Q_j + Y_{ij}^d \bar{d}_i H_d \cdot Q_j + Y_{ij}^\ell \bar{e}_i H_d \cdot Q_j + \mu H_u \cdot H_d \right), \quad (2.33)$$

where Y_{ij} are Yukawa couplings among generations, and the superscript is a label for the type of interaction rather than an index to be summed over. The first three terms are generalizations of SM Yukawa interactions. The last term is the globally supersymmetric mass for the Higgs fields.

2.3.5 R-Parity

The extension of the Standard Model of particle physics with supersymmetry immediately leads to processes that violate both baryon number (B) and lepton number (L) conservation. In addition to the interaction terms given in Equation 2.32, the most general MSSM Lagrangian may contain terms such as

$$W_{\Delta L=1} = \frac{1}{2} \lambda^{ijk} L_i L_j \bar{e}_k + \lambda'^{ijk} L_i Q_j \bar{d}_k + \mu'^i L_i H_u, \quad (2.34)$$

$$W_{\Delta B=1} = \frac{1}{2} \lambda''^{ijk} \bar{u}_i \bar{d}_j \bar{d}_k, \quad (2.35)$$

where i, j, k indicate the family indices. If both the lepton number violating and baryon number violating terms are allowed to contribute, the interactions lead to rapid proton decay ($p \rightarrow \pi^0 e^+$, and lepton-number-violating processes, such as unseen decays of $\mu \rightarrow e\gamma$, in conflict with experimental bounds. A conventional assumption to prevent these processes is to impose conservation of R -parity [60, 61, 62, 63, 64], defined as

$$R = (-1)^{3(B-L)+2s}, \quad (2.36)$$

where s is the spin of the particle. This has a value of +1 for Standard Model particles and -1 for SUSY particles. In this case, SUSY particles are produced in pairs, and the LSP is stable. Furthermore, the stable LSP cannot carry electric charge or color charge without coming into conflict with astrophysical data. A stable LSP also serves as a viable dark matter candidate. At the LHC, the conventional experimental signature for SUSY particles includes significant missing transverse momentum due to the non-interaction of the LSP with the detector.

2.4 B-L extension

While R -Parity conservation does prevent the rapid decay of the proton, it is a rather strict requirement. There exist alternative approaches, that accomplish the same goal, but allow for some of the interactions described in Equations 2.34 and 2.35. One such approach is to add a local symmetry $U(1)_{B-L}$ to the $SU(3)_C \times SU(2)_L \times U(1)_Y$ SM with right-handed neutrinos. The minimal supersymmetric extension then only needs a vacuum expectation value for a right-handed sneutrino in order to spontaneously break the $B - L$ symmetry [65, 66, 67, 68, 69, 70, 71, 72, 73, 74, 75, 76]. This minimal $B - L$ model violates lepton number conservation, but not baryon number conservation, and is consistent with proton stability and the bounds on lepton number violation. The LSP can now decay via R -parity-violating (RPV) processes, and may now carry color and electric charge.

2.4.1 Phenomenology

This leads to unique signatures [77, 78, 76, 79, 80] that are disallowed in conventional models with R -parity conservation. The case where the LSP is a scalar top (stop) is most interesting. Since the top quark is the heaviest SM particle, the lightest stop must be reasonably light in order to cancel the radiative corrections to the Higgs mass. Since the other quarks are significantly lighter, the other squarks may be heavy without introducing too much fine tuning [81, 82]. The stop decays via an RPV interaction to a charged lepton (of any flavor) and a b -quark. The decay branching fractions to eb , μb , and τb may be different, in a manner related to the neutrino mass hierarchy seen in Figure 2.5.

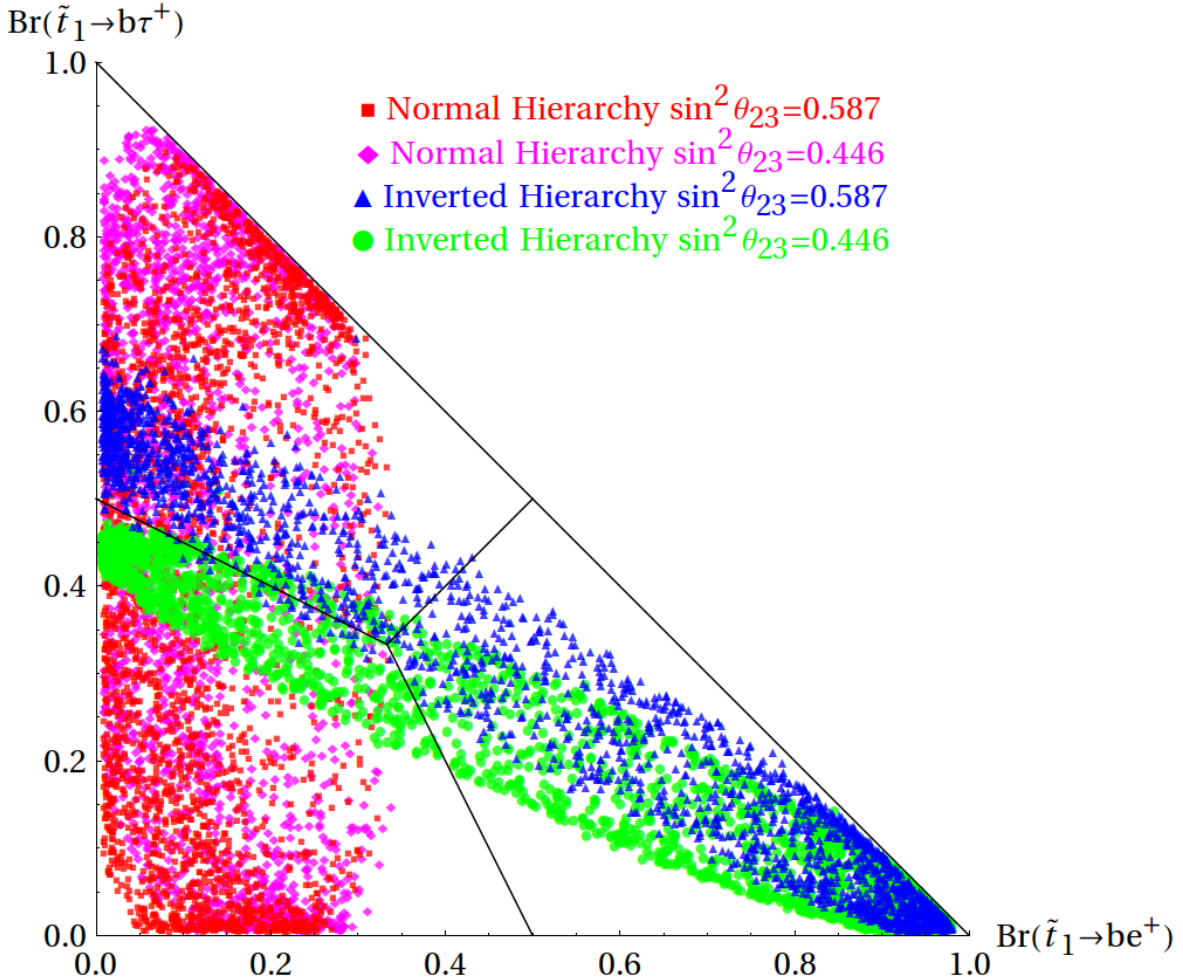


Figure 2.5: The allowed branching ratios for the stop LSP for various choices of the neutrino mass hierarchy and $\sin^2 \theta_{23}$, obtained by varying various model parameters within a range of natural values shown in Table 2.4 [2].

Each point in this plot represents a simulation with a particular choice of model parameters, all varied within a natural range of values, shown in Table 2.4, and the four colors represent different choices for the neutrino mass hierarchy and $\sin^2 \theta_{23}$ [2, 33]. There is a clear relation between the neutrino mass hierarchy and the allowed stop branching ratios. If a stop consistent with this model is discovered, its properties could potentially give information about the structure of the neutrino sector.

Within this model, a stop LSP can decay in one of two ways, depending on the handedness of the stop. A right-handed stop decays to a top quark and a right-handed neutrino with a coupling strength proportional to vacuum expectation value (vev) of the left-handed sneutrino mass. This must be small because the left-handed sneutrino interacts with the W and Z bosons, and a large vev would result in

Table 2.4: Ranges for the parameter scan used to generate the simulated models shown in Figures 2.5 and 2.6. The neutrino sector constrains all but one of the R-parity violating parameters, which is chosen to be ϵ_i where the generational index, i , is also scanned to avoid any biases. “NH” and “IH” represent the normal and inverted neutrino mass hierarchy respectively [2].

Parameter	Range
M_3 [TeV]	1.5 – 10
M_{Z_R} [TeV]	2.5 – 10
$\tan \beta$	2 – 55
μ [GeV]	150 – 1000
$m_{\tilde{t}_1}$ [GeV]	400 – 1000
θ_t [°]	0 – 90
$ \epsilon_i $ [GeV]	$10^{-4} – 1$
$\arg(\epsilon_i)$ [°]	0 – 360
i	1 – 3
ξ_0, ξ_3	-1, 1
δ, α [°]	0 – 360
Neutrino Hierarchy	NH, IH

these bosons gaining additional mass. A purely left-handed stop decays to a b -quark and a lepton with the coupling strength proportional to the vev of the right-handed sneutrino, which may be large, as the right-handed sneutrino does not couple to the electroweak bosons. In the scenario where the stop LSP is an admixture of left- and right-handed stops, the preferred decay mode depends on the stop mixing angle (θ_t). This dependence is plotted in Figure 2.6(a), which shows the ratio $\text{Br}(\tilde{t} \rightarrow t\nu)/\text{Br}(\tilde{t} \rightarrow b\ell)$ versus θ_t . Each point represents a simulation with a particular choice of model parameters, again scanning over the natural values in Table 2.4. The $\tilde{t} \rightarrow b\ell$ decay is the dominant decay mode for mixing angles less than about 80° , where the LSP stop is mostly right handed, and the $\tilde{t} \rightarrow t\nu$ decay becomes significant. The $\tilde{t} \rightarrow b\ell$ decay is still non-negligible for a mostly right-handed stop in many of the simulated models, however [2, 33].

The analysis described in this thesis focuses on the $\tilde{t} \rightarrow b\ell$ decay as it is preferred for most of parameter space. Additionally, if the $\tilde{t} \rightarrow t\nu$ decay is significant, the decay of stop pairs would lead to final states with $t\bar{t}$ associated with large missing energy, which is the same final state as stop pair production with R -Parity conserving decays, and the limits from traditional stop searches can be reinterpreted for this model.

It is also reasonable to assume the stop decays in this model are prompt, and decay with a negligible impact parameter, as shown in Figure 2.6(b). For most natural models, the stop is expected to have a

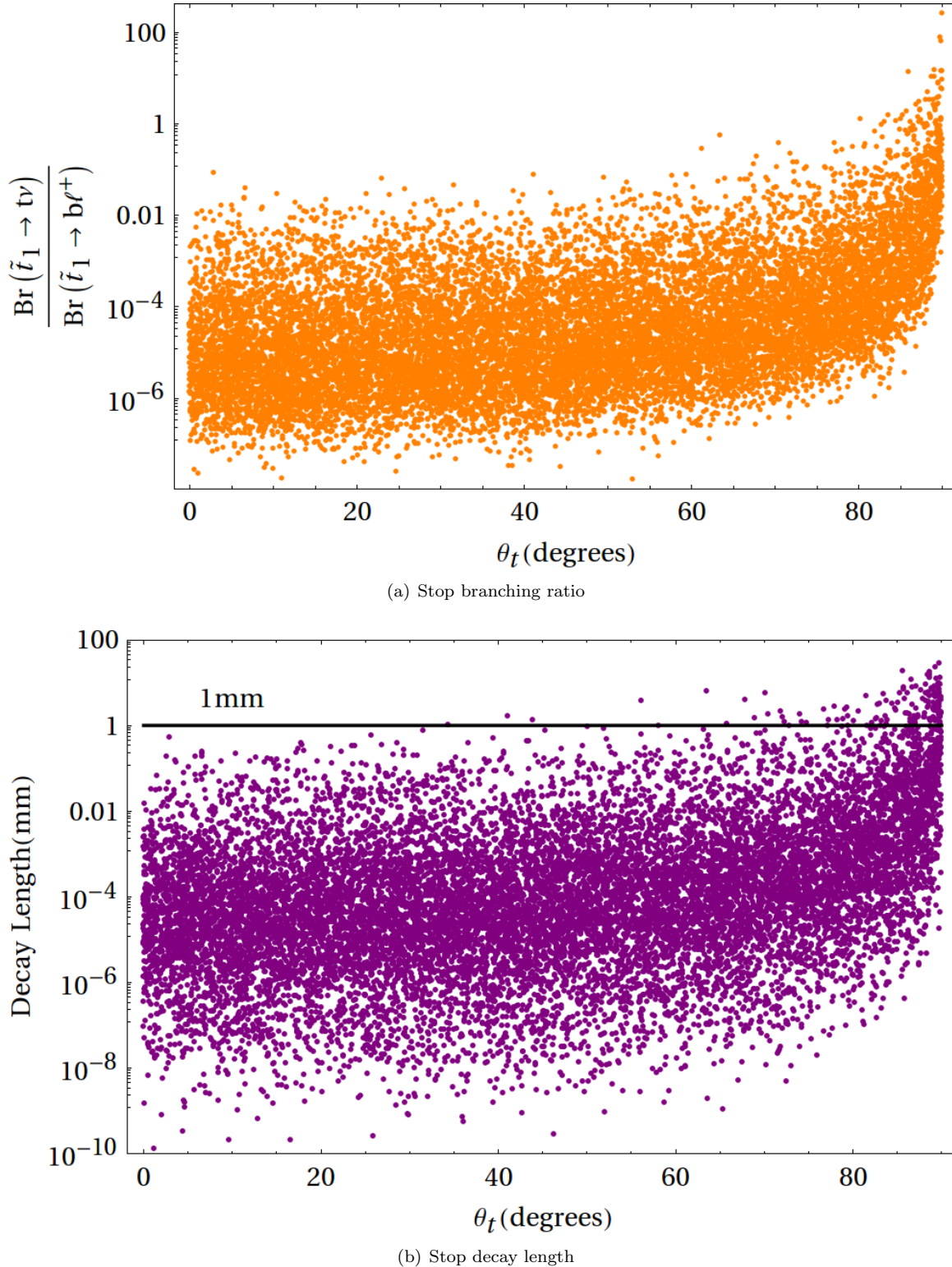


Figure 2.6: The stop decay branching ratio (a) and stop decay length (b) versus the stop mixing angle, assuming the stop is the LSP. Each point represents a simulation with a particular choice of model parameters, which are sampled from a range of natural values [2].

decay length of less than 10^{-3} mm; in particular, this is true for models where the stop is not mostly right-handed ($\theta_t \leq 80^\circ$) [2, 33].

In this $B - L$ extension to the MSSM, the R -Parity conserving terms are the same as the traditional MSSM model, and have larger coupling strength than the R -Parity violating terms. Therefore, stop pair production has the same production cross section as in the traditional MSSM. The expected production cross sections are shown in Figure 2.7. If the stop is assumed to be the LSP, it must decay via an R -Parity violating interaction.

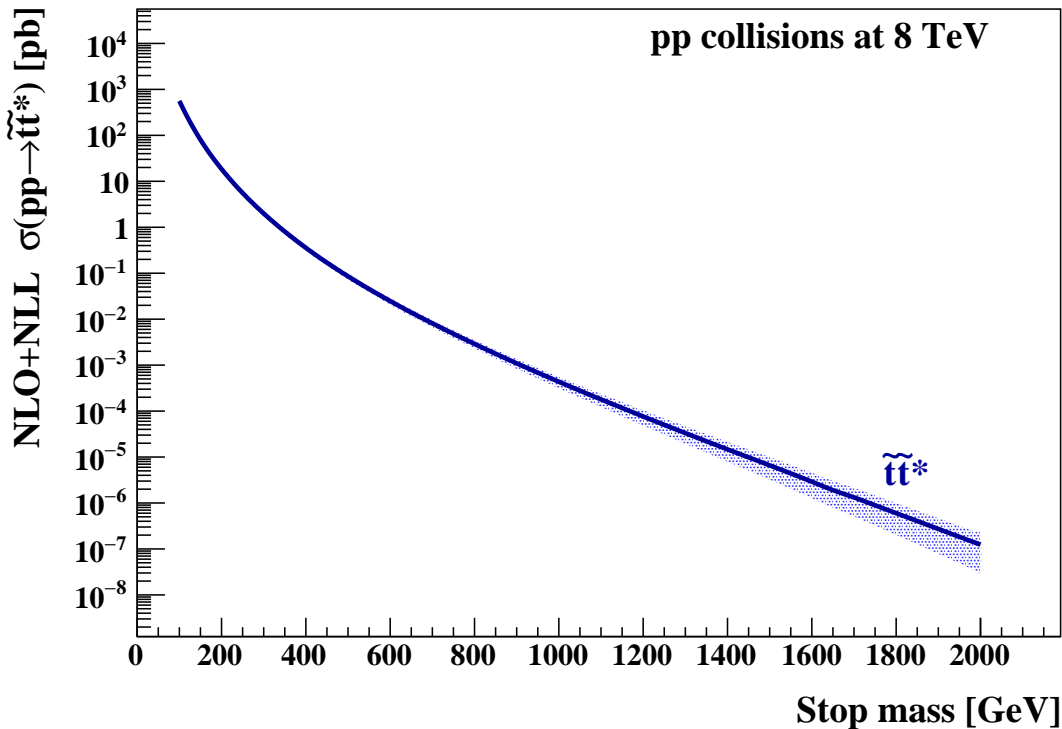


Figure 2.7: Stop cross sections and their associated uncertainties [3, 4, 5].

2.4.2 Previous results

The results from existing leptoquark searches performed at ATLAS were re-interpreted in the context of this $B - L$ SUSY model, and the limits obtained on the minimum allowable stop mass across the plane of physical stop branching ratios are shown in Figure 2.8 [2, 33]. The phenomenological reinterpretation used to produce the limits shown in Figure 2.8 assumes the stop is the LSP, and

it decays to a b -quark and a lepton. Previous leptoquark searches, including those used to obtain these mass limits, targeted models where the decay products of the leptoquark are in the same generation. As a result, b -tagging is only required in events associated with a τ lepton, and events with a light lepton simply require a jet, regardless of the flavor. Additionally, previous leptoquark searches only consider decays to a single lepton flavor, resulting in final states with either two leptons of the same flavor and two jets, or a single charged lepton and at least one jet. Previous analyses did not consider final states with two charged leptons with different flavors ($e\mu$) and at least two jets [25, 26, 27, 30, 31, 32, 83]. A dedicated search requiring b -tagged jets associated with light leptons (electrons and muons), and considering different flavored leptons in the final state provides additional sensitivity to this model, as well as other models which result in final states with b -quarks and light leptons in the final state.

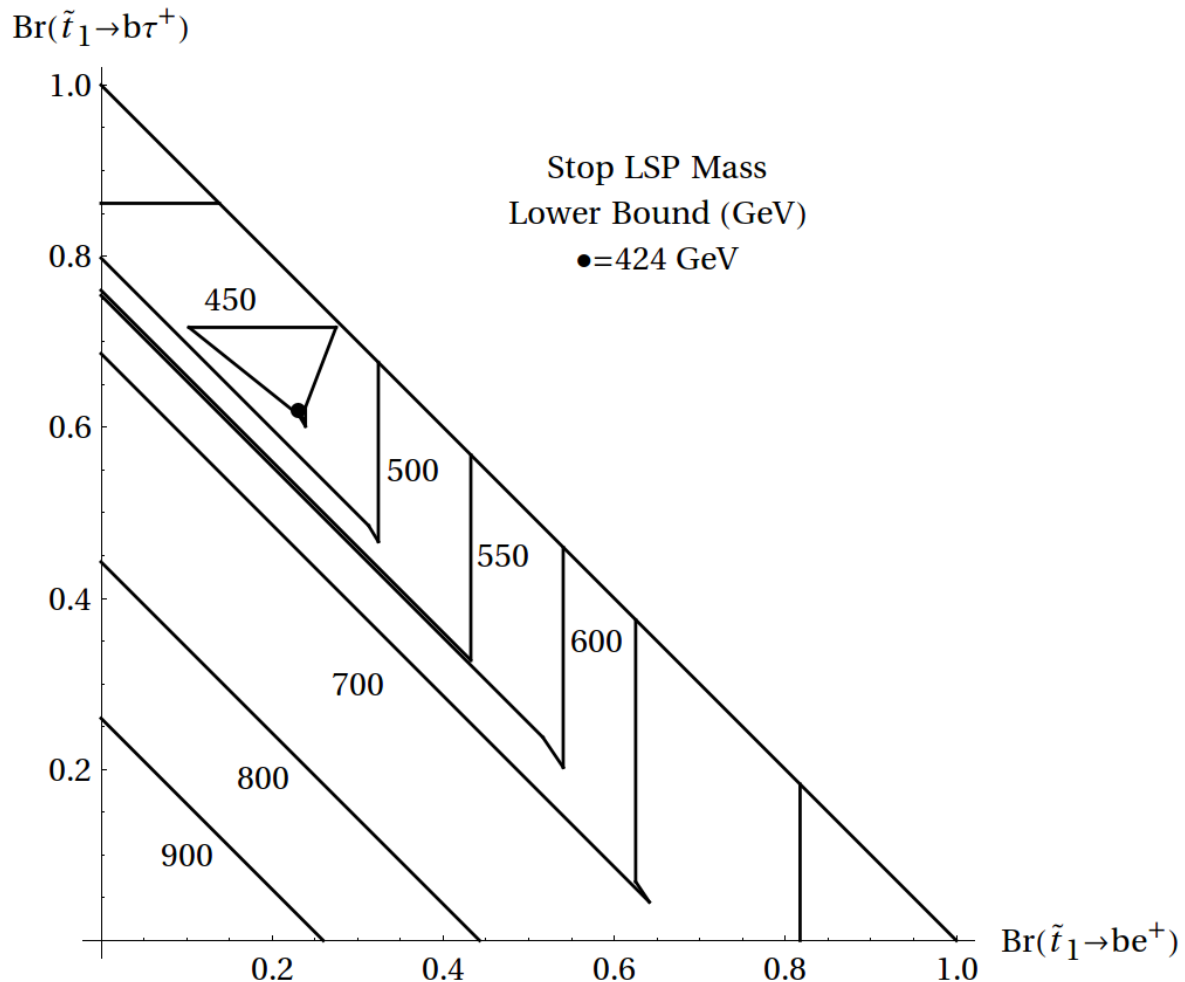


Figure 2.8: Limits on the stop mass obtained by reinterpreting leptoquark searches performed at ATLAS. The mass limits assume the stop is the LSP, and decays to a b -quark and a lepton [2].

CHAPTER 3

The Large Hadron Collider and the ATLAS experiment

As the name suggests, the Large Hadron Collider (LHC) is a particle collider, which collides particles at very high energies. There are four major experiments, including ATLAS, which collect and study data generated from these particle collisions in an effort to study the properties of nature, and search for signs of physics beyond the Standard Model. This chapter gives a brief introduction to the LHC machine, and the ATLAS experiment.

3.1 The LHC machine

The LHC [84] is circular particle accelerator, with a circumference of 27 km, built 100 m underground, underneath the French-Swiss border near the city of Geneva, Switzerland, shown in Figure 3.1. The LHC is operated by the European Organization for Nuclear Research (CERN¹). The LHC became fully operational in 2010, providing proton-proton collisions to the experiments along the ring at a record high center-of-mass energy of 7 TeV. In 2012, the energy was increased to 8 TeV.

Four major experiments are positioned around the LHC to collect and analyze data from the hadron collisions. The experiments include ATLAS [15], CMS [85], ALICE [86], and LHCb [87]. ATLAS and CMS are designed to be “general purpose experiments,” searching for physics beyond the Standard Model which may present itself in many ways. The two experiments complement each other by providing independent results, which can be verified against each other. ALICE is designed to study the heavy ion (lead nuclei) collisions, including the properties of a quark-gluon plasma. The LHCb experiment is primarily interested in studying the physics of b -hadrons.

¹Conseil Européen pour la Recherche Nucléaire

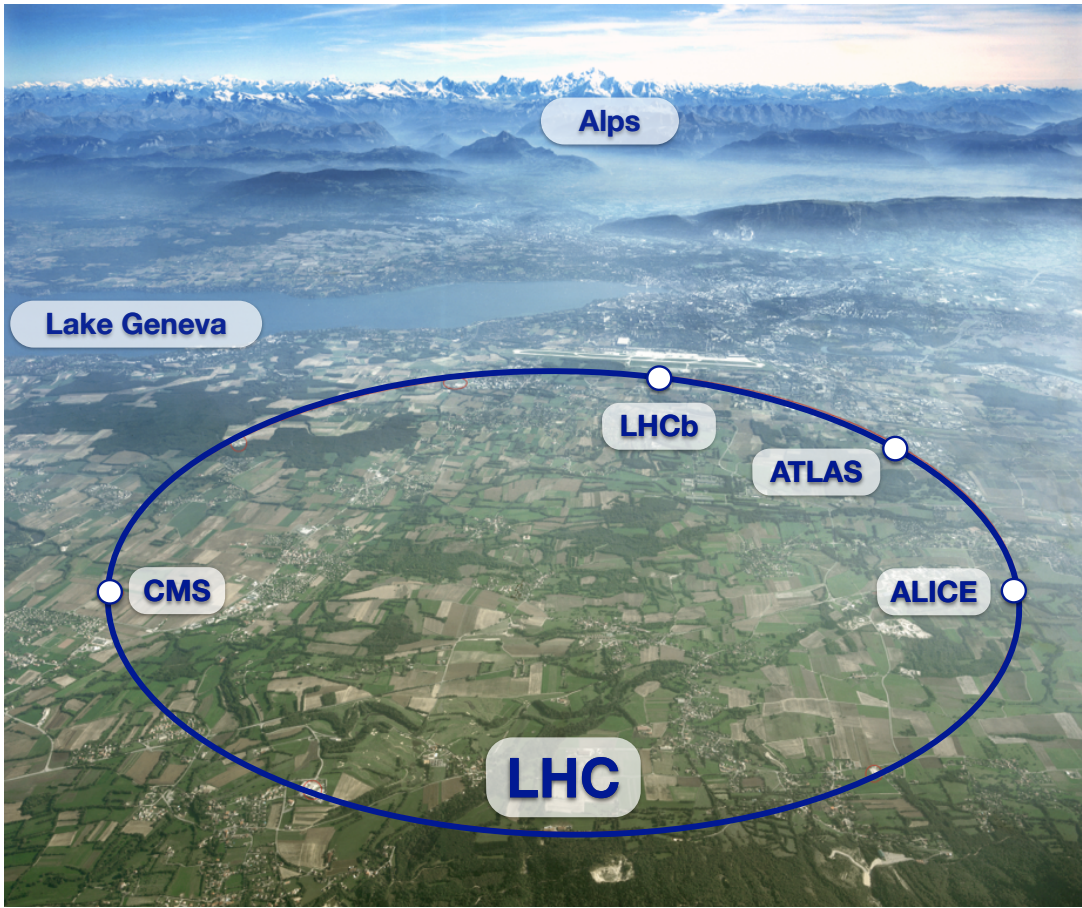


Figure 3.1: Areal view of the Geneva area with an overlaid drawing of the LHC and experiments [7].

3.1.1 CERN accelerator complex

The LHC is only the final stage in a series of accelerators, operated by CERN, used to provide high energy particle collisions. For proton-proton collisions, protons begin in the Linac 2 linear accelerator, where they are accelerated to an energy of 50 MeV per proton. From there, the protons are fed through several circular accelerators, including the Proton Synchrotron Booster (PSB), Proton Synchrotron (PS), and the Super Proton Synchrotron (SPS), where the protons are accelerated to energies of 1.4 GeV, 25 GeV, and 450 GeV respectively. At this stage, the protons are injected into the LHC accelerator, where in 2012, they were accelerated to an energy of 4 TeV per proton, and finally collided. A schematic of the CERN accelerator complex, and how the individual accelerators link to one another is shown in Figure 3.2.

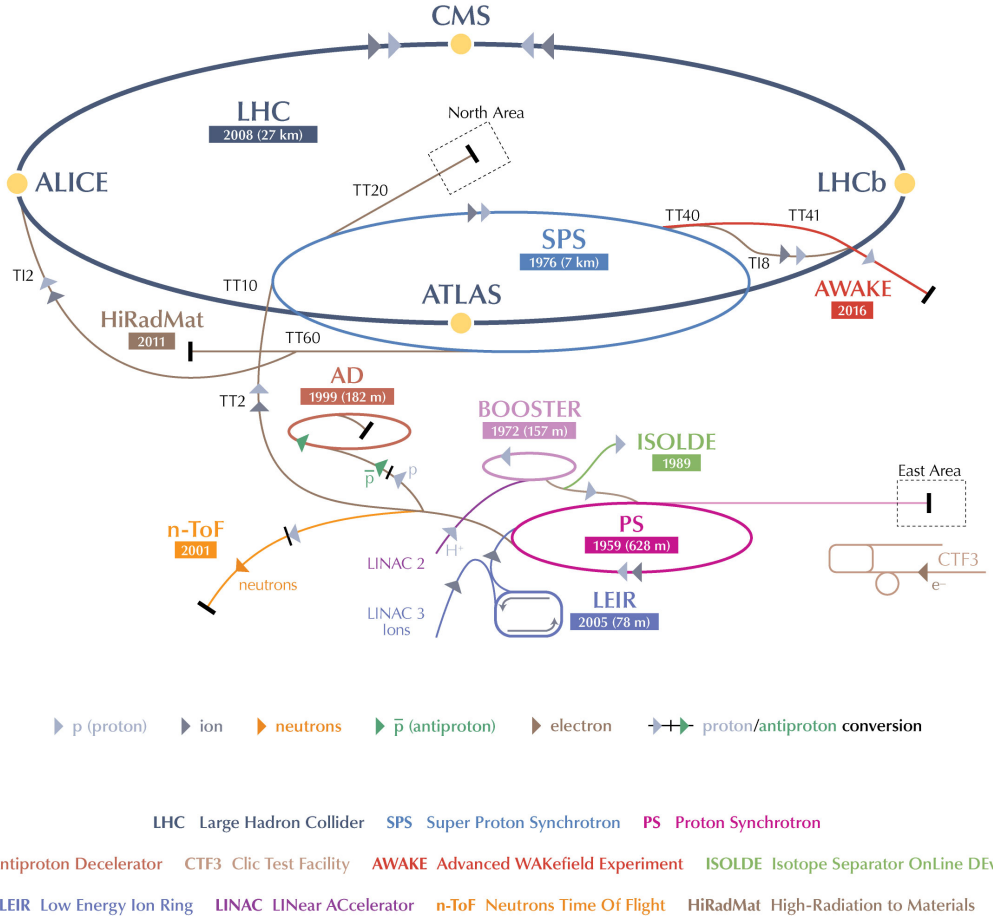


Figure 3.2: Schematic view of the CERN accelerator complex [8].

3.1.2 LHC beam conditions

Rather than a constant stream of protons, the protons in the LHC are separated into over 1000 bunches, each containing over 10^{11} protons. In each of the interaction points around the LHC ring, proton bunches cross once every 50 ns, where each crossing leads to potential collisions between the constituent protons. The instantaneous luminosity of collisions in these bunch crossings is given by

$$\mathcal{L}_{\text{instantaneous}} = \frac{N_1 N_2 n_b f_{\text{rev}}}{4\pi\sigma_x\sigma_y} F, \quad (3.1)$$

where $N_{1,2}$ are the number of protons per bunch (about 10^{11}), n_b is the number of bunches (up to 2808, though only 1404 for 50 ns operation), f_{rev} is the revolution frequency of each bunch (about 11,245 Hz), $\sigma_{x,y}$ is the width of the beam (about 20 μm after being brought into focus by strong

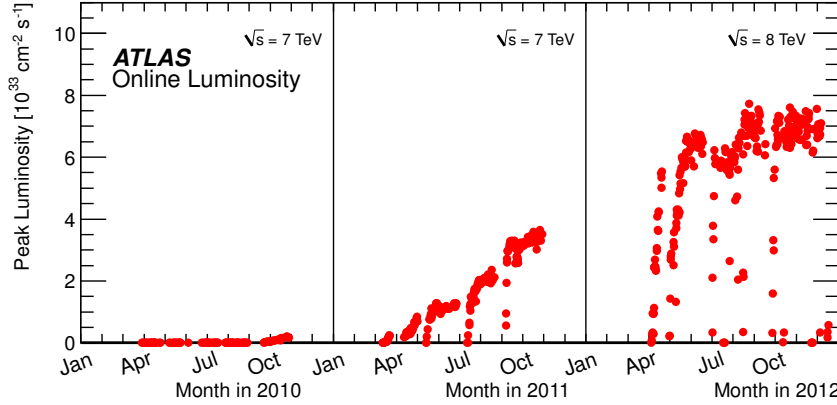


Figure 3.3: Instantaneous luminosity collected by the ATLAS detector throughout Run 1 [9].

quadrapole magnets near the collision point), and F is a reduction factor, accounting for the fact that the beams cross at an angle, rather than head-on. The proton beams tend to spread over time out as they circulate and undergo collisions, increasing $\sigma_{x,y}$, and reducing the instantaneous luminosity. Typically, the LHC is filled with proton beams at an injection energy of 450 GeV, then the proton beams are accelerated to the full energy of 4 TeV per beam in 2012, then the two counter-rotating proton beams are brought into collision for a period of several hours for stable data-taking by the experiments, and then finally the beams are dumped when the instantaneous luminosity has fallen below some threshold.

Figure 3.3 shows that the instantaneous luminosity of proton-proton collisions provided to ATLAS by the LHC increased throughout the running period as the machine was thoroughly tested and better understood. This is accomplished by adding more protons, and squeezing the beams into a smaller area for the collisions. The higher instantaneous luminosity allowed for faster data collection in later running periods, but came at the cost of a larger number of interactions per crossing, seen in Figure 3.4.

3.2 The ATLAS experiment

ATLAS is one of the two general purpose experiments, which collect and analyze data from LHC collisions [15]. ATLAS is located at interaction point 1 of the LHC, across the street from the CERN Meyrin campus. The experiment is made up of many “sub-detectors,” using an array of technologies, which work together to reconstruct the collision events. Figure 3.5 shows a cut-away diagram of the ATLAS experiment, highlighting the various sub-detectors. Starting from the interaction point, and

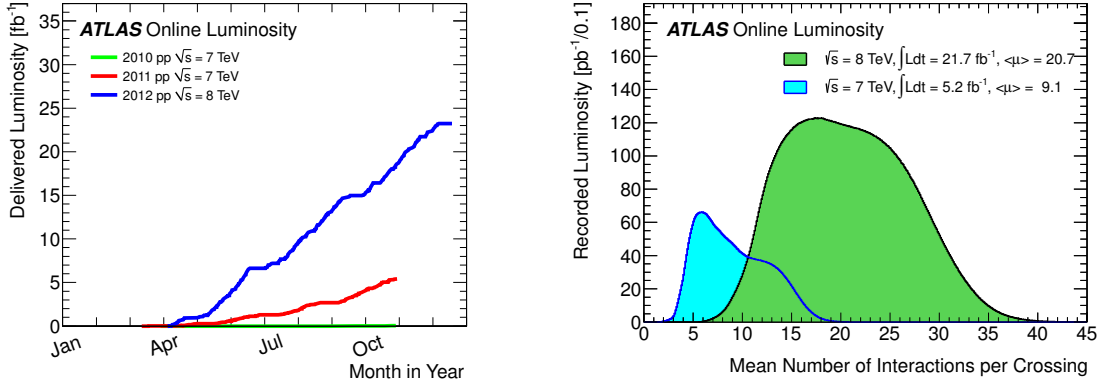


Figure 3.4: (Left) Integrated luminosity of proton-proton collision data collected by ATLAS during the three years of Run 1. The rate of data collection was increased in part by increasing the number of interactions per crossing (right).

moving outward, the sub-detectors are grouped into three main categories, an inner detector (Section 3.2.2), used to measure the trajectory of charged particles, the calorimetry system (Section 3.2.3), which records the energy deposition of particles, and a muon spectrometer (Section 3.2.4) which is used to identify and track muons. These systems and their components are described in more detail in the coming sections.

3.2.1 Coordinate system

ATLAS uses a right-handed coordinate system with its origin at the nominal interaction point (IP) in the center of the detector and the z -axis along the beam pipe. The x -axis points from the IP to the center of the LHC ring, and the y -axis points upward. Cylindrical coordinates (R, ϕ) are used in the transverse plane, ϕ being the azimuthal angle around the beam pipe. The pseudorapidity is defined in terms of the polar θ angle as

$$\eta = -\ln \left[\tan \left(\frac{\theta}{2} \right) \right]. \quad (3.2)$$

where η is preferred over θ because particle production is roughly constant in η at a hadron collider. The distance parameter (in η - ϕ space)

$$\Delta R = \sqrt{(\Delta\eta)^2 + (\Delta\phi)^2} \quad (3.3)$$

is used when measuring the distance between signatures in the detector.

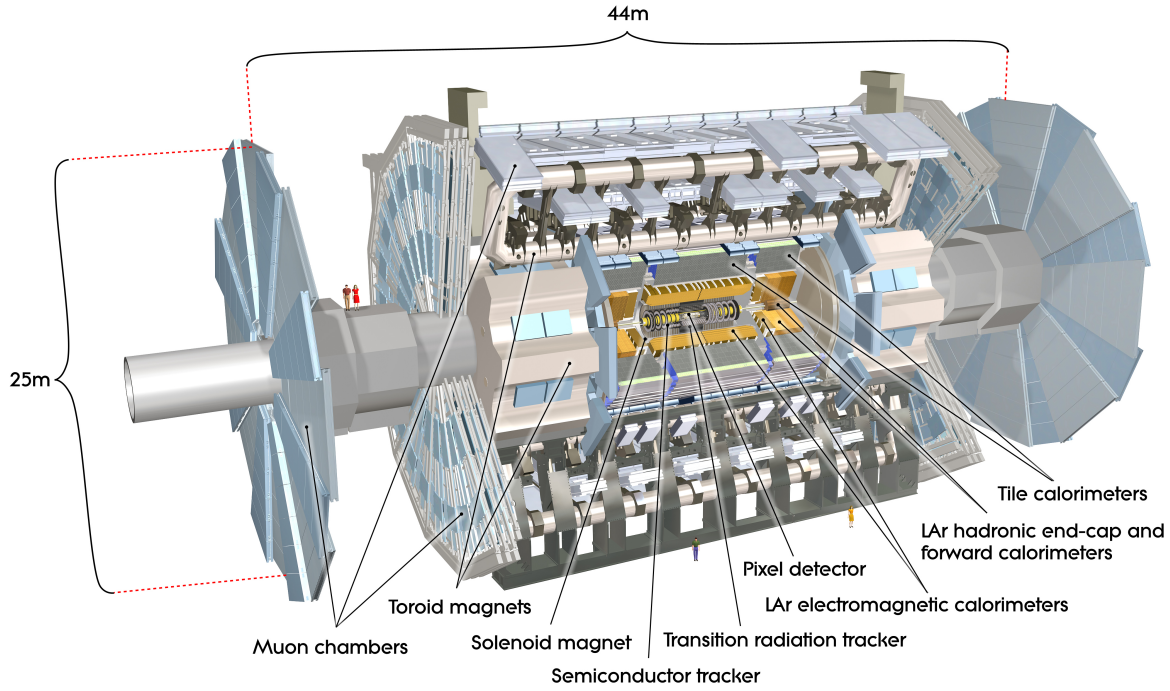


Figure 3.5: The ATLAS experiment [10].

3.2.2 Inner detector

The inner detector (ID) comprises the three innermost sub-detectors of ATLAS, the pixel detector, silicon semiconductor tracker (SCT), and the transition radiation tracker (TRT), shown in Figure 3.6. The passage of high energy charged particles is detected from the electron-hole pairs produced in the silicon semiconductor sensors of the pixel and SCT, and from the ionization production in the gas-filled straws of the TRT. The three sub-detectors are described in Sections 3.2.2.1 to 3.2.2.3, and tracking is reviewed in Section 3.2.2.4.

3.2.2.1 Pixel detector

The pixel detector, shown in Figure 3.7, is the closest sub-detector in ATLAS to the interaction point. It uses silicon pixel technology to provide high granularity for precision tracking. The detector consists of three barrel layers, at radii of 50.5 mm, 88.5 mm, and 122.5 mm, and three disks on either side of the barrel, with mean z -values of 495 mm, 580 mm, and 650 mm. The pixel detector provides coverage up to $|\eta| = 2.5$. In total, there are 80×10^6 channels in the pixel detector, each with a

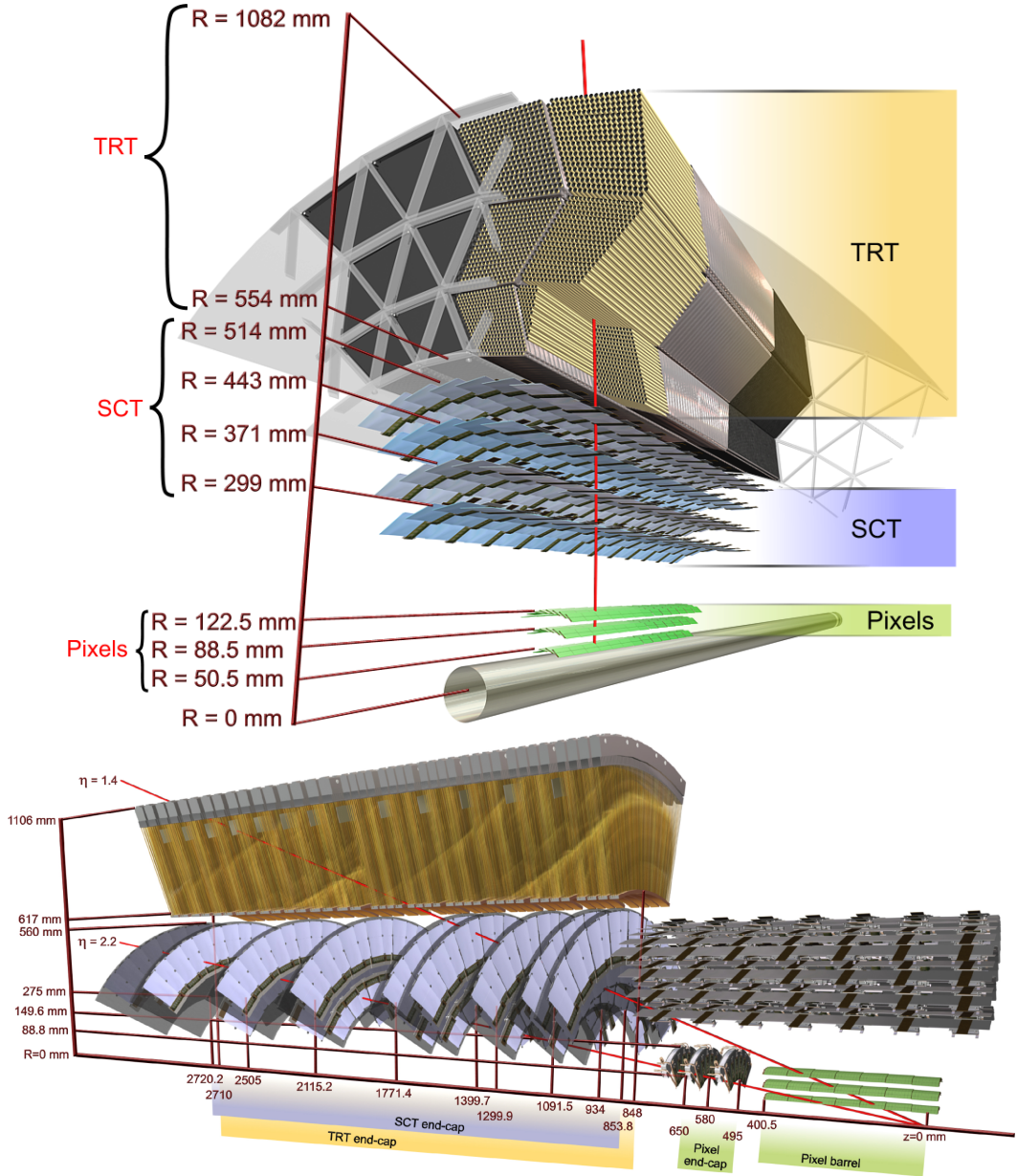


Figure 3.6: Schematic of the inner detector of the ATLAS experiment. The barrel (top) and endcap (bottom) are shown separately. The inner detector is made up of layers, consisting of the silicon pixels, the silicon semiconductor tracker (SCT), and the transition radiation tracker (TRT) [11].

nominal pixel size is $50 \mu\text{m}$ in the ϕ dimension, and $400 \mu\text{m}$ in z [88].

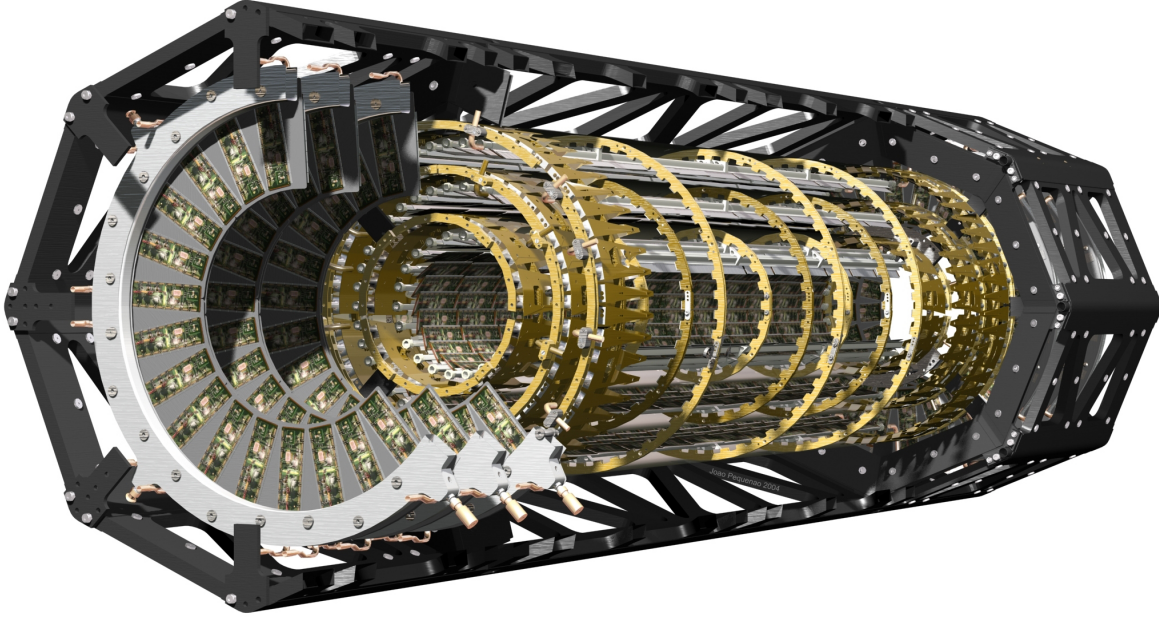


Figure 3.7: The Silicon pixel tracker of the ATLAS experiment [12].

3.2.2.2 Silicon semiconductor tracker

The SCT, shown in Figure 3.8, is also made of silicon detectors, but rather than pixels, the SCT uses microstrip technology. The detector is made up of four double layers in the barrel, and nine endcap layers on each side of the barrel. The SCT provides coverage up to $|\eta| = 2.5$. A charged particle has, on average, eight hits in the SCT, with each hit in the barrel (endcap) having a resolution of $17 \mu\text{m}$ in the $r - \phi$ ($z - \phi$) plane, and $580 \mu\text{m}$ in the z (r) dimension. There are 6.3 million read-out channels in the SCT.

3.2.2.3 Transition radiation tracker

The TRT, shown during the commissioning process in Figure 3.9 makes up the largest and outer layer of the ID, and is used for both tracking and particle identification. The TRT covers up to $|\eta| = 2.0$. The TRT employs 350,000 straws filled with a gas mixture made up of Xe (70%), CO₂ (27%), and O₂ (3%). Each straw of the TRT is 4 mm in diameter and has at its center a $30 \mu\text{m}$ diameter gold-plated tungsten wire at ground potential. The outer wall of the straw is a cathode at -1530 V , leading

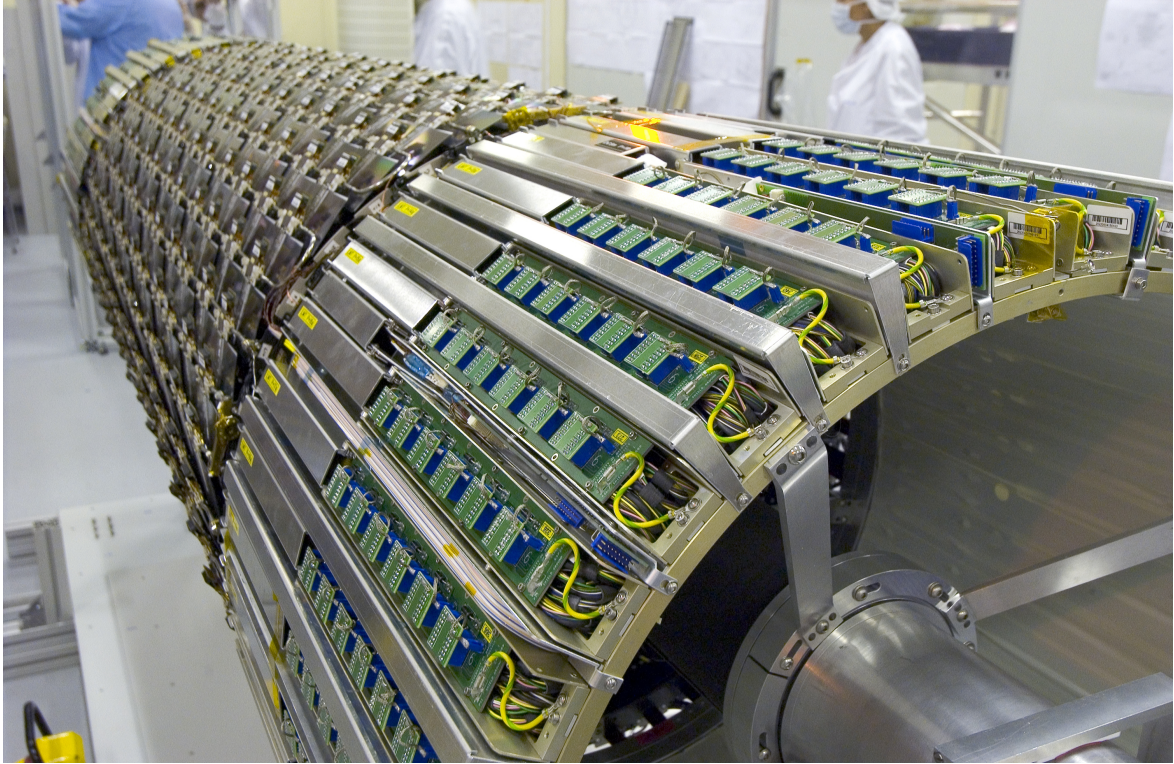


Figure 3.8: Photograph of the silicon semiconductor tracker of the ATLAS experiment [13].

to an electric field that separates the ionized electrons and ions, and a large gas gain of 2.5×10^4 in the high field region close to the wire.

The TRT has a less precise resolution than the silicon trackers, but a charged particle track may have more than 30 TRT hits and a large lever arm out to 1.1 m from the beamline. The TRT barrel has a precision of $130 \mu\text{m}$ in the $r - \phi$ plane, but much worse resolution z since there is little segmentation in this dimension.

The TRT is also designed for use in particle identification. Transition radiation (TR) is emitted when a charged particle crosses a boundary between media with different dielectric constants. The amount of TR is proportional to the Lorentz γ factor, which is in turn related to the particle mass. Electrons are roughly 200 times less massive than pions, so have a higher probability to emit TR while crossing a boundary. The space between the TRT straws is filled with radiator material providing many such boundaries to facilitate TR. Xe was chosen as the active gas because it has a large absorption cross section for TR photons. The absorption of the additional TR photons induces more ionization, and therefore, more charge to build up on the wire. All this results in a larger signal,

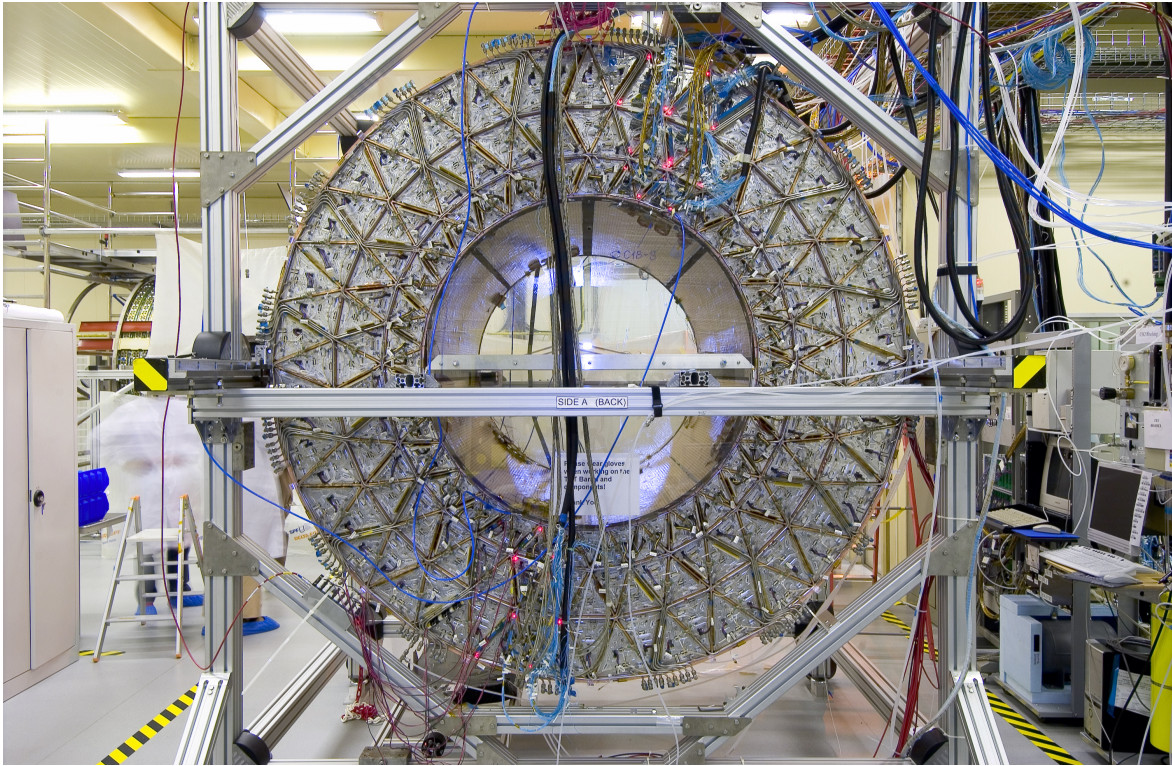


Figure 3.9: Photograph of the transition radiation tracker of the ATLAS experiment during its commissioning [14].

which can be detected by the TRT front-end electronics. The TRT operates with two threshold values (low- and high-threshold). The low-threshold is used for tracking, and is tuned for the typical amount of ionization from a charged particle passing through the TRT straws. The high-threshold is tuned to register the larger signal when the Xe gas absorbs the TR photons. The fraction of TRT hits associated with a charged particle track that exceed the high-threshold is a discriminating variable used to identify electrons.

3.2.2.4 Tracking

The ID is used to reconstruct the trajectory of charged particles. The individual measurements made along the trajectory of the charged particle are referred to as “hits.” Hits from the three ID sub-detectors are combined into tracks using Kalman filtering tools which account for multiple scattering as a particle traverses the ID [89, 90].

The ID is enclosed inside a solenoid magnet, with a field strength of 2 T. The magnetic field bends

the trajectory of moving charged particles perpendicular to the field direction according to $\vec{F} = q\vec{v} \times \vec{B}$. The magnetic field is pointing along the direction of the beam, so charged particles coming from the interaction point will form a helix, with radius of curvature determined by the transverse momentum (p_T). Particles with low p_T will bend more than those with higher p_T . As the particle p_T increases, the track becomes closer to a straight line. The p_T of charged particle tracks is related to the radius of curvature by

$$p_T = q \cdot B \cdot r. \quad (3.4)$$

It should be noted that we actually measure the sagitta of the arc (which is the amount the measured arc bows from a cord) for the hits on a particle's trajectory. The sagitta is inversely proportional to the radius of curvature ($s = \frac{L^2}{8r}$ where L is the length of the cord, or lever-arm) and s is the sagitta). Thus the uncertainty on the p_T is proportional to the square of the p_T . This is usually written as the relative momentum resolution being proportional to the p_T of the particle ($\frac{\Delta p_T}{p_T} \propto p_T$). The uncertainty on the sagitta decreases with better position resolution for each hit, higher number of hits, stronger magnetic field and larger radius for tracking. Although the position resolution of the TRT is worse per hit than for the silicon detectors, the TRT does provide a large number of hits (about 30) per track and doubles the active tracking radius. The TRT is in fact critical to obtaining the best possible momentum resolution at high p_T .

3.2.3 Calorimetry

The calorimetry system, situated outside the ID and the solenoid, is shown in Figure 3.10. The calorimetry systems of ATLAS are designed to complement one another and offer full coverage in the ϕ , and pseudorapidity coverage up to $|\eta| = 4.9$. The objective of the calorimeters is to stop particles like electrons, photons, and hadrons and measure their energy. ATLAS uses “sampling calorimeters,” which absorb a fraction of the total energy, and must infer the full shower energy. This is achieved using a dense absorber material to initiate a shower, and an active material to sample the energy deposition.

The calorimetry system is broken up into three sub-systems, the electromagnetic calorimeter (EM calorimeter), the hadronic calorimeter, and the forward calorimeter (FCal). Each of the sub-systems employ different absorber and active materials.

A calorimeter samples the scintillation light or ionization from the charged particles in the shower, and the number of charged particles in the shower increases with energy. Thus the relative energy resolution of the calorimeter is inversely proportional to the square root of the incident particle's energy ($\frac{\Delta E}{E} \propto \frac{1}{\sqrt{E}}$). It is important to note that the energy resolution of calorimeters improves with

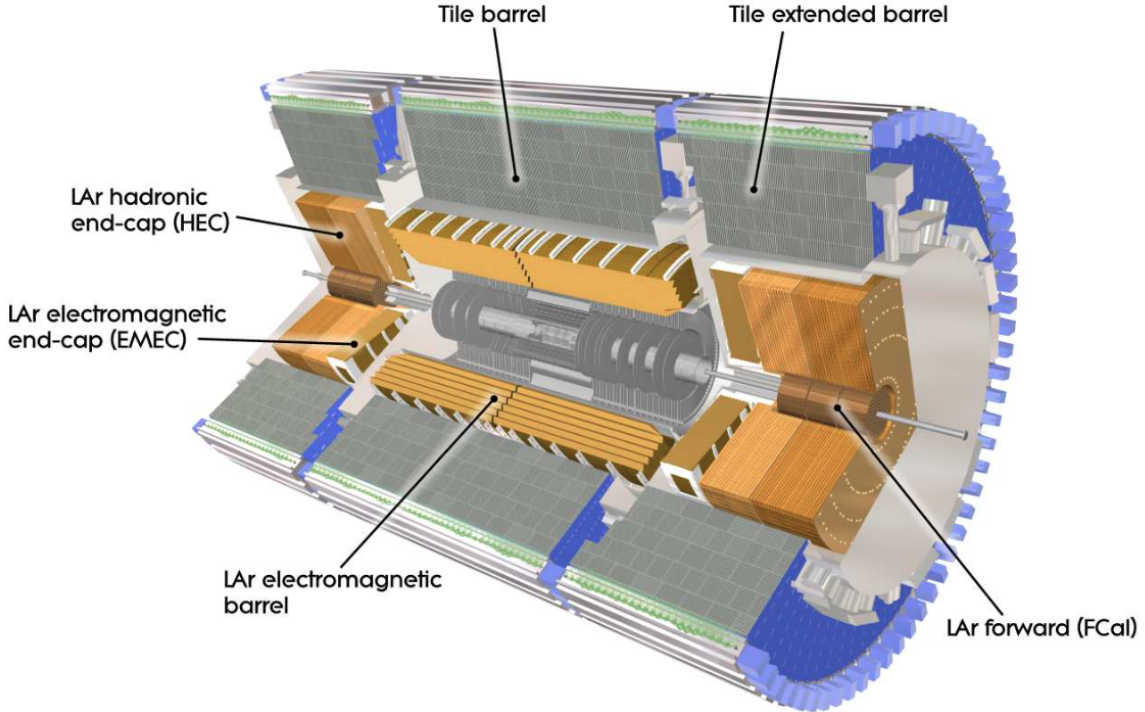


Figure 3.10: Schematic of the calorimeter system of the ATLAS experiment. The calorimetry system is comprised of the electromagnetic calorimeter, and a hadronic calorimeter [15].

increasing energy, while the momentum resolution of tracking detectors worsens with increasing p_T . Thus the relative energy resolution of electrons and jets will improve with increasing energy, while the relative momentum resolution of muons will worsen with increasing p_T .

3.2.3.1 Electromagnetic calorimeter

The EM calorimeter is used to stop and measure the energy of electrons, positrons, and photons. It is broken into a barrel component, covering $|\eta| < 1.5$, and two endcaps, covering $1.4 < |\eta| < 3.2$. Lead plates are used as an absorber material, and the active material is liquid argon (LAr). A pre-sampler is installed in the region $|\eta| < 1.8$ to sample energy from showers initiated before the first absorber plate.

The active material is arranged in an accordion-style geometry to ensure full coverage in ϕ . The barrel region is further sub-divided into three layers, with differing granularity. The first layer has the finest granularity, being arranged in strip-shaped cells with $\Delta\eta \times \Delta\phi = 0.025/8 \times 0.1$. This level of

granularity provides good position resolution, which is useful in particle identification to discriminate between photons and neutral pions. The second layer is arranged in square cells, measuring $\Delta\eta \times \Delta\phi = 0.025 \times 0.025$. Layer 2 is the thickest layer, with 16 radiation lengths. The third layer is coarser than the previous layers ($\Delta\eta \times \Delta\phi = 0.050 \times 0.025$), and is used to capture any remaining energy from the electromagnetic shower.

3.2.3.2 Hadronic calorimeter

The hadronic calorimeter is also broken up into barrel and endcap sections, but in this case, the two regions use different materials. The barrel section covers a region with $|\eta| < 1.7$, and uses steel absorbers and scintillating tiles as an active material. The endcaps use copper plates as an absorber material, and LAr for the active material. The hadronic calorimeter endcaps span $1.5 < |\eta| < 3.2$.

3.2.3.3 Forward calorimeter

The FCal captures energy from particles in the very forward region ($3.1 < |\eta| < 4.9$). It is made up of three layers in each endcap, each using LAr as the active material. The first layer uses copper absorber, while the second and third layers utilize a tungsten absorption material.

3.2.4 Muon spectrometer

The muon spectrometer (MS) comprises the four sub-detectors of the ATLAS experiment furthest from the interaction point, and is shown in Figure 3.11. Unlike electrons, muons are too massive to lose energy by radiation in the calorimeters. Muons only lose a very small amount of energy by ionization in the calorimeters and escape the calorimeters into the muon spectrometer. The MS has coverage up to $|\eta| = 2.7$, and is designed to make precision tracking measurements of the muon trajectory and momentum. A strong magnetic field is generated by eight large toroidal magnets in the barrel, and two endcap toroid systems. The magnetic field is situated such that the muons bend in the η direction. The four sub-detectors of the MS are

Monitored drift tubes (MDTs): Approximately 370,000 drift tubes, each with diameter of 30 mm, and made of aluminum with a wire in the middle. The gas in the tube is ionized in the presence of a muon, and attracted to the wire in the center of the tube, leading to a measurable signal, which is read out by the electronics. The MDTs span the full range of the MS system, $|\eta| < 2.7$.

Cathode strip chambers (CSCs): Chambers, consisting anode wires and cathode strips. As a muon passes through a CSC, the gas within the chamber is ionized, and drifts toward the

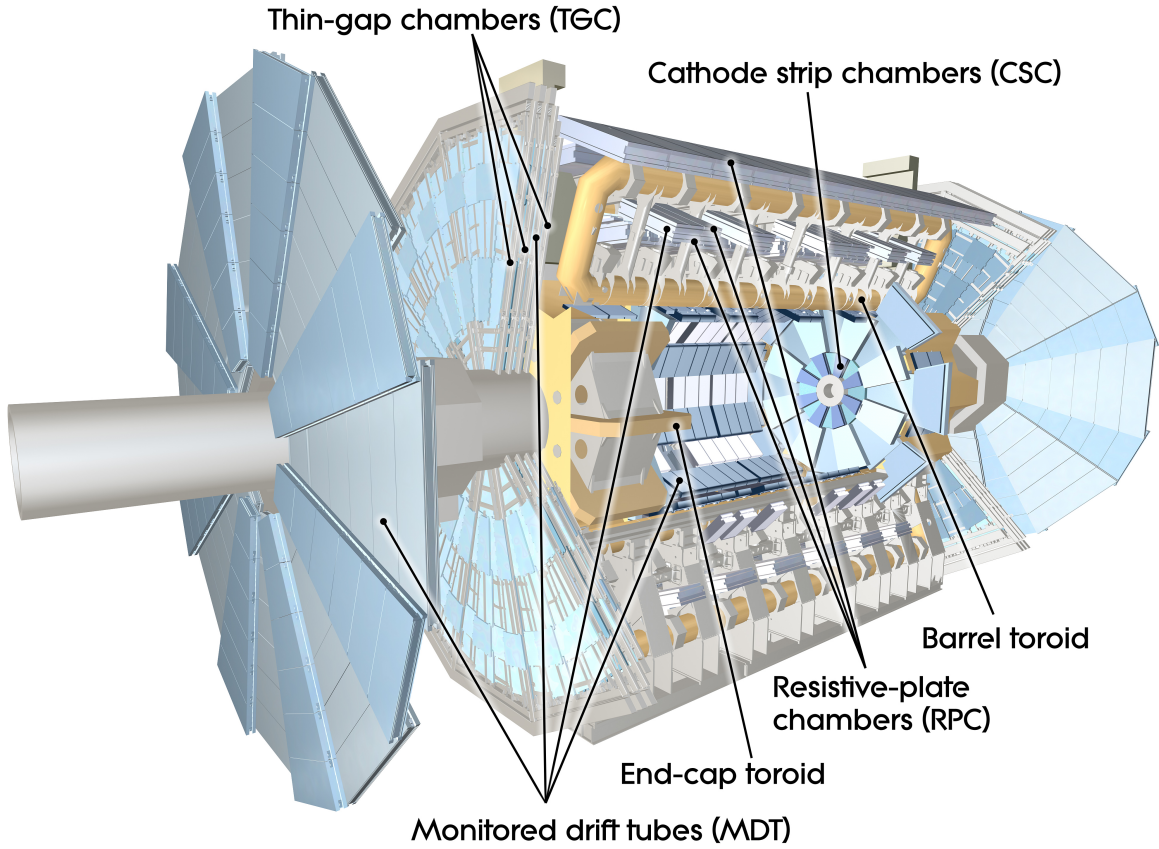


Figure 3.11: Schematic of the muon systems of the ATLAS experiment [16].

cathode strips, where the signal is read out. The relative size of the signal on adjacent strips is used to determine the location of the hit. The CSCs are located closer to the interaction point than the MDTs, in the region $2.0 < |\eta| < 2.7$.

Resistive plate chambers (RPCs): Consist of two resistive plates with a small gap, filled with gas. The gas is ionized in the presence of a muon, and drifts toward one of the plates. This results in a fast signature that can be used for triggering.

Thin gap chambers (TGCs): A multiple wire proportional counter used for triggering in the end-cap region.

3.3 Trigger system

In 2012, the LHC delivered proton collisions every 50 ns, corresponding to 20 MHz. Not only are most of these collisions already well-understood, ATLAS does not have the bandwidth or computing resources to read out every event, and reconstruct them for offline use. The trigger system uses a three step process to select only the rare potentially interesting events to reduce the data rate to something manageable.

The ATLAS trigger system includes a level 1 (L1) trigger, implemented in hardware, which is required to be fast. Only information from the calorimetry system and the MS is used in the L1 trigger since tracking takes too long to process. The second (level 2) and third (event filter) stages are referred to, collectively, as the high level trigger (HLT), and are implemented in computer farms, away from the ATLAS detector. These still have strict latency requirements, but they are allowed to take more time than L1. The level 2 stage includes the information in a region of interest (ROI) produced by the L1 trigger, and the event filter is able to use the full detector information, and run full event reconstruction. The specifications of each trigger level are given in Table 3.1.

Table 3.1: Specifications of the three levels of the ATLAS trigger system.

System	Input	Output	Reduction	Latency
Level 1	20 MHz	70 kHz	300x	2.5 μ s
Level 2	70 kHz	5 kHz	15x	75 ms
Event filter	5 kHz	700 Hz	7x	1 s

3.4 Event reconstruction and object identification

Particles created during collision events, and their decay products leave signatures in the various sub-detectors of ATLAS. In order to perform a physics analysis, these detector signatures are identified translated into reconstructed objects with calibrated momentum and energy measurements. Figure 3.12 shows a simplified diagram of the detector signatures left by various classes of particles.

The analysis described in this thesis relies on identified electrons (Section 3.4.1), muons (Section 3.4.2), jets (Section 3.4.3), and missing transverse momentum (Section 3.4.4). Flavor tagging (Section 3.4.3.1) is also used to identify the jets originating from the decay of B -hadrons. These signatures are described in more detail in the upcoming sections.

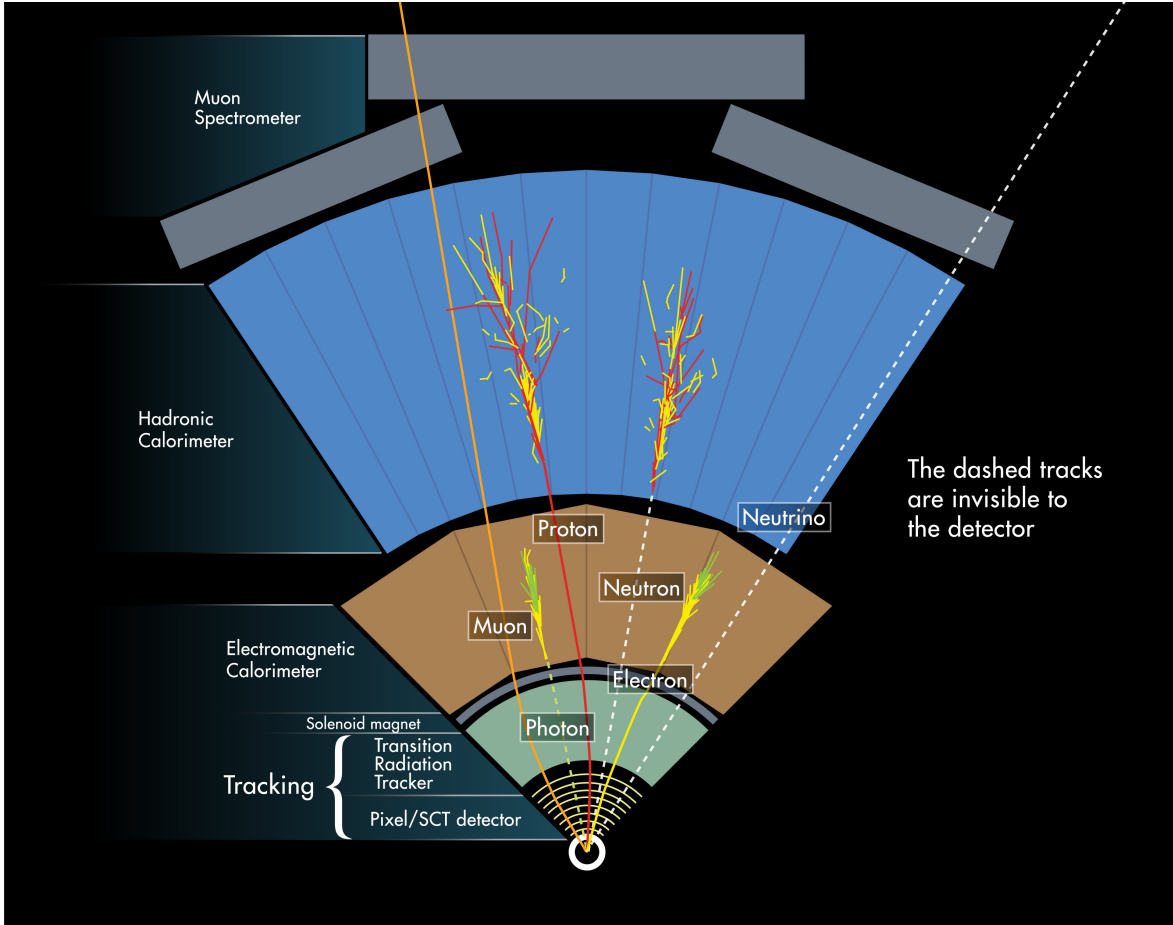


Figure 3.12: Schematic view of the signatures left in the various sub-detectors of ATLAS in response to the primary particles which pass through it [17].

3.4.1 Electrons

Electrons pass through the inner detector, leaving behind hits, and deposit a shower of energy in the EM calorimeter. The hits are combined to form a track, as described in Section 3.2.2.4, which points toward the EM shower. This signature can be faked by many charge particles, such as charged pions, so selection criteria are placed on the track and the shower shape to ensure the particle is indeed an electron. For instance, the EM shower from electrons is expected to be narrow, and the shower is expected to be fully absorbed within the EM calorimeter, resulting in little to no energy in the hadronic calorimeter. Additionally, electrons are more likely to emit TR photons while traversing through the TRT, resulting in some of the TRT hits passing the high-threshold. Heavier particles will have fewer high-threshold hits, so a requirement is placed on the fraction of TRT hits exceeding this

high-threshold.

3.4.2 Muons

Muons are the only charged particle able to reach the outermost detectors of ATLAS (the MS) while deposit little energy in the calorimetry system. A muon is identified as a track in the ID, and a track in the MS, which are consistent with one another. Quality criteria are placed on both the ID and MS track segments. The analysis described in this thesis uses the *Staco Combined* algorithm, which takes the two track segments as inputs, and performs a statistical combination to obtain a combined muon track.

3.4.3 Jets

Quarks and gluons produced during a proton-proton collision will hadronize, producing a collimated shower of charged and neutral hadrons. This spray of hadrons is collectively referred to as a jet. Jets are reconstructed using the anti- k_t algorithm [91, 92] with a radius parameter $R = 0.4$ from calibrated clusters of energy deposits in the calorimeters. The differences in calorimeter response between electrons, photons and hadrons are taken into account by classifying each cluster, prior to the jet reconstruction, as coming from an electromagnetic or hadronic shower on the basis of its shape [93]. The jet energy thus accounts for electromagnetic and hadronic energy deposits at the cluster level with correction factors derived from MC simulation. A further correction, used to calibrate the jet energy to the scale of its constituent particles, JES [93, 94], is then applied. The impact of pileup is accounted for using a technique, based on jet areas, that provides an event-by-event and jet-by-jet correction [95].

In order to reduce contamination from jets produced by pileup, the scalar sum of the p_T of the tracks matched to the jet and originating from the primary vertex must be at least 50% of the scalar sum of the p_T of all tracks matched to the jet. This criterion is only applied to jets with $p_T < 50$ GeV and $|\eta| < 2.4$.

3.4.3.1 Flavor tagging

Jets originating from B -hadrons can be distinguished from those originating from light quarks and gluons due to the relatively long lifetime of around 1.5 ps. For example, a B -hadron with mass 5 GeV and energy of 100 GeV would have a time dilation gamma factor (E/m) of about 20, so it would travel about 9 mm before decaying into several particles. The identification of b -jets uses the MV1 flavor tagging algorithm [96, 97], which is based on an artificial neural network algorithm that exploits

the impact parameters of charged particle tracks from the decay products of the B -hadrons, the parameters of reconstructed secondary vertices, and the topology of b - and c -hadron decays inside a jet. The operating point corresponds to an overall 80% b -tagging efficiency, as measured in simulated $t\bar{t}$ events, a rejection factor of 25 for jets originating from light quarks or gluons, and a rejection factor of 3 for jets originating from charm quarks.

3.4.4 Missing energy

Some particles such as neutrinos, and potentially new particles such as neutralinos, do not interact with the detector at all, and instead escape without being measured at all. The existence of these particles can be identified as an imbalance in vector sum of the momentum in an event, obtained from the negative vector sum of the reconstructed calibrated physics objects and “soft terms,” consisting of calorimeter energy clusters not associated with reconstructed objects. This is denoted as missing transverse momentum, and the symbol E_T^{miss} is used for its magnitude [98].

Conservation of momentum before and after the collision can be used to infer the momentum of the missing particles. This works well in the transverse plane to the beam, where the initial transverse momentum of the beams is zero, but not along the beamline since the fraction of momentum carried by the colliding constituents of the proton is unknown.

CHAPTER 4

Monte Carlo simulation

Monte Carlo (MC) simulations are an important tool for particle physics experiments. MC techniques are used to simulate the physics processes that occur during particle collisions. These simulated events also include the interactions of the decay products in the detector, and can be used to tune the selection of an analysis, estimate the expected event yields and kinematic shapes, and ultimately, evaluate the expected sensitivity of a particular search. MC simulation of background and signal processes are used on ATLAS. This chapter introduces some of the basic concepts of event generation, but focuses on the generation of the $B - L$ stop pairs from the model described in Section 2.4.

MC simulation of particle physics events can be broken into two major parts. The first step is the event generation, described in Section 4.1. In the event generation stage, the actual Physics processes that occur as a result of the collision are simulated. This includes the hard and soft interaction as well as the resulting decay of any unstable particles, and finally the hadronization of any decay products with color charge. As in the real detector, once the proton collisions are simulated, the decay products travel through the detector, and may leave a measurable signature which can be measured. The simulation of these material interactions with the detector is discussed in Section 4.2.

4.1 Event Generation

Before discussing the details of event generation, it is useful to first introduce the concept of an “event.” At the LHC, beams of protons are accelerated in opposite directions, and allowed to cross at specific locations as described in Section 3.1. At each of these crossings, protons from the two beams collide with one another, resulting in a spray of particles in the detector. Each of these

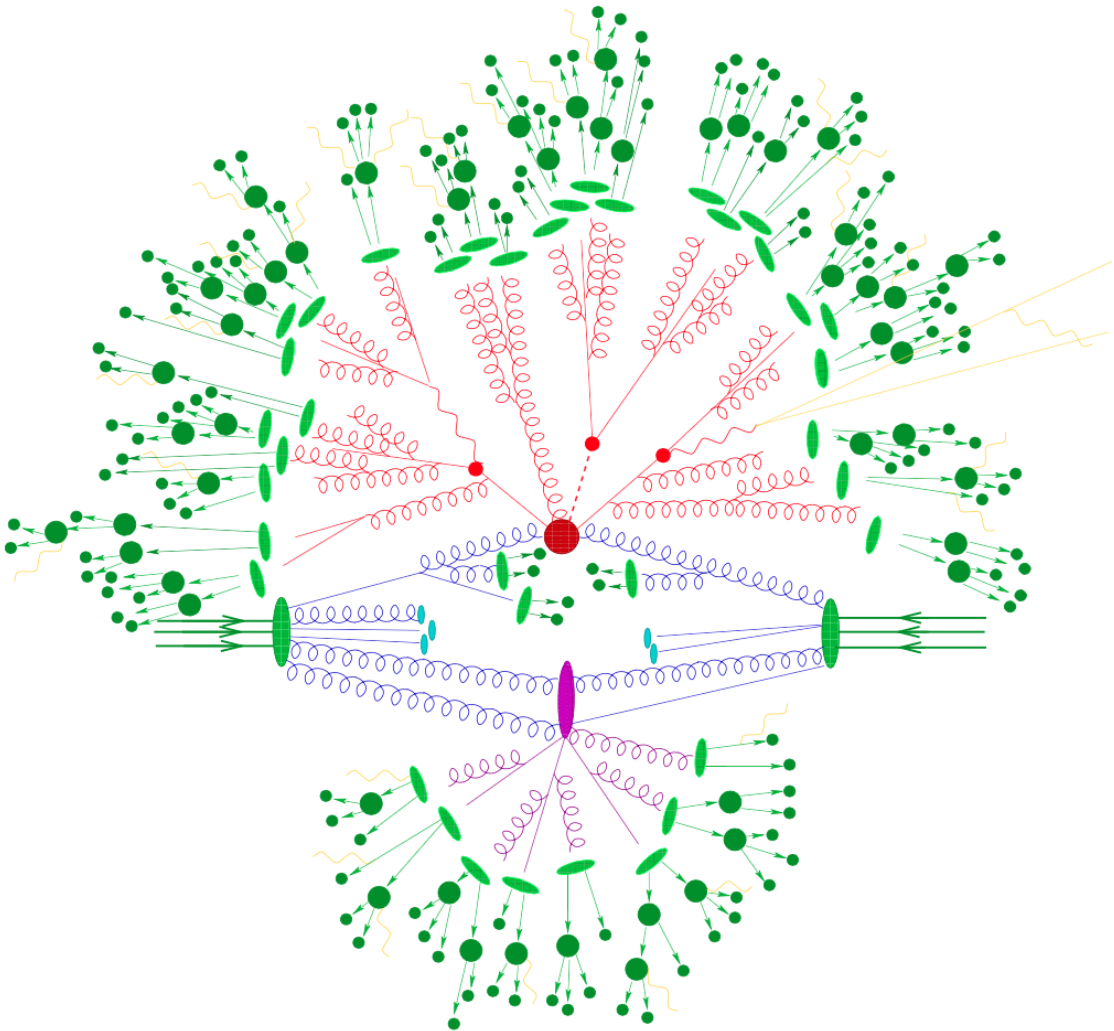


Figure 4.1: Pictorial representation of a $t\bar{t}H$ event as produced by an event generator. The hard interaction (big red blob) is followed by the decay of both top quarks and the Higgs boson (small red blobs). Additional hard QCD radiation is produced (red) and a secondary interaction takes place (purple blob) before the final-state partons hadronize (light green blobs) and hadrons decay (dark green blobs). Photon radiation occurs at any stage (yellow) [18].

crossings represents a single event. Figure 4.1 shows the many levels of event generation in a pictorial representation of a simulated $t\bar{t}H$ event. Looking closely at the interactions taking place, one notices that, rather than the full protons interacting with each other, the interactions take place between the constituent quarks and gluons within the two protons. In some cases, there is a “hard interaction,” or an inelastic scattering where additional particles are created. This is mathematically represented by the “matrix element” calculation. The calculation of the hard interaction process is discussed in more detail in Section 4.1.2. Section 4.1.3 introduces the “parton shower” technique, used to model additional quarks and gluons radiated from the incoming and outgoing partons in a collision event. Combining the matrix element and parton shower techniques introduces a potential double counting of certain event types. The double counting is eliminated using a “jet matching” algorithm described in Section 4.1.4.

There are also soft interactions between the remaining remnants of the proton after the hard interaction in a process called the “underlying event.” The underlying event produces charged particles and jets in the detector, in addition to those coming from the hard interaction [99].

Other protons may interact in the same bunch crossing as well. This is referred to as pileup. As with the underlying event, pileup events produce additional charged particles and jets that leave a signature in the detector.

4.1.1 Parton distribution function

It is often said a proton is made up of three quarks and the gluons holding them together. Due to the QCD effects, this is actually a simplification, and additional quarks and gluons are produced within hadrons, and have a large impact on the interactions between colliding protons. The parton content within a hadron is described by a parton distribution function (PDF).

The PDF of a proton, $p(x, \mu^2)$, gives the number of partons of a particular flavor p which are found in the proton with a fraction of the total momentum between x and $x + dx$, at a given energy scale μ^2 . A proton must satisfy the following sum rules in order to have the correct “valence quark” content.

$$\int_0^1 [u(x, \mu^2) - \bar{u}(x, \mu^2)] dx = 2, \quad (4.1)$$

$$\int_0^1 [d(x, \mu^2) - \bar{d}(x, \mu^2)] dx = 1, \quad (4.2)$$

$$\int_0^1 [q(x, \mu^2) - \bar{q}(x, \mu^2)] dx = 0, \quad (4.3)$$

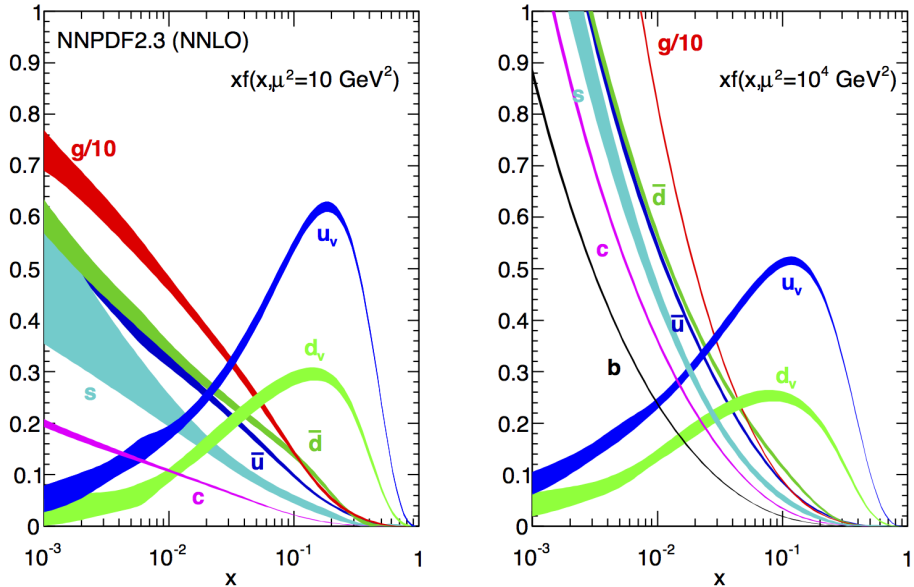


Figure 4.2: Parton distribution function (PDF) distributions for different parton species within the proton as obtained by the NNPDF collaboration. The two PDF distributions are obtained for different energy scales (μ^2) [19].

Where q is any other quark flavor. When the proton is described as uud , this refers to the valence quark composition.

PDFs are tuned to the observed data at collider experiments such as ATLAS, and improve over time as more data is collected at higher energy scales. Two example PDFs, provided by the NNPDF group, are shown in Figure 4.2, corresponding to different energy scales. The CTEQ 6L1 PDF tune is used for the simulated stop pair production in the analysis described in this thesis [100].

4.1.2 Hard interaction

The “hard interaction” refers to the process within a collision event with the highest $\sum p_T$ when summing over all the outgoing particles from a particular interaction. This is usually the most interesting part of the event, so MC simulation of collision events are generally categorized by the hard interaction process.

The cross section of a generic scattering process $a b \rightarrow F + X$ is given by

$$\sigma_{a b \rightarrow F + X} \propto |\mathcal{M}_{a b \rightarrow F + X}|^2 \Phi_F, \quad (4.4)$$

where a and b are the incoming partons, F is the final state, and X represents anything else that may be in the event, such as additional quarks or gluons which go on to form jets. The production cross

section is given in terms of a matrix element, $\mathcal{M}_{a b \rightarrow F+X}$, and a phase space term, Φ_F . The matrix element term is $\mathcal{M}_{a b \rightarrow F+X}$ is the scattering amplitude, and is given by the scattering potential. The phase space is related to the density of final states.

Several software tools exist to calculate the scattering cross section by generating the relevant diagrams, calculating these matrix element terms, and integrating over the phase space for the final states. The tools then use these cross sections, and Monte Carlo techniques, to simulate collision events, which have the same production cross section and kinematics as events one expects to observe in real collision data. The simulated events mimic the realistic collision events in that they have incoming and outgoing particles, and any unstable particles are allowed to decay. Each of the particles in the simulated event are represented by four-vectors, with values for the mass and momentum. Examples of these software tools include **SHERPA**, **POWHEG**, and **MADGRAPH**. In particular, **MADGRAPH** is used to generate the simulated signal events for the analysis described in this thesis.

4.1.3 Parton shower

The matrix element calculations are a useful tool in calculating the cross sections for processes with high p_T and well separated particles in the final state, but there can be cases, such as soft or collinear radiation, where the calculations diverge. These divergences are clearly non-physical, as such infinities don't exist in nature, so a different approach is needed in this regime. A common technique is the "parton shower" method implemented by software tools such as **PYTHIA**. The basic idea of the parton shower method can be illustrated in the context of gluon radiation off of a quark. Similar to Bremsstrahlung radiation of QED, a quark will radiate gluons as it travels. **PYTHIA** models the quark as moving along its trajectory, and in each step, there is some probability of radiating a gluon with a given momentum. Each time a gluon is radiated, the quark will lose momentum, until a threshold is reached, and the quark will begin to hadronize rather than continue to radiate.

4.1.4 Jet matching

As with the matrix element calculation, the parton shower method is not without its problems. The parton shower is not as well suited for calculating the cross section for very hard processes, where the momentum transfer is large, but this is exactly the regime where the matrix element calculations is accurate. For this reason, both methods are used when simulating collision events for use in analyses. The matrix element is used to generate the hard process and the initial decay products, then the parton shower takes over to add any additional radiation below the cutoff scale of the matrix element calculation.

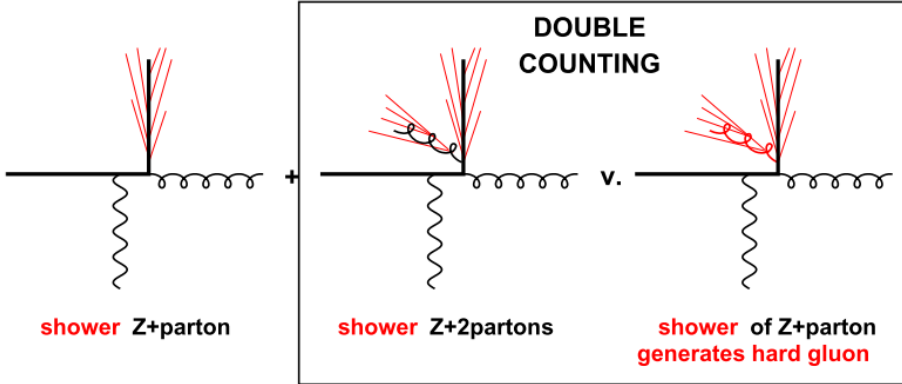


Figure 4.3: Illustration of the double counting issue that arises when combining the matrix element and parton shower event generation techniques. The diagrams show Z boson production associated with one or two additional partons included in the matrix element calculation [20].

Naively combining the matrix element calculation with the parton shower technique introduces a potential double counting of diagrams as illustrated in Figure 4.3. Figure 4.3 shows three diagrams for the production of a Z boson associated with additional partons, which lead to jets in the final state. The matrix element technique is used to generate the Z boson production along with one or two additional partons. Parton showering is applied to the additional partons, but not the initial state particles to simplify the example, but in a complete simulation, parton showering is applied to all partons.

In the left scenario only a single additional parton is included in the matrix element calculation, and the parton shower method is used to determine the soft collinear radiation off of the quark. One would like to add scenarios like the middle diagram, which includes a second additional parton in the matrix element calculation. The middle diagram includes a hard emission of a gluon in the matrix element calculation, and parton showering is used to include the soft radiation from the gluon. If these are the only two diagrams, there would be no problem, however, the parton shower will occasionally result in a hard, large-angle gluon emission from the quark, as shown in the right scenario. This leads to the possibility of double counting since both the middle and right diagrams generate the same process [20].

As mentioned before, the matrix element technique is well suited for processes with large momentum transfer, while parton showering is better for soft, collinear emissions. It is necessary to define a cutoff for when an additional parton emission is “hard enough” to be included in the matrix element calculation. This procedure of eliminating double counting is called “jet matching,” and many

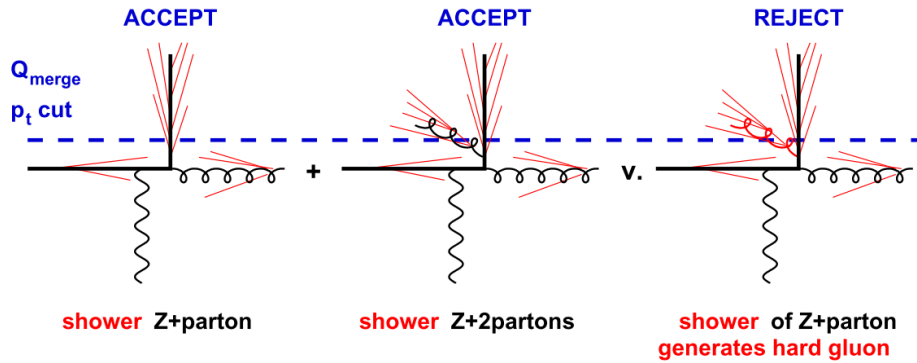


Figure 4.4: Illustration of the jet matching technique used to eliminate the double counting issue shown in Figure 4.3. The Q_{merge} cutoff scale is shown as a dashed blue line, and events failing this requirement are rejected [20].

methods exist. While the implementation differs for each of the algorithms, the basic approach for each of the methods is illustrated in Figure 4.4. A scale is defined for each of the additional partons produced, either in the matrix element calculation, or through the parton showering. The definition of the scale is different for each algorithm, but is it related to the momentum of the parton and the angle at which it is radiated. In this discussion, the scale will be referred to as k_T .

Two thresholds are defined, called Q_{ME} and Q_{merge} , where $Q_{\text{ME}} \leq Q_{\text{merge}}$. These thresholds mark the cutoff between the matrix element and parton showering stages of the event generation process. Partons generated in the matrix element calculation are required to have $k_T \geq Q_{\text{ME}}$. Similarly, the parton shower step may only add additional partons with $k_T \leq Q_{\text{ME}}$ [20].

For the analysis described in this thesis, the Shower k_T is used when generating stop pair events, with thresholds chosen such that $Q_{\text{ME}} = Q_{\text{merge}} = \frac{1}{4}m_{\tilde{t}}$ [101].

4.2 Detector simulation

The response of the detector in a candidate $t\bar{t}H$ event is shown in Figure 4.5. It is the task of the detector simulation step to transform the list of particles from Figure 4.1 into the energy deposits shown in the detector in Figure 4.5. The reconstruction described in Section 3.4 interprets these signals in exactly the same way for simulation and data. The interactions of particles with the material in the detector are simulated in one of two ways, known as full simulation or fast simulation.

In the full simulation, a model of the ATLAS detector is built within GEANT4. The simulation includes, not only, the active parts of the detector used in measuring particles, but also the support structure, and services such as cables and electronics. The particles are propagated through the

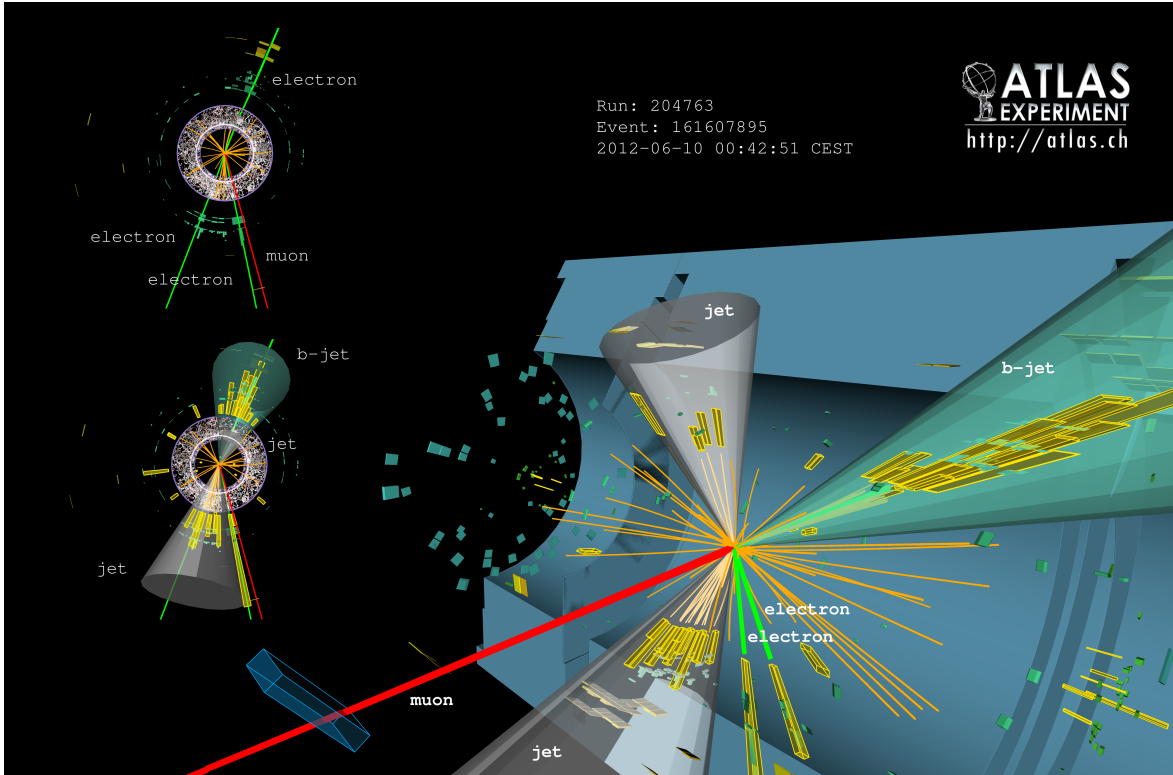


Figure 4.5: Candidate $t\bar{t}H$ event, observed in the ATLAS detector [21].

simulated detector, and allowed to interact in a way similar to a real particle traveling through the ATLAS detector. Simulated interaction in any of the subsystems result in simulated measurements, which can be put into the reconstruction software, just as data from the real detector.

Much like the full simulation, the fast simulation uses GEANT4 to simulate the interactions of particles through the inner detector and the muon systems. The two models differ in the treatment of the calorimeter. Rather than fully simulate the showers in the calorimetry system, the fast simulation uses parameterized shower shapes for particles that interact with the electromagnetic and hadronic calorimeters.

A more complete discussion of the ATLAS simulation setup can be found in Reference [102].

CHAPTER 5

B-L stop search

In this chapter, a search is presented for direct scalar top (stop) pair production where the stops decay via an R -parity violating (RPV) coupling to a final state with two leptons and two identified b -jets, show in Figure 1.1. The motivation and phenomenology of this model is described further in Section 2.4. For this search, data collected with the ATLAS detector at the LHC, corresponding to 20.3 fb^{-1} of $\sqrt{s} = 8\text{ TeV}$ proton-proton collision, is analyzed.

This analysis required the generation of simulated signal Monte Carlo (Section 5.1) to develop the selection criteria, and determine the expected sensitivity for the signatures of interest. The object definitions, event cleaning, and trigger selections are described in Sections 5.2 to 5.4. A “cuts-based” selection criteria is used to achieve a large separation between signal-like processes and Standard Model (SM) background processes. Two signal regions, expected to have a high signal-to-background ratio are defined in Section 5.5, and used to assess the compatibility of the data with the prediction from the target signal model, compared with that of the SM prediction alone. The background estimate is performed using MC simulation of SM processes, with the normalizations taken from the observed yields in dedicated Control Regions, defined in Section 5.6.2, using a maximum likelihood fit, described in Section 5.6.4. The extrapolation of the background estimate from the Control Regions to other regions in kinematic space is validated in several Validation Regions.

The observed event yields in the Signal Regions are consistent with the SM predictions, so limits are placed on the allowed stop masses and branching fractions in Chapter 6.

5.1 Signal model simulation

This search is optimized using Monte Carlo (MC) simulation of stop pair production and decay. Stop pair production is modeled using **MADGRAPH** version 1.5.12 [103] to generate stop-anti-stop pairs using the CTEQ 6L1 parton distribution functions (PDFs) [100], and **PYTHIA** version 6.427 [104] to perform the RPV stop decay as well as the parton shower calculation. Stop pairs are generated for stop masses between 400 GeV and 1100 GeV in steps of 100 GeV. Signal cross sections are calculated at next-to-leading order (NLO) in α_s , including the resummation of soft gluon emission at next-to-leading-logarithm accuracy (NLO+NLL) [3, 4, 5]. The nominal cross section and the uncertainty are taken from an envelope of cross section predictions using different PDF sets and factorization and renormalization scales, as described in Reference [105]. The simulated stop cross section ranges from 356 ± 51 fb for a stop mass of 400 GeV to 0.18 ± 0.06 fb for a stop mass of 1100 GeV. The cross sections and associated uncertainties for stop pair production are summarized in Table 5.1.

All samples have been generated with stop branching fractions of $Br(\tilde{t} \rightarrow be) = Br(\tilde{t} \rightarrow b\mu) = 0.5$. From this nominal branching fraction, the simulated events can be appropriately weighted to give any branching fraction hypothesis. This procedure is described in detail in Section 6.2. Except at high branching fraction for $Br(\tilde{t} \rightarrow b\tau)$, $\tilde{t} \rightarrow b\tau$ decays do not significantly contribute to the final state with two light leptons and two b -jets. This is due to the low branching fraction of $\tau^- \rightarrow e^- \bar{\nu}_e \nu_\tau$ and $\tau^- \rightarrow \mu^- \bar{\nu}_\mu \nu_\tau$ (17% each), as well as the addition of neutrinos to the final state, leading to poorer mass resolution on $m_{b\ell}$. The decay $\tilde{t} \rightarrow b\tau$ does not significantly contribute to the search sensitivity, and it is not included in the simulated samples.

Table 5.1: Stop cross sections and their associated uncertainties [3, 4, 5].

Stop Mass [GeV]	Cross section [fb]	Uncertainty [pb]
400	360	50
500	86	130
600	25	4
700	8.1	1.5
800	2.9	0.6
900	1.1	0.3
1000	0.44	0.12
1100	0.18	0.06

5.2 Object selection

Events are required to have at least two light leptons (electrons or muons) with opposite charge, and two b -tagged jets. The object selection is performed in multiple steps. First, lepton and jet objects are reconstructed using detector signatures as described in Sections 3.4.1 to 3.4.3. Baseline requirements are applied to remove poorly reconstructed objects. All baseline objects are required to have $E_T(p_T) \geq 40$ GeV since the stop signatures of interest are of high mass and produce high momentum decay products.

Baseline electrons must satisfy the **Medium++** identification requirement and have $|\eta| \leq 2.47$. A requirement of $\left| \frac{d_0}{\sigma(d_0)} \right| \leq 3$ and $|z_0 \sin(\theta)| \leq 0.4$ mm is placed on the impact parameter to reject electrons coming from the decay of long-lived particles. The baseline electron requirements are outlined in Table 5.2.

Table 5.2: Baseline electron requirements.

Quality	Medium++
p_T	≥ 40 GeV
$ \eta $	≤ 2.47
$\left \frac{d_0}{\sigma(d_0)} \right $	≤ 3
$ z_0 \sin(\theta) $	≤ 0.4 mm

Baseline muons are selected from the **STAC0** muon collection, and required to pass the **Loose** identification requirement. The baseline muons must also have $|\eta| \leq 2.5$. Impact parameter requirements of $\left| \frac{d_0}{\sigma(d_0)} \right| \leq 3$ and $|z_0 \sin(\theta)| \leq 1$ mm are applied to reduce the contamination of muons from secondary vertices and cosmic rays. Additional requirements are applied on the number of hits in the ID to ensure high quality tracks. These hit requirements include at least one hit on track in both the B layer and the Pixel detector. The ID track must also have at least 5 hits in the SCT, and at most 2 missing hits-on-track (holes) in both the Pixel detector and the SCT. If the muon has $|\eta| \leq 1.9$, there must additionally be at least 6 TRT hits, of which no more than 90% are outliers. The baseline muon requirements are outlined in Table 5.3.

Baseline jets are selected from the AntiKt4LCTopo jet collection, which apply a and required to have $|\eta| \leq 4.9$. These jets are build using the anti- k_T jet clustering algorithm with a cone size of $\Delta R \leq 0.4$ [91]. The baseline jet requirements are outlined in Table 5.4.

The overlap between baseline objects is removed to prevent a single detector signature from being included in multiple particle collections.²

²The angular separation between the objects is measured as $\Delta R = \sqrt{(\Delta\phi)^2 + (\Delta\eta)^2}$

Table 5.3: Baseline muon requirements.

Quality	Loose
p_T	$\geq 40 \text{ GeV}$
$ \eta $	≤ 2.5
Number B layer hits	≥ 1
Number Pixel hits	≥ 1
Number SCT hits	≥ 5
Number Silicon holes	≤ 2
TRT hits	See text
$\left \frac{d_0}{\sigma(d_0)} \right $	≤ 3
$ z_0 \sin(\theta) $	$\leq 1 \text{ mm}$

Table 5.4: Baseline jet requirements.

p_T	$\geq 40 \text{ GeV}$
$ \eta $	≤ 4.9

1. $\Delta R(e, e) \leq 0.05$: If two baseline electrons fall within a cone of $\Delta R(e, e) \leq 0.05$, the electron with the lower E_T is removed from the event.
2. $\Delta R(e, \text{jet}) \leq 0.20$: If a remaining electron and a jet are within a cone of $\Delta R(e, \text{jet}) \leq 0.20$, it is assumed that the electron is also reconstructed as a jet, and the jet is removed from the event.
3. $\Delta R(\ell, \text{jet}) \leq 0.40$: If remaining lepton (electron or muon) is within a cone of $\Delta R(\ell, \text{jet}) \leq 0.40$ of a remaining jet, the reconstructed lepton is assumed to be a constituent of the jet, and is removed from the event.
4. $\Delta R(e, \mu) \leq 0.01$: If a remaining electron and a remaining muon are within $\Delta R(e, \mu) \leq 0.01$, both are removed from the event.
5. $\Delta R(\mu, \mu) \leq 0.05$: If two remaining muons are within $\Delta R(\mu, \mu) \leq 0.05$, both are removed from the event.

Leptons from the decays of low hadronic mass resonances are rejected. The invariant mass of any remaining same-flavor lepton pairs with opposite charge is computed, and if the invariant mass of any of these pairs is less than 12 GeV, both leptons are removed from the event.

Additional requirements are placed on the leptons and jets after overlap removal to select the final “signal” objects. The scalar sum of the transverse momentum of all tracks with $p_T \geq 400 \text{ MeV}$ within a cone of $\Delta R \leq 0.30$ of a lepton ($p_T^{\text{cone}30}$) is used to determine if the lepton is isolated. Both electrons and muons require $p_T^{\text{cone}30}/\min(p_T, 60 \text{ GeV}) \leq 0.1$ in order to be declared signal leptons. Signal jets must

be within $|\eta| \leq 2.4$, and be tagged as a b -jet according to the MV1 flavor tagging algorithm [96, 97]. The operating point of $\text{MV1} \geq 0.3511$ corresponds to an overall 80% b -tagging efficiency, as measured in simulated $t\bar{t}$ events, to a rejection factor of 25 for jets originating from light quarks or gluons, and to a rejection factor of 3 for jets originating from charm quarks.

Events must contain at least two signal leptons and two b -tagged jets. If more are found, the event is kept, but only the two signal leptons and two b -tagged jets with the highest $E_T(p_T)$ are selected. Furthermore, the two highest $E_T(p_T)$ leptons are required to have opposite charge.

The identification efficiencies for the various objects used in this analysis differ in the data and the MC simulation. The efficiencies are determined in both data and MC simulation, by the relevant ATLAS performance working groups [106, 107]. The lepton identification scale factors are computed for each of the two signal leptons in a MC simulated event, and depend on both the p_T and η of the leptons. The product of the scale factors is taken as an event weight, ranging from 0.85 to 1.05.

Data and MC simulation also have different efficiencies for tagging a b -jet and for misidentifying jets originating from the fragmentation of light-flavor quarks, gluons, and charm quarks. An individual jet scale factor is defined as

$$SF_{\text{jet}}^{\text{eff}} = \frac{\epsilon_{\text{jet}}^{\text{data}}}{\epsilon_{\text{jet}}^{\text{MC}}}, \quad (5.1)$$

and depends on the E_T , η , and truth flavor of the jet. The individual jet scale factor is calculated for each of the baseline jets in a MC simulated event, and the overall event level b -tagging scale factor is given by

$$SF_{b\text{-tagging}}^{\text{event}} = \prod_{i \in \text{tagged}} SF_i^{\text{eff}} \times \prod_{j \in \text{Not tagged}} (1 - SF_j^{\text{eff}}), \quad (5.2)$$

where SF_i^{eff} is the tagging efficiency scale factor of jet i , and $(1 - SF_j^{\text{eff}})$ is the rejection efficiency for jet j . The two terms in equation 5.2, are the products over the b -tagged and non- b -tagged jets in the event respectively. This $SF_{b\text{-tagging}}^{\text{event}}$ quantity is taken as an additional event weight in MC simulated events.

A pairing of leptons and b -tagged jets must be defined to construct the mass of each of the $b\ell$ pairs in a event. In the target signal model, each $b\ell$ pair comes from a resonant decay of a stop particle with the same invariant mass. Therefore, the pairing which minimizes the difference in mass between the two $b\ell$ pairs is selected as follows.

In order of decreasing p_T , the two signal leptons and two b -jets are labeled ℓ_0 , ℓ_1 , b_0 , and b_1 . There are two possible choices of pairings for these four objects:

$$\text{Selection 1: } b_0 \text{ (red)} \quad \ell_0 \text{ (green)} \Rightarrow m_{b_0\ell_0} = m_{b\ell}^a \quad b_1 \text{ (red)} \quad \ell_1 \text{ (green)} \Rightarrow m_{b_1\ell_1} = m_{b\ell}^b$$

$$\text{Selection 2: } b_0 \text{ (red)} \quad \ell_1 \text{ (green)} \Rightarrow m_{b_0\ell_1} = m_{b\ell}^a \quad b_1 \text{ (red)} \quad \ell_0 \text{ (green)} \Rightarrow m_{b_1\ell_0} = m_{b\ell}^b$$

The choice that gives the smallest difference in the mass $|m_{b\ell}^a - m_{b\ell}^b|$ is chosen. The pairs are then ordered, and relabeled such that the higher mass pair has a mass of $m_{b\ell}^0$, and the lower mass pair has a mass of $m_{b\ell}^1$. This ensures $m_{b\ell}^0 \geq m_{b\ell}^1$ by definition.

This heuristic correctly identifies at least one correct pairing in over 70% of events in the simulated signal samples depending on the mass of the simulated stop. The relative abundance of identifying both, only one, or no correct pairs in simulated stop events is shown in Figure 5.1. The efficiency of identifying correct pairs improves once a cut is applied on the mass asymmetry of the two $b\ell$ pairs as described in Section 5.5. The scenario where one of the b -tagged jets or one of the leptons is not matched to a stop parent.

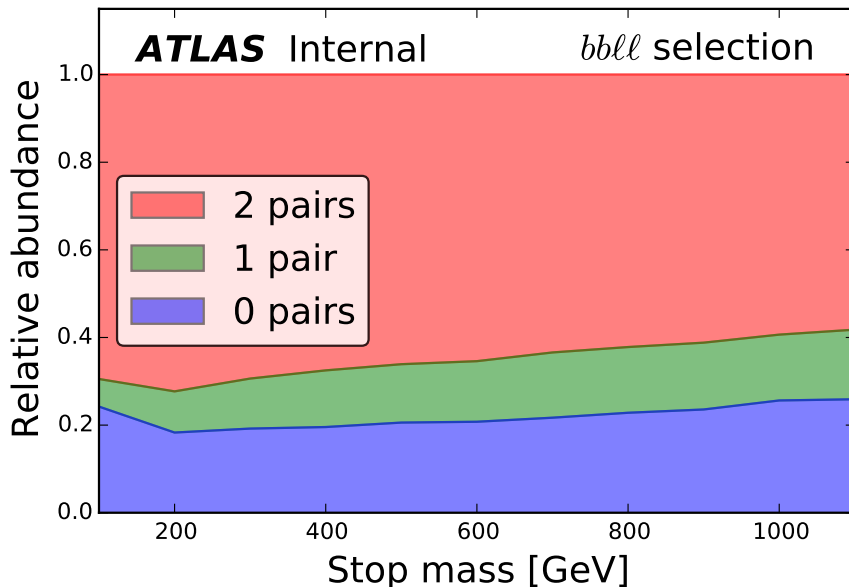


Figure 5.1: The relative abundance of events where two, one, and zero pairs are grouped correctly.

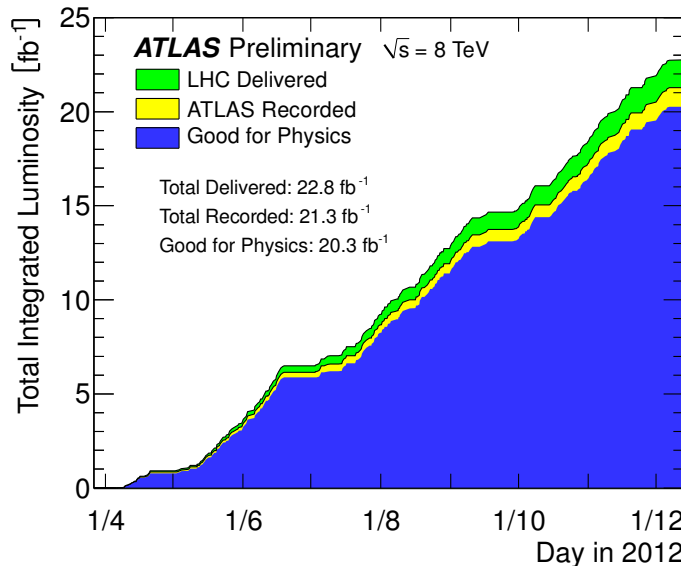


Figure 5.2: Integrated luminosity of proton-proton collision data delivered by the LHC (green) and recorded by the ATLAS experiment (yellow) throughout 2012. The blue area shows the integrated luminosity that passes data quality requirements, and is declared good for Physics [9].

5.3 Event cleaning

All sub-systems of the ATLAS detector are required to be operating acceptably during data-taking. This data quality requirement is implemented using a good runs list (GRL) provided by the Data Preparation group.³ By applying the GRL requirement, the total integrated luminosity is reduced from 21.4 fb^{-1} to 20.3 fb^{-1} as shown in Figure 5.2. The uncertainty in the luminosity is $\pm 2.8\%$. It is derived following the same methodology as that detailed in Reference [108]. The GRL requirement is applied to data events only; the MC simulation samples are scaled to match the target luminosity. Each event is also required to have at least one primary vertex with at least 5 associated tracks.

In the event of a certain detector busy condition, the Timing, Trigger, and Control system (TTC) may be restarted in order to recover the detector without a full run-restart. In the lumi-block after a TTC restart, it is possible for stored events to be incomplete. For this reason, events stored immediately after a TTC restart are rejected. Events are also rejected if either the LAr or tile calorimeter is flagged as having an error. During periods G-J several events are corrupt in a single channel of the tile calorimeter, but not flagged as having a tile calorimeter error. These events are

³The GRL version `data12_8TeV.periodAllYear_DetStatus-v61-pro14-02_DQDefects-00-01-00_PHYS_StandardGRL_All_Good` is used.

also rejected using the `TileTripTool`. During period B a hot spot developed in the tile calorimeter. As this can negatively impact the jet calibration and the E_T^{miss} calculations, events with a jet pointing toward this hot spot in the tile calorimeter are rejected.

Jet cleaning is performed to flag jets which are formed from various sources such as hardware problems, LHC beam conditions, or cosmic ray showers rather than real energy deposits in the calorimeter. If any of these bad jets remain after the overlap removal procedure, the event is rejected. Additionally, during periods E-H, a region of the LAr calorimeter ($-0.1 \leq \eta \leq 1.5$ and $-0.9 \leq \phi \leq -0.5$) malfunctioned resulting in energy not being collected from electrons and jets, and indirectly changing the E_T^{miss} measurement. A correction is applied to jets to account for the energy loss, however, if the correction is too large (greater than 0.05) and the E_T^{miss} is close to the jet ($\Delta\phi(E_T^{\text{miss}}, \text{jet}) \leq 0.3$), it is assumed the E_T^{miss} is mismeasured, and the event is rejected.

In addition to the impact parameter significance requirement on signal muons discussed in Section 5.2, an additional requirement of $|d_0| \leq 0.2$ mm is applied to muons passing the overlap removal to reject muons from cosmic ray showers. Any event failing this selection requirement is rejected. In order to ensure muons are well measured, any event containing a muon after overlap removal with $\sigma_{q/p}/|q/p| > 0.2$ is rejected. These poorly measured muons can arise from the MS and ID reconstructing different momenta for the same muon.

An additional requirement is applied to MC simulation events to avoid double counting backgrounds with heavy flavor quarks in the final state, the heavy flavor overlap removal procedure, described in Section 4.1.4.

Events in data are taken from both the `egamma` and `muons` data streams. It is possible for the same event to exist in both streams, in particular for $e\mu$ events, leading to the potential double counting of events in data. To prevent this double counting of data events, the data stream is chosen based on the flavor of the leading signal lepton in the event. If the highest p_T lepton in the event is an electron (muon), the event is required to be found in the `egamma` (`muons`) data stream. Events found in the wrong stream, are rejected.

5.4 Trigger selection

A combination of four single-lepton triggers are used to select events. The specific triggers used depend on the flavor channel of the event. Di-electron(muon) events are required to pass at least one of the two single electron (muon) triggers, while electron-muon events may pass any one of the four triggers. The specific triggers used for each flavor channel are outlined in Table 5.5, and the trigger requirements are described in Table 5.6.

Table 5.5: Trigger selection for each final state. If the event passes any of the triggers for the given final state, the event is accepted.

Final state	Trigger
$eebb$	<code>EF_e24vhi_medium1</code>
	<code>EF_e60_medium1</code>
$\mu\mu bb$	<code>EF_mu24i_tight</code>
	<code>EF_mu36_tight</code>
$e\mu bb$	<code>EF_e24vhi_medium1</code>
	<code>EF_e60_medium1</code>
	<code>EF_mu24i_tight</code>
	<code>EF_mu36_tight</code>

At least one of the reconstructed leptons is required to be within $\Delta R \leq 0.15$ of the detector signature found by the trigger. A reconstructed lepton must be matched to a trigger object of the correct flavor. For example, a reconstructed electron which is very close to a muon trigger object is not considered matched for these purposes. The expected trigger efficiencies for simulated stop events are shown for each trigger individually in Figure 5.3. The two muon triggers have roughly the same trigger efficiency, of about 93% for $\mu\mu$ events and 75% for $e\mu$ events, for all stop masses. The two electron triggers, however, have dramatically different shapes. The `EF_e24vhi_medium1` trigger is highly efficient for ee and $e\mu$ events only at low stop mass values. The `EF_e60_medium1` trigger only reaches 95% efficiency for ee and $e\mu$ events from stops with $m_{\tilde{t}} > 200$ GeV. Due to the trigger requirement, and the overlap removal procedure, ee ($\mu\mu$) events do not pass the single muon (electron) triggers.

Table 5.6: Requirements for the triggers used in this analysis.

Trigger	p_T threshold	Other requirements
<code>EF_e24vhi_medium1</code>	$p_T^e \geq 24$ GeV	hadronic core isolation ≤ 1 GeV $p_T^{\text{cone}20}/p_T < 0.1$
<code>EF_e60_medium1</code>	$p_T^e \geq 60$ GeV	–
<code>EF_mu24i_tight</code>	$p_T^\mu \geq 24$ GeV	$p_T^{\text{cone}20}/p_T < 0.12$
<code>EF_mu36_tight</code>	$p_T^\mu \geq 36$ GeV	–

The dependence on the stop mass is a result of the E_T dependence of the electron triggers. The decay products of lighter stops tend to have lower momentum. As a result, the electrons from the very light stops (≤ 300 GeV) are more likely to have E_T less than the threshold for the `EF_e60_medium1`

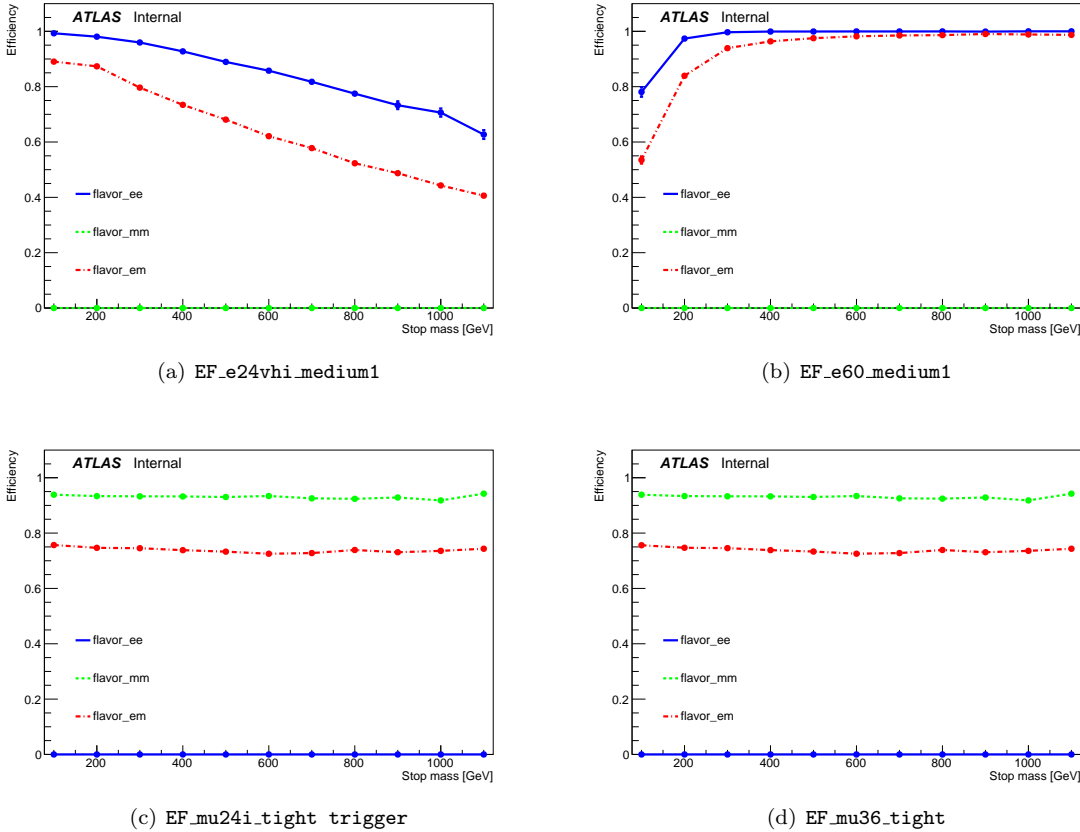


Figure 5.3: Efficiency of simulated stop events passing each single lepton trigger broken down by flavor channel.

trigger. High- E_T electrons will deposit more energy into the calorimeter, and some of this energy will reach the hadronic calorimeter. As the electron E_T increases, the probability that the energy deposition into the hadronic calorimeter is enough to fail the hadronic core isolation requirement of the `EF_e24vhi_medium1` trigger increases. The E_T dependence of the two electron triggers, shown in Figure 5.4, is consistent with the expected dependence.

The full trigger requirement is highly efficient for signal-like events, and does not depend on the stop mass; between 93% and 98% of simulated signal events pass the trigger selection depending on the flavor channel as shown in Figure 5.5.

The trigger requirement is applied in both data and MC simulation. To account for the difference in trigger efficiency, a trigger scale factor is applied to the MC events passing the trigger requirement. The trigger efficiencies for data and MC simulation are provided by the Egamma and Muon combined performance groups [109, 107]. The trigger scale factor is the ratio (data to MC simulation) of the

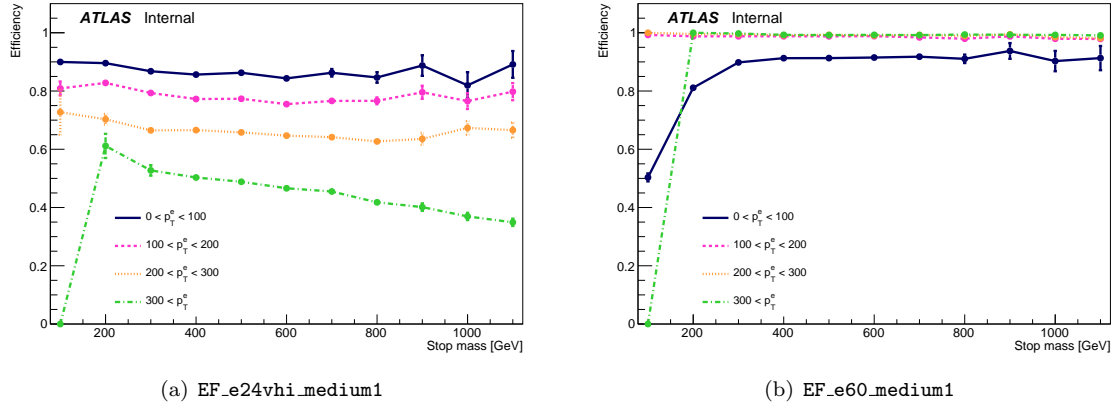


Figure 5.4: Efficiency of simulated stop events passing each of the single electron triggers for several ranges of electron E_T . Only $e\mu$ events are shown in order to show to isolate the effect of the electron E_T on the single electron trigger efficiency.

efficiencies for an event passing the trigger requirement, described in Table 5.5, and is given by

$$SF_{\text{trigger}} = \frac{1 - \prod_{t \in \text{triggers}} \prod_{\ell \in \{0,1\}} (1 - \epsilon_{\ell,t}^{\text{data}})}{1 - \prod_{t \in \text{triggers}} \prod_{\ell \in \{0,1\}} (1 - \epsilon_{\ell,t}^{\text{MC}})}, \quad (5.3)$$

where $\epsilon_{\ell,t}^{\text{data}}$ ($\epsilon_{\ell,t}^{\text{MC}}$) is the trigger efficiency (electron or muon) for lepton ℓ to pass trigger t in the data

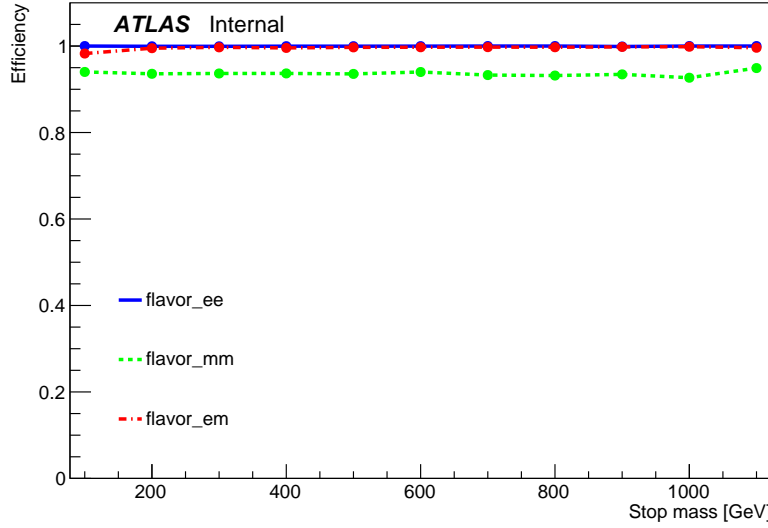


Figure 5.5: Efficiency of simulated stop events passing the full trigger selection broken down by flavor channel.

(MC simulation). The trigger scale factor is calculated using the two signal leptons in the event, as these are the only objects considered when checking the trigger requirement. The efficiency for an electron (muon) to pass one of the muon (electron) triggers is set to zero. This is justified based on the trigger efficiencies shown in Figure 5.3. The trigger scale factor is treated as an additional event weight for events in the MC simulation.

5.5 Signal regions

The goal of this analysis is to define a signal region with low background contamination in order to search for pair production of massive stops. As the analysis targets a wide range of stop masses; therefore, the expected kinematics of the stop decay products have a large range as well. Two overlapping signal regions (SRs) are defined to search for an excess of signal-like events, inconsistent with the prediction from the SM alone. Several kinematic quantities, calculated from the four-vectors of the two leptons and two b -tagged jets provide excellent discrimination to reject background. These quantities are discussed below and shown in Figure 5.6 for an region, applying only event cleaning, and requiring two b -tagged jets and two leptons (electrons or muons). The signal models have an assumed $Br(\tilde{t} \rightarrow b e) = Br(\tilde{t} \rightarrow b \mu) = 0.5$.

The largest SM processes of background events are $Z/\gamma^* + \text{jets}$, $t\bar{t}$, and single top production. The selection requirements are optimized using MC simulation to achieve a large signal to background ratio in the SRs. The optimization assumes a stop branching fraction of $Br(\tilde{t} \rightarrow b e) = Br(\tilde{t} \rightarrow b \mu) = 0.5$. The following selection criteria effectively reduces these, and other (smaller) SM background, while leaving a reasonably high expected signal efficiency.

$\mathbf{m}_{\ell\ell}$

The background from $Z/\gamma^* + \text{jets}$ has a narrow resonance in the invariant mass of the two leptons ($\mathbf{m}_{\ell\ell}$) around the Z boson mass of 91 GeV, as seen in Figure 5.6. Events with two leptons of the same flavor (ee or $\mu\mu$), with a reconstructed invariant mass consistent with the Z boson ($|m_{\ell\ell} - m_Z| \leq 10$ GeV) are rejected to reduce the contributions of the $Z/\gamma^* + \text{jets}$ background.

\mathbf{H}_T

The leptons and b -jets from the two-body decays of massive stops tend to have more p_T than those from the decays of lower mass SM particles. The \mathbf{H}_T variable, shown in Figure 5.6, is the scalar sum of the $E_T(p_T)$ of the two b -tagged jets and the two leptons. Events in the SRs are required to have $H_T \geq 1100$ GeV.

$\mathbf{m}_{b\ell}^0$

The invariant masses of the two $b\ell$ pairs provide two ways to reduce the background from SM processes. Firstly, the highest invariant mass value, $\mathbf{m}_{b\ell}^0$, has a broad resonance about the stop mass, as seen in Figure 5.6, while the SM backgrounds have lower values. Since a large range of stop masses are considered, two overlapping SRs are defined, differing in the $m_{b\ell}$ -requirement. SR 400 is optimal for lower stop masses, and has a requirement of $m_{b\ell}^0 \geq 400$ GeV, while SR 600, with a requirement of $m_{b\ell}^0 \geq 600$ GeV, is optimal for higher stop masses.

Two additional SRs were considered with $m_{b\ell}^0 \geq 200$ GeV and $m_{b\ell}^0 \geq 800$ GeV (SR 200 and SR 800 respectively), however these were dropped from the analysis. The SR 200 region did not provide additional expected sensitivity compared with the SR 400 region, and the statistical uncertainty in the SR 800 region was very large, and reduced expected sensitivity.

$\mathbf{m}_{b\ell}$ asymmetry

Secondly, even when $m_{b\ell}^0$ is large, the difference in invariant mass between the highest and lowest pair can be large for SM processes as seen in Figure 5.6. To quantify the difference in the two masses, the **$\mathbf{m}_{b\ell}$ asymmetry** is defined as $m_{b\ell}$ asymmetry = $m_{b\ell}^0 - m_{b\ell}^1 / m_{b\ell}^0 + m_{b\ell}^1$. The $m_{b\ell}$ asymmetry is used rather than the simple difference in the masses because it is incorporates the effects of the mass scale, and as single requirement on the $m_{b\ell}$ asymmetry can be used for all stop masses which are considered. In order to be selected for one or both of the SRs, an event requires $m_{b\ell}$ asymmetry ≤ 0.2 .

Figure 5.7 shows the expected H_T , $m_{b\ell}$ asymmetry, and $m_{b\ell}^0$ distributions after applying all the SR selection criteria except that on the variable being shown. This figure includes the simulated background processes and three signal models. The number of expected signal events (for the same three signal models) passing each selection requirement is shown in Table 5.7. The estimates shown in Figure 5.7 and Table 5.7 are taken from MC simulation, and the event yields are normalized to 20.3 fb^{-1} .

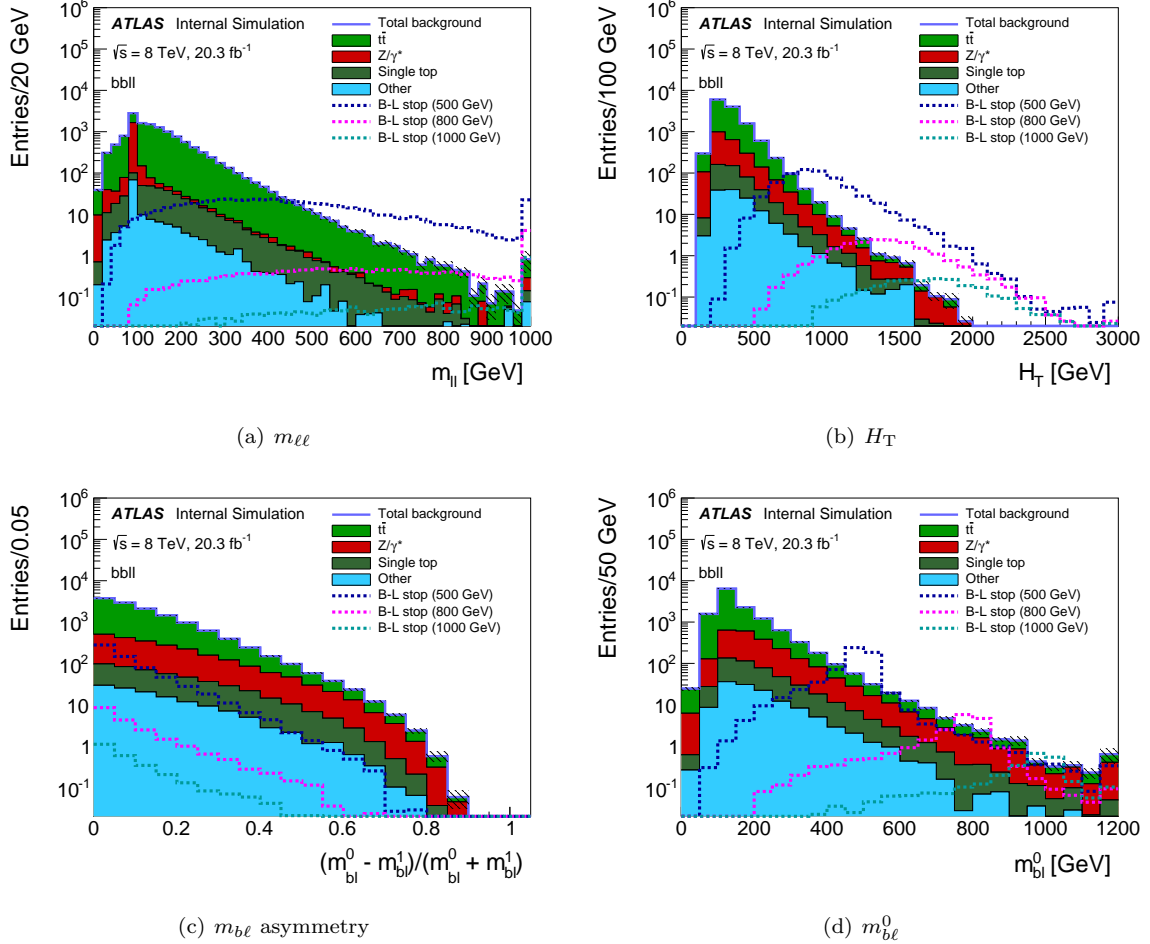


Figure 5.6: Expected m_{ll} , H_T , $m_{b\ell}$ asymmetry, and m_{bl}^0 distributions for SM background processes and three simulated stop samples with different masses. In each plot, the last bin includes the overflow for values beyond the maximum shown. The hashed error bands show only the statistical uncertainty in the background MC simulation samples.

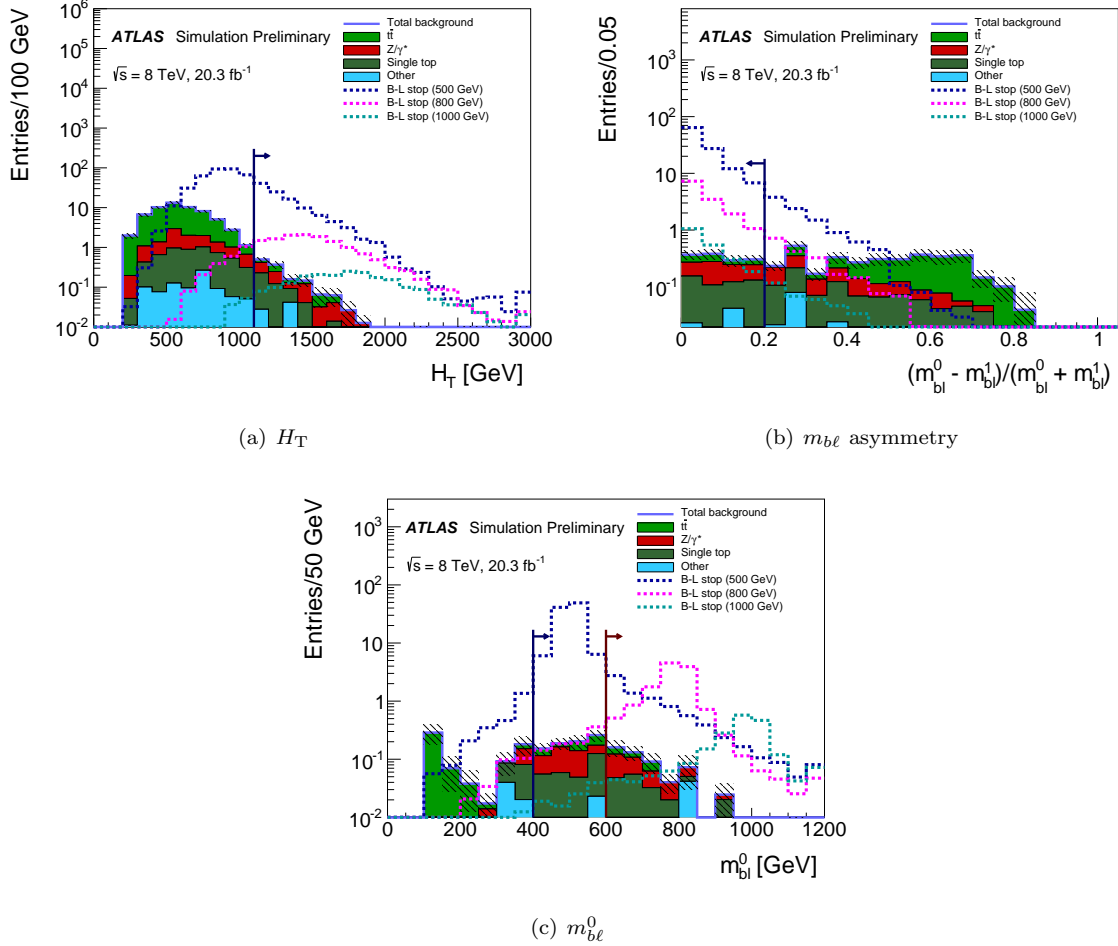


Figure 5.7: Distributions of the variables which are used to define the SRs. These plots show the MC simulated background samples and three signal models, and are made after applying all the SR selection criteria except for that on the variable shown. The arrows show the SR requirement on the variable being shown. In each plot, the last bin includes the overflow for values beyond the maximum shown. The hashed error bands show only the statistical uncertainty in the background MC simulation samples. The signal models have an assumed branching fraction of $Br(\tilde{t} \rightarrow be) = Br(\tilde{t} \rightarrow b\mu) = 0.5$.

Table 5.7: The number of expected signal events passing each of the signal for stop masses of 500 GeV, 800 GeV, and 1000 GeV. The estimated yields are taken from MC simulation, and are normalized to 20.3 fb^{-1} , and the uncertainty given is the MC statistical uncertainty. The signal models have an assumed branching fraction of $Br(\tilde{t} \rightarrow be) = Br(\tilde{t} \rightarrow b\mu) = 0.5$.

Selection	$m_{\tilde{t}} = 500 \text{ GeV}$	$m_{\tilde{t}} = 800 \text{ GeV}$	$m_{\tilde{t}} = 1000 \text{ GeV}$
$\sigma \cdot L$	1750 ± 260	59 ± 12	8.9 ± 2.5
$b\ell\ell\ell$	624 ± 4	19.65 ± 0.18	2.68 ± 0.05
Z veto	619 ± 4	19.62 ± 0.18	2.68 ± 0.05
$H_T \geq 1100 \text{ GeV}$	122.9 ± 1.8	16.01 ± 0.17	2.50 ± 0.04
$m_{b\ell}$ asymmetry ≤ 0.2	112.8 ± 1.7	14.00 ± 0.15	2.11 ± 0.04
$m_{b\ell} \geq 400 \text{ GeV}$	110.3 ± 1.7	13.74 ± 0.15	2.09 ± 0.04
$m_{b\ell} \geq 600 \text{ GeV}$	7.7 ± 0.4	12.86 ± 0.15	1.99 ± 0.04

5.6 Background estimate

The final state targeted by this analysis is two b -tagged jets and two light leptons. The three largest sources of SM background which contribute to this final state are $t\bar{t}$, $Z/\gamma^* + \text{jets}$, and single top production. Other sources, such as di-boson and Higgs boson production, contribute as background events as well, however in much smaller amounts. The full list of MC simulation samples used to estimate the background contribution from SM processes is given in Section 5.6.1. The background estimates for the $t\bar{t}$ and the $Z/\gamma^* + \text{jets}$ backgrounds use MC simulation normalized in dedicated data control regions (CRs). Several validation regions (VRs) are defined to validate the extrapolation of the fitted background estimate in the CRs to regions with different kinematics. The remaining backgrounds are estimated using MC simulation only, and the normalization is scaled based on the cross section of the production process and the integrated luminosity collected in data. The CRs and VRs are described in more detail in Sections 5.6.2 and 5.6.3 respectively. The full selection criteria for the analysis regions, including the SRs, CRs, and VRs, is outlined in Table 5.8 and Figure 5.8.

The $t\bar{t}$ and $Z/\gamma^* + \text{jets}$ normalization factors are determined using a simultaneous fit to the data in the CRs, allowing the normalization of each background to float independent of one another to obtain the best agreement between the prediction and observation in the CRs. The background fit procedure and results are described in Section 5.6.4. In addition to the statistical uncertainty, several sources of systematic uncertainty, described in Section 5.7, are considered when performing the simultaneous fit.

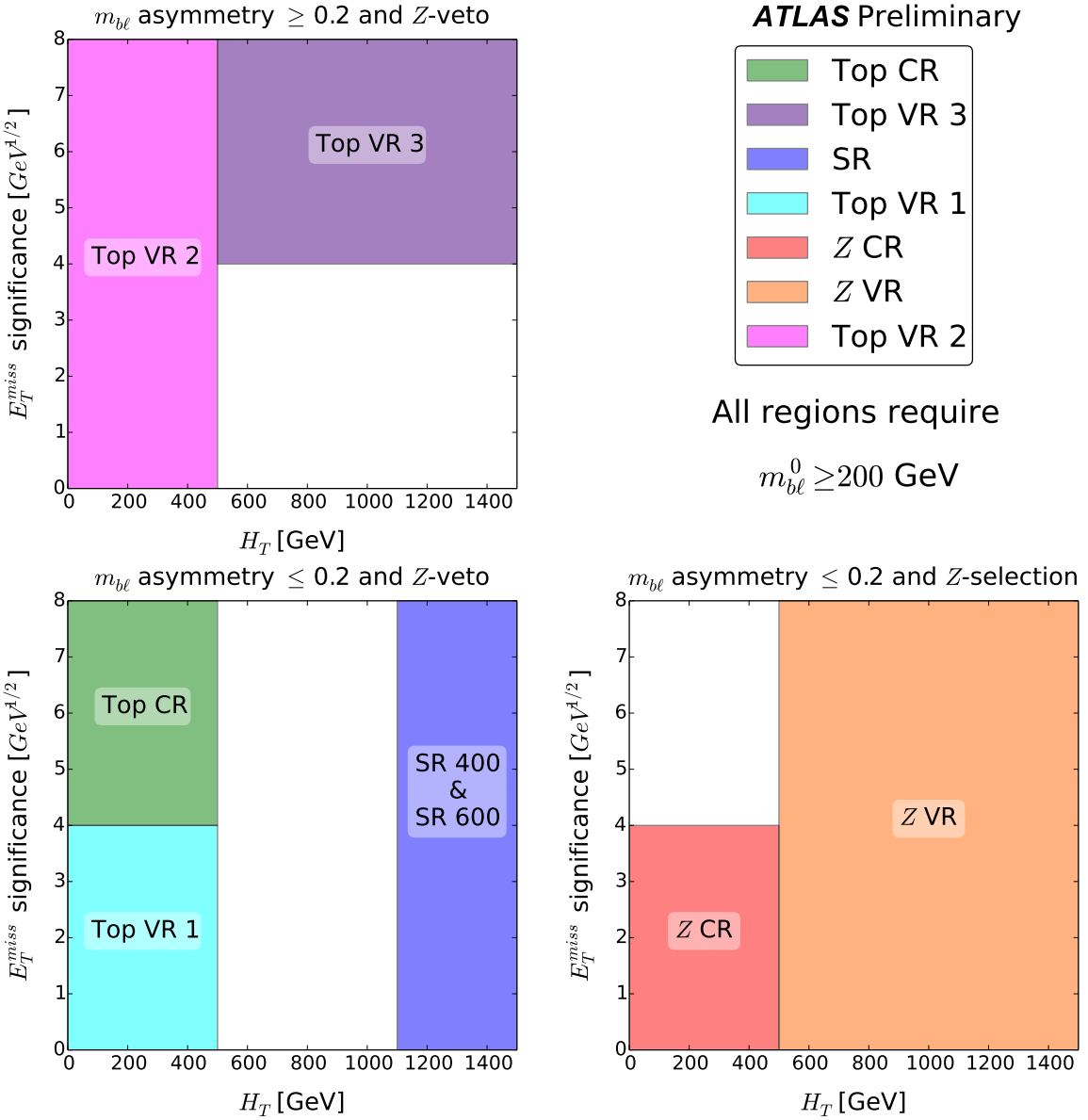


Figure 5.8: Position of the control, validation, and signal regions in the E_T^{miss} significance versus H_T plane. The two left plots show the plane after vetoing events within the Z window, with the top plot requiring $m_{b\ell}$ asymmetry ≥ 0.2 and the bottom requiring $m_{b\ell}$ asymmetry ≤ 0.2 . The right plot shows the plane when requiring events be within the Z window. The two SRs apply a different requirement on the invariant mass of the higher-mass $b\ell$ pair. SR 400 requires $m_{b\ell}^0 \geq 400 \text{ GeV}$, and SR 600 requires $m_{b\ell}^0 \geq 600 \text{ GeV}$.

Table 5.8: Summary of signal, control, and validation regions used for this analysis. The control and validation regions are explained in Section 5.6. All regions require two b -tagged jets and two oppositely charged leptons. An event is in the Z window if it contains two same-flavored leptons with an invariant mass within 10 GeV of the mass of the Z boson.

Region	$m_{b\ell}^0$ [GeV]	H_T [GeV]	E_T^{miss} significance [GeV $^{1/2}$]	$m_{b\ell}$ asymmetry	Z window Z window
SR 400	≥ 400	≥ 1100	–	≤ 0.2	Veto
SR 600	≥ 600	≥ 1100	–	≤ 0.2	Veto
Top CR	≥ 200	≤ 500	≥ 4	≤ 0.2	Veto
Z CR	≥ 200	≤ 500	≤ 4	≤ 0.2	Select
Top VR 1	≥ 200	≤ 500	< 4	≤ 0.2	Veto
Top VR 2	≥ 200	≤ 500	–	> 0.2	Veto
Top VR 3	≥ 200	> 500	> 4	> 0.2	Veto
Z VR	≥ 200	> 500	–	≤ 0.2	Select

5.6.1 Monte Carlo simulation samples

MC simulation samples are used to estimate the selection efficiency and kinematic distributions for SM processes. The $t\bar{t}$, Z/γ^* +jets, and single top production processes are shown separately, while all the other SM background processes are grouped into an “other” category. The $t\bar{t}$ background is modeled using the next-to-leading order (NLO) generator POWHEG revision 2129 [110, 111, 112, 113] with NLO PDF set CTEQ 6L1 [100], and showered with PYTHIA version 6.426. When using the baseline POWHEG+PYTHIA $t\bar{t}$ production sample, events are reweighted in bins of the transverse mass (p_T) of the $t\bar{t}$ system to match the top quark pair differential cross section observed in ATLAS data [114, 115]. The Wt -channel and s -channel of the single top background are modeled using POWHEG revision 1556 [116] with PYTHIA version 6.426, while the t -channel is modeled using ACERMC version 3.8 [117] with PYTHIA version 6.426, both with PDF set CTEQ 6L1 [100]. The Z/γ^* +jets production process is modeled using SHERPA version 1.4.1 [18] with NLO PDF set CT10. Charm and bottom quarks are treated as massive.

Various filters are applied to the Z/γ^* +jets samples to achieve reasonable coverage of final states and kinematics in the finite MC simulation samples. A dedicated set of samples are generated for each of the di-lepton flavor combinations from the Z boson (ee , $\mu\mu$, and $\tau\tau$). Filters are also applied based on the quark content of the simulated event. Samples are generated with a filter requiring at least one b -quark in the event. These samples have the largest contribution to the final background estimate. Samples are also produced which require at least one c -quark, but veto events including

a b -quark. The last set of samples is generated which vetoes events with either b -quark or c -quark content. The samples are further sliced by the p_T of the Z boson. Dedicated samples with generator filters are produced in slices above 40 GeV, and an inclusive sample is used to cover the kinematic space with $p_T^Z \leq 40$ GeV. To avoid overlap between the inclusive sample and the higher p_T^Z slices, an additional requirement of $p_T^{Z,\text{truth}} \leq 40$ GeV is applied for the inclusive $Z/\gamma^* + \text{jets}$ samples simulated using **SHERPA**. As **SHERPA** does not include the intermediate Z boson in the truth record, the $p_T^{Z,\text{truth}}$ quantity is obtained by searching through all the truth leptons in the event, picking the two leptons with a parent ID consistent with a Z boson, and calculating the p_T of the (truth level) di-lepton pair.

Similar filters to the $Z/\gamma^* + \text{jets}$ MC samples are applied to the Drell Yan (DY) samples. The DY samples apply the same filters on the lepton flavor combinations and the quark content. Rather than slicing based on the p_T of the Z boson, the DY samples are sliced based on the mass of the off-shell Z/γ^* in the event. Two sets of samples are produced with requirements of $8 \leq m_{Z/\gamma^*}^{\text{truth}} \leq 15$ GeV and $15 \leq m_{Z/\gamma^*}^{\text{truth}} \leq 40$ GeV respectively, where m_{Z/γ^*} is obtained by searching through the truth record for the decay products of the Z/γ^* , and computing the (truth level) invariant mass of the di-lepton pair.

The full list of background samples used, as well as the event generator used, SM production cross section, and the effective luminosity generated is given in Tables 5.9 and 5.10.⁴ Unless PYTHIA8 is specified, PYTHIA version 6 is used for samples labeled with PYTHIA.

The MC simulation is generated with an assumption on the distribution of the number of simulated interactions per crossing that differs from that recorded in the data. A weight is applied to the MC samples based on this difference.

Additionally, several of the MC generators provide event weights, which can be positive or negative. These weights account for the diagram subtraction that enters the NLL or NLO calculations, and are commonly referred to as the “MC event weight.” When the generator provides MC event weights, they are applied to each event in the MC background sample; otherwise, they are not used.

⁴The effective luminosity is given by $N_{\text{gen}}\sigma/\epsilon_{\text{filter}}$, where N_{gen} is the number of MC events which were generated, σ is the production cross section, and ϵ_{filter} is the efficiency of any filter which was applied to the MC sample.

Table 5.9: Partial summary of background samples and their cross sections used in this analysis. For each di-lepton flavor channel, samples are generated with requirements on the p_T of the Z boson. For the inclusive $Z/\gamma^* + \text{jets}$ sample, only events with $p_T^Z \leq 40$ GeV were used. For each combination of di-lepton flavor and p_T requirement, three samples are generated, with filters applied on the three jet flavors different lepton flavor channels and filters applied on the jet flavor. The different filter efficiencies, lead to different effective luminosities. The left column shows the effective luminosity for the sample generated with a b -filter. The middle column represents the sample with a c -filter and b -veto. The right column shows the effective luminosity of the sample generated with a veto on both b - and c -quarks.

Grouping	Process	Cross-section [pb]	Luminosity [fb^{-1}]			Generator
$t\bar{t}$	$t\bar{t}$	253	727.4			POWHEG+PYTHIA
Single top	t -channel	25.8	320			ACERMC+PYTHIA
	s -channel	1.64	330			POWHEG+PYTHIA
	Wt -channel	2.15	4200			POWHEG+PYTHIA
$Z/\gamma^* + \text{jets}$	$Z \rightarrow \ell\ell(ee, \mu\mu, \tau\tau)$	1110	110	9	6	SHERPA
	$Z \rightarrow \ell\ell(ee, \mu\mu, \tau\tau)$ $p_T^Z \in [40, 70]$ GeV	70.5	110	22	30	SHERPA
	$Z \rightarrow \ell\ell(ee, \mu\mu, \tau\tau)$ $p_T^Z \in [70, 140]$ GeV	29.5	510	90	110	SHERPA
	$Z \rightarrow \ell\ell(ee, \mu\mu, \tau\tau)$ $p_T^Z \in [140, 280]$ GeV	3.99	470	240	250	SHERPA
	$Z \rightarrow \ell\ell(ee, \mu\mu, \tau\tau)$ $p_T^Z \in [280, 500]$ GeV	0.24	680	480	360	SHERPA
	$Z \rightarrow \ell\ell(ee, \mu\mu, \tau\tau)$ $p_T^Z \geq 500$ GeV	1.3×10^{-2}	5700	1700	7000	SHERPA
	$DY \rightarrow \ell\ell(ee, \mu\mu, \tau\tau)$ $m_{Z/\gamma^*} \in [8, 15]$ GeV	92.1		50		SHERPA
	$DY \rightarrow \ell\ell(ee, \mu\mu, \tau\tau)$ $m_{Z/\gamma^*} \in [15, 40]$ GeV	279		50		SHERPA

Table 5.10: Summary of other background samples and their cross sections used in this analysis. The $W \rightarrow \ell\nu$ and $Z \rightarrow \ell\ell$ processes have dedicated samples for each lepton flavor as indicated in the parentheses. The W samples are generated with filters on the jet flavor. As in Table 5.9, the three columns under the effective luminosity represent the three samples (b -filter, c -filter and b -veto, veto on both b - and c -quarks).

Grouping	Process	Cross-section [pb]	Luminosity [fb^{-1}]	Generator		
Other	$t\bar{t}W$	0.10	3300	MADGRAPH+PYTHIA		
	$t\bar{t}Wj$	9.3×10^{-2}	3600	MADGRAPH+PYTHIA		
	$t\bar{t}Z$	6.8×10^{-2}	4400	MADGRAPH+PYTHIA		
	$t\bar{t}Zj$	8.7×10^{-2}	3400	MADGRAPH+PYTHIA		
	$t\bar{t}WW$	9.2×10^{-4}	11000	MADGRAPH+PYTHIA		
	$WW \rightarrow \ell\ell\nu\nu$	5.30	1400	SHERPA		
	$WW \rightarrow \ell\nu qq(e, \mu, \tau)$	7.3	100	SHERPA		
	$WZ \rightarrow \ell\ell\ell\nu$	9.74	260	SHERPA		
	$WZ \rightarrow \ell\nu\nu\nu$	1.40	270	SHERPA		
	$WZ \rightarrow \ell\nu qq(e, \mu, \tau)$	1.9	110	SHERPA		
	$WZ \rightarrow \ell\ell qq(ee, \mu\mu, \tau\tau)$	1.46	110	SHERPA		
	$WZ \rightarrow \nu\nu qq$	2.70	64	SHERPA		
	$ZZ \rightarrow \ell\ell\nu\nu$	0.49	1700	SHERPA		
	$ZZ \rightarrow \ell\ell qq(ee, \mu\mu, \tau\tau)$	0.25	120	SHERPA		
	$ZZ \rightarrow \nu\nu qq$	1.74	69	SHERPA		
	$ggf H \rightarrow WW$	0.44	2000	POWHEG+PYTHIA8		
	$ggf H \rightarrow ZZ$	4.7×10^{-2}	2000	POWHEG+PYTHIA8		
	$VBF H \rightarrow WW$	3.6×10^{-2}	17000	POWHEG+PYTHIA8		
	$VBF H \rightarrow ZZ$	3.8×10^{-3}	18000	POWHEG+PYTHIA8		
	$WH \rightarrow W\ell\nu\ell\nu$	0.15	1000	PYTHIA8		
	$WH \rightarrow W\ell\ell\nu\nu$	1.7×10^{-3}	27000	PYTHIA8		
	$ZH \rightarrow Z\ell\nu\ell\nu$	8.9×10^{-3}	2000	PYTHIA8		
	$ZH \rightarrow Z\ell\ell\nu\nu$	1.0×10^{-2}	48000	PYTHIA8		
	$t\bar{t}H \rightarrow t\bar{t}WW$	2.8×10^{-2}	7000	PYTHIA8		
	$W \rightarrow \ell\nu(e, \mu, \tau)$	11000	100	17	4	SHERPA
	$W \rightarrow \ell\nu(e, \mu, \tau)$ $p_T^W \in [40, 70] \text{ GeV}$	653	44	7	30	SHERPA
	$W \rightarrow \ell\nu(e, \mu, \tau)$ $p_T^W \in [70, 140] \text{ GeV}$	251	160	54	24	SHERPA
	$W \rightarrow \ell\nu(e, \mu, \tau)$ $p_T^W \in [140, 280] \text{ GeV}$	31.2	460	260	80	SHERPA
	$W \rightarrow \ell\nu(e, \mu, \tau)$ $p_T^W \in [280, 500] \text{ GeV}$	1.84	590	420	360	SHERPA
	$W \rightarrow \ell\nu(e, \mu, \tau)$ $p_T^W \geq 500 \text{ GeV}$	0.10	890	360	140	SHERPA

5.6.2 Control regions

The normalization of the $t\bar{t}$ and $Z/\gamma^* + \text{jets}$ backgrounds are determined using the observed data in two dedicated CRs, labeled the top control region (Top CR) and Z control region (Z CR) respectively. To reduce the uncertainty in the $t\bar{t}$ and $Z/\gamma^* + \text{jets}$ normalization factors, the CRs are defined such that they are expected to be fairly pure in events coming from the single background process of interest.

There must also be little signal contamination in the CRs to prevent potential signal events from influencing the background normalization. To reduce signal contamination, the Top and Z CRs both require $H_T \leq 500$ GeV. In addition to reducing the expected signal contamination, the CRs should have kinematics as similar as possible to the SRs to make the extrapolation from the CRs to SRs more reliable. For this reason, a requirement of $m_{b\ell}$ asymmetry ≤ 0.2 is applied to both the Top and Z CRs to match the $m_{b\ell}$ asymmetry requirement in the SRs. A requirement of $m_{b\ell}^0 \geq 200$ GeV is applied so the background normalization is taken from a region of $m_{b\ell}^0$ which is more similar to that of the SRs. Imposing a stricter requirement on $m_{b\ell}^0$ reduces the expected and observed number of events in both CRs, and a reliable estimate of the $t\bar{t}$ and $Z/\gamma^* + \text{jets}$ normalizations cannot be obtained due to statistical uncertainties. No requirement is made on the $m_{b\ell}^1$.

To ensure the CRs are relatively pure in $t\bar{t}$ or $Z/\gamma^* + \text{jets}$, the missing transverse energy (E_T^{miss}) is used. Rather than select on the E_T^{miss} alone, E_T^{miss} significance is defined as

$$E_T^{\text{miss}} \text{ significance} = \frac{E_T^{\text{miss}}}{\sqrt{H_T}}. \quad (5.4)$$

By scaling the E_T^{miss} by the total amount of energy in the event, the E_T^{miss} significance is less susceptible to the effects of fake E_T^{miss} from of mismeasurement of objects in an event. This makes the E_T^{miss} significance more robust to the energy scale of the event. Processes like $t\bar{t}$ and single top, with E_T^{miss} in the final state from neutrinos, tend to have large E_T^{miss} significance, while processes with E_T^{miss} coming entirely from mismeasurement, such as $Z/\gamma^* + \text{jets}$, tend to have low values for E_T^{miss} significance. The Top CR requires E_T^{miss} significance $\geq 4 \text{ GeV}^{1/2}$ and the Z CR requires E_T^{miss} significance $\leq 4 \text{ GeV}^{1/2}$.

Lastly, events containing like-flavor leptons, with a reconstructed invariant mass within 10 GeV of the Z boson mass are rejected from the Top CR. The Z CR, requires events be within this Z region. The definitions of the CRs are summarized in Table 5.8 and Figure 5.8.

The expected and observed $m_{b\ell}^0$ distributions in the Top CR and Z CR, shown in Figure 5.9 show reasonable agreement between the predicted and observed data in the Top CR. However, the background normalization is underpredicted in the Z CR. This disagreement seems to be caused by a poor modeling of the $Z/\gamma^* + \text{jets}$ background process when heavy flavor jets are required in the

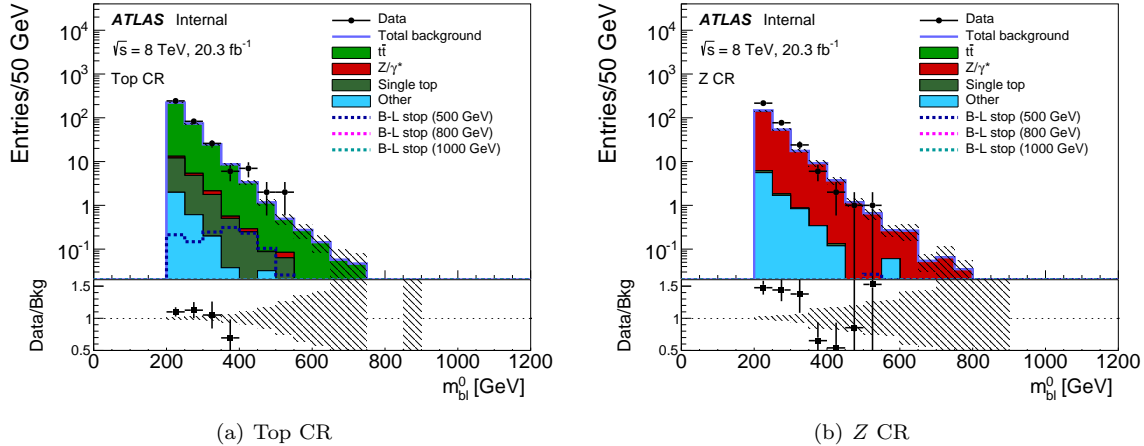


Figure 5.9: Expected and observed $m_{b\ell}^0$ distribution in the Top CR and Z CR when all flavor channels are combined. The prediction in the Top CR shows reasonable agreement with the observed data. The hashed error bands show only the statistical uncertainty in the background MC simulation samples. The signal models have assumed stop branching fractions of $Br(\tilde{t} \rightarrow b e) = Br(\tilde{t} \rightarrow b \mu) = 0.5$.

final state. For the final result, a maximum likelihood fit is used to determine the normalization of the $Z/\gamma^* + \text{jets}$ background as described in Section 5.6.4; however, due to the large disagreement in the data and MC simulation, it is useful to scale the $Z/\gamma^* + \text{jets}$ background based on the observed difference in normalization for exploratory plots and tables to obtain a more realistic estimate of the expected backgrounds in each region. The scaling factor is calculated in the expression

$$k_Z = \frac{N_{\text{data}}^{Z \text{ CR}} - \sum_{p \neq Z} N_p^{Z \text{ CR}}}{N_Z^{Z \text{ CR}}} \quad (5.5)$$

where $N_{\text{data}}^{Z \text{ CR}}$ is the number of observed events in the Z CR, and $N_p^{Z \text{ CR}}$ is the number of expected events in Z CR from process p based on the MC background simulation. This scaling factor is determined to be $k_Z = 1.39$, and will be applied to the $Z/\gamma^* + \text{jets}$ background prediction in many of the plots and tables in this section. This normalization factor is not included in the final fit to data, and any plot or figure which is produced using this normalization factor explicitly states this in the description.

After applying the k_Z normalization factor the $m_{b\ell}^0$ distributions in the Top CR and Z CR are shown in Figure 5.10. While the prediction is roughly unchanged in the Top CR, the prediction in the Z CR shows much better agreement with the data. The expected and observed event yields in the two CRs, broken out by background production process, are shown in Table 5.11. The expected signal yield in each of the CRs is low, with a signal to background ratio of less than 0.01. Additional

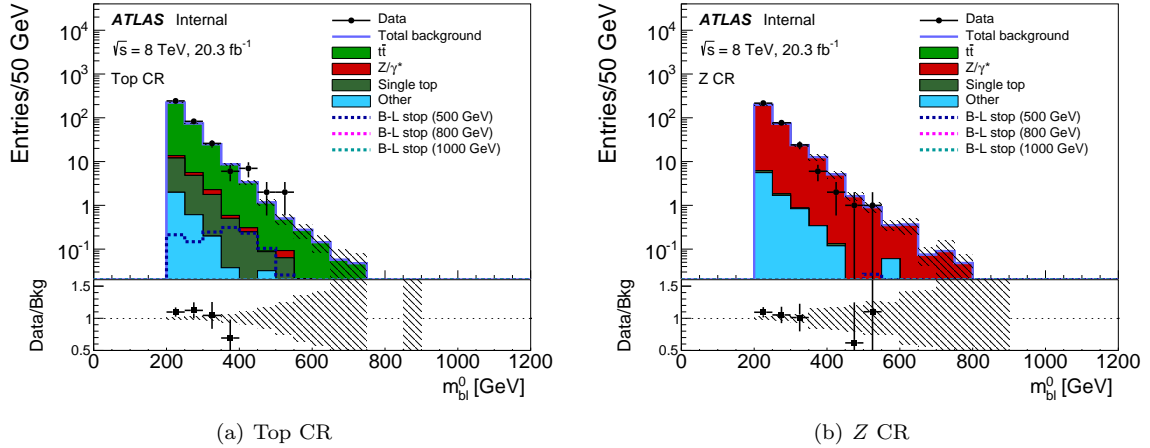


Figure 5.10: Expected and observed $m_{b\ell}^0$ distribution in the Top CR and Z CR after applying the k_Z normalization factor derived in the Z CR when all flavor channels are combined. The hashed error bands show only the statistical uncertainty in the background MC simulation samples. The signal models have assumed stop branching fractions of $Br(\tilde{t} \rightarrow b e) = Br(\tilde{t} \rightarrow b \mu) = 0.5$.

kinematic distributions including the p_T of the leptons and b -jets are shown in Figures 5.11 to 5.14.

5.6.3 Validation regions

The normalization factors for the $t\bar{t}$ and $Z/\gamma^* + \text{jets}$ background processes are determined using the observed data in the CRs, then used to estimate the background contribution in the SRs. To show these normalization factors are valid in regions of kinematic space away from the CRs, Validation regions (VRs), which are orthogonal to the CRs and SRs are defined, where the background prediction can be compared with the observation. These VRs should have low expected signal contamination, but do not need to be pure in any particular background process, as is required of the CRs. Since this analysis targets stops with reasonably high mass, all VRs require $m_{b\ell}^0 \geq 200$ GeV as is required in the CRs. As with the CRs, regions with higher $m_{b\ell}$ requires were tested, but the expected and observed event yields were too low to make a reliable comparison.

As shown in Figure 5.8 and Table 5.8, three orthogonal VRs are defined to validate the $t\bar{t}$ background estimate, labeled Top VR 1, Top VR 2, and Top VR 3. Top VR 1 is constructed by reversing the cut on E_T^{miss} significance in the Top CR. That is, Top VR 1 requires events have E_T^{miss} significance $< 4 \text{ GeV}^{1/2}$, and is otherwise identical to the Top CR. Top VR 2 is obtained by reversing the $m_{b\ell}$ asymmetry requirement in the Top CR and relaxing the E_T^{miss} significance requirement. Top VR 3 is intended to validate the extrapolation of the $t\bar{t}$ background prediction from the

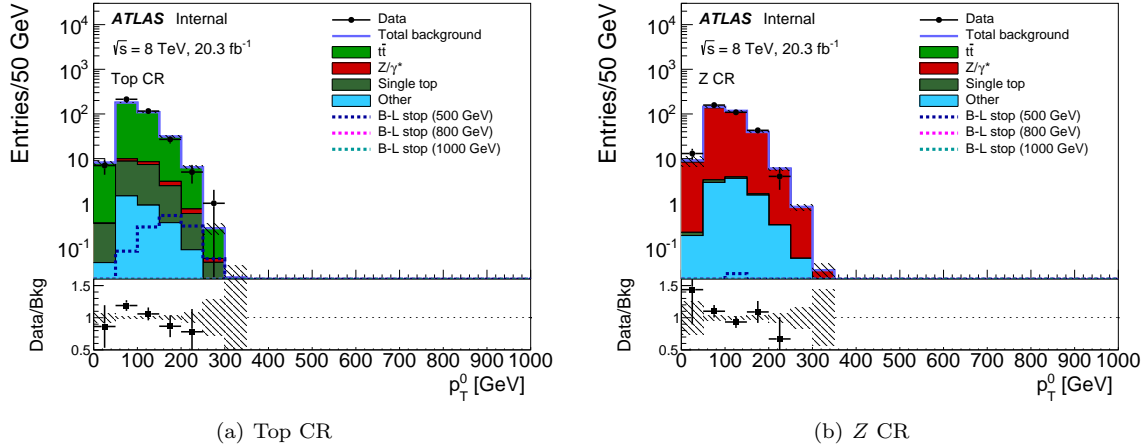


Figure 5.11: Expected and observed p_T distribution for the leading lepton in the Top CR and Z CR after applying the k_Z normalization factor derived in the Z CR when all flavor channels are combined. The hashed error bands show only the statistical uncertainty in the background MC simulation samples. The signal models have assumed stop branching fractions of $Br(\tilde{t} \rightarrow b\ell) = Br(\tilde{t} \rightarrow b\mu) = 0.5$.

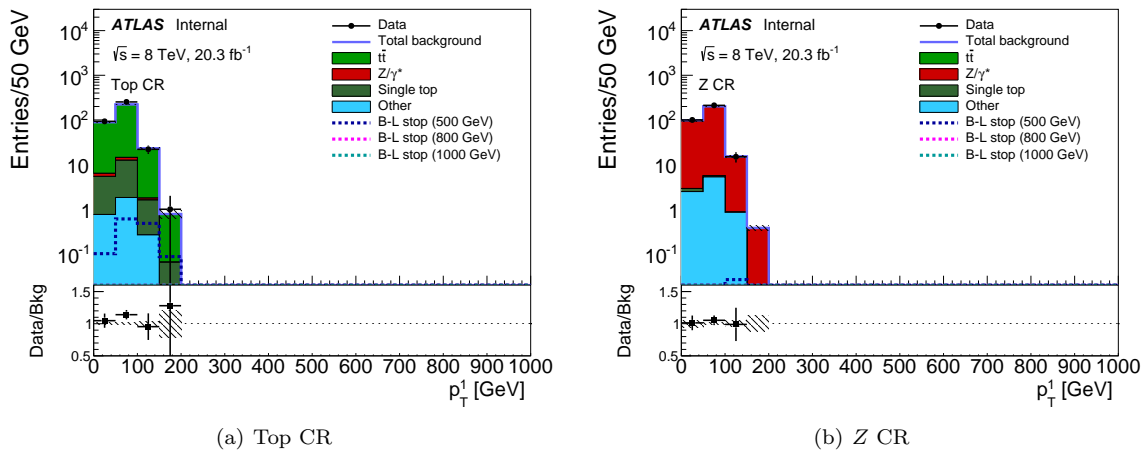


Figure 5.12: Expected and observed p_T distribution for the sub-leading lepton in the Top CR and Z CR after applying the k_Z normalization factor derived in the Z CR when all flavor channels are combined. The hashed error bands show only the statistical uncertainty in the background MC simulation samples. The signal models have assumed stop branching fractions of $Br(\tilde{t} \rightarrow b\ell) = Br(\tilde{t} \rightarrow b\mu) = 0.5$.

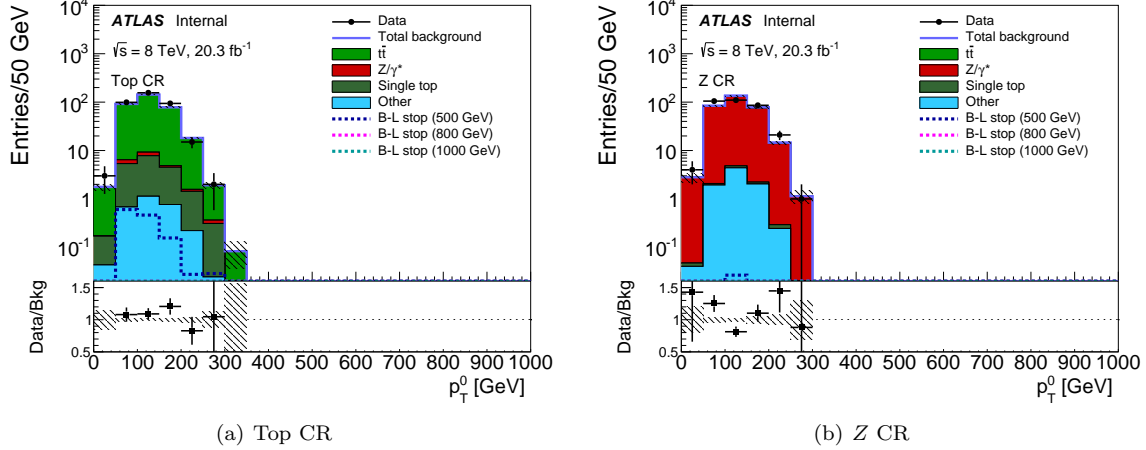


Figure 5.13: Expected and observed p_T distribution for the leading b -jet in the Top CR and Z CR after applying the k_Z normalization factor derived in the Z CR when all flavor channels are combined. The hashed error bands show only the statistical uncertainty in the background MC simulation samples. The signal models have assumed stop branching fractions of $Br(\tilde{t} \rightarrow be) = Br(\tilde{t} \rightarrow b\mu) = 0.5$.

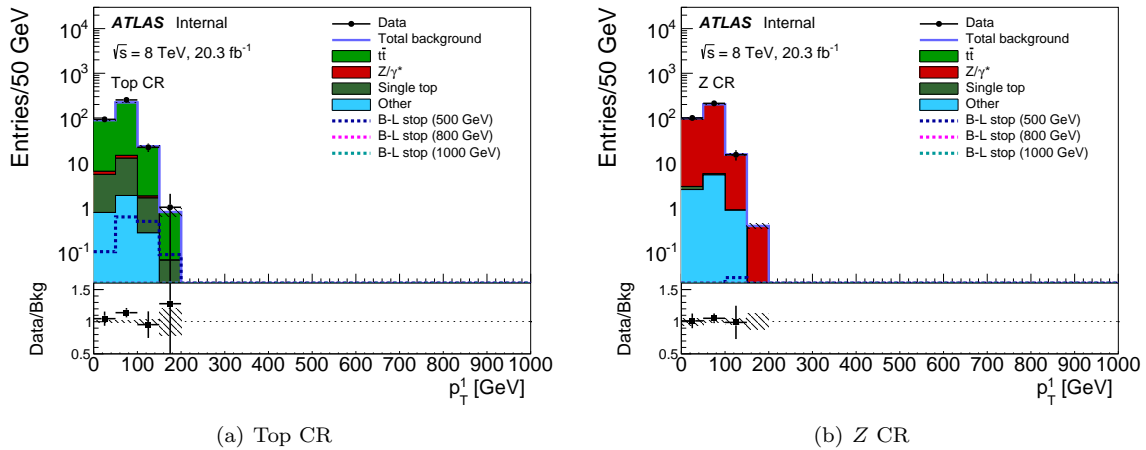


Figure 5.14: Expected and observed p_T distribution for the sub-leading b -jet in the Top CR and Z CR after applying the k_Z normalization factor derived in the Z CR when all flavor channels are combined. The hashed error bands show only the statistical uncertainty in the background MC simulation samples. The signal models have assumed stop branching fractions of $Br(\tilde{t} \rightarrow be) = Br(\tilde{t} \rightarrow b\mu) = 0.5$.

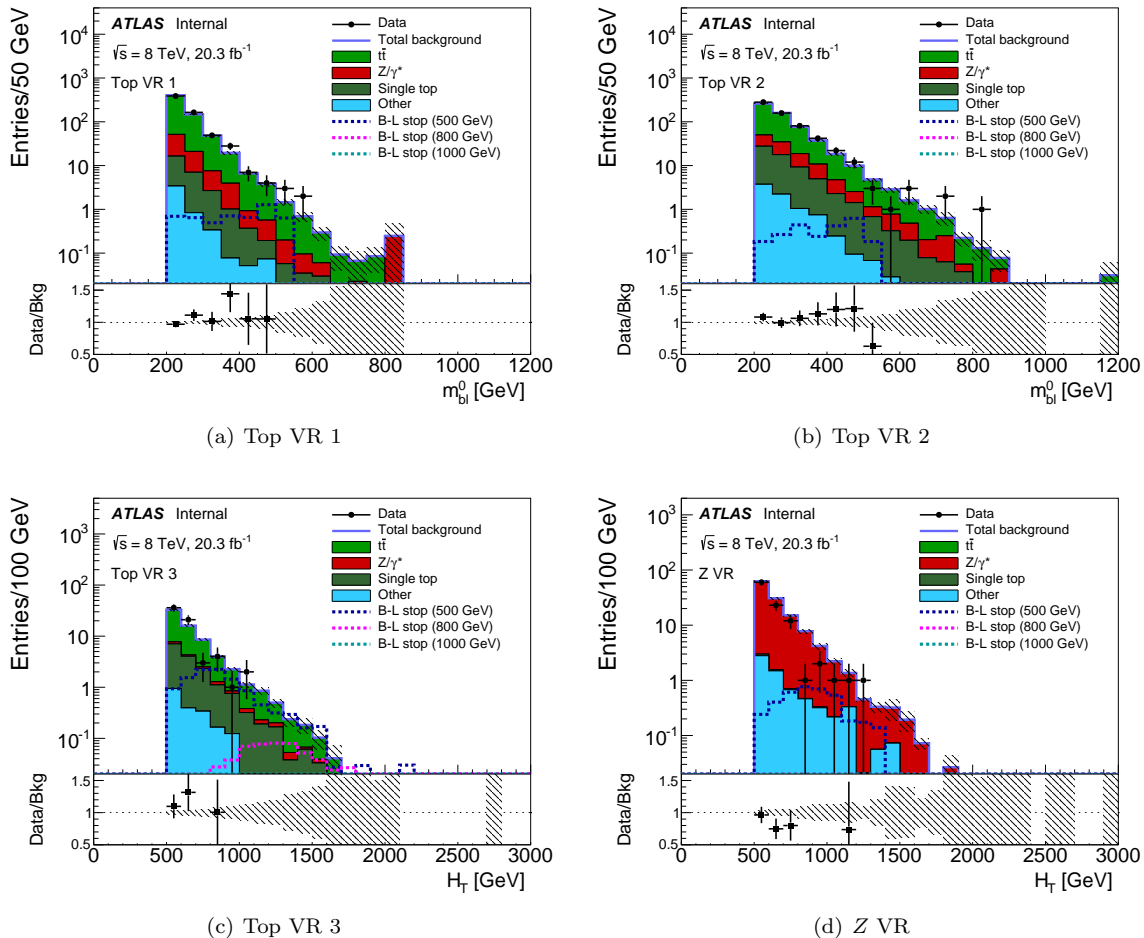


Figure 5.15: Expected and observed $m_{b\ell}$ and H_T distributions in the VRs. The hashed error bands show only the statistical uncertainty in the background MC simulation samples. The signal models have an assumed $Br(\tilde{t} \rightarrow b e) = Br(\tilde{t} \rightarrow b \mu) = 0.5$.

low H_T Top CR to the high H_T region of the SRs. The Top VR 3 region is obtained by reversing the H_T selection criteria from the Top VR 2 region, giving a region with $m_{b\ell}$ asymmetry > 0.2 and $H_T > 500$ GeV.

The Z VR is used to validate the extrapolation of the $Z/\gamma^* + \text{jets}$ background prediction from the Z CR to kinematic regions higher H_T . This region is constructed by reversing the H_T selection criteria from the Z CR, and relaxing the E_T^{miss} significance requirement. The full VR selection criteria are outlined along with the other analysis regions in Table 5.8 and Figure 5.8. The expected and observed event yields in the VRs, broken out by background production process, are shown in Table 5.11. Select kinematic distributions in the VRs are shown in Figure 5.15. The agreement between the observed

Table 5.11: The observed and expected event yields in the CRs and VRs. The expected event yields are shown before and after a fit to the data in the CRs. The fitted background yields in the CRs match the observed number of events in data by construction.

	Top CR	Z CR	Top VR 1	Top VR 2	Top VR 3	Z VR
Observed	369	327	645	606	67	101
Fitted background	369 ± 19	327 ± 18	690 ± 50	630 ± 40	72 ± 5	130 ± 60
Fitted $t\bar{t}$	346 ± 19	9.1 ± 0.7	600 ± 40	497 ± 35	54 ± 5	2.99 ± 0.24
Fitted $Z/\gamma^* + \text{jets}$	3.2 ± 0.5	309 ± 18	63 ± 5	64 ± 5	1.5 ± 0.8	120 ± 60
Single top	16.7 ± 2.0	0.83 ± 0.09	23.0 ± 2.6	56 ± 6	14.1 ± 1.9	0.32 ± 0.04
Other	2.83 ± 0.27	8.64 ± 1.0	4.7 ± 0.4	8.2 ± 0.8	2.03 ± 0.27	6.4 ± 0.7
Input SM	330	230	614	557	66	93
Input $t\bar{t}$	310	8.2	543	447	49	2.7
Input $Z/\gamma^* + \text{jets}$	2.2	220	44	45	1.1	83
Input single top	17	0.8	23	57	14	0.30
Input other	2.8	8.6	4.7	8.2	2.0	6.40
$B - L$ stop (500 GeV)	1.3	0.03	5.1	2.4	10.7	3.8
$B - L$ stop (800 GeV)	< 0.01	< 0.01	< 0.01	< 0.01	0.6	0.02
$B - L$ stop (1000 GeV)	< 0.01	< 0.01	< 0.01	< 0.01	0.1	< 0.01

and predicted yields and distributions in the VRs is explored in more detail in Section 5.6.4.

5.6.4 Background fit

The normalization of the $t\bar{t}$ and the $Z/\gamma^* + \text{jets}$ backgrounds are determined using a simultaneous fit, which takes into account cross-contamination of the different background processes between the CRs as well as the statistical and systematic uncertainties (described in Section 5.7). The fit is implemented using the `HistFitter` version 1.2.1, a framework for statistical data analysis [118]. The remaining background estimates, due to single top and other SM processes, are taken from the MC simulation.

The background-only estimate is performed using a maximum likelihood fit to the data in the Top and Z CRs. The three flavor channels (ee , $\mu\mu$, and $e\mu$) are summed over, and the total event yield in each CR is considered. The predicted event yield for a background process p ($t\bar{t}$ or $Z/\gamma^* + \text{jets}$) in a particular region r is $\mu_p \cdot N_{r,p}^{\text{MC}}$, where $N_{r,p}^{\text{MC}}$ is the number of events from process p in region r .

predicted by the MC simulation estimate, after applying all the relevant scale factors and efficiencies. μ_p is a strength parameter for each process which enters the likelihood fit, and is used to model any under/over-prediction in the MC simulation which is assumed to be constant across all regions. A strength parameter is defined for the $t\bar{t}$ and $Z/\gamma^*+{\rm jets}$ background predictions, $\mu_{t\bar{t}}$ and μ_Z respectively.

The background fit is performed by first summing the total background estimate for all background processes in each of the CRs. The strength parameters are varied to obtain the best agreement between the observed event yields and the background predictions. The systematic uncertainties are treated as Gaussian nuisance parameters. The background only fit finds that the best fit values for $\mu_{t\bar{t}}$ and μ_Z are 1.11 ± 0.14 and 1.43 ± 0.19 respectively. It should be noted that the μ_Z is consistent with the k_Z derived in Section 5.6.2.

The number of observed events as well as the post-fit expected number of events in each of the CRs and VRs are shown in Table 5.11. The agreement between the observed number of events and the fitted event yields in the CRs and VRs is summarized in Figures 5.16 and 5.17 respectively. Using the fitted backgrounds, the dominant process in the same-flavor channels of the SRs is $Z/\gamma^*+{\rm jets}$ followed by single top and $t\bar{t}$. In the $e\mu$ channel, the $Z/\gamma^*+{\rm jets}$ background does not contribute, thus, the largest backgrounds are single top and $t\bar{t}$.

As a result of the fit, the $Z/\gamma^*+{\rm jets}$ background is scaled up by approximately 40%. Due to this large normalization factor, the background is over-predicted in the Z VR. The over-prediction is understood to be due to the difficulty in modeling the production of Z/γ^* in association with heavy flavor quarks. This mismodeling is also observed by ATLAS in the SM measurement of the Z boson differential cross section [119, 120]. To account for this over-prediction, an additional systematic uncertainty of 50% is taken on the background estimate from $Z/\gamma^*+{\rm jets}$ events in regions with large values of H_T . This is described in Section 5.7 along with the other systematic uncertainties.

The extrapolation from low H_T CRs to the high H_T region where the SRs are located is validated using the Top VR 3 and Z VR. These validation regions show fair agreement between the observed and predicted event yields as well as for the shape of the $m_{b\ell}^0$ and H_T distributions as shown in Figures 5.18 and 5.19.

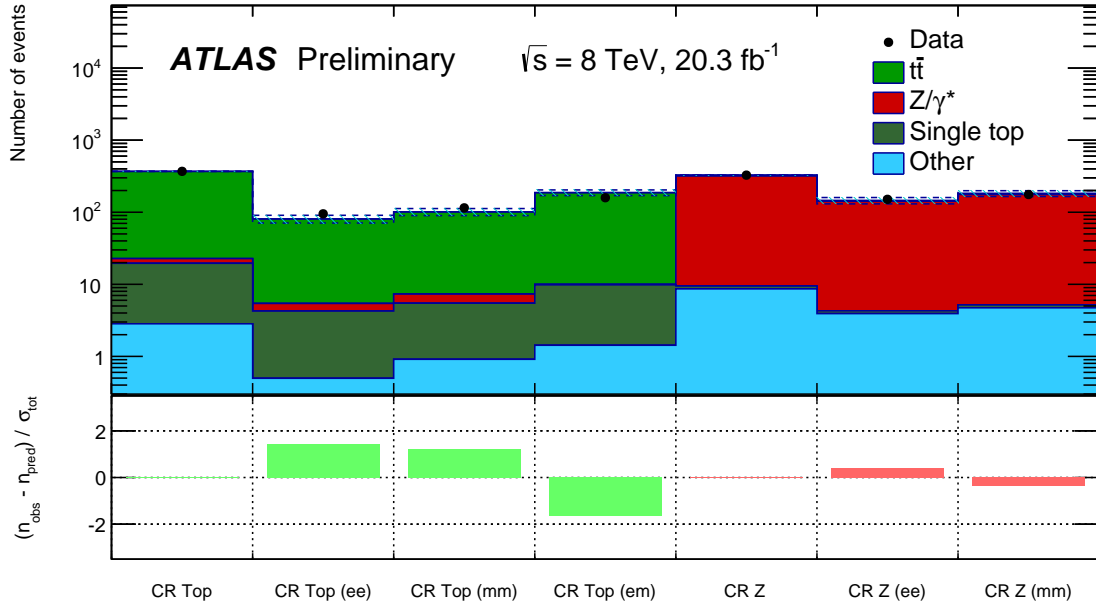


Figure 5.16: The number of observed and expected events in the CRs, broken down by flavor channel. The uncertainty band includes the statistical uncertainty as well as the systematic uncertainty (described in Section 5.7). The deviation of that channel's prediction from the observed number of events divided by the uncertainty in the prediction is also shown. The normalization of the background yields are determined by fitting the $t\bar{t}$ and $Z/\gamma^* + \text{jets}$ backgrounds to the observed data in the two CRs, so the Top CR and Z CR bins have perfect agreement by construction.

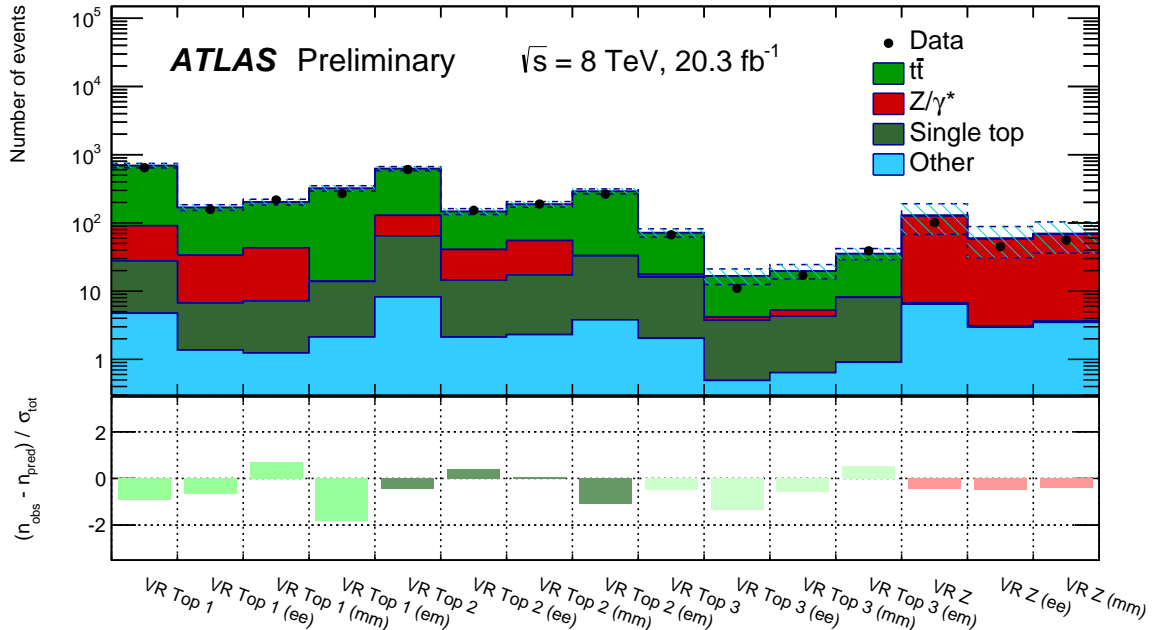


Figure 5.17: The number of observed and expected events in the VRs, broken down by flavor channel. The uncertainty band includes the statistical uncertainty as well as the systematic uncertainty (described in Section 5.7). The deviation of that channel's prediction from the observed number of events divided by the uncertainty in the prediction is also shown. The normalization of the background yields are determined by fitting the $t\bar{t}$ and $Z/\gamma^* + \text{jets}$ backgrounds to the observed data in the two CRs.

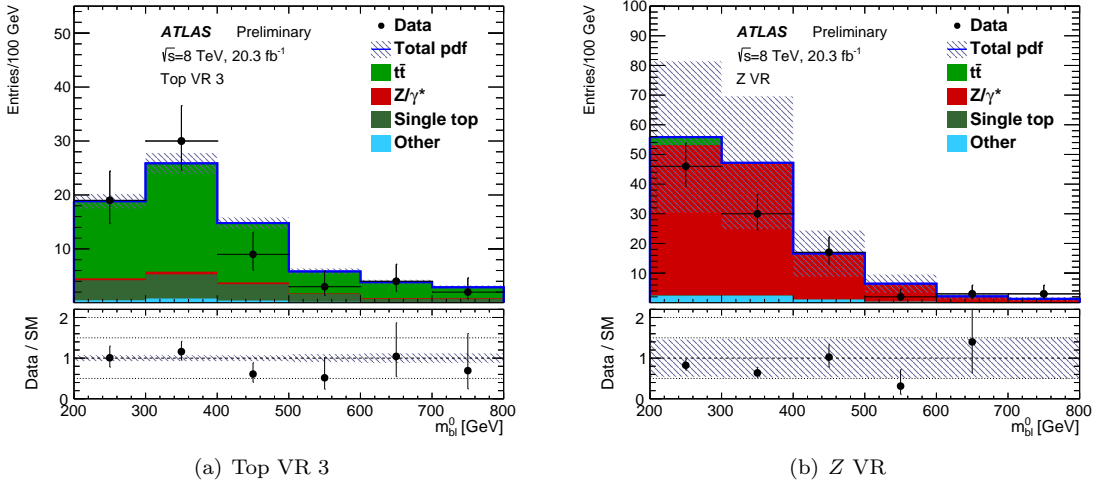


Figure 5.18: The $m_{b\ell}^0$ distribution in Top VR 3 (left) and Z VR (right). The Standard Model background prediction is shown after setting the normalization of the $t\bar{t}$ and $Z/\gamma^* + \text{jets}$ backgrounds based on the observed data in the CRs. The hashed bands show the uncertainty in the fitted background prediction including all statistical and systematics uncertainties. The bottom of each plot shows the ratio of the observed data to the Standard Model background prediction.

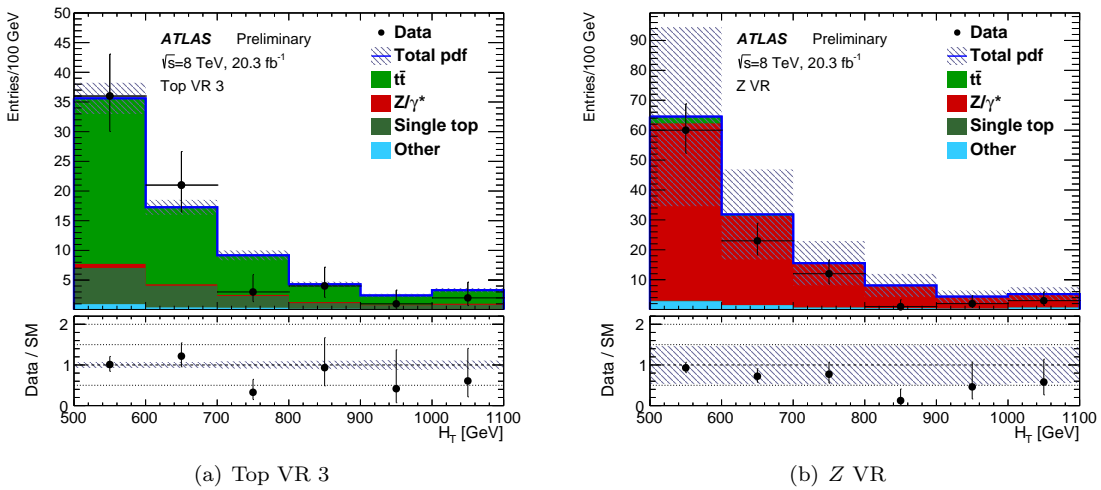


Figure 5.19: The H_T distribution in Top VR 3 (left) and Z VR (right). The Standard Model background prediction is shown after setting the normalization of the $t\bar{t}$ and $Z/\gamma^* + \text{jets}$ backgrounds based on the observed data in the CRs. The hashed bands show the uncertainty in the fitted background prediction including all statistical and systematics uncertainties. The bottom of each plot shows the ratio of the observed data to the Standard Model background prediction.

5.7 Systematic uncertainties

Several sources of systematic uncertainty are considered when determining the estimated signal and background contributions. The largest sources of systematic uncertainty are those related to the MC statistical uncertainty in the SRs, the jet energy scale (JES), and the b -tagging efficiency. The uncertainty in the lepton energy scale and resolution was considered, but shown to be negligible.

The uncertainty in the JES has an impact on both the jet selection criteria and the derived kinematic variables of the event, such as the H_T and the E_T^{miss} measurements. The JES uncertainty is evaluated using the EM+JES scheme as described in [93], and the scaling is provided by the `MultijetJESUncertaintyProvider` tool. The uncertainty in the JES is composed of 16 parameters, and takes into account the dependence on p_T , η , jet flavor, and the number of primary vertices. The effect of each component on the event yield is estimated by varying the component by $\pm 1\sigma$ in the MC simulation and re-running the full event selection, propagating the variation in the JES to the jet selection and related kinematic quantities.

The uncertainty in the jet energy resolution (JER) is evaluated by applying an additional smearing to the p_T measurement of each of the jets in the MC simulation. The size of the smearing is determined in dijet events as described in [121]. The smearing is provided by the `JetSmearingTool` tool, and depends on the p_T and η of the jets within an event. The JER smearing alters the p_T of the jets within the event, and therefore the event selection. As with the JES, the JER uncertainty is evaluated by applying the smearing, propagating the variations to the event kinematic variables, and re-running the full event selection on MC simulation to determine the new event yields.

The efficiency of the b -tagging algorithms affects the overall yields in each of the analysis regions. This includes the possibility of a light flavor jet being incorrectly tagged as a b -jet, or a jet which initiated by a b -quark failing the b -tagging requirement. The b -tagging efficiency uncertainty is broken into three components, corresponding to the tagging efficiency of b -jets, c -jets, and light flavor jets (light quarks and gluons). These uncertainties take into account the dependence on p_T and jet flavor. For the MC simulation, the weight associated with the b -tagging scale factor is varied up or down based on the specific parameter of interest, and used to determine the uncertainty in the event yield.

The backgrounds are constrained in the CRs which are regions with low H_T , while the SRs require high H_T . Top VR 3 and Z VR are used to assess any uncertainty associated with the extrapolation from low H_T to high H_T . The $t\bar{t}$ background extrapolation is assessed using Top VR 3. It can be seen from Table 5.11 that the post-fit background estimate in Top VR 3 is in reasonably agreement with the observed data, so no additional uncertainty is applied to the $t\bar{t}$ backgrounds due to the H_T extrapolation. The $Z/\gamma^* + \text{jets}$ background extrapolation is assessed using the Z VR. The overall

background is overpredicted in this region by 29%, and the prediction is the worst in the highest H_T bins. An additional uncertainty of 50% is applied to the $Z/\gamma^* + \text{jets}$ background for events with $H_T > 500 \text{ GeV}$.

Several uncertainties related to the theoretical modeling of the major background processes in MC simulation are considered. These include the uncertainty in the cross sections, renormalization and factorization scale variations, and generator uncertainties. These uncertainties are evaluated by performing the event selection using only the MC truth information, and comparing the expected event yields obtained from MC simulation samples produced using different generator configurations. An additional systematic uncertainty, due to the $\pm 2.8\%$ uncertainty in the integrated luminosity is evaluated for all background processes except $t\bar{t}$ and $Z/\gamma^* + \text{jets}$, because these backgrounds take the normalization from data control regions. A summary of the estimated effect of each source of systematic uncertainty (both experimental and theoretical) is in Table 5.12. Several sources of theoretical systematic uncertainty which have a small effect on the total background estimate are grouped into the “Other theory” category.

Table 5.12: Summary of the effect of each considered sources of systematic uncertainty on the total background estimate in SR 400 and SR 600. If the uncertainty is asymmetric, the larger deviation is reported in this table.

Systematic Uncertainty (%)	SR 400	SR 600
JES	15	3
b -tagging	13	12
JER	5	1
Luminosity	1	1
H_T extrapolation	19	20
MC statistical	13	23
CR statistical	3	3
Wt cross section	2	2
Other theory	1	2

The sources of systematic uncertainty evaluated for the $t\bar{t}$ background include the renormalization and factorization scale variations, MC generator uncertainties, parton shower, and the amount of initial or final state radiation (ISR or FSR) in the event. The scale variations are evaluated by comparing the expected event yields at the truth level obtained using dedicated $t\bar{t}$ samples, each generated using **POWHEG** and **PYTHIA**, where the factorization and renormalization scales are separately varied up and down by a factor of 2. This isolates the effect of each of the scale variations. The

differences in the expected event yields for these samples is taken to be the uncertainty due to the scale variations. The MC generator uncertainty accounts for the difference in the MC predictions obtained using different generator programs. These are assessed by comparing the truth level event selection for a $t\bar{t}$ sample generated using **POWHEG** and **JIMMY** with a sample generated using **MC@NLO** and **JIMMY**. Since **JIMMY** is used to perform the parton shower in both of these samples, the differences can be attributed to the differences in the generation rather than the parton shower step.

The uncertainty in the parton shower in $t\bar{t}$ samples is estimated by comparing the expected event yields using the truth level information for two $t\bar{t}$ samples each generated using **POWHEG**. One sample uses **PYTHIA** for the parton shower step, while the other uses **JIMMY**. This isolates the parton shower part of the MC simulation, which is performed either using **PYTHIA** or **JIMMY**. The uncertainty in the ISR and FSR is evaluated by comparing the expected number of events in a truth level event selection found in two $t\bar{t}$ samples, each generated using **ACERMC** and **PYTHIA**. The two samples differ in the amount of ISR and FSR is included in the simulation.

For the single top background, the sources of systematic uncertainty include the single top cross section, the MC generator uncertainties, the parton shower, ISR and FSR, and the interference with $t\bar{t}$. Single top can be produced through three production channels, with production cross sections

- s -channel: 5.61 ± 0.22 pb
- t -channel: $87.76^{+3.44}_{-1.91}$ pb
- Wt -channel: 22.37 ± 1.52 pb.

It was shown that the Wt -channel is the dominant single top production channel for the regions of interest. For this reason, the 7% uncertainty in the Wt -channel cross section is the only single top cross section uncertainty which is considered. The MC generator uncertainty in the single top background estimate is evaluated by comparing the predicted yields from two single top samples, one generated using **POWHEG**, and the other generated using **MC@NLO**. Both MC samples use **HERWIG** to calculate the parton shower. The parton shower uncertainty is determined by comparing the truth level yields of two simulated Wt -channel samples, each generated using **HERWIG**. The parton shower step was performed using **PYTHIA** and **HERWIG**. Similar to the $t\bar{t}$ background, the uncertainty in the single top background estimate due to ISR and FSR uncertainties is determined by comparing two samples, each generated using **ACERMC** and **PYTHIA**. Interference between the $t\bar{t}$ and the Wt -channel single top background processes is handled by applying an additional uncertainty to the single top background estimate by comparing the truth level event selection of two Wt -channel samples, each

generated using **POWHEG**, but one using the DS renormalization scheme, and the other using the DR renormalization scheme.

For the $Z/\gamma^* + \text{jets}$ background, the H_T extrapolation uncertainty of 50%, previously discussed in this Section. A separate an additional uncertainty is applied to account for the finite number of partons in the $Z/\gamma^* + \text{jets}$ background MC samples. This uncertainty is evaluated by comparing the truth level event yields for two $Z/\gamma^* + \text{jets}$ samples, generated with different numbers of additional partons included in the matrix element calculation. The first sample has exactly four additional partons in the matrix element calculation, while the second set has four or five additional partons. Both samples are generated using **SHERPA**.

In addition to the above sources of systematic uncertainty, the uncertainty in the background estimate due to limited MC statistics in the CRs and SRs is considered. The MC statistical uncertainty is evaluated for each background process independently in each analysis region as \sqrt{N} , where N is the number of MC simulated events from a given background process in a particular region. No weights or scale factors are applied to this number of simulated events. The total relative uncertainty in a region r due to MC statistical limitations ($\sigma_r^{\text{MC stat,relative}}$) is obtained by summing the relative uncertainties for each process in region r in quadrature. The total MC statistical uncertainty is evaluated in each region, and treated as a systematic uncertainty in the background estimate. The Top CR and Z CR are used to constrain the $t\bar{t}$ and $Z/\gamma^* + \text{jets}$ background estimates, so the MC statistical uncertainty in the CRs results in additional uncertainty in the background estimate in the SRs. For this reason, the MC statistical uncertainty in the Top (Z) CR is applied as an additional systematic uncertainty in the $t\bar{t}$ ($Z/\gamma^* + \text{jets}$) background estimate in the SRs.

When determining the expected contributions of each of the signal models, the effects of the JES, b -tagging efficiency, JER, and luminosity are considered as well as the uncertainty in the signal model cross section, from in Table 5.1.

CHAPTER 6

Results

This chapter presents the results of the $B - L$ stop search, which was introduced in Chapter 5. The observed event yields and the background prediction, obtained using a maximum likelihood fit, are shown in Section 6.1. The chapter concludes in Section 6.2 with the expected and observed limits limits on the allowable stop masses in the context of the particular supersymmetric model with $B - L$ stop pair production.

6.1 Event Yields

The fitted background yields and the observed number of events in each signal region are shown in Tables 6.1 and 6.2. The background yields in the signal regions are determined using a maximum likelihood fit [118] for the $t\bar{t}$ and $Z/\gamma^* + \text{jets}$ normalizations, which are constrained by the observed data in the Top and Z CRs. The systematic uncertainties described in Section 5.7 are included as Gaussian-distributed nuisance parameters.

Two events are observed, in agreement with the SM prediction. The kinematics of the two selected events are shown in Table 6.3, the $m_{b\ell}^0$ and H_T distributions in SR 400 are shown in Figure 6.1. Event displays of the two events are shown in Figure 6.2.

As the observed number of events is consistent with the SM prediction, upper limits at 95% confidence level (CL) on the number of beyond the Standard Model (BSM) events for each signal region are derived using the CL_S prescription and neglecting any possible contamination in the control regions [118]. Normalizing these by the integrated luminosity of the data sample they can be interpreted as upper limits on the visible BSM cross section, σ_{vis} , where σ_{vis} is defined as the product of acceptance, reconstruction efficiency and production cross section. The model independent limits are given in Tables 6.1 (SR 400) and 6.2 (SR 600), and are shown for each flavor channel separately,

and for the combined SRs which sum over the three flavor channels. Since the two observed events are in the $\mu\mu$ channel, the limit on σ_{vis} is stronger than expected in the ee and $e\mu$ channels, and weaker than expected in the $\mu\mu$ channel.

6.2 Model dependent limits

In the absence of an excess of events in the SRs beyond the SM prediction, limits are set on the allowable stop masses and branching fractions for this model. Expected and observed exclusion limits on the signal model are determined using the CL_S prescription based on a simultaneous fit of the SRs and CRs [118]. The predicted small signal contamination in the CRs is taken into account for each signal model tested. An expected and observed mass limit is first determined for a single choice of stop branching fraction, $Br(\tilde{t} \rightarrow eb) = Br(\tilde{t} \rightarrow \mu b) = 0.5$, the nominal branching fraction simulated in the MC signal models. Then, the simulated signal samples are rescaled in order to determine mass limits for different choices of stop branching fractions.

6.2.1 Single mass limit

Each SR (SR 400 and SR 600) is interpreted separately, using the predicted and observed event yields in the CRs and the SR of interest. A maximum likelihood fit is performed to obtain the model-dependent estimate of the background and signal strengths. When calculating the expected limit, the data in the SR is replaced with the pre-fit MC prediction. An expected and observed CL_S value is computed for each simulated stop mass, in each SR to assess the relative compatibility of the data with the signal + background hypothesis and the background only hypothesis. For each stop mass, the SR which gives the best expected sensitivity, as measured by the lower CL_S value is selected, and used to interpret the model at that mass. The `HistFitter` package limits the precision of the CL_S value to 10^{-6} ; if the two SRs are affected by this cutoff, SR 400 is chosen by convention. This simplification is not expected to affect the final result, as these points are far from the limit, where the expected CL_S is 0.05. If the observed CL_S value in the selected SR is less than 0.05, the signal model is rejected at 95% CL. An observed (expected) limit on the stop mass is determined by taking the highest stop mass, with an observed (expected) CL_S value less than 0.05. Figure 6.3 shows an example CL_S plot (both SRs) for the scenario with $Br(\tilde{t} \rightarrow eb) = Br(\tilde{t} \rightarrow \mu b) = 0.5$. In the high mass regime, SR 600 is selected to interpret the mode, and the points where the solid line is below 0.05 (indicated with a dashed red line) are excluded. No interpolation between the mass points is performed, so the mass limit for this choice of stop branching fractions is 900 GeV.

6.2.2 Branching fraction scan

This procedure of finding a stop mass limit is repeated for branching fractions across the plane of allowed values. The MC simulation stop samples are generated with fixed branching fractions of $Br(\tilde{t} \rightarrow be) = Br(\tilde{t} \rightarrow b\mu) = 0.5$, however, an additional event weight is constructed to scale the simulated signal process to the desired choice of stop branching fraction. This event weight depends on the lepton flavor channel of each MC simulated event.

For a choice of stop branching fraction, the di-stop branching fractions are given by

$$\begin{aligned} Br_{\text{flavor}}(\tilde{t}\tilde{t}^* \rightarrow bbee) &= Br_{\text{flavor}}(\tilde{t} \rightarrow be)^2 \\ Br_{\text{flavor}}(\tilde{t}\tilde{t}^* \rightarrow bb\mu\mu) &= Br_{\text{flavor}}(\tilde{t} \rightarrow b\mu)^2 \\ Br_{\text{flavor}}(\tilde{t}\tilde{t}^* \rightarrow bbe\mu) &= 2Br_{\text{flavor}}(\tilde{t} \rightarrow be)Br_{\text{flavor}}(\tilde{t} \rightarrow b\mu). \end{aligned} \quad (6.1)$$

The di-stop branching fractions for each flavor channel are plotted for choices of the single-stop branching fraction in Figure 6.4(a), where darker colors represent a higher branching fraction. The simulated stop samples correspond to the center of the x -axis, and have di-stop branching fractions of 0.25, 0.25, and 0.50 for the $eebb$, $\mu\mu bb$, $e\mu bb$ channels respectively. As the value of $Br(\tilde{t} \rightarrow be)$ increases (represented by moving toward the bottom right corner of each of the plots), the fraction of events decaying to the $eebb$ final state increases, while the other two flavor channels have fewer expected events. Similarly, as the value of $Br(\tilde{t} \rightarrow b\mu)$ increases (represented by moving toward the bottom left corner of each of the plots), the fraction of events decaying to the $\mu\mu bb$ final state increases. Finally, increasing branching fraction of the $\tilde{t} \rightarrow b\tau$ decay (represented by moving toward the upper left corner of the plots) results in a decreasing number of expected events with two light leptons.

Taking the ratio of the target and nominal di-stop branching fraction, a scale factor is defined for each flavor channel to weight the MC simulation such that it can represent any stop branching fraction. These scale factors are given by

$$\begin{aligned} SF_{\text{flavor}}(\tilde{t}\tilde{t}^* \rightarrow bbee) &= \frac{Br(\tilde{t} \rightarrow be)^2}{0.25} \\ SF_{\text{flavor}}(\tilde{t}\tilde{t}^* \rightarrow bb\mu\mu) &= \frac{Br(\tilde{t} \rightarrow b\mu)^2}{0.25} \\ SF_{\text{flavor}}(\tilde{t}\tilde{t}^* \rightarrow bbe\mu) &= \frac{2Br(\tilde{t} \rightarrow be)Br(\tilde{t} \rightarrow b\mu)}{0.50}. \end{aligned} \quad (6.2)$$

The appropriate flavor scale factor is applied to each simulated signal event depending on the reconstructed flavor channel. The values of the scale factors are shown in Figure 6.4(b), where a darker color corresponds to a larger value for the scale factor (with a maximum value of 4).

The expected and observed CL_S values in SR 400 and SR 600 are shown over a range of stop branching fraction hypotheses in Figures 6.5 and 6.6 respectively for select stop masses of 500 GeV and 900 GeV. A complete collection of the expected and observed CL_S plots are found in Appendix B.

A limit on the allowed stop masses and stop branching fractions is obtained similar to the example with a single branching fraction hypothesis. For each combination of stop mass and branching fractions, the SR which gives the lowest expected value of CL_S is selected. The SR selection for select masses are shown in Figure 6.7. Based on the selected SR, the model is rejected at 95% CL if the observed CL_S is less than 0.05, and for each branching fraction, the highest stop mass which is excluded is taken to be the mass limit.

Figure 6.8 shows the expected 95% CL mass limit for each point on the stop branching fraction plane. These limits are obtained by selecting the highest stop mass with an expected $CL_S < 0.05$ in the selected SR. For each point on the stop branching fraction plane, the color corresponds to the maximum excluded stop mass or the selected branching fraction hypothesis. The nominal stop cross section is used when determining these limit contours.

The expected and observed limits for each stop mass are shown in Figure 6.9. This figure shows, for each simulated stop mass, the observed (expected) 95% exclusion limit on the branching fraction under the red (blue) line. A yellow band shows the $\pm 1\sigma$ uncertainty in the expected limit, determined from the systematic uncertainty in the signal and background prediction excluding the effect of the signal cross section uncertainty. The effect of varying the signal cross section on the observed limit is indicated by the dashed red lines. Since the two observed events are in the $\mu\mu$ channel, the observed limit is somewhat stronger than expected in scenarios with a large stop branching fraction to $b\tau$ (on the right side of the branching fraction plane), and somewhat weaker than expected when the branching fraction to $b\mu$ becomes significant. This explains why the red (observed) limit contour crosses the dashed blue (expected) limit contour.

The observed limit on the stop mass is shown in Figure 6.10. This plot shows the 95% CL on the mass obtained by choosing the maximum excluded mass for each branching fraction on the plane using the nominal cross section value. As the branching fraction of $\tilde{t} \rightarrow b\tau$ increases, the number of expected events with electrons or muons in the final state decreases for the same simulated stop mass. Therefore, the limit on the mass is strongest at the bottom of the plane. In the top corner of the plot, the SRs described in this analysis note have no sensitivity, however traditional leptoquark searches for final states with b -tagged jets and τ leptons are able to place experimental limits in this region [25].

Table 6.1: The expected and observed event yields in SR 400. The expected event yields are shown before and after performing the fit to the data in the control regions. The last three rows show the model-independent 95% CL on the visible cross section and the upper limit on the number of events (expected and observed) in SR 400 from a generic non-Standard Model process.

	SR 400	SR 400 ee	SR 400 $\mu\mu$	SR 400 $e\mu$
Observed	2	0	2	0
Fitted background	1.39 ± 0.35	0.36 ± 0.15	0.57 ± 0.20	0.45 ± 0.11
Fitted $t\bar{t}$	0.33 ± 0.09	0.07 ± 0.08	0.07 ± 0.02	0.19 ± 0.05
Fitted $Z/\gamma^* + \text{jets}$	0.54 ± 0.28	0.20 ± 0.10	0.35 ± 0.18	≤ 0.01
Single Top	0.44 ± 0.08	0.10 ± 0.03	0.11 ± 0.03	0.23 ± 0.05
Other	0.07 ± 0.04	≤ 0.01	0.04 ± 0.02	0.03 ± 0.03
Input SM	1.2	0.30	0.46	0.43
Input $t\bar{t}$	0.30	0.06	0.06	0.17
Input $Z/\gamma^* + \text{jets}$	0.38	0.14	0.24	0.00
Input single Top	0.44	0.10	0.11	0.23
Input other	0.07	0.00	0.04	0.03
Upper limits				
$\sigma_{\text{vis}} [\text{fb}]$	0.23	0.11	0.26	0.11
Observed $N_{\text{non-SM}}$	4.8	2.2	5.4	2.3
Expected $N_{\text{non-SM}}$	$4.0^{+2.2}_{-1.1}$	$3.2^{+1.7}_{-1.1}$	$3.6^{+1.9}_{-1.5}$	$3.3^{+1.8}_{-1.3}$

Table 6.2: The expected and observed event yields in SR 600. The expected event yields are shown before and after performing the fit to the data in the control regions. The last three rows show the model-independent 95% CL on the visible cross section and the upper limit on the number of events (expected and observed) in SR 600 from a generic non-Standard Model process.

	SR 600	SR 600 ee	SR 600 $\mu\mu$	SR 600 $e\mu$
Observed	1	0	1	0
Fitted background	0.55 ± 0.15	0.15 ± 0.06	0.24 ± 0.10	0.16 ± 0.06
Fitted $t\bar{t}$	0.10 ± 0.02	0.03 ± 0.01	≤ 0.01	0.07 ± 0.03
Fitted $Z/\gamma^* + \text{jets}$	0.23 ± 0.12	0.08 ± 0.05	0.15 ± 0.08	≤ 0.01
Single Top	0.18 ± 0.04	0.03 ± 0.01	0.05 ± 0.02	0.09 ± 0.03
Other	0.04 ± 0.01	≤ 0.01	0.04 ± 0.02	≤ 0.01
Input SM	0.47	0.12	0.20	0.16
Input $t\bar{t}$	0.09	0.03	0.00	0.06
Input $Z/\gamma^* + \text{jets}$	0.16	0.06	0.10	0.00
Input single Top	0.18	0.03	0.05	0.09
Input other	0.04	0.00	0.04	0.00
Upper limits				
σ_{vis} [fb]	0.19	0.10	0.20	0.10
Observed $N_{\text{non-SM}}$	3.9	2.1	4.0	2.1
Expected $N_{\text{non-SM}}$	$3.5^{+1.9}_{-1.4}$	$2.6^{+1.6}_{-0.6}$	$3.0^{+1.7}_{-1.0}$	$2.7^{+1.6}_{-0.7}$

Table 6.3: The event and object kinematics for the two events passing the signal region selection. The first event passes the SR 400 selection while the second event passes both SR 400 and SR 600 selections.

Run number	214216	210302
Event number	121272046	2292645861
$m_{b\ell}^0$ [GeV]	558	686
ℓ_0 flavor	μ	μ
ℓ_0 charge	—	—
ℓ_0 p_T [GeV]	375	272
b_0 p_T [GeV]	330	460
ℓ_0 η	-0.11	1.22
b_0 η	0.56	0.95
ℓ_0 ϕ	2.0	-1.3
b_0 ϕ	-2.7	2.5
$m_{b\ell}^1$ [GeV]	526	528
ℓ_1 flavor	μ	μ
ℓ_1 charge	+	+
ℓ_1 p_T [GeV]	88	96
b_1 p_T [GeV]	542	374
ℓ_1 η	0.45	1.43
b_1 η	-1.1	-0.26
ℓ_1 ϕ	-2.3	-0.91
b_1 ϕ	-0.21	2.3
$m_{b\ell}$ asymmetry	0.03	0.13
H_T [GeV]	1335	1203
E_T^{miss} significance [GeV $^{1/2}$]	2.9	6.4
E_T^{miss} [GeV]	107	223
$m_{\ell\ell}$ [GeV]	324	71

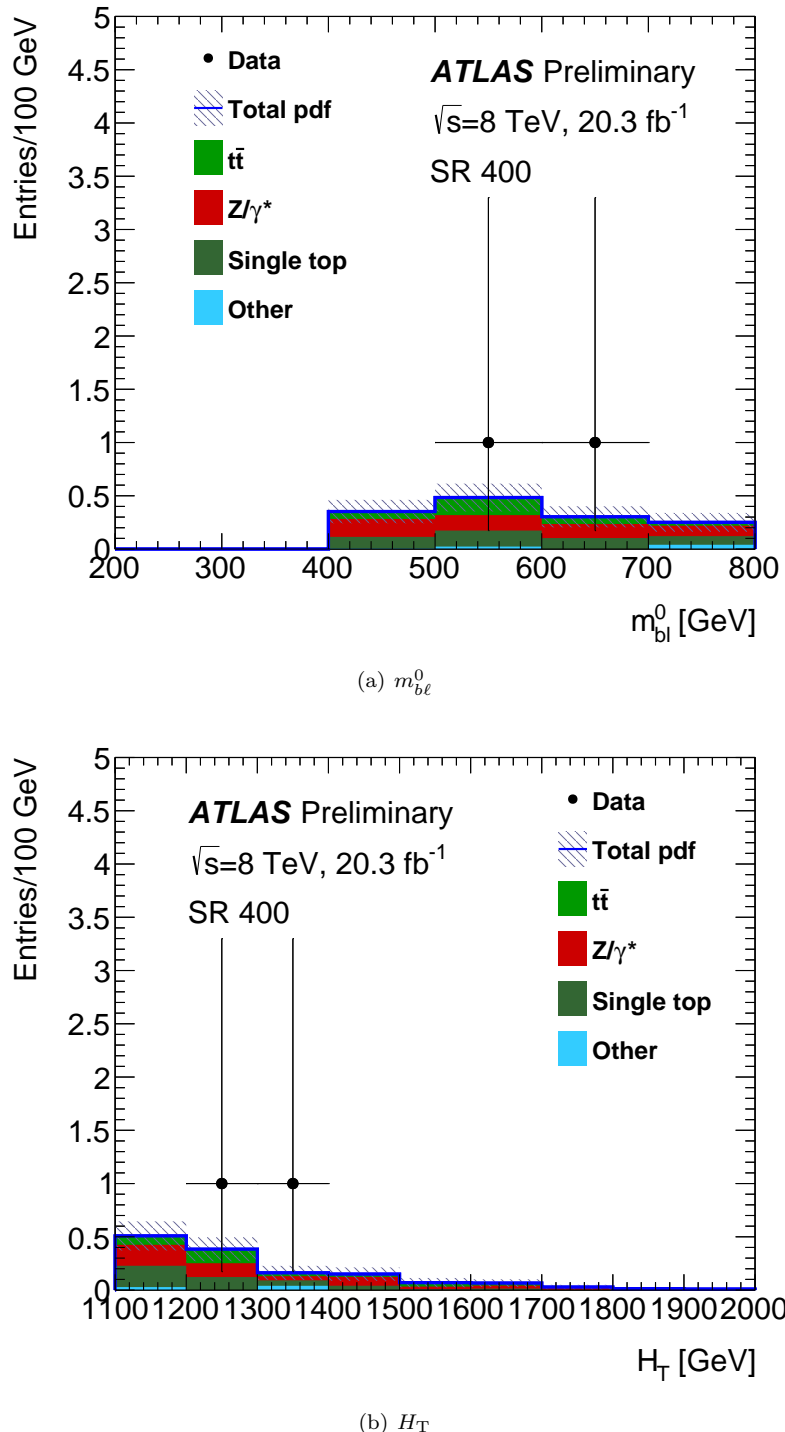
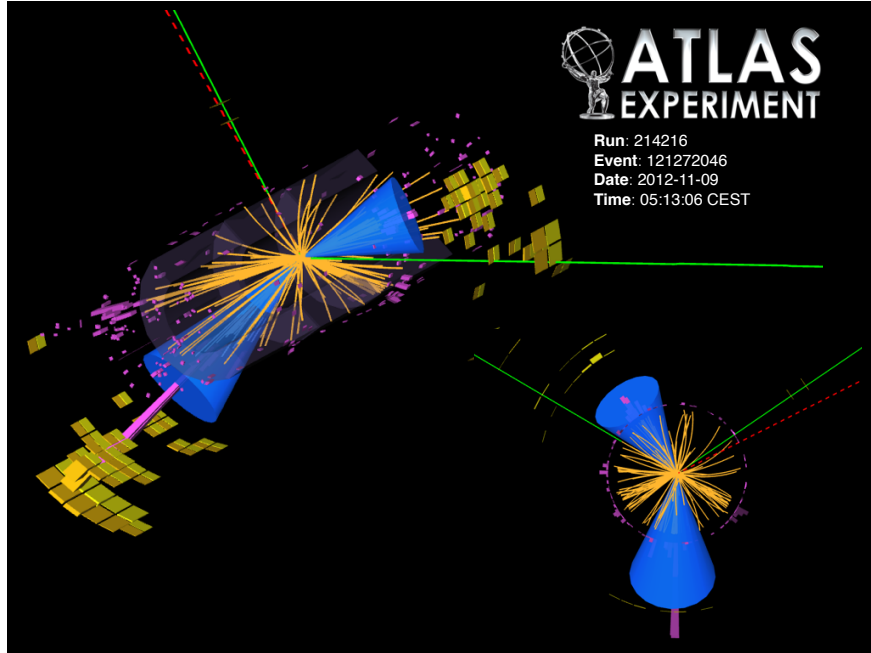
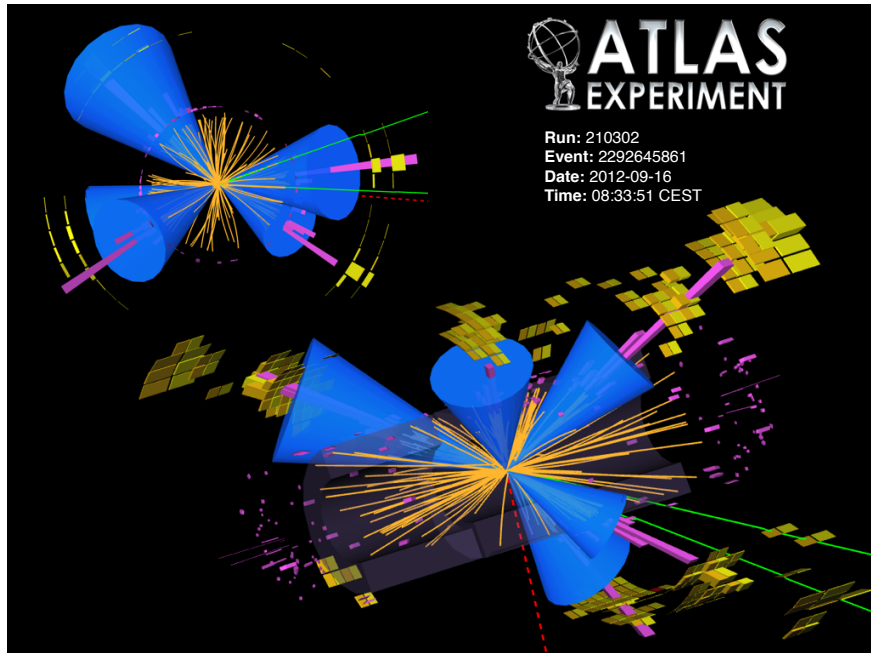


Figure 6.1: The $m_{b\ell}^0$ (top) and H_T (bottom) distributions in SR 400. The Standard Model background prediction is taken from the fitted background prediction. The hashed bands show the uncertainty in the fitted background prediction including the MC statistical and sources of systematic uncertainty.



(a) Run 214216, Event 121272046



(b) Run 210302, Event 2292645761

Figure 6.2: Event displays for the two observed events passing the signal region criteria. The top event passes the SR 400 selection with $m_{b\ell}^0 = 558$ GeV. The event shown on the bottom passes both the SR 400 and SR 600 selection with $m_{b\ell}^0 = 686$ GeV.

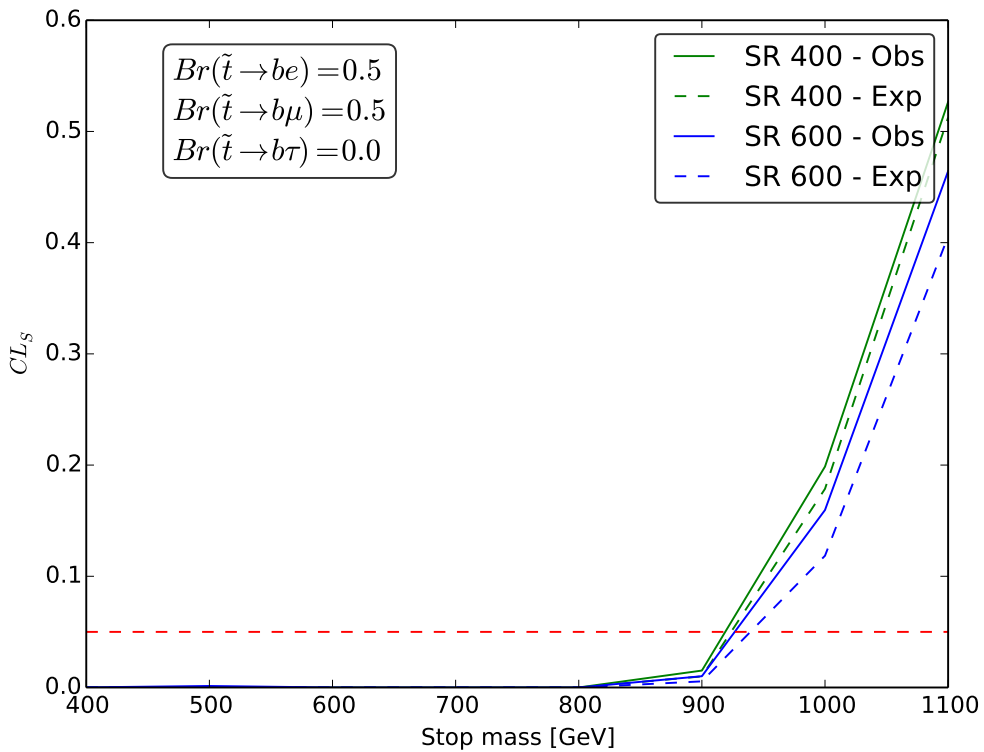


Figure 6.3: Expected and observed CL_S value as a function of stop mass for the scenario with $Br(\tilde{t} \rightarrow eb) = Br(\tilde{t} \rightarrow \mu b) = 0.5$. The last mass which has an observed $CL_S < 0.05$ is where the limit is to be set.

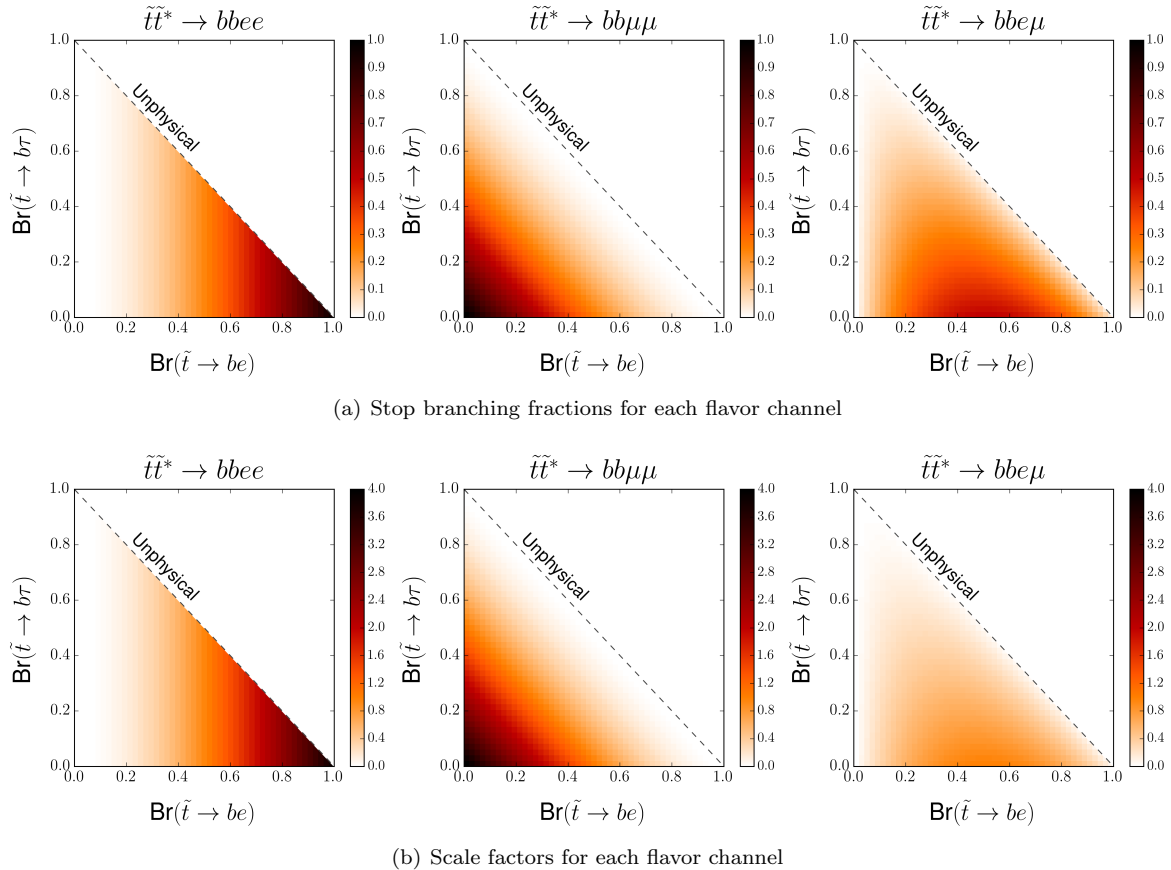


Figure 6.4: Stop pair branching fraction and corresponding scale factor to each di-lepton flavor channel depending on the branching fractions of a single stop. The di-stop branching fractions are given by Equation 6.1. The scale factor plot obtained by plotting Equation 6.2. In all six plots, a darker color corresponds to a higher value for the branching fraction or the scale factor.

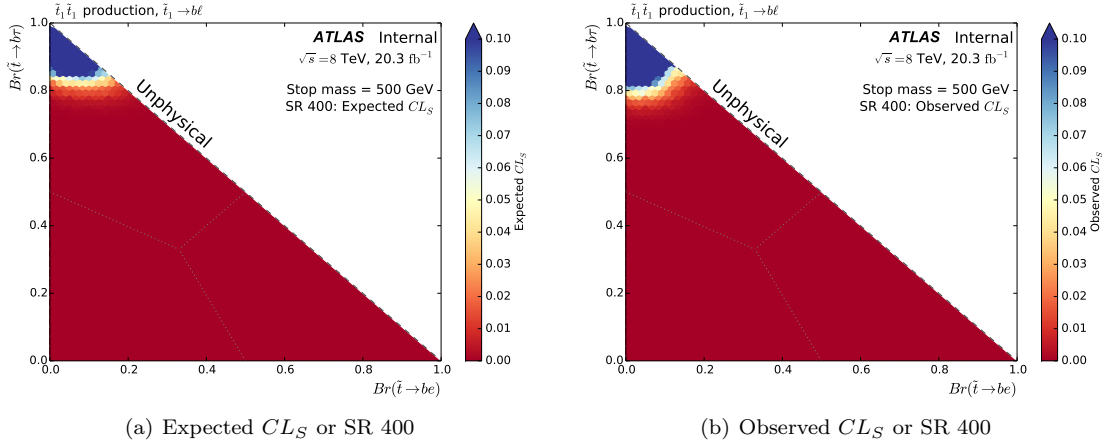


Figure 6.5: The expected and observed CL_S values in SR 400 for a stop mass of 500 GeV, shown across the plane of physical stop branching fractions.

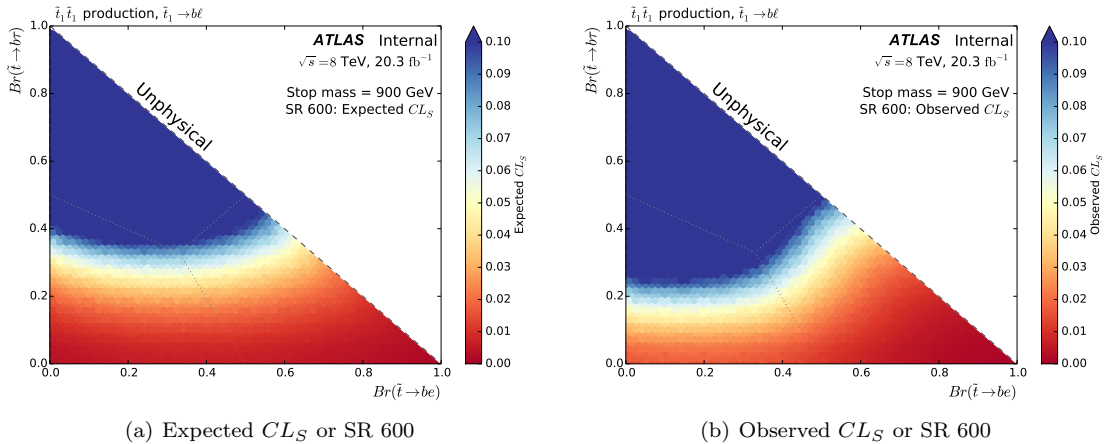


Figure 6.6: The expected and observed CL_S values in SR 600 for a stop mass of 900 GeV, shown across the plane of physical stop branching fractions.

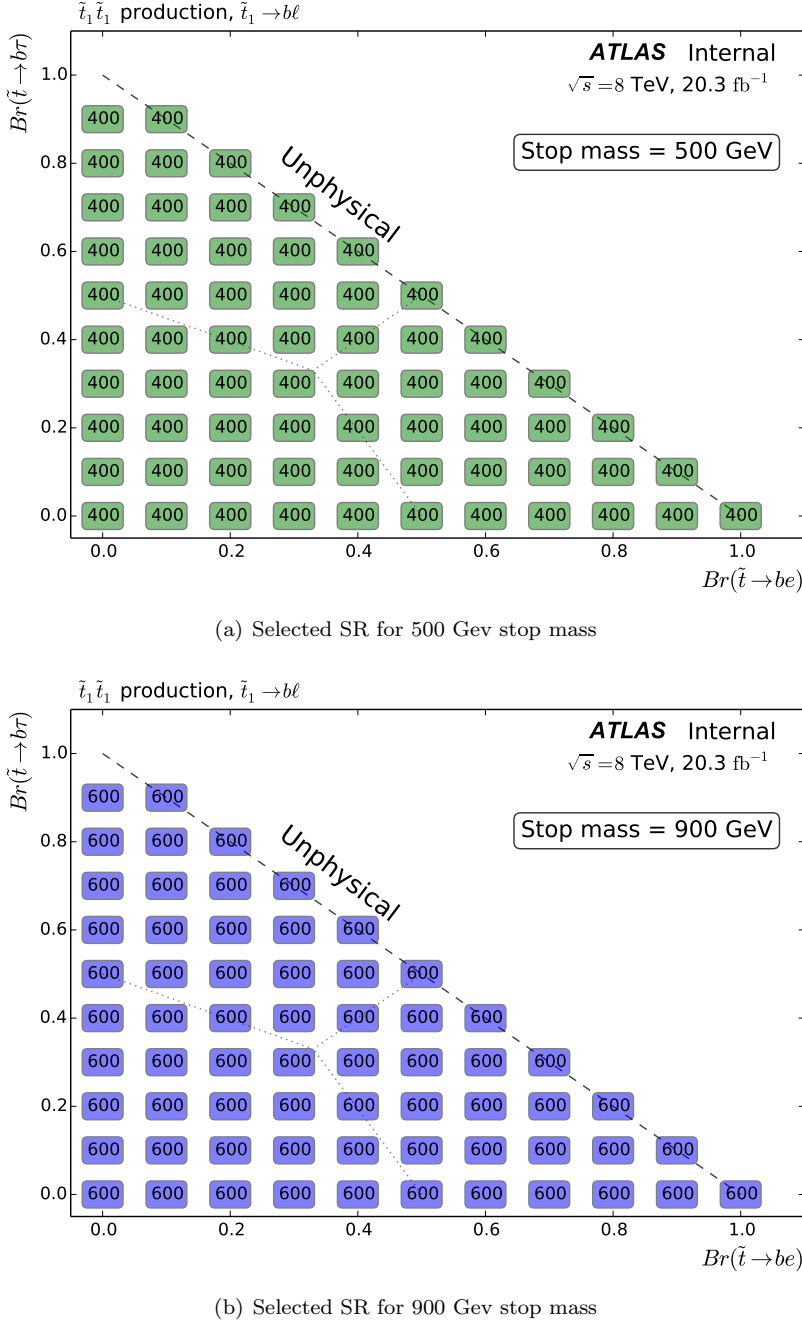


Figure 6.7: The selected SR for several stop branching fractions for a stop mass of 500 GeV(left) and 900 GeV(right). The SR is selected by choosing the SR with the smallest expected CL_S value for a given branching fraction.

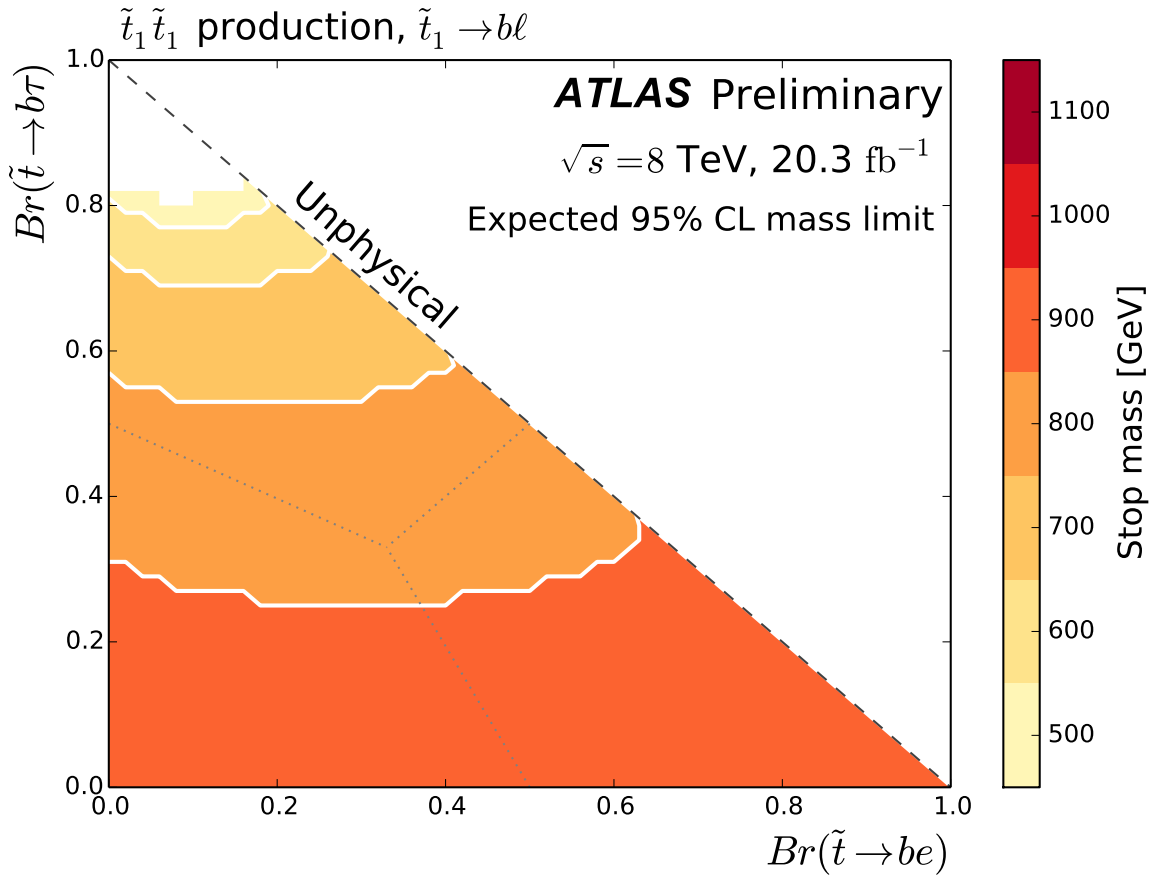


Figure 6.8: The **expected** mass limit on the stop at 95% CL. This limit is obtained using the nominal stop cross section. Stop masses between 400 GeV and 1100 GeV, in steps of 100 GeV, are tested. The mass limit shown corresponds to the highest-mass stop sample which is excluded.

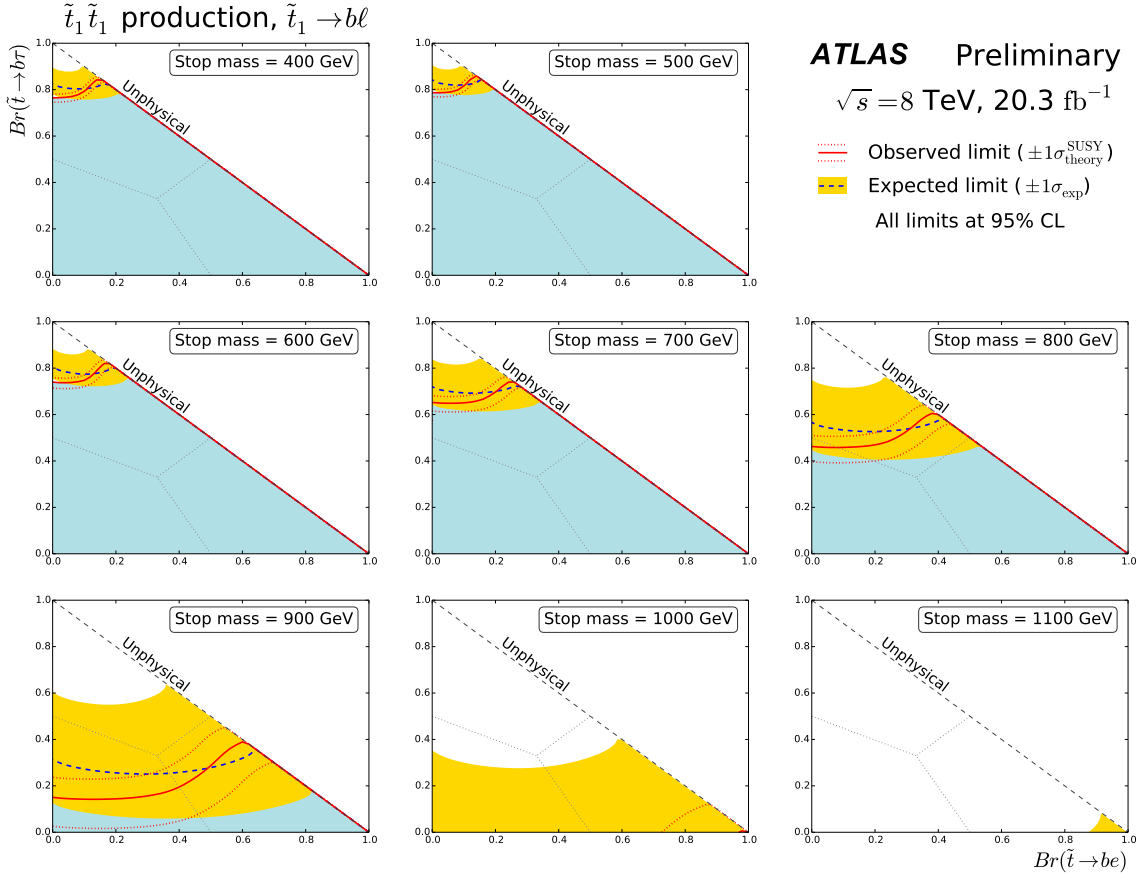


Figure 6.9: Expected and observed limit on the branching fractions for the stop decaying to different lepton flavors shown for different stop mass hypotheses between 400 GeV and 1.1 TeV. The shaded area under the solid line represents the branching fractions which are excluded at 95% CL for each stop mass. The dotted lines represent the uncertainty in the observed mass limit obtained by varying the signal model cross section up and down one standard deviation from the nominal value. The dashed line shows the expected 95% CL exclusion for each stop mass, and the shaded band shows the uncertainty in this expected exclusion limit from statistical uncertainty and the sources of systematic uncertainty discussed in Section 5.7.

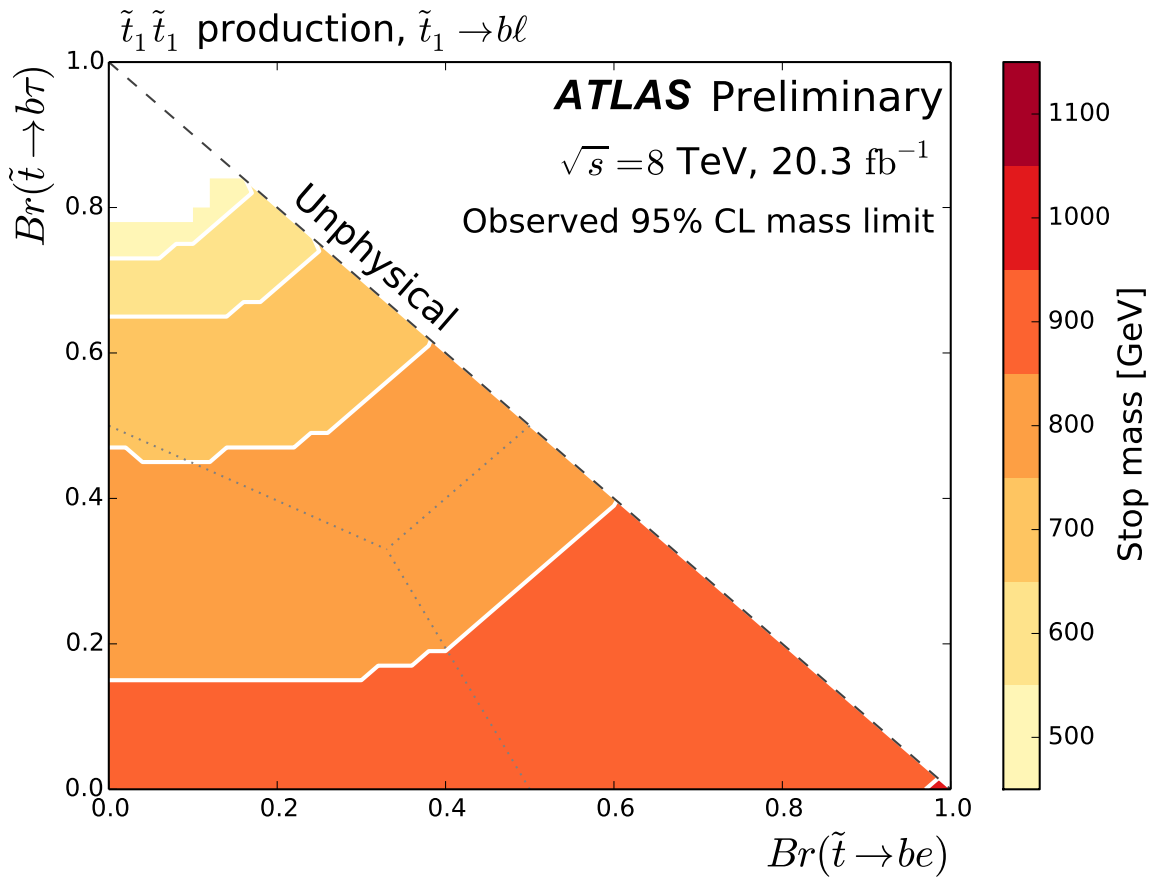


Figure 6.10: The **observed** mass limit on the stop at 95% CL. This limit is obtained using the nominal stop cross section. Stop masses between 400 GeV and 1100 GeV, in steps of 100 GeV, are tested. The mass limit shown corresponds to the highest-mass stop sample which is excluded.

CHAPTER 7

Conclusion

This thesis describes the search for direct scalar top production where the scalar tops decay via an R -parity-violating coupling to a final state with two leptons and two identified b -jets. The search uses 20.3 fb^{-1} of $\sqrt{s} = 8 \text{ TeV}$ proton-proton data collected with the ATLAS detector at the LHC. No significant excess of events over the Standard Model prediction is observed, and limits are set on the mass of the scalar top at 95% confidence level. A scan of possible stop branching fractions are tested, the mass limit ranges between 500 GeV, when the stop has a branching fraction to a b -quark and a tau lepton of 80%, to 1 TeV when the stop decays entirely to a b -quark and an electron.

With the upcoming Run-II of the Large Hadron Collider, the collisions will have a center-of-mass energy of 13 TeV, resulting in a huge gain in the expected cross section for scalar top pair production. This analysis, will benefit from the higher cross section, and will be able to test higher stop masses. Hopefully, the future LHC runs will find signs of new physics beyond the Standard Model!

APPENDIX A

Statistical interpretation technique

Statistical interpretation is a critical part of any Physics analysis. It is used in many aspects of an analysis, including background fits, and to translate the observation into a result, either a discovery or an exclusion.

The analysis presented in this thesis uses a maximum likelihood fit to the data to obtain a background fit. The particular likelihood function uses for this analysis is described in Section A.1. Ultimately, the CL_S method is used to set exclusion limits on the stop mass and branching fraction. The CL_S method uses a modified frequentest technique, and is described in Section A.2.

A.1 Likelihood function

This analysis uses a maximum likelihood fit to determine the normalization factors of the major backgrounds, and to constrain the systematic uncertainties based on the observations in the signal and control regions.

The maximum likelihood treats the systematic uncertainties as “nuisance parameters,” which are profiled using a Gaussian distribution. This means the size of a particular uncertainty can be further constrained (or made larger) compared to the nominal value based on the compatibility of the data with the prediction. The Gaussian distribution applies a penalty in the likelihood function for varying the nuisance parameters to ensure they cannot float freely.

The most general form of the maximum likelihood function used in this analysis incorporates several signal and control regions, referred to as “channels,” where each channel may have several

bins. A template form of the maximum likelihood function can be written as

$$\mathcal{L}(\mathbf{n}, \boldsymbol{\vartheta} | \mu_{\text{sig}}, \boldsymbol{\mu}_{\text{bkg}}, \boldsymbol{\vartheta}) = \prod_{\substack{c \in \text{channels} \\ b \in \text{bins}}} \underbrace{P(n_{cb} | \nu_{cb}(\boldsymbol{\mu}_{\text{sig}}, \boldsymbol{\mu}_{\text{bkg}}, \boldsymbol{\vartheta}))}_{\text{Poisson for each bin in each channel}} \cdot \prod_{p \in \text{parameters}} \underbrace{G(\vartheta_p | \theta_p)}_{\text{Gaussian constraints}}, \quad (\text{A.1})$$

where the parameters can be interpreted as

n_{cb}: The number of **observed** events in channel c and bin b .

ν_{cb}: The **expected** number of events in channel c and bin b . These quantities depend on the other parameters that enter the likelihood.

θ_p: The **best fit** value for the nuisance parameter p . These quantities are varied to achieve a maximum likelihood, but there is a penalty associated with these variations.

θ_p: The **nominal value** for the nuisance parameter p .

μ_{sig}: Normalization factor of the signal sample. This quantity is allowed to vary without penalty.

μ_{bkg}: Vector of the normalization factors of the background samples. There is one normalization factor for each background process whose normalization is allowed to vary. The components of **μ_{bkg}** are allowed to vary independent of one another, and as with **μ_{sig}**, there is no penalty for these variations

The first term in Equation A.1 is a product of Poisson functions, where the product is taken over each of the channels (c) considered and the bins (b) within each channel. The analysis described in this thesis does not use binned signal and control regions. The product is only taken over the channels in this situation. The second term is a product of Gaussian functions, taken over each of the systematic uncertainties, taken as nuisance parameters.

In order to find the normalization factors (μ_{sig} and $\boldsymbol{\mu}_{\text{bkg}}$) and nuisance parameters ($\boldsymbol{\vartheta}$) which maximize the likelihood function, $-\log \mathcal{L}$ is minimized. The log-likelihood function is easier to work with numerically because the raw likelihood spans many orders of magnitude, so the gradient is very steep. The negative of the log-likelihood is a convention often used, but not meaningful.

A.2 The CL_s method

The search results presented in this thesis are interpreted using the CL_S technique. CL_S is a method for determining limits developed at LEP, but is commonly used in analyses on ATLAS. It is, at its core, a frequentist technique, but it does adopt some Bayesian properties [122, 123].

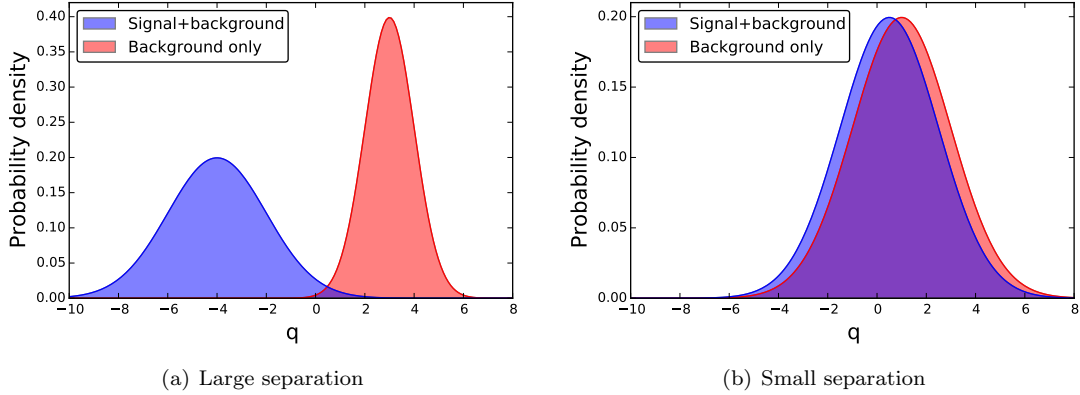


Figure A.1: Examples of probability distribution functions for signal+background and background-only hypotheses.

When making a discovery, a p -value test is commonly used to evaluate the confidence level of the result. The background-only model is declared the “null hypothesis,” and the “alternate hypothesis” is defined as the scenario where the data contain both signal and background events. The observation is compared with the prediction from the background-only hypothesis, and if the data is incompatible (p -value less than some threshold, α), the null hypothesis is rejected, and the alternate hypothesis is accepted with a confidence level of $(1 - \alpha)$.

While the p -value test is useful for evaluating a discovery, but if the data is found to be compatible with the prediction, limits can be set, where signal models are rejected if they are expected to be observed in the available data. One method that was commonly used in particle physics is the CL_{S+B} technique. This technique defines a test statistic

$$q(\mu) = -2 \ln \frac{\mathcal{L}(\mu, \boldsymbol{\theta})}{\mathcal{L}_{\max}}, \quad (\text{A.2})$$

where \mathcal{L} is a likelihood ratio, μ is the signal strength being tested, and $\boldsymbol{\theta}$ are the values of the nuisance parameters which maximize the likelihood ratio. The test statistic is calculated for the observation in the analysis regions, and the quantity CL_{S+B} is defined in such a way to give the probability of a measurement at least as extreme as the observed test statistic. If the observed test statistic is greater than the mean of the expected signal+background probability distribution function, CL_{S+B} is defined as

$$CL_{S+B} = \int_{q_{\text{obs}}}^{\infty} P(q(\mu)) dq. \quad (\text{A.3})$$

CL_{S+B} is treated similar to a p -value for the signal+background model with signal strength equal to μ . That is, if $CL_{S+B} < \alpha$ (where α is often set to 0.05), the signal model with signal strength, μ , is rejected with a $(1 - \alpha)$ confidence level.

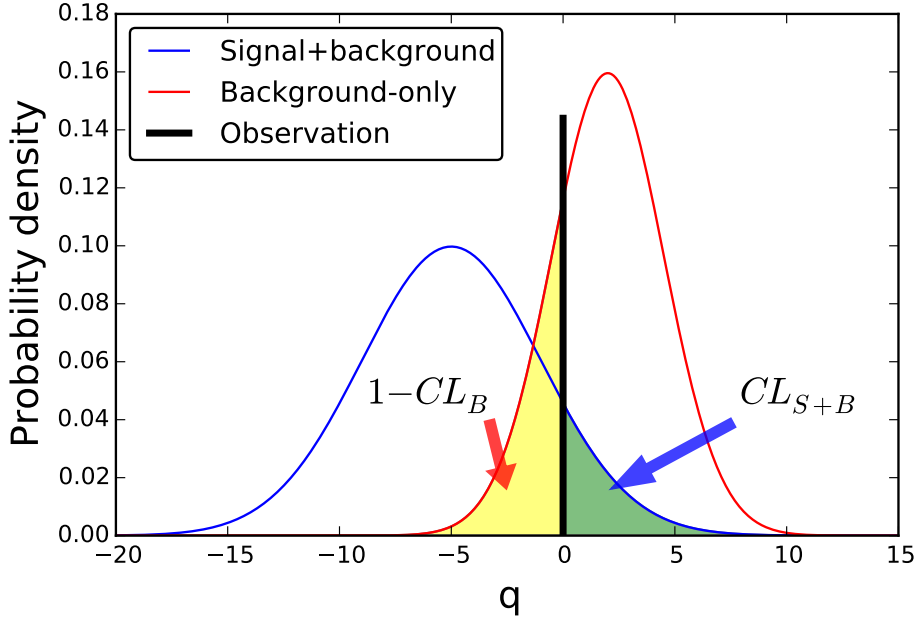


Figure A.2: Examples probability distribution functions used to calculate the CL_S quantity. The area shaded in red and blue are equal to CL_B and CL_{S+B} respectively, and CL_S is given by taking the ratio of the two.

The CL_{S+B} technique works well in scenarios where the test has good statistical significance, as shown in Figure A.1(a). If, however, the background-only and the signal+background hypotheses are not well separated, as shown in Figure A.1(b), the CL_{S+B} technique can (and does) reject signal models in favor of the background-only hypothesis, when the data is incompatible with both!

The CL_S technique provides protection from this sort of error by including the agreement with the background-only hypothesis. The compatibility of the observation with the background-only hypothesis is

$$CL_B = \int_{q_{\text{obs}}}^{-\infty} P(q(\mu = 0)) dq, \quad (\text{A.4})$$

assuming q_{obs} less than the mean of the expected background-only probability distribution function.

The CL_{S+B} and CL_B quantities are used to construct CL_S , which is defined as

$$CL_S = \frac{CL_{S+B}}{CL_B}, \quad (\text{A.5})$$

An example of the application of the CL_S method is shown in Figure A.2. The two curves represent the expected probability distributions for the signal+background hypothesis (blue) and the background-only hypotheses (red), and the black line is placed at the value of q corresponding to the observation.

The shaded areas are equal to the CL_{S+B} (green) and $1 - CL_B$ (yellow), thus CL_S is equal to the ratio of these areas.

The CL_S value is penalized if the data is incompatible with both the signal+background and background-only hypotheses or if the two hypotheses are indistinguishable. This is particularly important when the number of expected and observed events is low, leading to large statistical uncertainties. In these cases, a downward fluctuation of only a few events may result in a signal model being excluded by the CL_{S+B} , but the CL_S method tends to be more conservative in this respect.

APPENDIX B

Signal model interpretation

This appendix includes plots of the expected and observed CL_S values in each of the two SRs. The CL_S values are computed for each of the tested stop masses from 400 GeV to 1100 GeV, and over the range of physical stop branching ratios. In addition to the CL_S values, the selected SR for a selection of stop branching ratios is shown for each stop mass. The SR is selected by choosing the SR which gives the lowest expected CL_S value for the particular choice of stop mass and branching ratios as described in Section 6.2

B.1 400 GeV stop mass

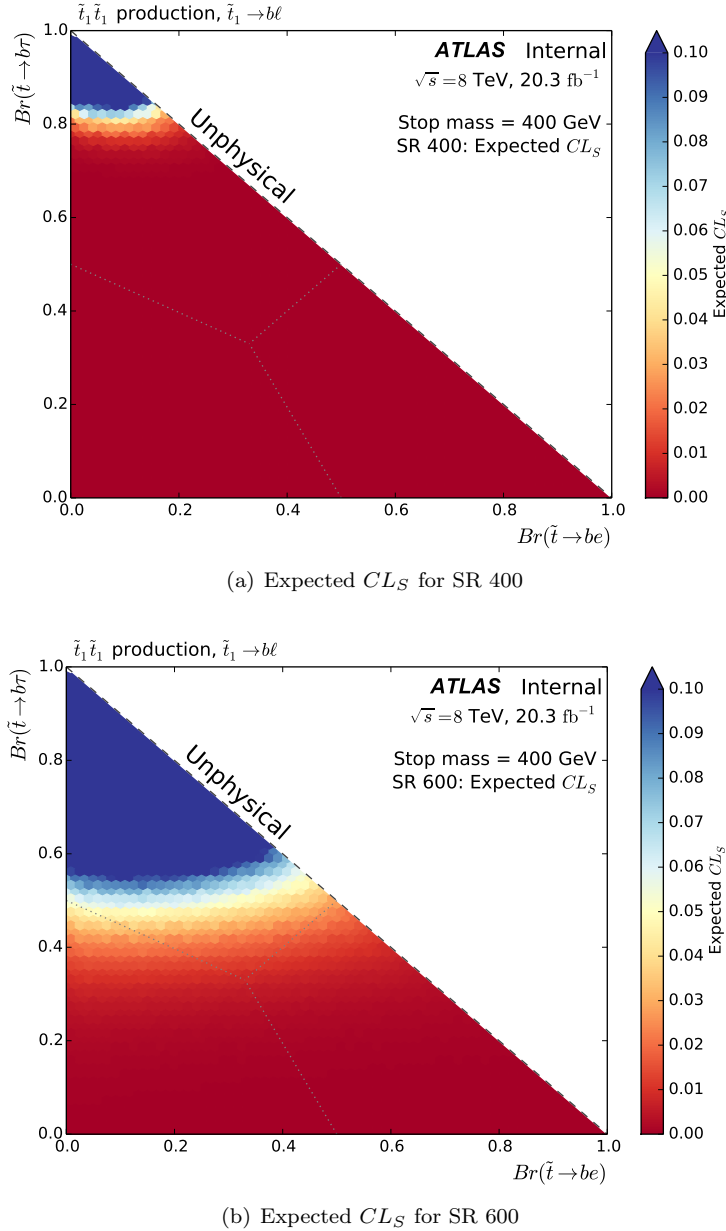


Figure B.1: Expected CL_S values for SR 400 (top) and SR 600 (bottom) for a stop mass of 400 GeV, shown across the plane of physical stop branching ratios.

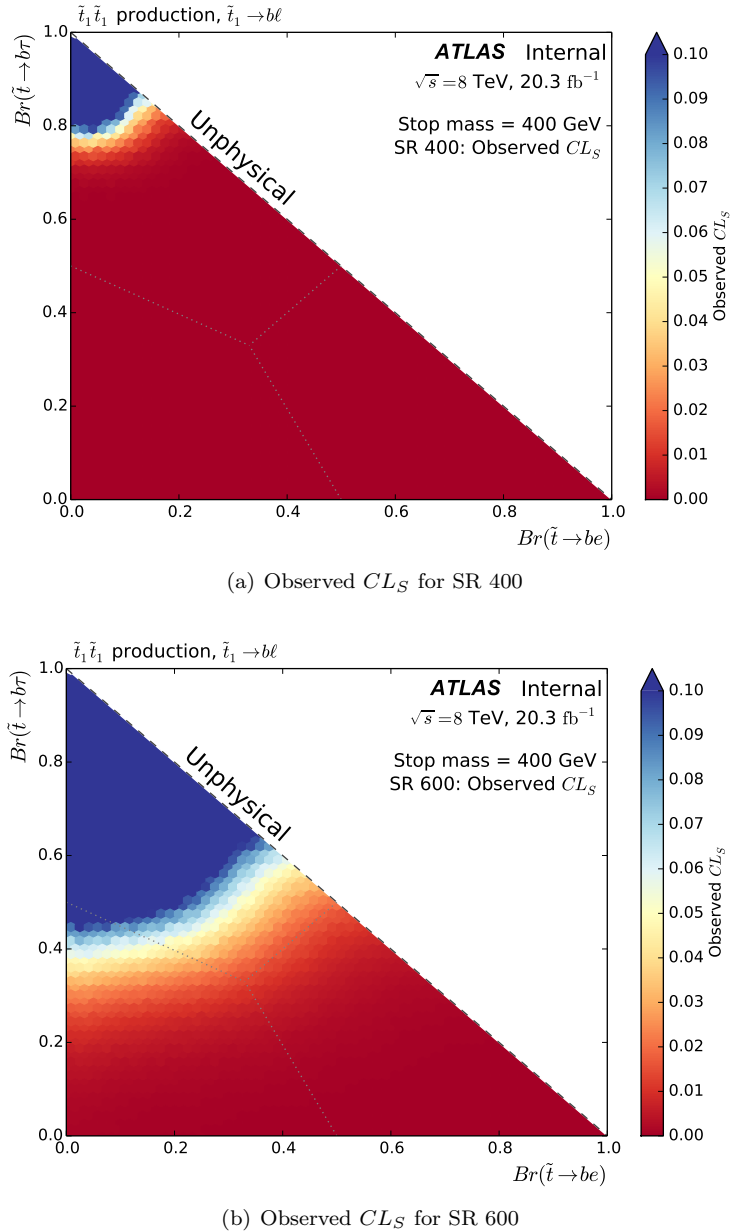


Figure B.2: Observed CL_S values for SR 400 (top) and SR 600 (bottom) for a stop mass of 400 GeV, shown across the plane of physical stop branching ratios.

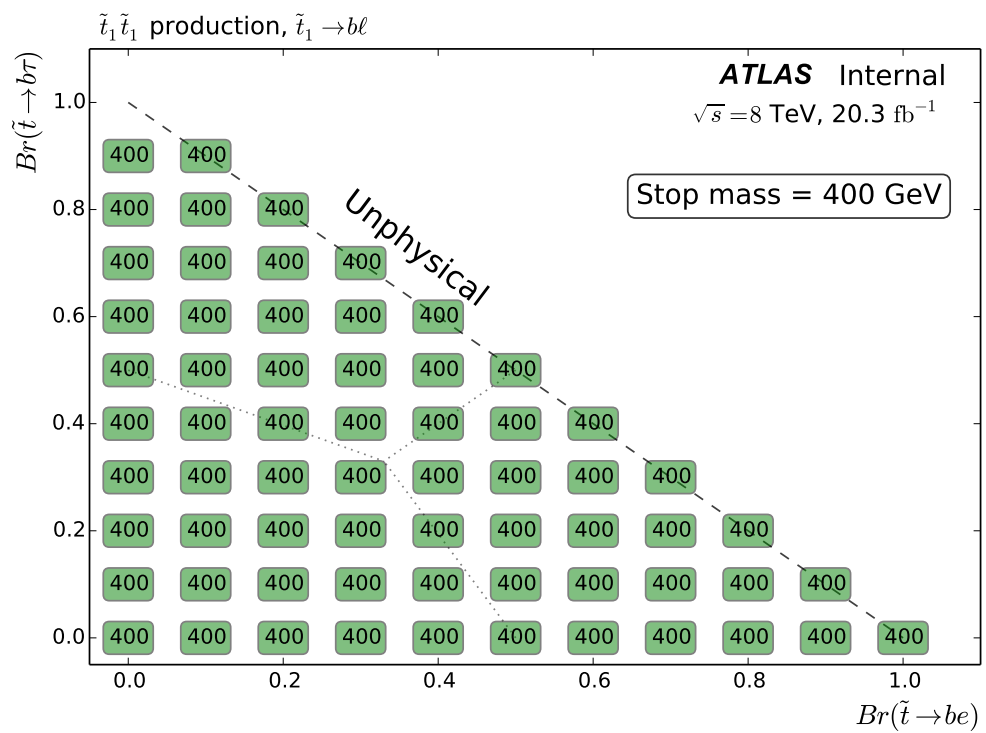


Figure B.3: SR selection for a stop mass of 400 GeV.

B.2 500 GeV stop mass

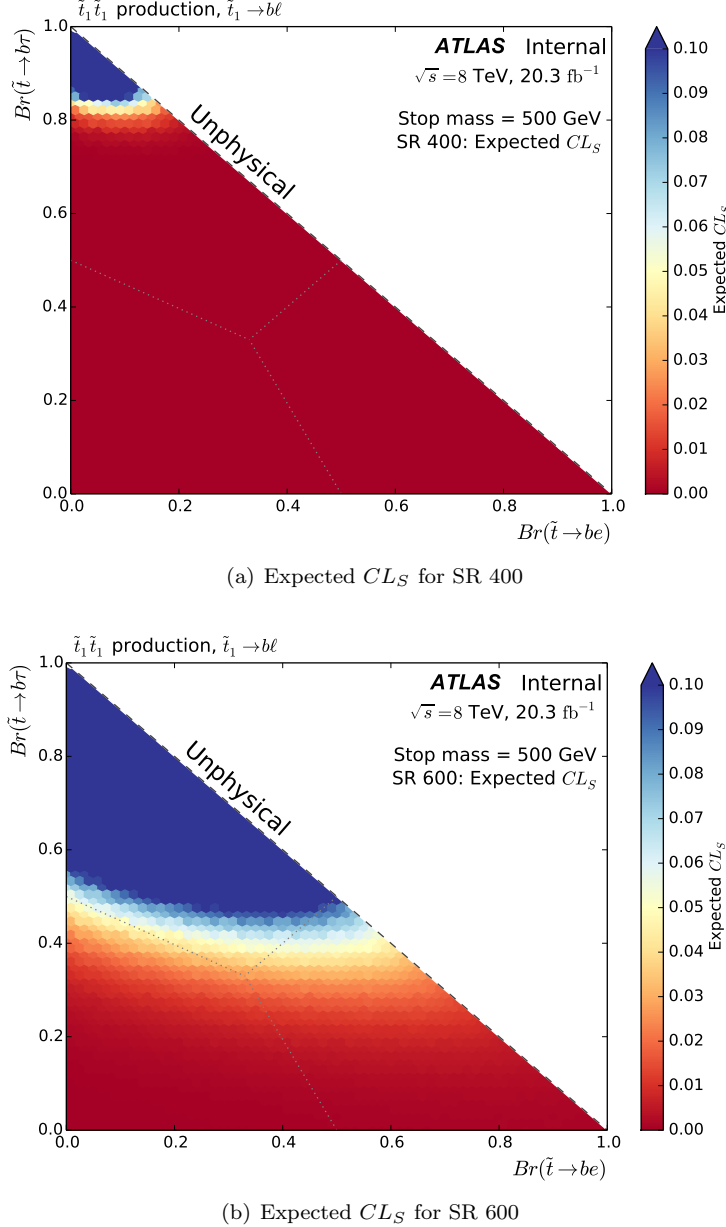


Figure B.4: Expected CL_S values for SR 400 (top) and SR 600 (bottom) for a stop mass of 500 GeV, shown across the plane of physical stop branching ratios.

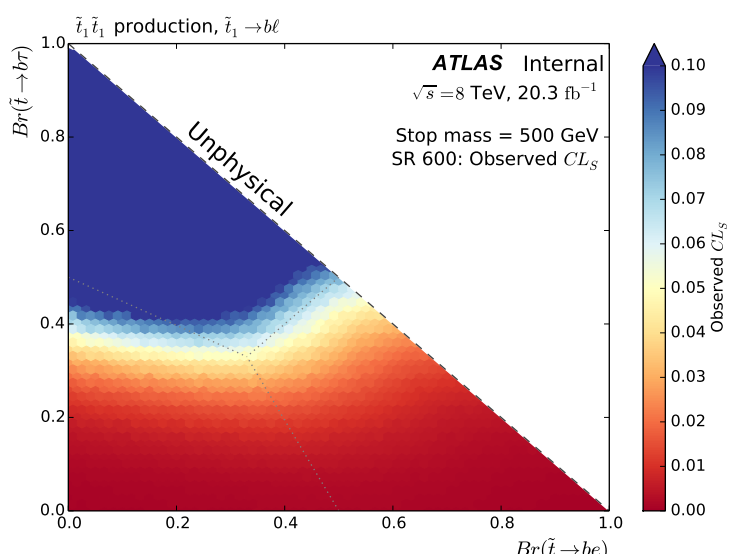
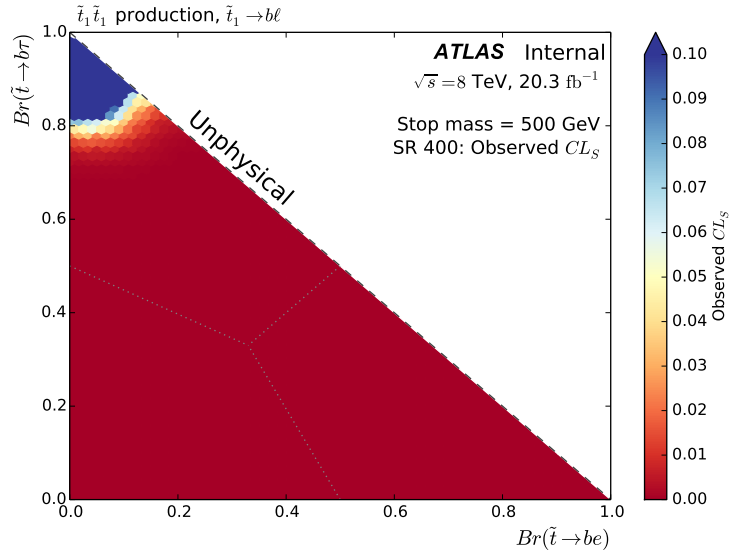


Figure B.5: Observed CL_S values for SR 400 (top) and SR 600 (bottom) for a stop mass of 500 GeV, shown across the plane of physical stop branching ratios.

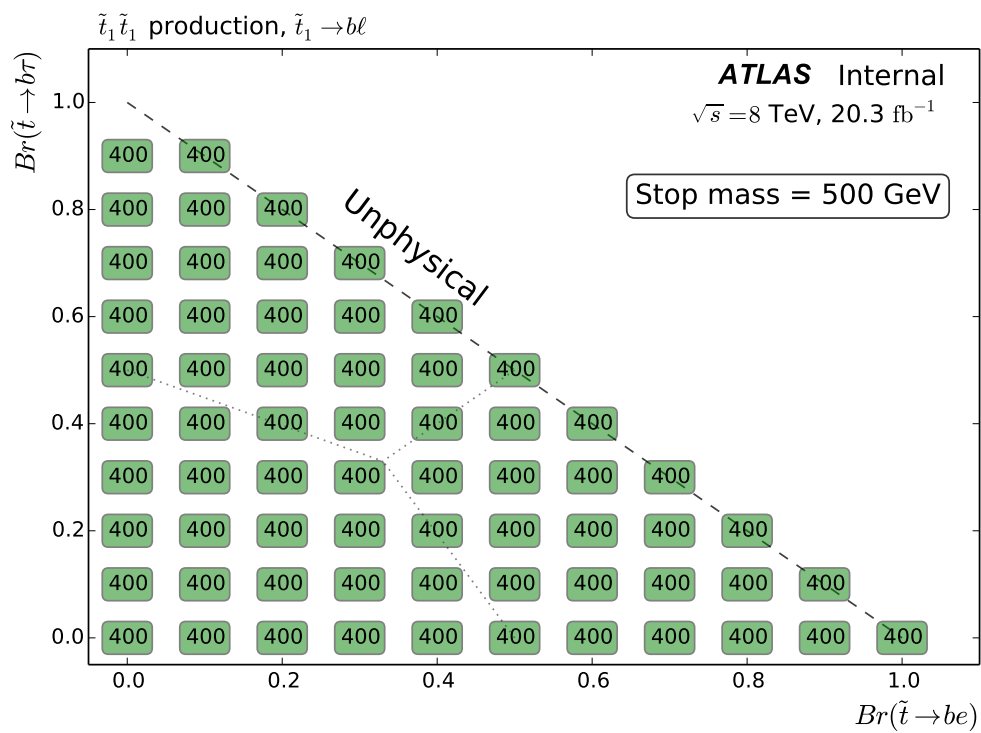


Figure B.6: SR selection for a stop mass of 500 GeV.

B.3 600 GeV stop mass

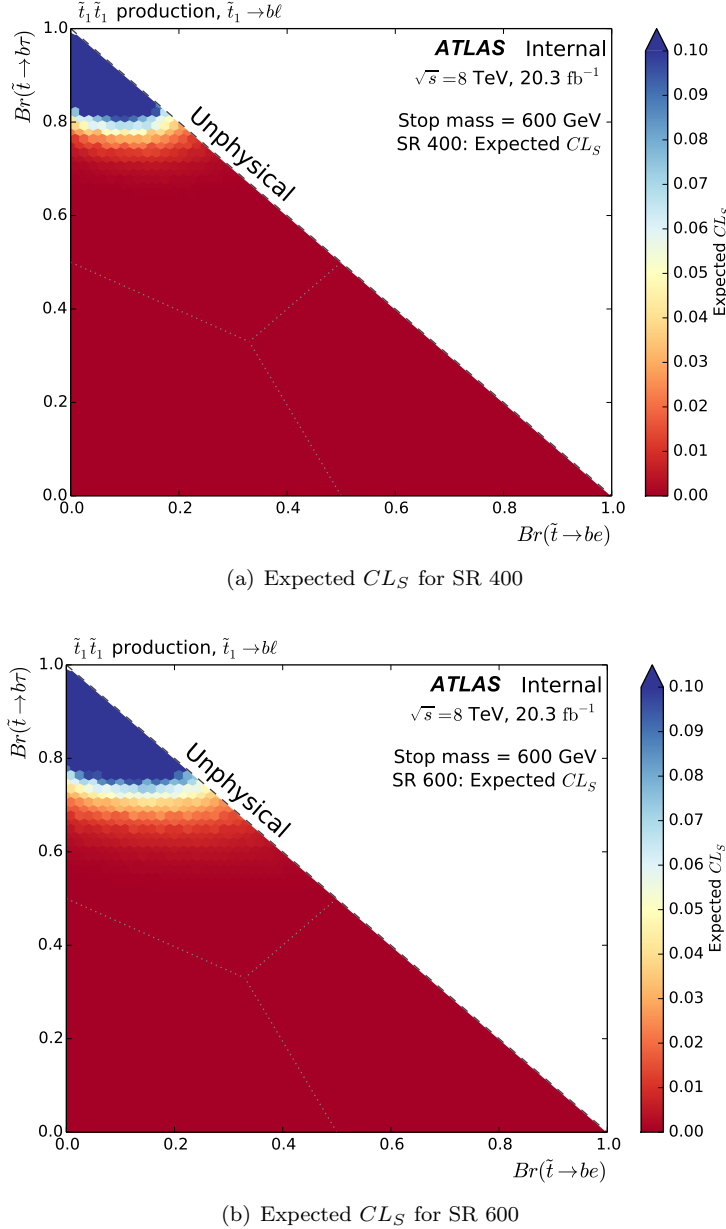


Figure B.7: Expected CL_S values for SR 400 (top) and SR 600 (bottom) for a stop mass of 600 GeV, shown across the plane of physical stop branching ratios.

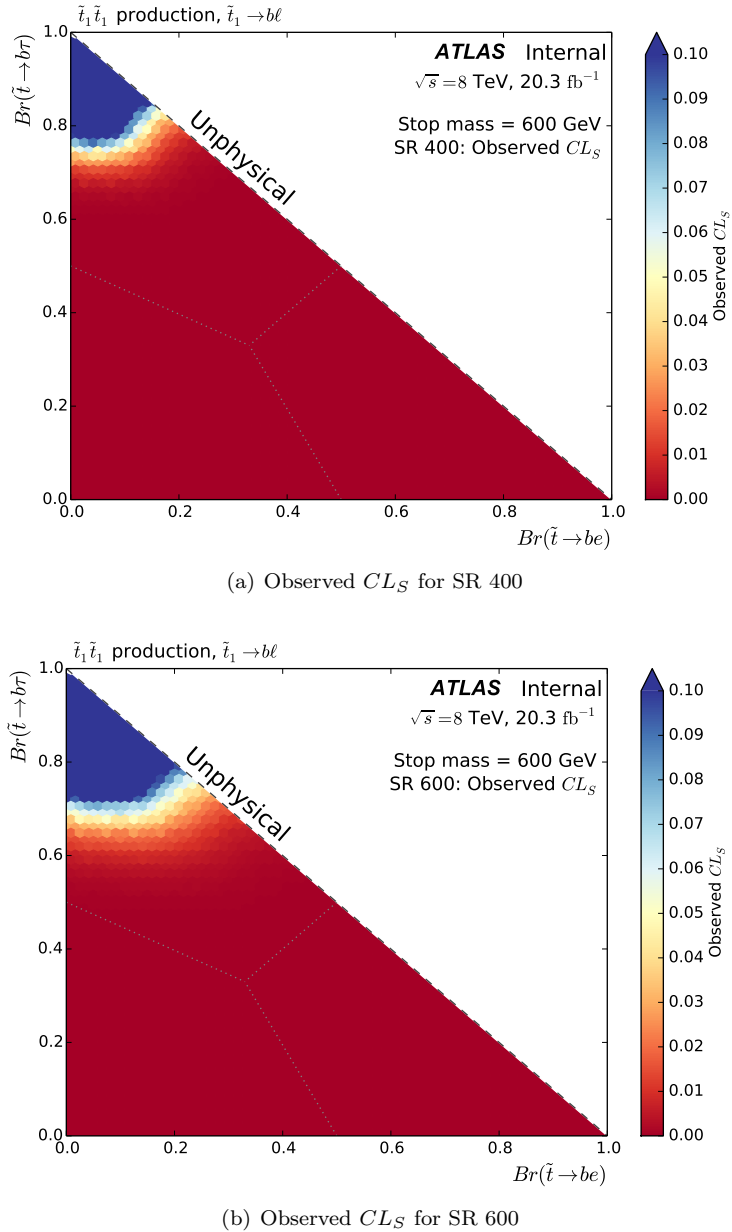


Figure B.8: Observed CL_S values for SR 400 (top) and SR 600 (bottom) for a stop mass of 600 GeV, shown across the plane of physical stop branching ratios.

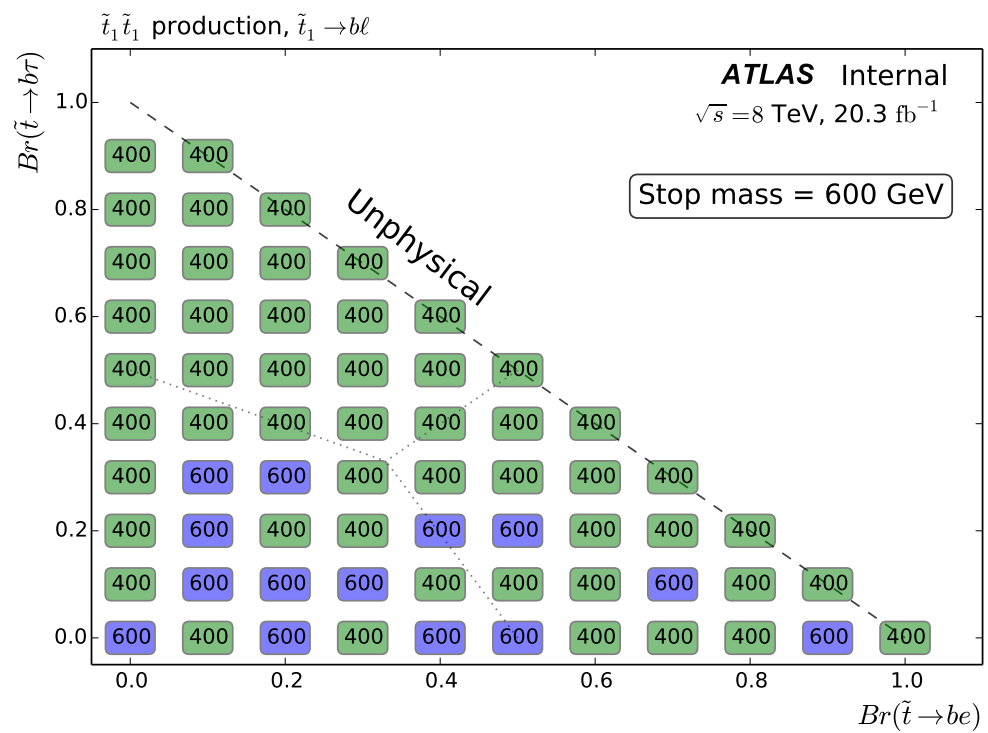


Figure B.9: SR selection for a stop mass of 600 GeV.

B.4 700 GeV stop mass

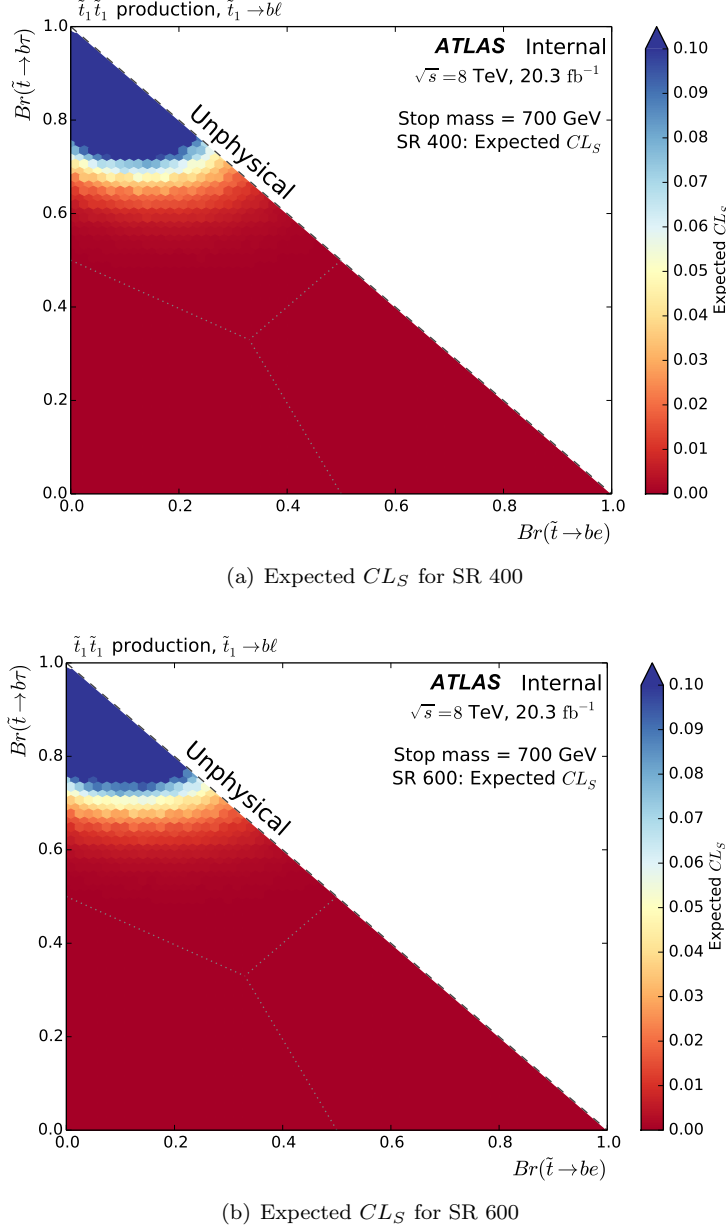
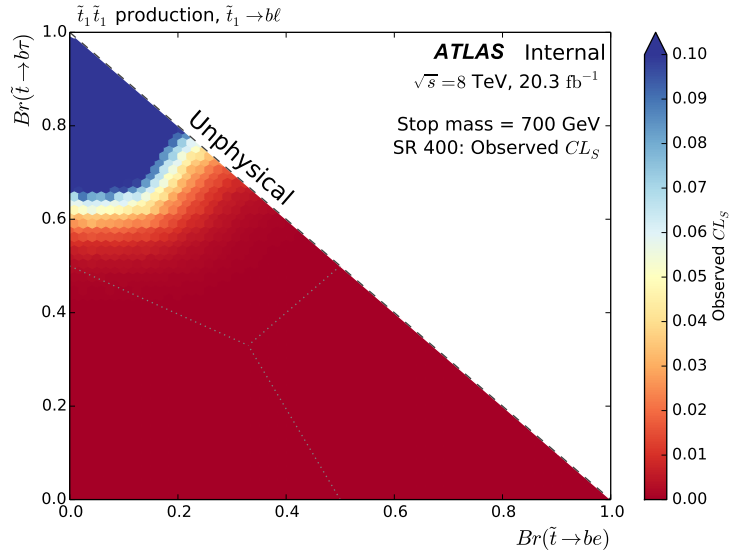
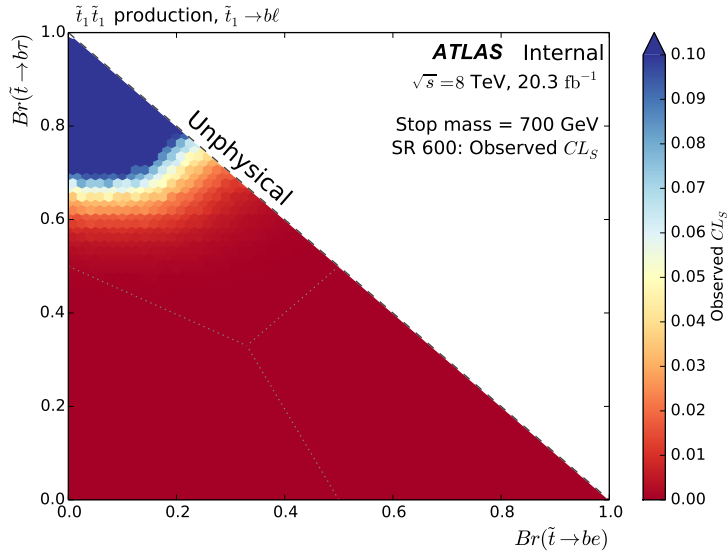


Figure B.10: Expected CL_S values for SR 400 (top) and SR 600 (bottom) for a stop mass of 700 GeV, shown across the plane of physical stop branching ratios.



(a) Observed CL_S for SR 400



(b) Observed CL_S for SR 600

Figure B.11: Observed CL_S values for SR 400 (top) and SR 600 (bottom) for a stop mass of 700 GeV, shown across the plane of physical stop branching ratios.

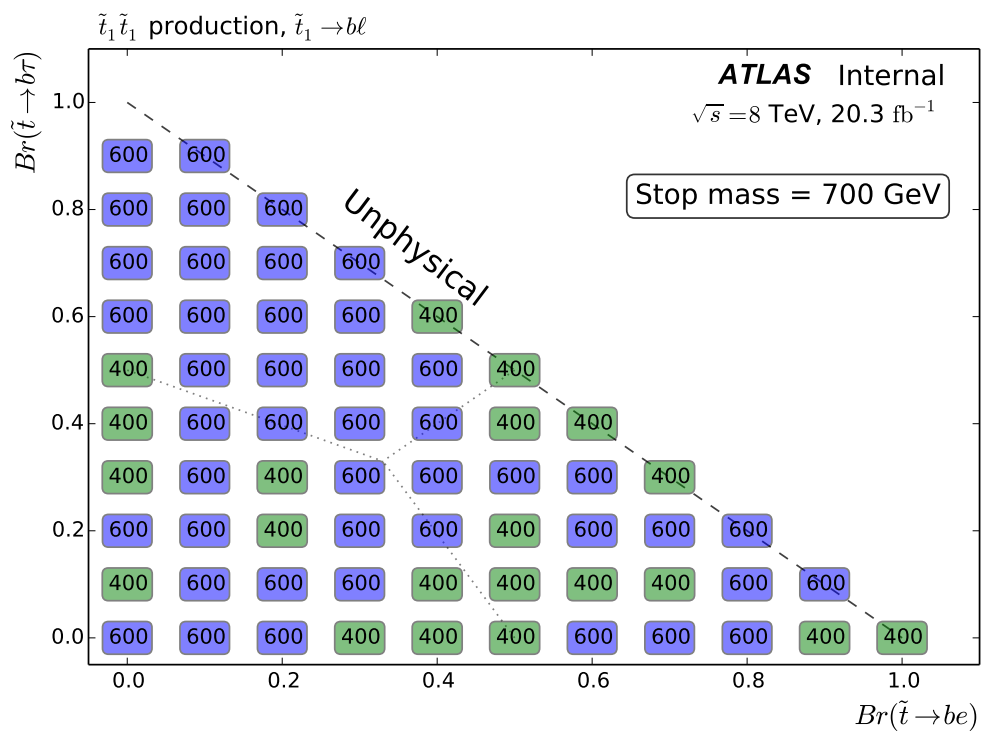


Figure B.12: SR selection for a stop mass of 700 GeV.

B.5 800 GeV stop mass

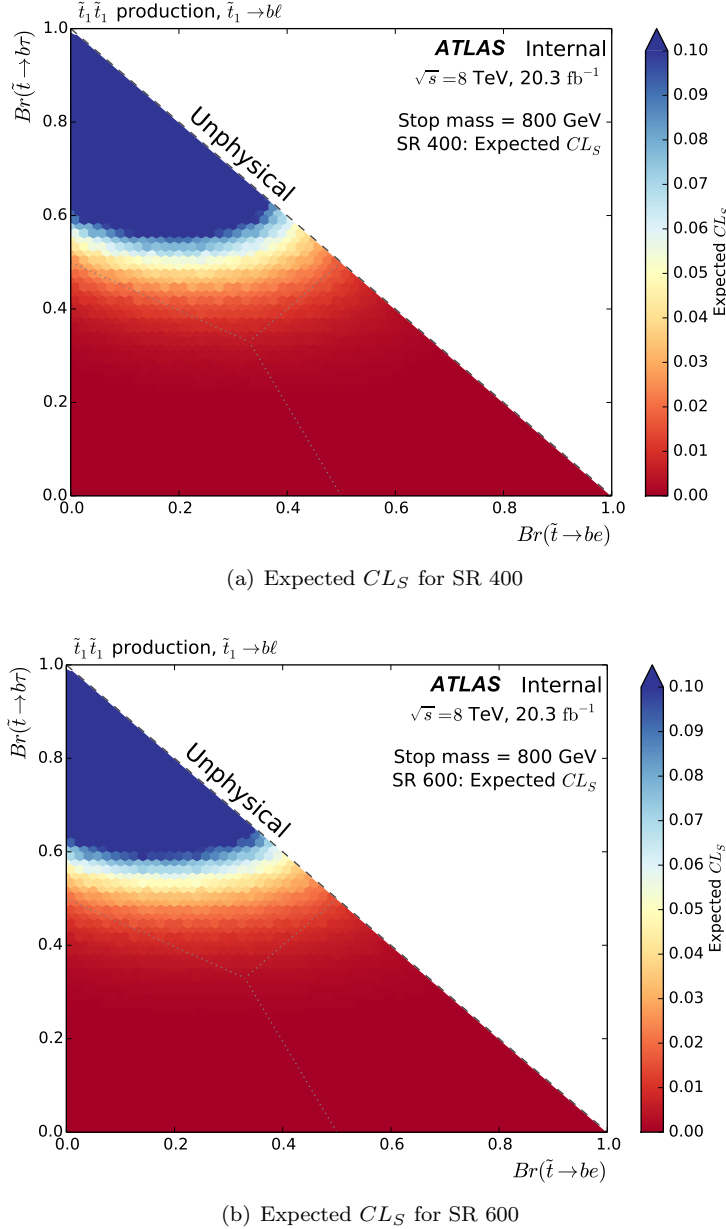


Figure B.13: Expected CL_S values for SR 400 (top) and SR 600 (bottom) for a stop mass of 800 GeV, shown across the plane of physical stop branching ratios.

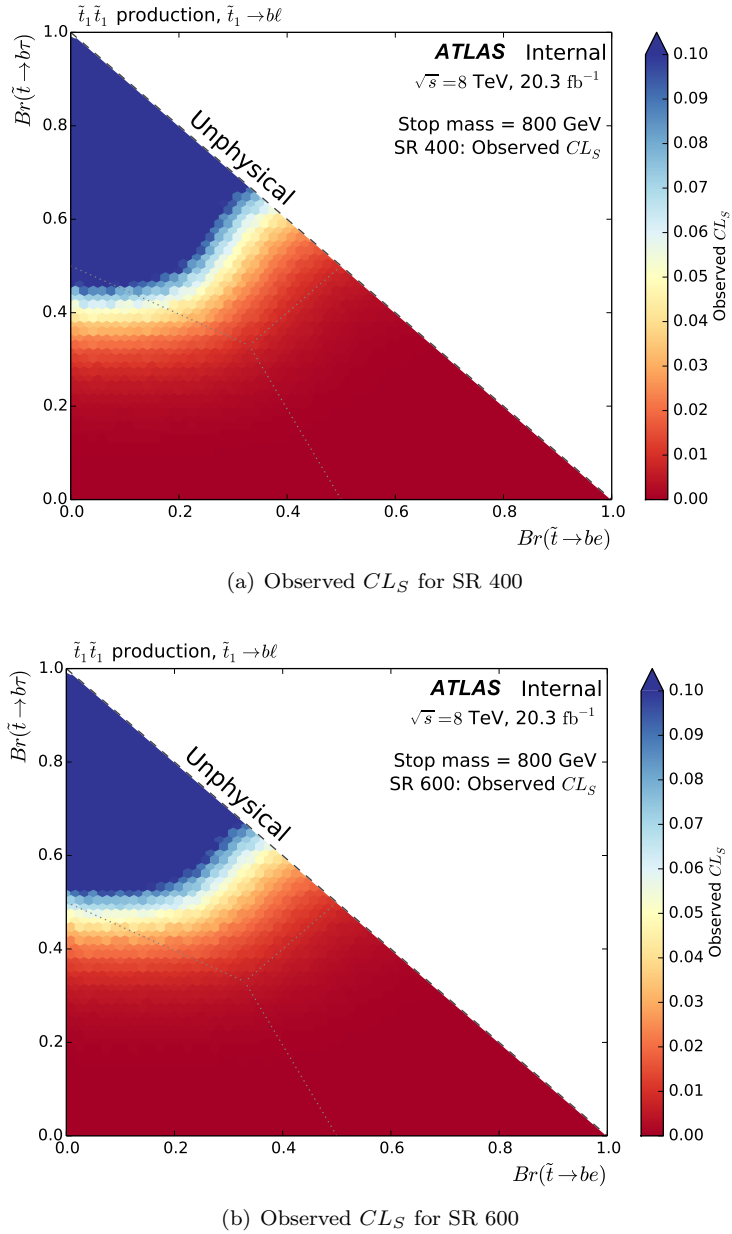


Figure B.14: Observed CL_S values for SR 400 (top) and SR 600 (bottom) for a stop mass of 800 GeV, shown across the plane of physical stop branching ratios.

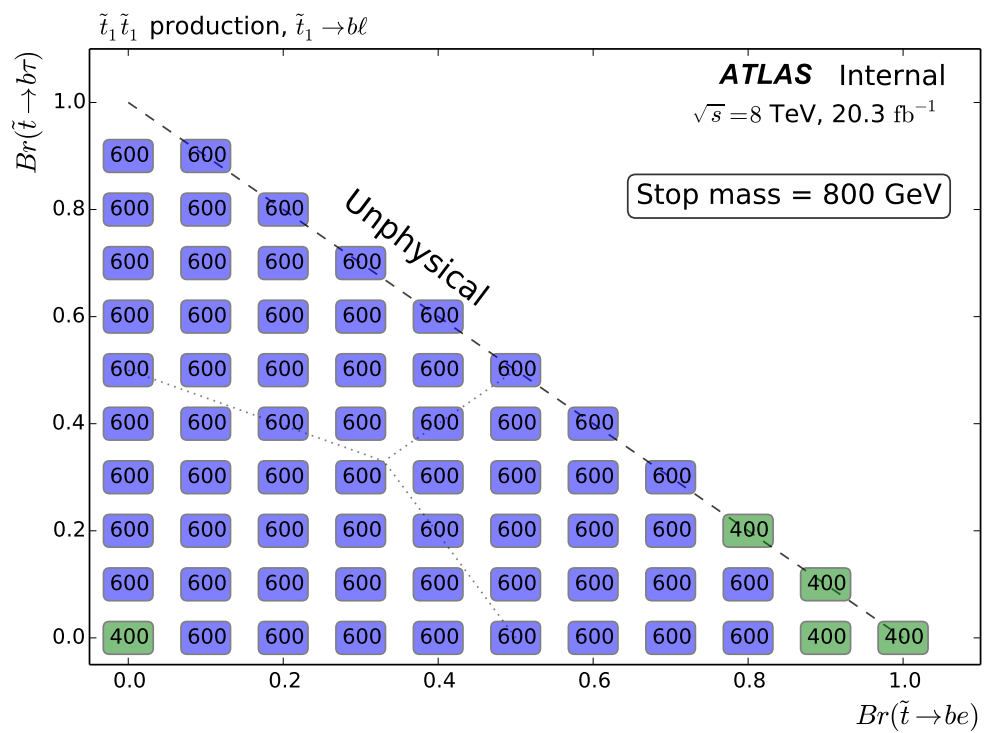


Figure B.15: SR selection for a stop mass of 800 GeV.

B.6 900 GeV stop mass

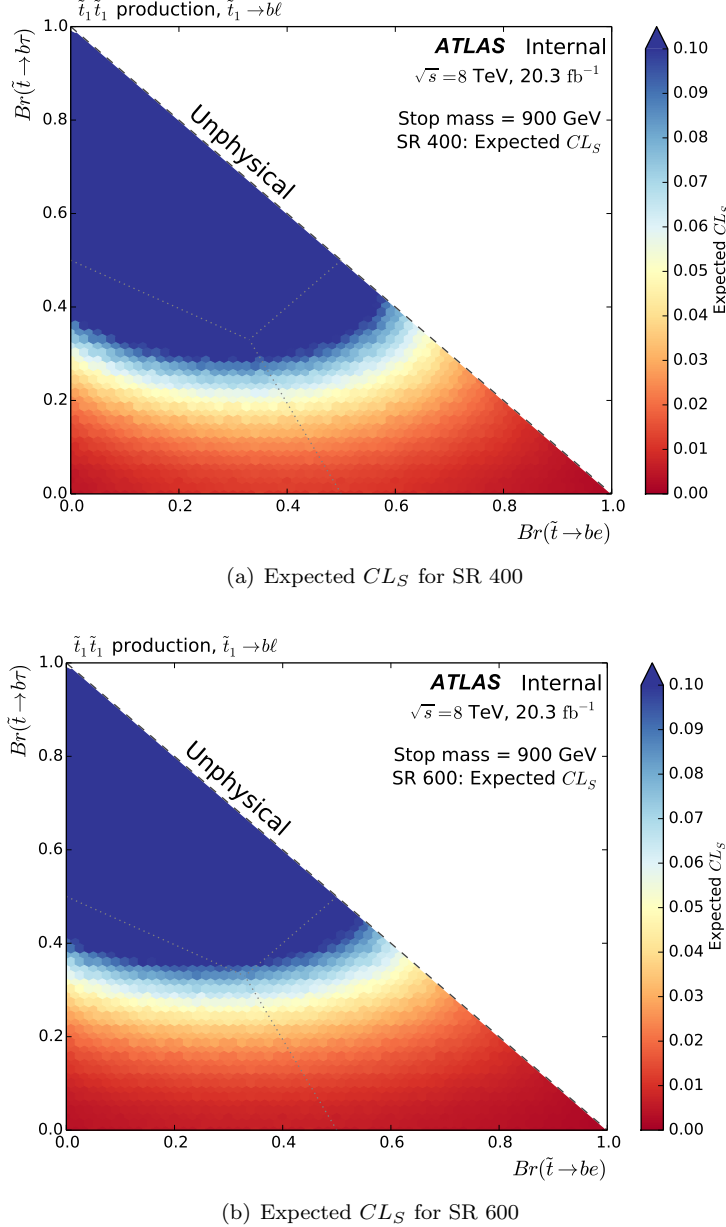
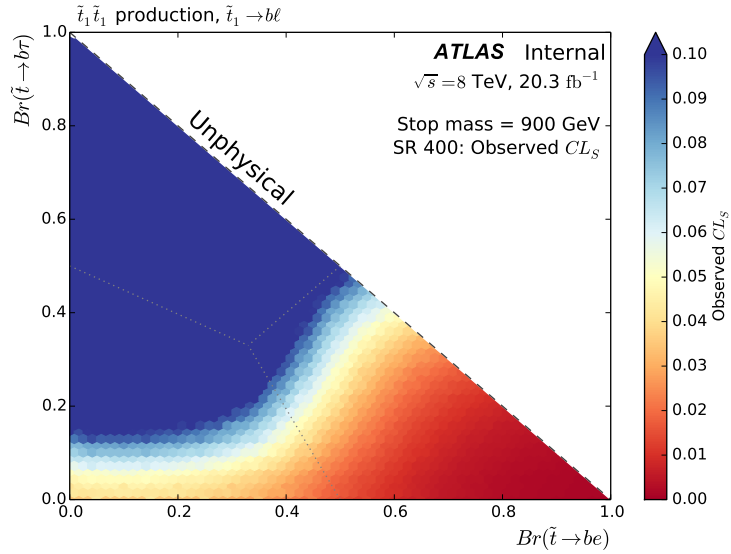
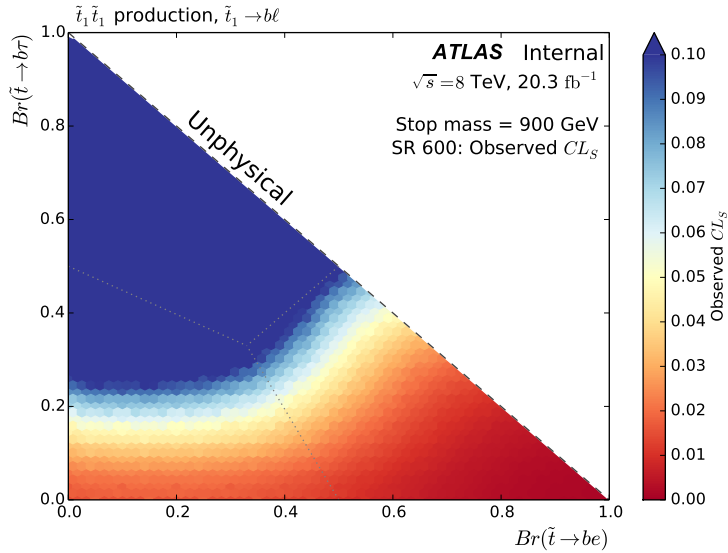


Figure B.16: Expected CL_S values for SR 400 (top) and SR 600 (bottom) for a stop mass of 900 GeV, shown across the plane of physical stop branching ratios.



(a) Observed CL_S for SR 400



(b) Observed CL_S for SR 600

Figure B.17: Observed CL_S values for SR 400 (top) and SR 600 (bottom) for a stop mass of 900 GeV, shown across the plane of physical stop branching ratios.

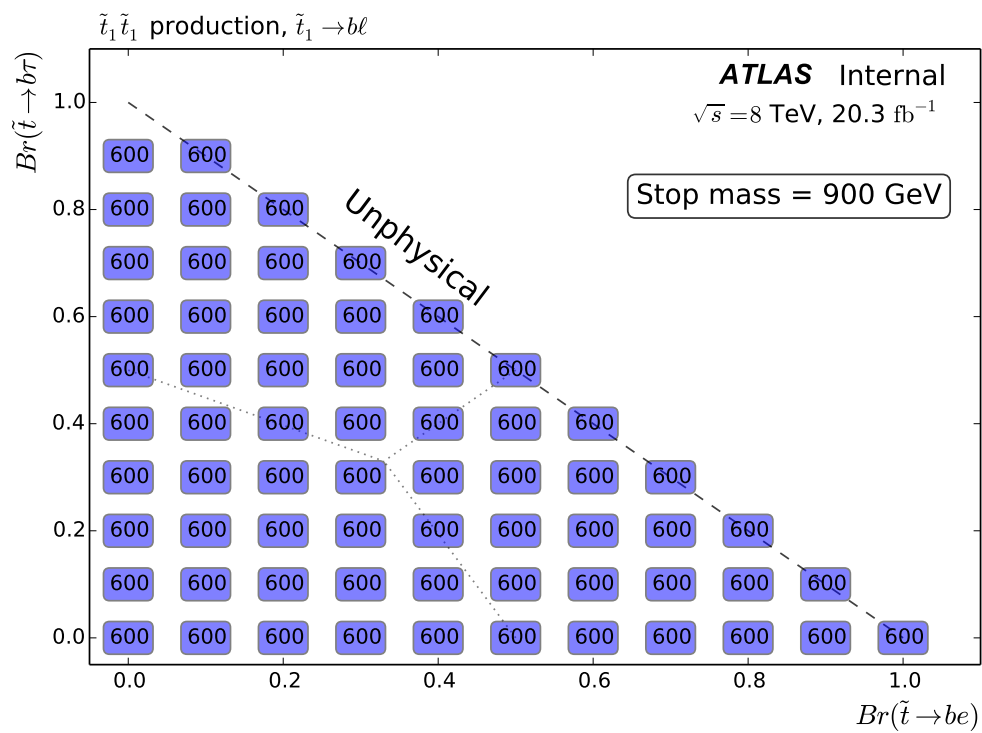


Figure B.18: SR selection for a stop mass of 900 GeV.

B.7 1000 GeV stop mass

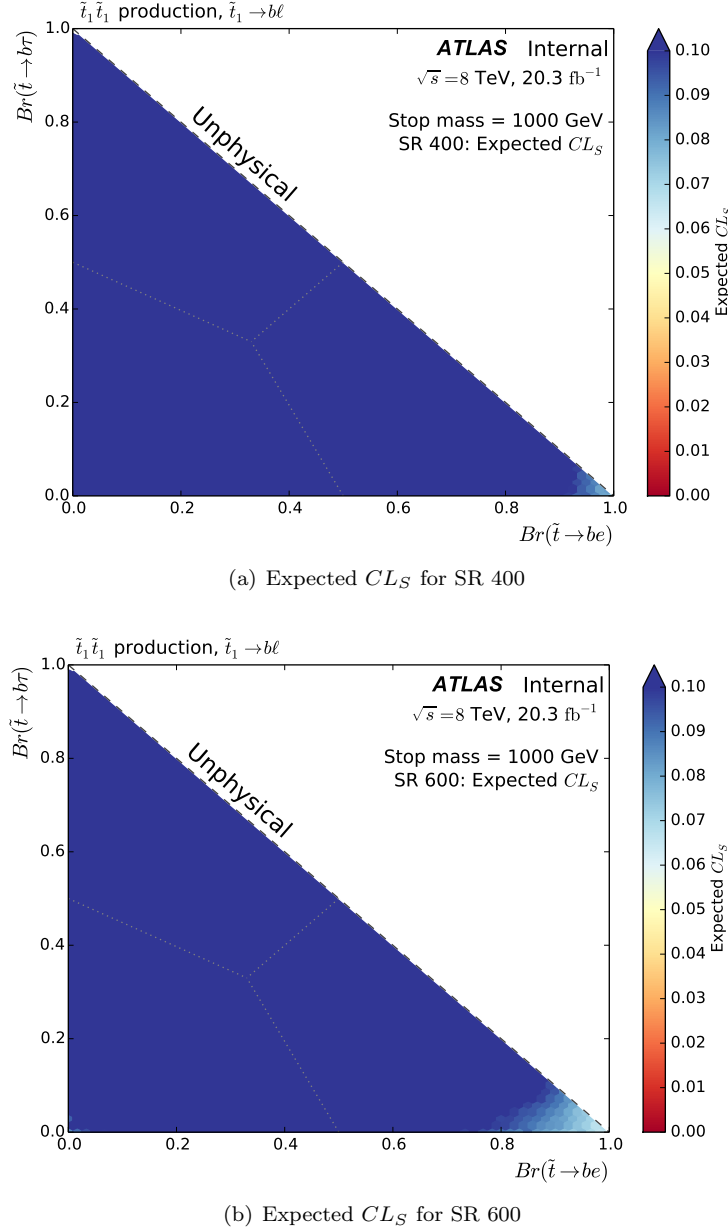


Figure B.19: Expected CL_S values for SR 400 (top) and SR 600 (bottom) for a stop mass of 1 TeV, shown across the plane of physical stop branching ratios.

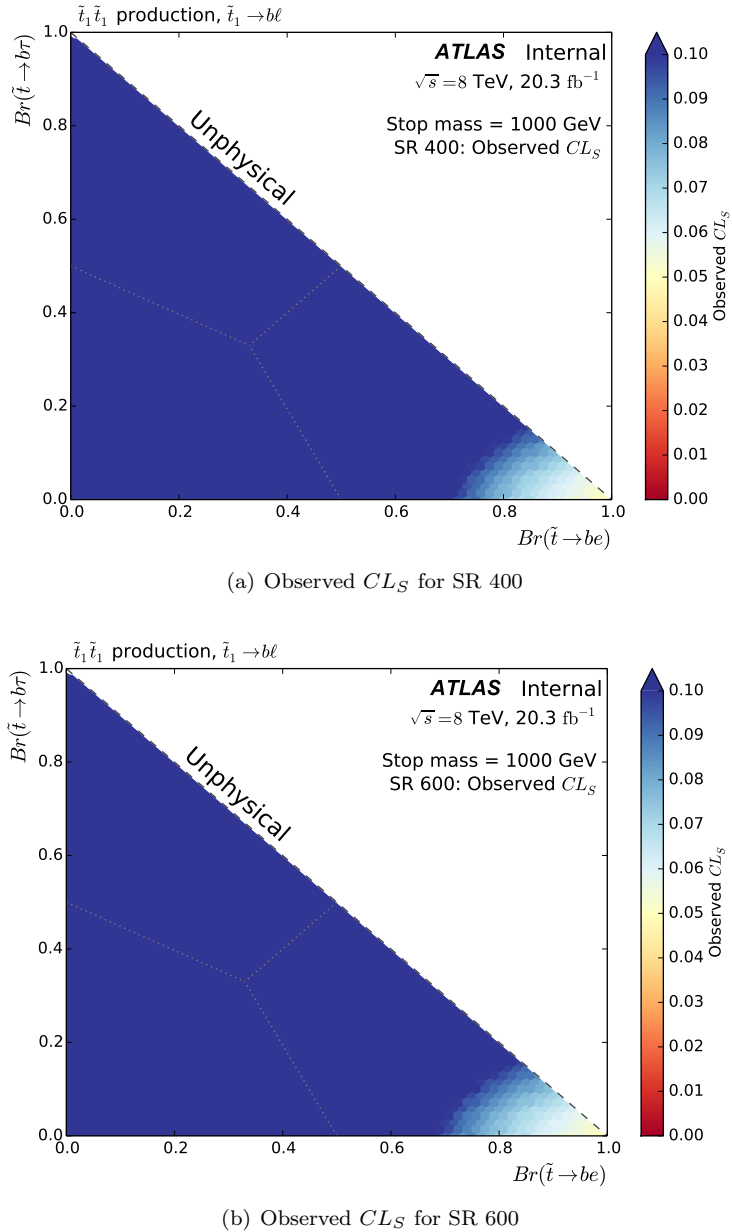


Figure B.20: Observed CL_S values for SR 400 (top) and SR 600 (bottom) for a stop mass of 1 TeV, shown across the plane of physical stop branching ratios.

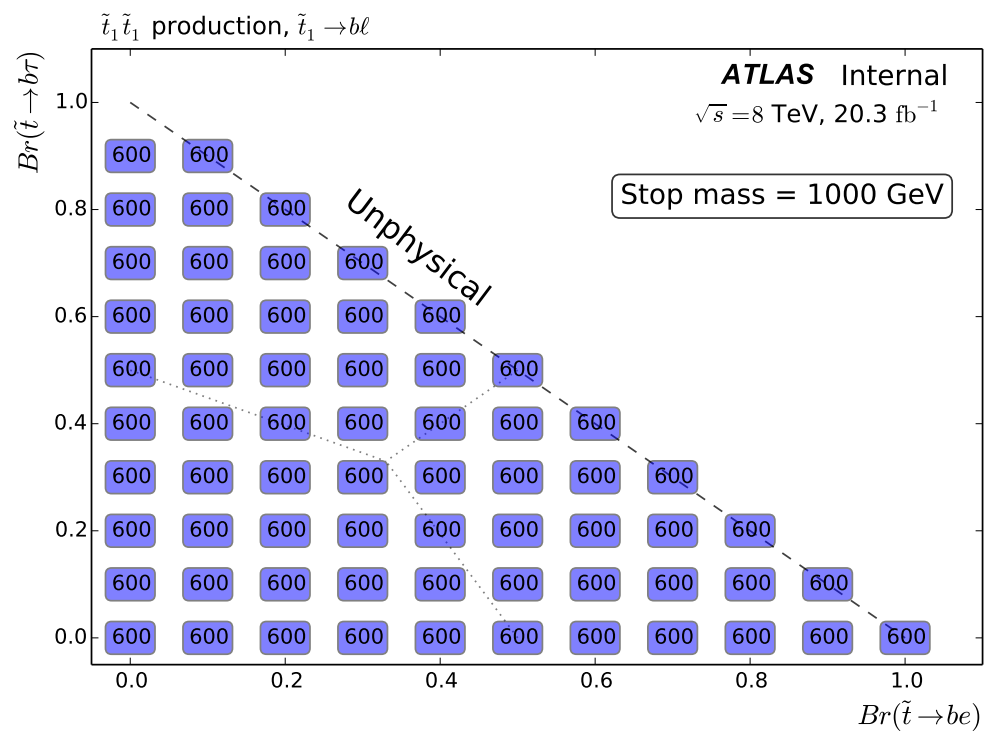


Figure B.21: SR selection for a stop mass of 1 TeV.

B.8 1100 GeV stop mass

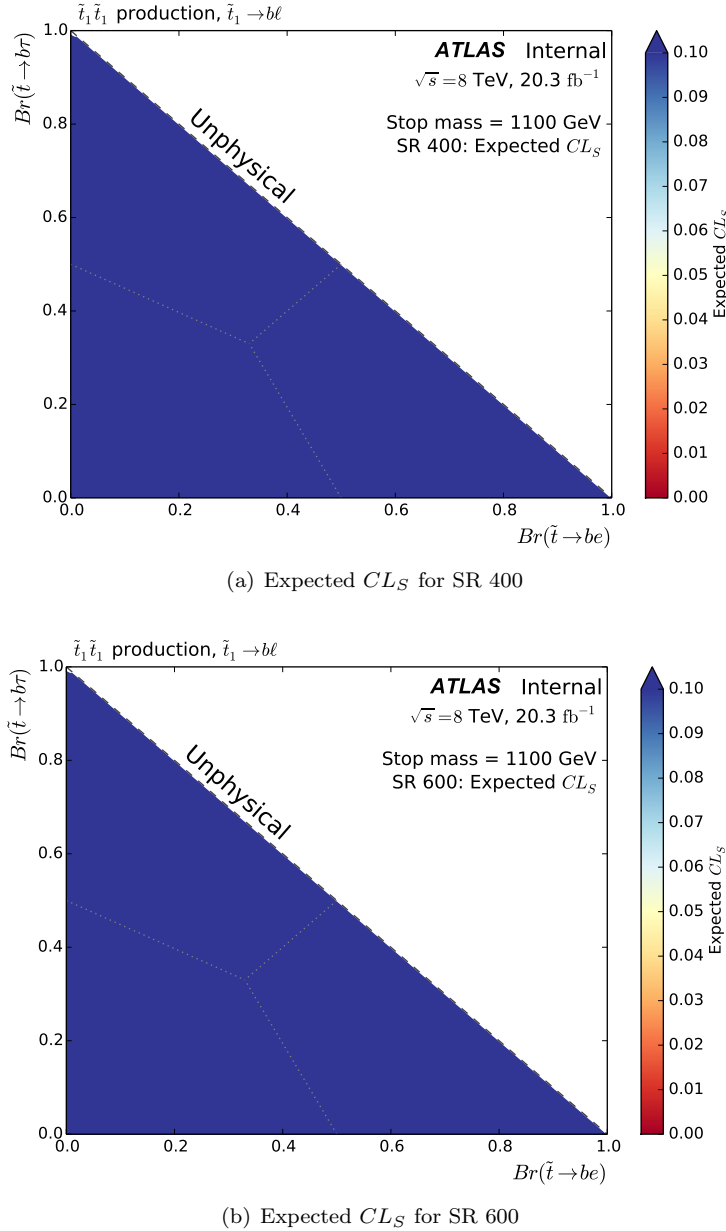
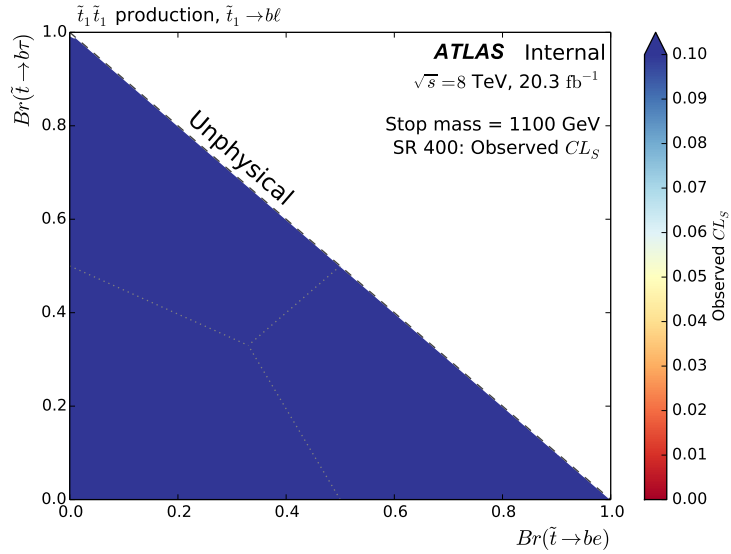
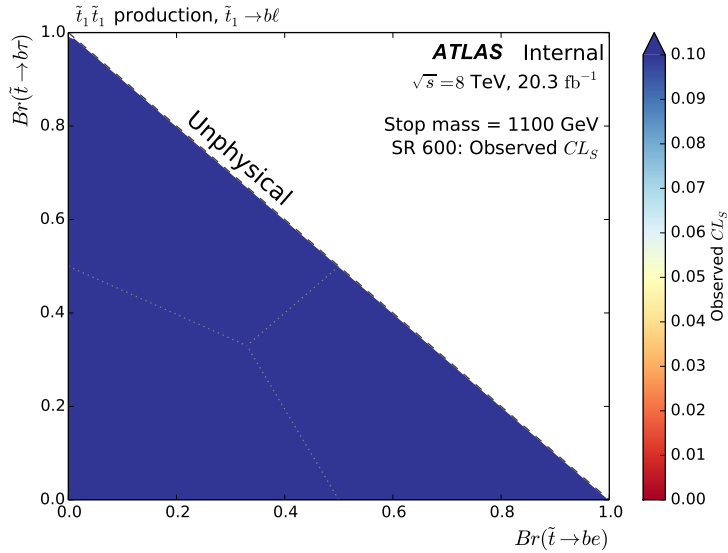


Figure B.22: Expected CL_S values for SR 400 (top) and SR 600 (bottom) for a stop mass of 1.1 TeV, shown across the plane of physical stop branching ratios.



(a) Observed CL_S for SR 400



(b) Observed CL_S for SR 600

Figure B.23: Observed CL_S values for SR 400 (top) and SR 600 (bottom) for a stop mass of 1.1 TeV, shown across the plane of physical stop branching ratios.

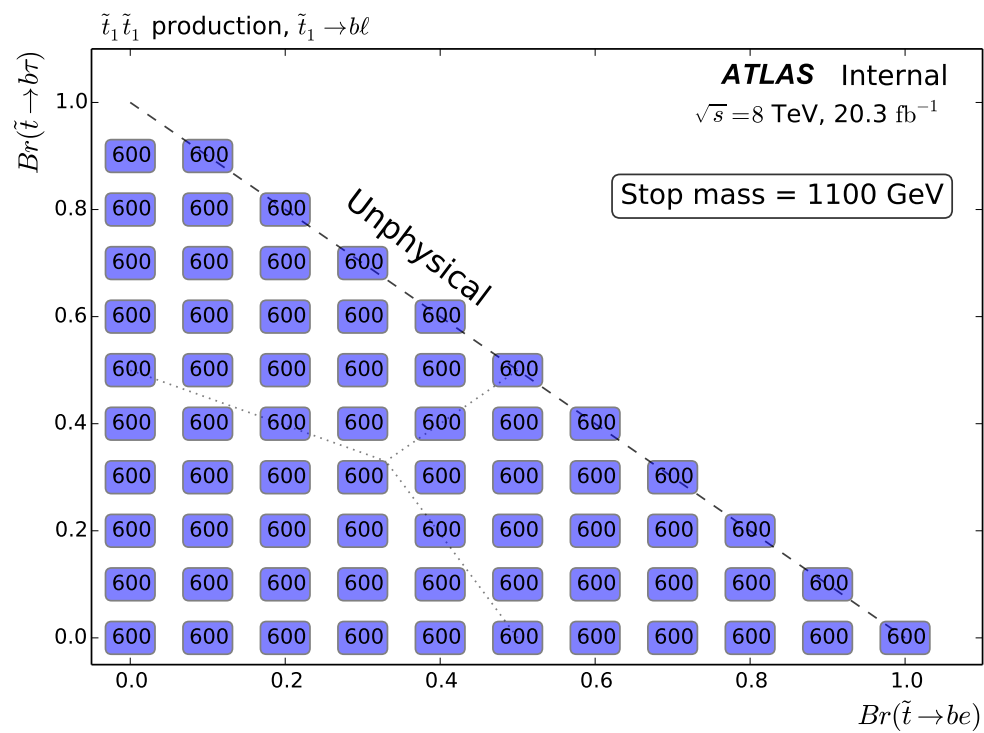


Figure B.24: SR selection for a stop mass of 1.1 TeV.

Bibliography

- [1] I. Aitchison, *Supersymmetry in Particle Physics: An Elementary Introduction*. Cambridge University Press, 2007. <https://books.google.com/books?id=x3QVeJhPBeUC>. (document), 2.3.2, 2.2, 2.3
- [2] Z. Marshall, B. A. Ovrut, A. Purves, and S. Spinner, *LSP Squark Decays at the LHC and the Neutrino Mass Hierarchy*, *Phys. Rev.* **D90** (2014) no. 1, 015034, arXiv:1402.5434 [hep-ph]. (document), 1, 2.5, 2.4.1, 2.4, 2.4.1, 2.6, 2.4.1, 2.4.2, 2.8
- [3] W. Beenakker, M. Kramer, T. Plehn, M. Spira, and P. Zerwas, *Stop Production at Hadron Colliders*, *Nucl. Phys.* **B515** (1998) 3–14, arXiv:hep-ph/9710451 [hep-ph]. (document), 2.7, 5.1, 5.1
- [4] W. Beenakker, S. Brening, M. Kramer, A. Kulesza, E. Laenen, et al., *Supersymmetric Top and Bottom Squark Production at Hadron Colliders*, *J. High Energy Phys.* **1008** (2010) 098, arXiv:1006.4771 [hep-ph]. (document), 2.7, 5.1, 5.1
- [5] W. Beenakker, S. Brening, M. Kramer, A. Kulesza, E. Laenen, et al., *Squark and Gluino Hadroproduction*, *Int. J. Mod. Phys.* **A26** (2011) 2637–2664, arXiv:1105.1110 [hep-ph]. (document), 2.7, 5.1, 5.1
- [6] F. Tanedo. <http://www.quantumdiaries.org/2011/11/21/why-do-we-expect-a-higgs-boson-part-i-electroweak-symmetry-breaking/>. (document), 2.2, 2.3
- [7] ATLAS Collaboration, *ATLAS Photos*, Detector Site, Surface, 2015. (document), 3.1
- [8] F. Marcastel, *CERN’s Accelerator Complex. La chane des accrateurs du CERN*, . <https://cds.cern.ch/record/1621583>. General Photo. (document), 3.2
- [9] ATLAS Collaboration, *Luminosity public results*, LuminosityPublicResults, 2012. (document), 3.3, 5.2
- [10] J. Pequenao, *Computer generated image of the whole ATLAS detector*, Mar, 2008. (document), 3.5
- [11] ATLAS Collaboration, *The ATLAS Experiment at the CERN Large Hadron Collider*, *Journal of Instrumentation* **3** (2008) no. 08, S08003. <http://stacks.iop.org/1748-0221/3/i=08/a=S08003>. (document), 3.6

-
- [12] J. Pequenao, *Computer generated images of the Pixel, part of the ATLAS inner detector.*, Mar, 2008. ([document](#)), 3.7
 - [13] M. Brice, *Vue divers du sub-detector Silicon Tracker de l'exprience Atlas*, Sep, 2005. ([document](#)), 3.8
 - [14] M. Brice, *ATLAS Experiment - View of the inner detector ATLAS TRT.*, Sep, 2005. ([document](#)), 3.9
 - [15] ATLAS Collaboration, *The ATLAS Experiment at the CERN Large Hadron Collider*, Journal of Instrumentation **3** (2008) S08003. jinst.sissa.it/LHC/. ([document](#)), 3.1, 3.2, 3.10
 - [16] J. Pequenao, *Computer generated image of the ATLAS Muons subsystem*, Mar, 2008. ([document](#)), 3.11
 - [17] J. Pequenao and P. Schaffner, *An computer generated image representing how ATLAS detects particles*, Jan, 2013. ([document](#)), 3.12
 - [18] T. Gleisberg, S. Hoeche, F. Krauss, M. Schonherr, S. Schumann, et al., *Event Generation with SHERPA 1.1*, J. High Energy Phys. **0902** (2009) 007, [arXiv:0811.4622 \[hep-ph\]](https://arxiv.org/abs/0811.4622). ([document](#)), 4.1, 5.6.1
 - [19] . ([document](#)), 4.2
 - [20] G. P. Salam, *Elements of QCD for hadron colliders*, [arXiv:1011.5131 \[hep-ph\]](https://arxiv.org/abs/1011.5131). ([document](#)), 4.3, 4.1.4, 4.4, 4.1.4
 - [21] ATLAS Collaboration, ATLAS Collaboration, *Search for the associated production of the Higgs boson with a top quark pair in multilepton final states with the ATLAS detector*, [arXiv:1506.05988 \[hep-ex\]](https://arxiv.org/abs/1506.05988). ([document](#)), 4.5
 - [22] T. Cornelissen, S. Fratina, B. Jackson, C. Schmitt, E. Thomson, and B. Williams, *The Measurement of Cosmic-Ray Time with the Transition Radiation Tracker*, Tech. Rep. ATL-COM-INDET-2010-045, CERN, Geneva, Mar, 2010.
<https://cds.cern.ch/record/1255892>. ([document](#))
 - [23] S. Fratina, B. Jackson, E. Thomson, P. Wagner, and B. Williams, *Track and event time measurement with the ATLAS Transition Radiation Tracker*, Tech. Rep. ATL-COM-INDET-2011-007, CERN, Geneva, Mar, 2011.
<https://cds.cern.ch/record/1340946>. ([document](#))
 - [24] *A search for $B - L$ R-Parity violating scalar top decays in $\sqrt{s} = 8$ TeV pp collisions with the ATLAS experiment*, Tech. Rep. ATLAS-CONF-2015-015, CERN, Geneva, Mar, 2015.
<https://cds.cern.ch/record/2002885>. ([document](#))
 - [25] ATLAS Collaboration, ATLAS Collaboration, *Search for Third Generation Scalar Leptoquarks in pp Collisions at $\sqrt{s} = 7$ TeV with the ATLAS Detector*, J. High Energy Phys. **1306** (2013) 033, [arXiv:1303.0526 \[hep-ex\]](https://arxiv.org/abs/1303.0526). 1, 2.4.2, 6.2.2
 - [26] ATLAS Collaboration, ATLAS Collaboration, *Search for Second Generation Scalar Leptoquarks in pp Collisions at $\sqrt{s} = 7$ TeV with the ATLAS Detector*, Eur. Phys. J. **C72** (2012) 2151, [arXiv:1203.3172 \[hep-ex\]](https://arxiv.org/abs/1203.3172). 1, 2.4.2
 - [27] ATLAS Collaboration, ATLAS Collaboration, *Search for First Generation Scalar Leptoquarks in pp Collisions at $\sqrt{s} = 7$ TeV with the ATLAS Detector*, Phys. Lett. **B709** (2012) 158–176, [arXiv:1112.4828 \[hep-ex\]](https://arxiv.org/abs/1112.4828). 1, 2.4.2

- [28] ATLAS Collaboration, ATLAS Collaboration, *Search for Pair Production of First or Second Generation Leptoquarks in Proton-Proton Collisions at $\sqrt{s} = 7$ TeV Using the ATLAS Detector at the LHC*, *Phys. Rev.* **D83** (2011) 112006, [arXiv:1104.4481 \[hep-ex\]](https://arxiv.org/abs/1104.4481). 1
- [29] CMS Collaboration, CMS Collaboration, *Search for Pair Production of Third-Generation Scalar Leptoquarks and Top Squarks in Proton-Proton Collisions at $\sqrt{s} = 8$ TeV*, *Phys. Lett.* **B739** (2014) 229, [arXiv:1408.0806 \[hep-ex\]](https://arxiv.org/abs/1408.0806). 1
- [30] CMS Collaboration, CMS Collaboration, *Search for Pair-production of First Generation Scalar Leptoquarks in pp Collisions at $\sqrt{s} = 8$ TeV*, Report No. CMS-PAS-EXO-12-041 (2014) . <https://cds.cern.ch/record/1742179>. 1, 2.4.2
- [31] CMS Collaboration, CMS Collaboration, *Search for Pair Production of Third-Generation Leptoquarks and Top Squarks in pp Collisions at $\sqrt{s} = 7$ TeV*, *Phys. Rev. Lett.* **110** (2013) no. 8, 081801, [arXiv:1210.5629 \[hep-ex\]](https://arxiv.org/abs/1210.5629). 1, 2.4.2
- [32] CMS Collaboration, CMS Collaboration, *Search for Pair Production of First- and Second-Generation Scalar Leptoquarks in pp Collisions at $\sqrt{s} = 7$ TeV*, *Phys. Rev.* **D86** (2012) 052013, [arXiv:1207.5406 \[hep-ex\]](https://arxiv.org/abs/1207.5406). 1, 2.4.2
- [33] Z. Marshall, B. A. Ovrut, A. Purves, and S. Spinner, *Spontaneous R-Parity Breaking, Stop LSP Decays and the Neutrino Mass Hierarchy*, *Phys. Lett.* **B732** (2014) 325–329, [arXiv:1401.7989 \[hep-ph\]](https://arxiv.org/abs/1401.7989). 1, 2.4.1, 2.4.1, 2.4.1, 2.4.2
- [34] Particle Data Group Collaboration, K. Olive et al., *Review of Particle Physics*, *Chin.Phys.* **C38** (2014) 090001. 2.1
- [35] M. E. Peskin and D. V. Schroeder, *An introduction to quantum field theory*. Advanced book program. Westview Press Reading (Mass.), Boulder (Colo.), 1995.
<http://opac.inria.fr/record=b1131978>. Autre tirage : 1997. 2.1
- [36] F. Halzen and A. Martin, *Quarks and leptons: an introductory course in modern particle physics*. Wiley, 1984. <https://books.google.com/books?id=zwDvAAAAMAAJ>. 2.1
- [37] LHCb Collaboration, The LHCb Collaboration, *Observation of $J/\psi p$ resonances consistent with pentaquark states in $\Lambda_b^0 \rightarrow J/\psi K^- p$ decays*, [arXiv:1507.03414 \[hep-ex\]](https://arxiv.org/abs/1507.03414). 2.1.3
- [38] F. Englert and R. Brout, *Broken Symmetry and the Mass of Gauge Vector Mesons*, *Phys. Rev. Lett.* **13** (Aug, 1964) 321–323.
<http://link.aps.org/doi/10.1103/PhysRevLett.13.321>. 2.1.4
- [39] P. Higgs, *Broken symmetries, massless particles and gauge fields*, *Physics Letters* **12** (1964) no. 2, 132 – 133.
<http://www.sciencedirect.com/science/article/pii/0031916364911369>. 2.1.4
- [40] P. W. Higgs, *Broken Symmetries and the Masses of Gauge Bosons*, *Phys. Rev. Lett.* **13** (Oct, 1964) 508–509. <http://link.aps.org/doi/10.1103/PhysRevLett.13.508>. 2.1.4
- [41] G. S. Guralnik, C. R. Hagen, and T. W. B. Kibble, *Global Conservation Laws and Massless Particles*, *Phys. Rev. Lett.* **13** (Nov, 1964) 585–587.
<http://link.aps.org/doi/10.1103/PhysRevLett.13.585>. 2.1.4
- [42] ATLAS, CMS Collaboration, The ATLAS Collaboration, *Combined Measurement of the Higgs Boson Mass in pp Collisions at $\sqrt{s} = 7$ and 8 TeV with the ATLAS and CMS Experiments*, *Phys. Rev. Lett.* **114** (2015) 191803, [arXiv:1503.07589 \[hep-ex\]](https://arxiv.org/abs/1503.07589). 2.1.4

-
- [43] D. Clowe, M. Bradac, A. H. Gonzalez, M. Markevitch, S. W. Randall, et al., *A direct empirical proof of the existence of dark matter*, *Astrophys.J.* **648** (2006) L109–L113, [arXiv:astro-ph/0608407 \[astro-ph\]](https://arxiv.org/abs/astro-ph/0608407). [2.2.2](#)
- [44] Planck Collaboration, P. Ade et al., *Planck 2013 results. XVI. Cosmological parameters*, *Astron.Astrophys.* **571** (2014) A16, [arXiv:1303.5076 \[astro-ph.CO\]](https://arxiv.org/abs/1303.5076). [2.2.2](#)
- [45] J. B. e. a. Particle Data Group Collaboration, *Review of Particle Physics**, *Phys. Rev. D* **86** (Jul, 2012) 010001. <http://link.aps.org/doi/10.1103/PhysRevD.86.010001>. [2.2.3](#)
- [46] H. Miyazawa, *Baryon Number Changing Currents*, *Prog. Theor. Phys.* **36** (6) (1966) 1266–1276. [2.3](#)
- [47] H. Miyazawa, *Spinor Currents and Symmetries of Baryons and Mesons*, *Phys. Rev.* **170** (Jun, 1968) 1586–1590. <http://link.aps.org/doi/10.1103/PhysRev.170.1586>. [2.3](#)
- [48] V. A. D.V. Volkov, *Possible universal neutrino interaction*, *JETP Lett.* **16** (1972) 438–440. [2.3](#)
- [49] V. A. D.V. Volkov, *Is the Neutrino a Goldstone Particle?*, *Phys.Lett.* **B46** (1973) 109–110. [2.3](#)
- [50] V. S. D.V. Volkov, *Higgs Effect for Goldstone Particles with Spin 1/2*, *JETP Lett.* **18** (1973) 312–314. [2.3](#)
- [51] P. Ramond, *Dual Theory for Free Fermions*, *Phys. Rev.* **D3** (1971) 2415–2418. [2.3](#)
- [52] Y. A. Golfand and E. P. Likhtman, *Extension of the Algebra of Poincare Group Generators and Violation of p Invariance*, *JETP Lett.* **13** (1971) 323–326. [2.3](#)
- [53] A. Neveu and J. H. Schwarz, *Factorizable Dual Model of Pions*, *Nucl. Phys.* **B31** (1971) 86–112. [2.3](#)
- [54] A. Neveu and J. H. Schwarz, *Quark Model of Dual Pions*, *Phys. Rev.* **D4** (1971) 1109–1111. [2.3](#)
- [55] J. Gervais and B. Sakita, *Field Theory Interpretation of Supergauges in Dual Models*, *Nucl. Phys.* **B34** (1971) 632–639. [2.3](#)
- [56] J. Wess and B. Zumino, *A Lagrangian Model Invariant Under Supergauge Transformations*, *Phys. Lett.* **B49** (1974) 52. [2.3](#)
- [57] J. Wess and B. Zumino, *Supergauge Transformations in Four-Dimensions*, *Nucl. Phys.* **B70** (1974) 39–50. [2.3](#)
- [58] S. P. Martin, *A Supersymmetry primer*, *Adv.Ser.Direct.High Energy Phys.* **21** (2010) 1–153, [arXiv:hep-ph/9709356 \[hep-ph\]](https://arxiv.org/abs/hep-ph/9709356). [2.3.2](#)
- [59] N. Polonsky, *Supersymmetry: Structure and phenomena. Extensions of the standard model*, *Lect.Notes Phys.* **M68** (2001) 1–169, [arXiv:hep-ph/0108236 \[hep-ph\]](https://arxiv.org/abs/hep-ph/0108236). [2.3.2](#)
- [60] P. Fayet, *Supersymmetry and Weak, Electromagnetic and Strong Interactions*, *Phys. Lett.* **B64** (1976) 159. [2.3.5](#)
- [61] P. Fayet, *Spontaneously Broken Supersymmetric Theories of Weak, Electromagnetic and Strong Interactions*, *Phys. Lett.* **B69** (1977) 489. [2.3.5](#)
- [62] G. R. Farrar and P. Fayet, *Phenomenology of the Production, Decay, and Detection of New Hadronic States Associated with Supersymmetry*, *Phys. Lett.* **B76** (1978) 575–579. [2.3.5](#)

- [63] P. Fayet, *Relations Between the Masses of the Superpartners of Leptons and Quarks, the Goldstino Couplings and the Neutral Currents*, *Phys. Lett.* **B84** (1979) 416. [2.3.5](#)
- [64] S. Dimopoulos and H. Georgi, *Softly Broken Supersymmetry and SU(5)*, *Nucl. Phys.* **B193** (1981) 150. [2.3.5](#)
- [65] P. Fileviez Perez and S. Spinner, *Spontaneous R-Parity Breaking and Left-Right Symmetry*, *Phys. Lett.* **B673** (2009) 251–254, [arXiv:0811.3424 \[hep-ph\]](#). [2.4](#)
- [66] V. Barger, P. Fileviez Perez, and S. Spinner, *Minimal Gauged $U(1)_{B-L}$ Model with Spontaneous R-Parity Violation*, *Phys. Rev. Lett.* **102** (2009) 181802, [arXiv:0812.3661 \[hep-ph\]](#). [2.4](#)
- [67] P. Fileviez Perez and S. Spinner, *Spontaneous R-Parity Breaking in SUSY Models*, *Phys. Rev.* **D80** (2009) 015004, [arXiv:0904.2213 \[hep-ph\]](#). [2.4](#)
- [68] L. L. Everett, P. Fileviez Perez, and S. Spinner, *The Right Side of TeV Scale Spontaneous R-Parity Violation*, *Phys. Rev.* **D80** (2009) 055007, [arXiv:0906.4095 \[hep-ph\]](#). [2.4](#)
- [69] M. Evans and B. A. Ovrut, *The World Sheet Supergravity of the Heterotic String*, *Phys. Lett.* **B171** (1986) 177. [2.4](#)
- [70] A. Lukas, B. A. Ovrut, K. Stelle, and D. Waldram, *The Universe As a Domain Wall*, *Phys. Rev.* **D59** (1999) 086001, [arXiv:hep-th/9803235 \[hep-th\]](#). [2.4](#)
- [71] V. Braun, Y.-H. He, B. A. Ovrut, and T. Pantev, *A Heterotic Standard Model*, *Phys. Lett.* **B618** (2005) 252–258, [arXiv:hep-th/0501070 \[hep-th\]](#). [2.4](#)
- [72] V. Braun, Y.-H. He, B. A. Ovrut, and T. Pantev, *The Exact MSSM Spectrum From String Theory*, *J. High Energy Phys.* **0605** (2006) 043, [arXiv:hep-th/0512177 \[hep-th\]](#). [2.4](#)
- [73] V. Braun, Y.-H. He, and B. A. Ovrut, *Stability of the Minimal Heterotic Standard Model Bundle*, *J. High Energy Phys.* **0606** (2006) 032, [arXiv:hep-th/0602073 \[hep-th\]](#). [2.4](#)
- [74] M. Ambroso and B. Ovrut, *The $B-L$ /Electroweak Hierarchy in Heterotic String and M-Theory*, *J. High Energy Phys.* **0910** (2009) 011, [arXiv:0904.4509 \[hep-th\]](#). [2.4](#)
- [75] M. Ambroso and B. A. Ovrut, *The Mass Spectra, Hierarchy and Cosmology of $B-L$ MSSM Heterotic Compactifications*, *Int. J. Mod. Phys.* **A26** (2011) 1569–1627, [arXiv:1005.5392 \[hep-th\]](#). [2.4](#)
- [76] B. A. Ovrut, A. Purves, and S. Spinner, *Wilson Lines and a Canonical Basis of $SU(4)$ Heterotic Standard Models*, *J. High Energy Phys.* **1211** (2012) 026, [arXiv:1203.1325 \[hep-th\]](#). [2.4, 2.4.1](#)
- [77] P. Fileviez Perez and S. Spinner, *The Minimal Theory for R-parity Violation at the LHC*, *J. High Energy Phys.* **1204** (2012) 118, [arXiv:1201.5923 \[hep-ph\]](#). [2.4.1](#)
- [78] P. Fileviez Perez and S. Spinner, *Supersymmetry at the LHC and the Theory of R-parity*, *Phys. Lett.* **B728** (2014) 489–495, [arXiv:1308.0524 \[hep-ph\]](#). [2.4.1](#)
- [79] B. A. Ovrut, A. Purves, and S. Spinner, *A Statistical Analysis of the Minimal SUSY $B-L$ Theory*, [arXiv:1412.6103 \[hep-ph\]](#). [2.4.1](#)
- [80] B. A. Ovrut, A. Purves, and S. Spinner, *The Minimal SUSY $B-L$ Model: From the Unification Scale to the LHC*, [arXiv:1503.01473 \[hep-ph\]](#). [2.4.1](#)

-
- [81] R. Barbieri and G. Giudice, *Upper Bounds on Supersymmetric Particle Masses*, Nucl. Phys. **B306** (1988) 63. [2.4.1](#)
 - [82] B. de Carlos and J. Casas, *One Loop Analysis of the Electroweak Breaking in Supersymmetric Models and the Fine Tuning Problem*, Phys. Lett. **B309** (1993) 320–328, [arXiv:hep-ph/9303291 \[hep-ph\]](#). [2.4.1](#)
 - [83] CMS Collaboration, CMS Collaboration, *Search for third-generation leptoquarks and scalar bottom quarks in pp collisions at $\sqrt{s} = 7$ TeV*, J. High Energy Phys. **1212** (2012) 055, [arXiv:1210.5627 \[hep-ex\]](#). [2.4.2](#)
 - [84] L. Evans and P. Bryant, *LHC Machine*, Journal of Instrumentation **3** (2008) S08001. [jinst.sissa.it/LHC/](#). [3.1](#)
 - [85] CMS Collaboration, *The CMS experiment at the CERN LHC*, Journal of Instrumentation **3** (2008) S08004. [jinst.sissa.it/LHC/](#). [3.1](#)
 - [86] ALICE Collaboration, *The ALICE experiment at the CERN LHC*, Journal of Instrumentation **3** (2008) S08002. [jinst.sissa.it/LHC/](#). [3.1](#)
 - [87] LHCb Collaboration, *The LHCb Detector at the LHC*, Journal of Instrumentation **3** (2008) S08005. [jinst.sissa.it/LHC/](#). [3.1](#)
 - [88] ATLAS Collaboration, *ATLAS pixel detector electronics and sensors*, Journal of Instrumentation **3** (2008) no. 07, P07007. [http://stacks.iop.org/1748-0221/3/i=07/a=P07007](#). [3.2.2.1](#)
 - [89] The ATLAS Collaboration Collaboration, *Alignment of the ATLAS Inner Detector and its Performance in 2012*, [ATLAS-CONF-2014-047](#), 2014. [3.2.2.4](#)
 - [90] The ATLAS Collaboration Collaboration, *Performance of the ATLAS Inner Detector Track and Vertex Reconstruction in the High Pile-Up LHC Environment*, [ATLAS-CONF-2012-042](#), 2012. [3.2.2.4](#)
 - [91] M. Cacciari, G. P. Salam, and G. Soyez, *The Anti- k_t Jet Clustering Algorithm*, J. High Energy Phys. **04** (2008) 063, [arXiv:0802.1189 \[hep-ph\]](#). [3.4.3](#), [5.2](#)
 - [92] M. Cacciari and G. P. Salam, *Dispelling the N^3 Myth for the k_t Jet-Finder*, Phys. Lett. B **641** (2006) 57–61, [arXiv:hep-ph/0512210](#). [3.4.3](#)
 - [93] ATLAS Collaboration, ATLAS Collaboration, *Jet Energy Measurement with the ATLAS Detector in Proton-Proton Collisions at $\sqrt{s} = 7$ TeV*, Eur. Phys. J. **C** **73** (2013) 2304, [arXiv:1112.6426 \[hep-ex\]](#). [3.4.3](#), [5.7](#)
 - [94] ATLAS Collaboration, ATLAS Collaboration, *Single Hadron Response Measurement and Calorimeter Jet Energy Scale Uncertainty with the ATLAS Detector at the LHC*, Eur.Phys.J. **C73** (2013) no. 3, 2305, [arXiv:1203.1302 \[hep-ex\]](#). [3.4.3](#)
 - [95] M. Cacciari and G. P. Salam, *Pileup Subtraction Using Jet Areas*, Phys. Lett. **B659** (2008) 119–126, [arXiv:0707.1378 \[hep-ph\]](#). [3.4.3](#)
 - [96] ATLAS Collaboration, *Calibration of b-Tagging Using Dileptonic Top Pair Events in a Combinatorial Likelihood Approach with the ATLAS Experiment*, Report No. ATLAS-CONF-2014-004 (2014) . [https://cds.cern.ch/record/1664335](#). [3.4.3.1](#), [5.2](#)

- [97] ATLAS Collaboration, *Calibration of the Performance of b-Tagging for c and Light-Flavour Jets in the 2012 ATLAS Data*, Report No. ATLAS-CONF-2014-046 (2014) .
<https://cds.cern.ch/record/1741020>. 3.4.3.1, 5.2
- [98] ATLAS Collaboration, *Performance of Missing Transverse Momentum Reconstruction in ATLAS Studied in Proton-Proton Collisions Recorded in 2012 at 8 TeV*, Report No. ATLAS-CONF-2013-082 (2013) . <https://cds.cern.ch/record/1570993>. 3.4.4
- [99] CDF Collaboration, R. D. Field, *The Underlying event in hard scattering processes*, eConf C010630 (2001) P501, arXiv:hep-ph/0201192 [hep-ph]. 4.1
- [100] P. M. Nadolsky, H.-L. Lai, Q.-H. Cao, J. Huston, J. Pumplin, et al., *Implications of CTEQ Global Analysis for Collider Observables*, Phys. Rev. **D78** (2008) 013004, arXiv:0802.0007 [hep-ph]. 4.1.1, 5.1, 5.6.1
- [101] J. Alwall, S. de Visscher, and F. Maltoni, *QCD radiation in the production of heavy colored particles at the LHC*, JHEP **0902** (2009) 017, arXiv:0810.5350 [hep-ph]. 4.1.4
- [102] ATLAS Collaboration, *The ATLAS Simulation Infrastructure*, European Physical Journal C **70** (Dec., 2010) 823–874, arXiv:1005.4568 [physics.ins-det]. 4.2
- [103] J. Alwall, M. Herquet, F. Maltoni, O. Mattelaer, and T. Stelzer, *MadGraph 5 : Going Beyond*, J. High Energy Phys. **1106** (2011) 128, arXiv:1106.0522 [hep-ph]. 5.1
- [104] T. Sjöstrand., S. Mrenna, and P. Z. Skands, *PYTHIA 6.4 Physics and Manual*, J. High Energy Phys. **0605** (2006) 026, arXiv:hep-ph/0603175 [hep-ph]. 5.1
- [105] M. Kramer, A. Kulesza, R. van der Leeuw, M. Mangano, S. Padhi, et al., *Supersymmetry Production Cross Sections in pp Collisions at $\sqrt{s} = 7$ TeV*, arXiv:1206.2892 [hep-ph]. 5.1
- [106] ATLAS Collaboration, ATLAS Collaboration, *Electron and photon energy calibration with the ATLAS detector using LHC Run 1 data*, Eur. Phys. J. **C74** (2014) no. 10, 3071, arXiv:1407.5063 [hep-ex]. 5.2
- [107] ATLAS Collaboration, ATLAS Collaboration, *Measurement of the Muon Reconstruction Performance of the ATLAS Detector Using 2011 and 2012 LHC Proton-Proton Collision Data*, Eur. Phys. J. **C74** (2014) no. 11, 3130, arXiv:1407.3935 [hep-ex]. 5.2, 5.4
- [108] ATLAS Collaboration, ATLAS Collaboration, *Improved Luminosity Determination in pp Collisions at $\sqrt{s} = 7$ TeV Using the ATLAS Detector at the LHC*, Eur. Phys. J. **C73** (2013) no. 8, 2518, arXiv:1302.4393 [hep-ex]. 5.3
- [109] ATLAS Collaboration, *Electron efficiency measurements with the ATLAS detector using the 2012 LHC proton-proton collision data*, Tech. Rep. ATLAS-CONF-2014-032, CERN, Geneva, Jun, 2014. <https://cds.cern.ch/record/1706245>. 5.4
- [110] P. Nason, *A New Method for Combining NLO QCD with Shower Monte Carlo Algorithms*, J. High Energy Phys. **0411** (2004) 040, arXiv:hep-ph/0409146 [hep-ph]. 5.6.1
- [111] S. Frixione, P. Nason, and C. Oleari, *Matching NLO QCD Computations with Parton Shower Simulations: the POWHEG Method*, J. High Energy Phys. **0711** (2007) 070, arXiv:0709.2092 [hep-ph]. 5.6.1
- [112] S. Alioli, P. Nason, C. Oleari, and E. Re, *A General Framework for Implementing NLO Calculations in Shower Monte Carlo Programs: the POWHEG BOX*, J. High Energy Phys. **1006** (2010) 043, arXiv:1002.2581 [hep-ph]. 5.6.1

-
- [113] S. Frixione, P. Nason, and G. Ridolfi, *A Positive-Weight Next-to-Leading-Order Monte Carlo for Heavy Flavour Hadroproduction*, *J. High Energy Phys.* **0709** (2007) 126, [arXiv:0707.3088 \[hep-ph\]](#). [5.6.1](#)
 - [114] ATLAS Collaboration, ATLAS Collaboration, *Measurements of Top Quark Pair Relative Differential Cross-Sections with ATLAS in pp Collisions at $\sqrt{s} = 7$ TeV*, *Eur. Phys. J.* **C73** (2013) no. 1, 2261, [arXiv:1207.5644 \[hep-ex\]](#). [5.6.1](#)
 - [115] ATLAS Collaboration, ATLAS Collaboration, *Measurements of Normalized Differential Cross Sections for $t\bar{t}$ Production in pp Collisions at $\sqrt{s} = 7$ TeV Using the ATLAS Detector*, *Phys. Rev.* **D90** (2014) no. 7, 072004, [arXiv:1407.0371 \[hep-ex\]](#). [5.6.1](#)
 - [116] S. Alioli, P. Nason, C. Oleari, and E. Re, *NLO Single-Top Production Matched with Shower in POWHEG: s- and t-Channel Contributions*, *J. High Energy Phys.* **0909** (2009) 111, [arXiv:0907.4076 \[hep-ph\]](#). [5.6.1](#)
 - [117] B. P. Kersevan and E. Richter-Was, *The Monte Carlo Event Generator AcerMC Versions 2.0 to 3.8 with Interfaces to PYTHIA 6.4, HERWIG 6.5 and ARIADNE 4.1*, *Comput. Phys. Commun.* **184** (2013) 919–985, [arXiv:hep-ph/0405247 \[hep-ph\]](#). [5.6.1](#)
 - [118] M. Baak, G. Besjes, D. Cote, A. Koutsman, J. Lorenz, et al., *HistFitter Software Framework for Statistical Data Analysis*, [arXiv:1410.1280 \[hep-ex\]](#). [5.6.4](#), [6.1](#), [6.1](#), [6.2](#)
 - [119] ATLAS Collaboration, ATLAS Collaboration, *Measurement of the production cross section of jets in association with a Z boson in pp collisions at $\sqrt{s} = 7$ TeV with the ATLAS detector*, *JHEP* **1307** (2013) 032, [arXiv:1304.7098 \[hep-ex\]](#). [5.6.4](#)
 - [120] ATLAS Collaboration, ATLAS Collaboration, *Measurement of differential production cross-sections for a Z boson in association with b-jets in 7 TeV proton-proton collisions with the ATLAS detector*, *JHEP* **1410** (2014) 141, [arXiv:1407.3643 \[hep-ex\]](#). [5.6.4](#)
 - [121] ATLAS Collaboration, ATLAS Collaboration, *Jet Energy Resolution and Selection Efficiency Relative to Track Jets from In-Situ Techniques with the ATLAS Detector Using Proton-Proton Collisions at a Center of Mass Energy $\sqrt{s} = 7$ TeV*, Report No. ATLAS-CONF-2010-054 (2010) . <https://cds.cern.ch/record/1281311>. [5.7](#)
 - [122] A. L. Read, *Presentation of search results: the CL s technique*, *Journal of Physics G: Nuclear and Particle Physics* **28** (2002) no. 10, 2693.
<http://stacks.iop.org/0954-3899/28/i=10/a=313>. [A.2](#)
 - [123] G. Cowan, K. Cranmer, E. Gross, and O. Vitells, *Asymptotic formulae for likelihood-based tests of new physics*, *European Physical Journal C* **71** (Feb., 2011) 1554, [arXiv:1007.1727 \[physics.data-an\]](#). [A.2](#)